Photosensitive Targeted Nanocarriers for Selective Delivery of Photodynamic Therapy

Elena de las Heras Guilarte

UNIVERSITAT RAMON LLULL

DOCTORAL THESIS

Title	Photosensitive Targeted Nanocarriers for Selective Delivery of Photodynamic Therapy
Presented by	Elena de las Heras Guilarte
Centre	IQS School of Engineering
Department	Analytical and Applied Chemistry
Directed by	Prof. Dr. Montserrat Agut Bonsfills Prof. Dr. Santi Nonell Marrugat

C. Claravall, 1-3 | 08022 Barcelona | Tel. 93 602 22 00 | Fax 93 602 22 49 | info@url.edu | www.url.edu

Equipped with his five senses, man explores the universe around him and calls the adventure **Science**.

Edwin Powell Hubble

ACKNOWLEDGMENTS

El soporte financiero para la realización de esta tesis ha sido proporcionado por el Ministerio de Economía y Competitividad de España mediante el proyecto CTQ2016-78454-C2-1-R. Así mismo, me gustaría agradecer al Instituto Químico de Sarrià por la beca predoctoral que me ha ayudado económicamente durante la realización de mis estudios de doctorado. Gracias también a los profesores Ross W. Boyle (Universidad de Hull), Norbert Lange (Universidad de Ginebra) y Anzhela Galstyan (Universidad de Münster) por proporcionarnos algunos de los compuestos usados en esta tesis.

Seguidamente, quiero dar las gracias a todos aquellos que han sido participes de este viaje de 3 años, especialmente a los miembros de FotoQ. Quiero mencionar específicamente y con gran afecto a mis directores de tesis, Montse y Santi, por darme la oportunidad de formar parte de este increíble equipo. Gracias por vuestra ayuda y dedicación durante este tiempo, no sólo en el aspecto científico, sino también en lo personal. Igualmente, me gustaría agradecer a M. Lluïsa por guiarme en el ámbito celular.

Por último, pero no menos importante, agradecer a mi familia por su apoyo incondicional, a quienes dedico con un enorme cariño esta tesis.

ABSTRACT

This thesis reports the study of active-targeting nanocarriers as drug delivery systems for photodynamic therapy for cancer purposes. Poly-(*D,L*-lactide-*co*-glycolide) (PLGA) nanoparticles and mesoporous silica nanoparticles (MSNPs) are the two nanovehicles of different nature employed.

The vehiculization of drugs through nanodelivery systems can overcome limitations that conventional delivery experiences, such as increasing its selectivity. In this regard, the major limitation of any cancer therapy lies on the difficulty to precisely control the localization of the drug in the tumor tissue and not in a healthy one. In order to improve this drawback, the delivery of drugs through nanocarriers can actively-target to tumor cells by grafting targeting ligands to the nanosystem that can recognize and bind to surface receptors overexpressed by these cells. In this thesis, two active-targeting ligands have been explored: the c(RGDfK) peptide and the Cetuximab antibody.

First, PLGA nanoparticles with the photosensitizer ZnTriMPyP covalently attached and grafted with the c(RGDfK) peptide have been developed. Their physicochemical and photophysical properties have been studied, as also assessing their phototoxic activity. Covalent binding of the hydrophilic ZnTriMPyP to the surface of PEG-coated PLGA nanoparticles improves the phototoxicity and dark toxicity of the nanosystem compared to related nanocarriers with the photosensitizer occluded. The conjugation of c(RGDfK) peptide provides an enhancement in photodynamic action against tumor cells expressing the $\alpha_v\beta_3$ integrin receptor but does not prevent damage to cells lacking this integrin.

Secondly, immuno-photo-nanocarriers have been explored. For this, PEG-coated MSNPs decorated with phthalocyanine and Cetuximab have been synthesized. The physicochemical, photophysical and photobiological properties have been studied. Initially, this nanosystem has been prepared with the novel phthalocyanine ZnPcSMP, however, it is strongly aggregated and its photosensitizing ability is quenched when it is covalently attached to MSNPs. In contrast, the phthalocyanine IRDye700DX maintains its ability to generate singlet oxygen and thus the nanosystem achieves photodynamic action in cells. Furthermore, the conjugation of Cetuximab improves the aqueous dispersibility of these nanoparticles and enables their internalization in cells according to the EGFR expression level.

Lastly, chemo-immuno-photo-nanocarriers have been developed. PEG-coated MSNPs

grafted with phthalocyanine, Cetuximab and Doxorubicin have been designed to allow the release on-demand of the antineoplastic agent triggered by light. They have been characterized in terms of their physicochemical and photophysical properties, as also evaluating their phototoxicity *in vitro*. The attachment of small amounts of Doxorubicin onto nanoparticle surface induces a reduction in their singlet oxygen production ability and photodynamic activity. In contrast, with higher concentrations of Doxorubicin, the nanocarrier shows efficient and selective photokilling of EGFR-expressing cells mainly through singlet oxygen-induced cleavage of the Doxorubicin. Therefore, this novel triply functionalized nanosystem is an effective and safe nanodevice for light-triggered on-demand Doxorubicin delivery.

RESUMEN

Esta tesis profundiza en el estudio de nanotransportadores de vehiculización activa como sistemas de distribución de fármacos para terapia fotodinámica contra el cáncer. Se han empleado dos tipos de nanovehículos de diferente naturaleza: nanopartículas de poli-(*D,L*-láctido-*co*-glicólido) (PLGA) y nanopartículas mesoporosas de sílice (MSNPs).

La vehiculización de fármacos mediante sistemas de nanotransporte puede superar ciertas limitaciones que experimenta el suministro de fármacos convencional, como por ejemplo aumentar su selectividad. En relación a esto último, el mayor inconveniente que presenta cualquier terapia contra el cáncer radica en la dificultad de controlar con precisión la localización del fármaco en el tejido tumoral y no en uno sano. Para mejorar esto, la administración de fármacos mediante nanotransportadores permite su vectorización activa a células tumorales gracias a la decoración del nanosistema con ligandos dirigidos a reconocer y unirse a receptores de la superficie celular sobreexpresados en estas células. En esta tesis, se han explorado dos tipos de ligandos vectorizados: el péptido c(RGDfK) y el anticuerpo Cetuximab.

Primero, se han desarrollado nanopartículas de PLGA con el fotosensibilizador ZnTriMPyP unido covalentemente y decoradas con el péptido c(RGDfK). Se han evaluado sus propiedades fisicoquímicas y fotofísicas, al igual que su actividad fototóxica. La unión covalente del compuesto hidrofílico ZnTriMPyP a la superficie de nanopartículas de PLGA-PEG mejora la fototoxicidad y toxicidad a oscuras del nanosistema en comparación con nanotransportadores similares con el fotosensibilizador ocluido. La conjugación del péptido c(RGDfK) mejora la acción fotodinámica contra células tumorales que expresan el receptor de integrina $\alpha_v\beta_3$; pero no evita el daño a células sin dicha integrina.

En segundo lugar, se ha explorado el diseño de inmuno-foto-nanotransportadores. Para esto se han sintetizado PEG-MSNPs decoradas con ftalocianina y Cetuximab. Se han estudiado sus propiedades fisicoquímicas, fotofísicas y fotobiológicas. De entrada, las nanopartículas se han preparado con la ftalocianina ZnPcSMP, no obstante, ésta está fuertemente agregada y su habilidad para producir oxígeno singlete se ve disminuida cuando está unida covalentemente a MSNPs. Por otro lado, la ftalocianina IRDye700DX mantiene su habilidad para generar oxígeno singlete y, por ende, el nanotransportador consigue acción fotodinámica en células. Además, la unión del Cetuximab mejora la dispersión de las nanopartículas en agua, permitiendo su internalización celular según el grado de expresión

de EGFR.

Por último, se han desarrollado quimio-inmuno-foto-nanotransportadores. Se han diseñado MSNPs decoradas con ftalocianina, Cetuximab y Doxorrubicina para permitir la liberación a demanda del agente quimioterapéutico provocado por el oxígeno singlete. Este nanosistema ha sido caracterizado según sus propiedades fisicoquímicas y fotofísicas, al igual que se ha evaluado su fototoxicidad celular. La unión de pequeñas cantidades de Doxorrubicina a la nanopartícula provoca una reducción en su capacidad de producción de oxígeno singlete y actividad fotodinámica. En cambio, con mayores concentraciones de Doxorrubicina, el nanotransportador muestra fototoxicidad eficiente y selectiva contra células que expresan EGFR, principalmente por acción de la Doxorrubicina liberada mediante la rotura de su cadena de unión por oxígeno singlete.

RESUM

Aquesta tesi aprofundeix en l'estudi de nanotransportadors de vehiculització activa com sistemes de distribució de fàrmacs per a teràpia fotodinàmica contra el càncer. Dos tipus de nanovehicles de diferent naturalesa s'han fet servir: nanopartícules de poli-(*D,L*-làctid-*co*-glicòlid) (PLGA) i nanopartícules mesoporoses de sílice (MSNPs).

La vehiculització de fàrmacs mitjançant sistemes de nanotransport pot superar certes limitacions que experimenta el subministrament de fàrmacs convencional, com per exemple, augmentar la seva selectivitat. En relació a aquest últim aspecte, el major inconvenient que presenta qualsevol teràpia contra el càncer és la dificultat de controlar amb precisió la localització del fàrmac en el teixit tumoral i no en un de sà. Per millorar això, l'administració de fàrmacs mitjançant nanotransportadors permet la seva vectorització activa a cèl·lules tumorals gràcies a la decoració del nanosistema amb lligands dirigits a reconèixer i unir-se a receptors de la superfície cel·lular sobreexpressats en aquestes cèl·lules. En aquesta tesi, s'han explorat dos tipus de lligands vectoritzats: el pèptid c(RGDfK) i l'anticòs Cetuximab.

Primer, s'han desenvolupat nanopartícules de PLGA amb el fotosensibilitzador ZnTriMPyP unit covalentment i decorades amb el pèptid c(RGDfK). S'ha avaluat les seves propietats fisicoquímiques i fotofísiques, així com la seva activitat fototóxica. La unió covalent del compost hidrofílic ZnTriMPyP a la superfície de nanopartícules de PLGA-PEG millora la fototoxicitat i toxicitat a les fosques del nanosistema en comparació amb altres nanotransportadors similars amb el fotosensibilitzador oclòs. La conjugació del pèptid c(RGDfK) millora l'acció fotodinàmica contra cèl·lules tumorals que expressen el receptor de integrina $\alpha_v\beta_3$; però no evita el dany a cèl·lules sense aquesta integrina.

En segon lloc, s'ha explorat el disseny d'immuno-foto-nanotransportadors. Per això s'han sintetitzat MSNPs decorades amb ftalocianina i Cetuximab. S'ha estudiat les seves propietats fisicoquímiques, fotofísiques i fotobiològiques. D'entrada, les nanopartícules s'han preparat amb la ftalocianina ZnPcSMP, però aquesta està fortament agregada i la seva capacitat per produir oxigen singlet es veu disminuïda quan està unida covalentment a MSNPs. D'altre banda, la ftalocianina IRDye700DX manté la seva habilitat per produir oxigen singlet i, per tant, el nanotransportador aconsegueix acció fotodinàmica en cèl·lules. A més, la unió del Cetuximab millora la dispersió de les nanopartícules en aigua, permetent la seva internalització cel·lular segons el grau d'expressió d'EGFR.

Per últim, s'han desenvolupat quimio-immuno-foto-nanotransportadors. S'han dissenyat MSNPs decorades amb ftalocianina, Cetuximab i Doxorrubicina per permetre l'alliberament a demanda de l'agent quimioterapèutic provocat per l'oxigen singlet. Aquest nanosistema ha sigut caracteritzant segons les seves propietats fisicoquímiques i fotofísiques i, així mateix, s'ha avaluat la seva fototoxicitat cel·lular. La unió de petites quantitats de Doxorrubicina a la nanopartícula provoca una reducció de la seva capacitat de producció d'oxigen singlet i activitat fotodinàmica. Contràriament, amb majors concentracions de Doxorrubicina, el nanotransportador mostra fototoxicitat eficient i selectiva contra cèl·lules que expressen EGFR, principalment per acció de la Doxorrubicina alliberada mitjançant la ruptura de la seva cadena d'unió per oxigen singlet.

ACRONYMS AND SYMBOLS

^{13}C-NMR	Carbon 13 nuclear magnetic resonance
^{1}H-NMR	Hydrogen 1 nuclear magnetic resonance
$^{1}O_2$	Singlet oxygen
^{1}PS*	Singlet excited state photosensitizer
$^{1}PS_0$	Ground state photosensitizer
$^{1}PS_1$*	First singlet excited state photosensitizer
3-MPA	3-Mercaptopropionic acid
^{3}PS*	Triplet excited state photosensitizer
APTES	(3-Aminopropyl)triethoxilane
AU	Arbitrary units
BCA	Bicinchroninic acid
BSA	Bovine serum albumin
CD_3OD	Deuterated methanol
Cet	Cetuximab
cm	Centimeter
CTAC	Cetyltrimethylammonium chloride
D_2O	Deuterium oxide
DIPEA	*N*,*N*-Diisopropylethylamine
DL	Drug loading
DLS	Dynamic light scattering

DMAP	4-*N,N*-Dimethylaminopyridine
DMF	*N,N*-Dimethylformamide
DMSO	Dimethyl sulfoxide
DOX	Doxorubicin
dPBS	Deuterated phosphate buffered saline
EDC	1-Ethyl-3-(3-dimethylaminopropyl)carbodiimide
EE	Entrapment efficiency
EGF	Epidermal growth factor
EGFR	Epidermal growth factor receptor
EI	Electron ionization
em	Emission
EMA	European medicines agency
EPR	Enhanced permeability and retention
eq	Equivalent
EtOAc	Ethyl acetate
EtOH	Ethanol
exc	Excitation
FDA	U.S. food and drug administration
FITC	Fluorescein-5-isothiocyanate
h	Hour
HPD	Hematoporphyrin derivative
$h\nu$	Light
IC	Internal conversion
IR	Infrared

IRF	Instrumental response factor
ISC	Intersystem crossing
J	Joule
kDa	Kilo Dalton
log	Base 10 logarithm
M	Molar
mAb	Monoclonal antibody
MeOH	Methanol
min	Minutes
mL	Milliliter
mM	Millimolar
mPEG	Methoxy polyethylene glycol
ms	Millisecond
MS	Mass spectroscopy
MSNP	Mesoporous silica nanoparticle
MTT	3-(4,5-dimethylthiazol-2-yl)-2,5-diphenyltetrazolium bromide
mW	Milliwatt
NHS	*N*-hydroxysuccinimide
NIR	Near-infrared
nM	Nanomolar
nm	Nanometer
NMR	Nuclear magnetic resonance
NP	Nanoparticle

ns	Nanosecond
º C	Degree Celsius
PBS	Phosphate buffered saline
Pc	Phthalocyanine
PdI	Polydispersity index
PDT	Photodynamic therapy
PEG	Polyethylene glycol
PIT	Photoimmunotherapy
PLA	Poly-(*D,L*-lactide)
PLGA	Poly-(*D,L*-lactide-*co*-glycolide)
PNS	1H-phenalen-1-one-2-sulphonate
PPa	Pheophorbide a
PS	Photosensitizer
Ref	Reference
ROS	Reactive oxygen species
RT	Room temperature
s	Second
SiNP	Silica nanoparticle
TCSPC	Time-correlated single photon counting
TEOS	Tetraethyl orthosilicate
TESPIC	(Triethoxysilylpropyl)isocyanate
TLC	Thin-layer chromatography
TRPD	Time-resolved NIR phosphorescence detection
UV	Ultraviolet

Vis	Visible
VR	Vibrational relaxation
υ	Wavenumber
wt	Weight
ZnPc	Zinc phthalocyanine
ZnPcSMP	1,8(11),15(18)-tri-(2-mercapto-*N*-methylpyridinium)-23(24)-3-(2-{2-[2-(2-hydroxyethoxy)-ethoxy]ethoxy}ethoxy)phthalocyaninato zinc(II)
ZnTPP	Zn(II)-5-(4-azidophenyl)-10,15,20-triphenyl-porphine
ZnTriMPyP	5-[4-Azidophenyl]-10,15,20-tri-(*N*-methyl-4-pyridinium)porphyrinato zinc (II) trichloride
ε	Molar absorptivity
λ	Wavelength
µg	Microgram
µL	Microliter
µM	Micromolar
µs	Microsecond
Φ_F	Fluorescence quantum yield
Φ_Δ	Singlet oxygen quantum yield
τ_S	Photosensitizer's singlet lifetime
τ_T	Photosensitizer's triplet lifetime

CONTENTS

CHAPTER 1: GENERAL

INTRODUCTION

To provide context and for the better comprehension of the reader, an introduction of the main topics of this thesis is discussed in this chapter.

Moreover, the reader will find a brief introduction at Chapters 4 and 5 in order to give a clearer picture about the research performed in each of them.

1.1 Photodynamic Therapy: An Overview

The use of light for therapeutic purposes has been exploited for thousands of years. Ancient cultures used the combination of plants with sunlight as treatment for various diseases. However, the scientific basis for such use was vague or non-existent before 1900.[1,2] Nowadays, light therapies have become established and widely used treatment modalities for several medical indications. Photodynamic therapy (PDT) is one of those phototherapies.

PDT is a clinically approved therapeutic modality employed against solid tumors and localized microbial infections.[3] The basis of it relies on the combination of three individually non-toxic components: i) a photoactive drug called photosensitizer (PS); ii) a light of a specific wavelength; and iii) molecular oxygen (O_2). The absorption of light by the PS leads to the formation of cytotoxic reactive oxygen species (ROS) that yields to the killing of the tumor or bacterial cells.[4,5] Light can be accurately delivered in a spatial confined and focused manner only on the lesion area. Moreover, ROS are short-lived species that rapidly react with nearby biomolecules, thus their presence is also localized. Therefore, since photodynamic action occurs only when and where these 3 components are found, this treatment has the advantage of being spatially and temporally selective, reducing the adverse side-effects.[6,7]

Furthermore, the multi-target approach of PDT derived from the high reactivity and non-specificity of ROS is believed to hamper the development of cellular defense mechanism or resistances. In this regard, PDT has been exploited for diseases that are resistant to conventional treatment such as aggressive types of cancer and antibiotic-resistant microorganisms.[8]

Nevertheless, despite the advantages that PDT presents over conventional treatments and the reported success in cancer and infections, its use is not widespread due to several limitations. For instance, the broad and high reactivity of ROS is a drawback if the precise localization of the PS or light is not achieved since they will damage both healthy and unhealthy cells. Another limitation of PDT is the treatment of non-superficial lesions since the light has to penetrate through tissues.

The enormous potential of PDT as an alternative therapy for cancer and infections has stimulated and triggered the investigation of novel smart strategies to render the drawbacks

of PDT and make it a more efficient and safe therapy.

1.1.1 Molecular Basis of Photodynamic Therapy

The photophysical processes in PDT are illustrated in the Jablonski diagram (Figure 1).

The process starts with light absorption by the PS in its ground state ($^1PS_0$, which is a singlet because it has two electrons with opposite spins). Upon absorption of light with the appropriate wavelength (λ), one electron is shifted to a higher-energy orbital, yielding an excited singlet state ($^1PS^*$). The electron rapidly falls to the first excited singlet state ($^1PS_1^*$). Singlet states are usually very short-lived (~10^{-9} s). PSs in excited states are unstable and either undergo a process of modification of their chemical structure or release this excess energy returning to their ground state through two different processes: i) non-radiative processes in which the energy is dissipated as heat *via* vibrational relaxation or internal conversion; and ii) a radiative process called fluorescence in which the molecule return to its ground state from $^1PS_1^*$ as emission of light. According to spin selection rules, both processes are allowed since the spin number is preserved between $^1PS^*$ and $^1PS_0$.

However, the electron from $^1PS_1^*$ may also reverse its spin and undergo a process called intersystem crossing to yield the excited triplet state ($^3PS^*$). Triplet states are relatively long-lived (~10^{-9} to 1 s) since the transition to the singlet ground state is now a “spin forbidden process” due to the change in spin number. Thanks to its longer life, $^3PS^*$ may react with molecules nearby, such as molecular oxygen. However, these photochemical reactions are competing with non-radiative (back intersystem crossing) and radiative (phosphorescence) processes to return the molecule to its ground state.[9]

The photochemical reactions occurred to $^3PS^*$ are generally classified in Type-I and Type-II for electron transfer and energy transfer processes, respectively. On the one hand, Type-I process involves an electron transfer to the triplet state PS from another substrate, initiating a cascade of radical reaction which in the presence of O_2 may culminate in the formation of various types of ROS (HO·, $O_2^{\cdot -}$, etc). On the other hand, Type-II reactions comprise the energy transfer from the $^3PS^*$ to triplet ground state molecular oxygen ($^3O_2$). This step leads to the formation of the highly reactive singlet oxygen ($^1O_2$). During this process, the PS returns to its ground state and it is then ready to be excited again, restarting the photosensitization cycle.[10] The prevalence of Type-I or Type-II process is mainly conditioned by the PS and its micro-environment. However, most PSs used in PDT are known to act through Type-II reactions, therefore, $^1O_2$ is regarded as the central molecule causing oxidative cellular damage in PDT.[3,11]

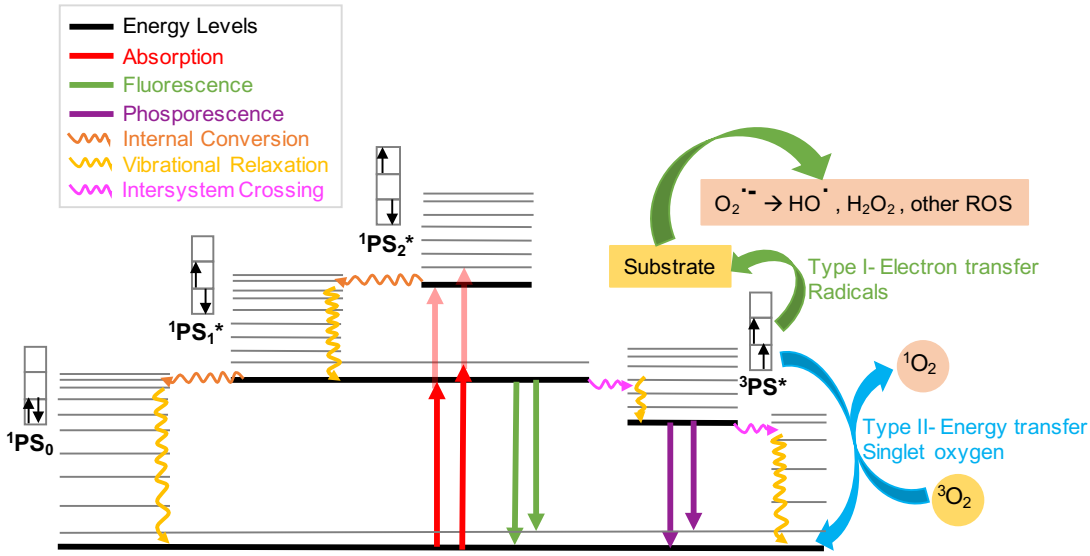

Figure 1. Jablonski diagram illustrating the photophysical processes in PDT. $^1PS_0$, ^1PS* and ^3PS* denote ground singlet state, excited singlet state and excited triplet state respectively. Waved lines: non-radiative processes. Straight lines: radiative processes.

1.1.2 *The Three Components: Light, Photosensitizer and Oxygen*

The efficiency of PDT depends on the three main components: the light, the photosensitizer employed and the concentration of oxygen. Below, a discussion about each one of them is detailed.

1.1.2.1 Light

Light is the first of the three components needed to achieve photodynamic action. It can be modulated in space, time, wavelength (or frequency) and intensity. However, the use of light in photodynamic therapy has several drawbacks that should be considered. Illuminating the surface of a tumor tissue is usually not enough for an effective treatment. This is because light interacts with tissues by processes such as reflection, refraction, absorption and scattering and as a consequence, the incident light energy is attenuated.[9] Scattering phenomena occurs when radiation penetrates a non-transparent area, in this case tissues. The scattering coefficient decreases with increasing wavelengths. As a result, the light penetration depth can potentially be increased by using longer wavelengths (Figure 2).[12,13] Nevertheless, at wavelengths longer than ~1400 nm (infrared region), the light is absorbed by the water molecules present in tissues. The optimal range of wavelengths in which endogenous chromophores have a minimal absorbance is between 600 to 1400 nm, the so-called optical or therapeutic window.[14,15] However, the active optical window is narrower for

PDT purposes since light of wavelength longer than 850 nm has insufficient energy to produce $^1O_2$.[16] Therefore, wavelengths between 600 – 850 nm are preferentially selected for PDT since they reach maximum tissue penetration and minimal absorption by intrinsic chromophores (Figure 3). However, even using these wavelengths, light can only penetrate up to some centimeters. Thereby, to deliver light to hidden parts of the body minor invasive techniques such as catheters and endoscopies have to be employed.[17,18] To avoid the use of these invasive physical treatments, new strategies capable of overcoming the depth limitation of traditional PDT are emerging, such as self-illuminated PDT and X-PDT. The first modality is based on light-emitting nanotechnology, it explores the use of nanoparticles containing molecules with persistent luminescence able to excite a PS and thus, to produce ROS.[19,20] X-PDT exploits the use of X-rays as excitation source for PDT due to their excellent tissue penetration depth.[21]

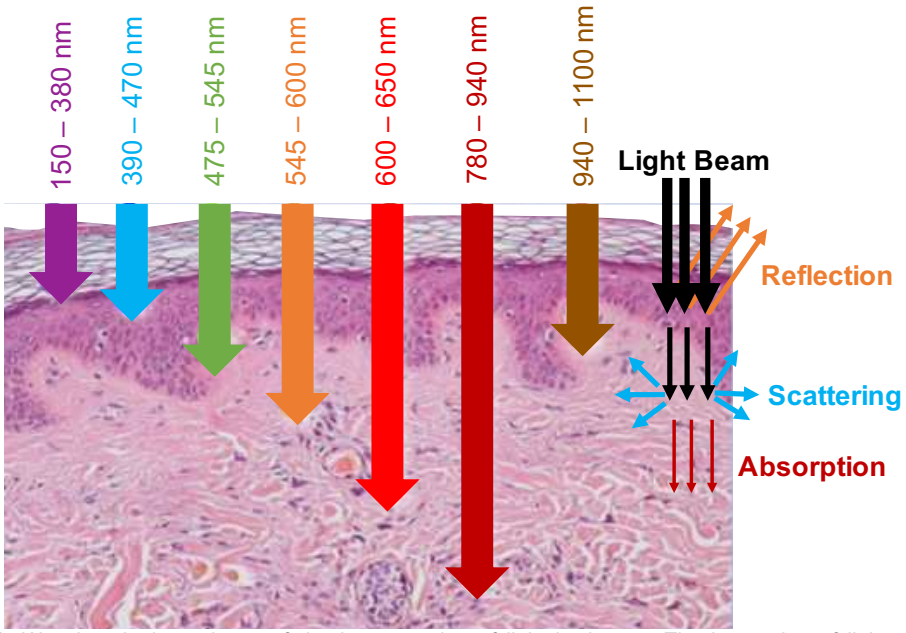

Figure 2. Wavelength dependency of depth penetration of light in tissues. The interaction of light with tissues undergoes processes such as reflection and scattering and as a consequence, the light absorbed is attenuated.

On the other hand, notwithstanding the presence of several chromophores in tissues that absorb at shorter visible wavelengths, such as hemoglobin derivatives and melanin, light of wavelengths in the range between 400 to 600 nm can be also employed to achieve photodynamic action for superficial lesions.

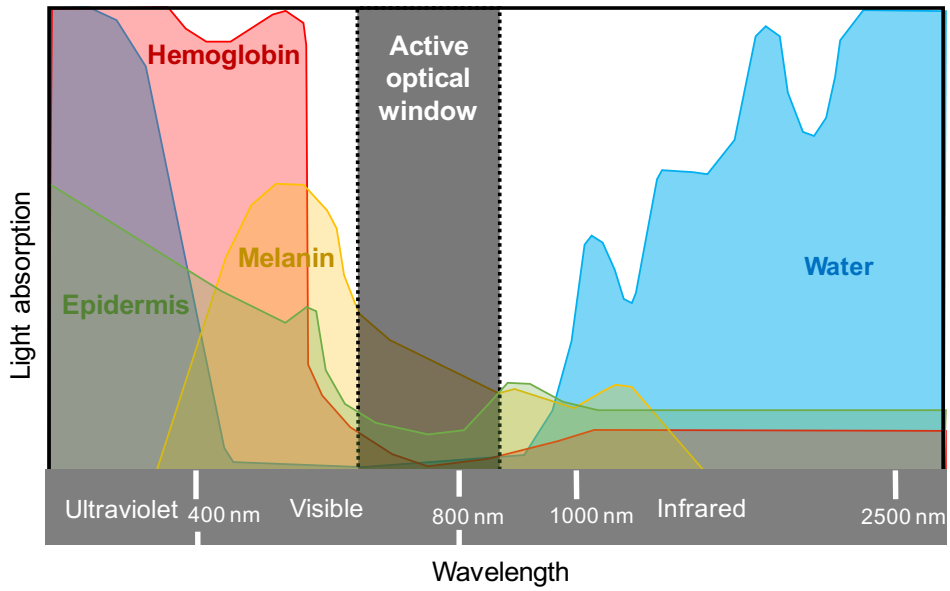

Figure 3. Absorbance of endogenous tissue chromophores and the active optical window range (600 – 850 nm).

1.1.2.2 Photosensitizer

Any molecule that absorbs light and has a reasonable high quantum yield of triplet formation is a potential candidate as PS. Most of PSs currently in use in PDT are organic molecules or metal complexes with notable π-electron systems that enable light absorption in the visible and near-infrared range of the spectrum. In this regard, many PS have been developed over the years, covering a broad part of the electromagnetic spectrum, from the ultraviolet (UV) to the near infrared (NIR) (Figure 4). In addition, the purpose of the photosensitization is to form ROS, thereby, a PS has to be able to transfer electrons or energy to O_2 efficiently.

A PS should ideally be a molecule endowed with the following properties:[22]

- High ability of PS molecules to undergo intersystem crossing to produce triplet excited states, i.e. high quantum yield of triplet formation.
- Long triplet excited state lifetime to increase the probability of reacting with O_2.
- Sufficient triplet energy (at least 94 kJ/mol) to allow for efficient energy transfer to ground state O_2.
- High absorption coefficient in the active therapeutic window for deeper light penetration.
- High photostability so the photosensitization cycle can be restarted more times.

- Soluble in physiological media.
- Non-toxic but greatly phototoxic.

Despite the considerable research effort and promising advances in the design and synthesis of novel PSs, most PS are excellent in some of the mentioned properties but deficient in others. Thus, only a relatively small number of photosensitizing drugs have received approval for clinical use so far.[23] The major drawbacks that PSs generally present are poor aqueous solubility and high dark toxicity, hampering its administration to the patients and inducing side effects. To overcome these deficiencies, smart strategies in targeted-nanomedicine have been developed to deliver the PS to the target tissue by means of a carrier vehicle that also protects it from external factors. This is the strategy followed along this thesis and will be discussed in detail in further sections.

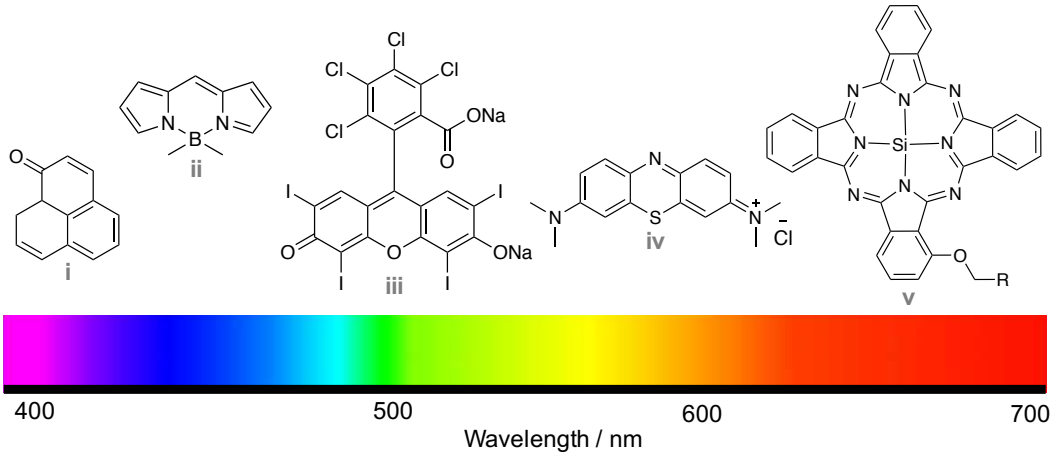

Figure 4. Spectral diversity of some photosensitizers: i) phenalenone, ii) BODIPY, iii) rose Bengal, iv) methylene blue and v) phthalocyanine.

1.1.2.2.1 Photosensitizers of Interest: Porphyrins and Phthalocyanines

Tetrapyrrolic PSs are a family of compounds, including porphyrins and phthalocyanines among others, whose fundamental structures are based on 4 pyrrole rings link together. Their excitation wavelength drops within the ultraviolet and visible region.

On the one hand, porphyrins are a class of tetrapyrroles whose pyrrole rings are linked symmetrically together by means of methine bridges generating a 18π electron system. Due to the presence of this electron system, porphyrin-type PS usually own an intense absorption band in the UV-blue range named Soret and other minor absorption bands between 500-600 nm called Q-bands, these last bands are inside the active optical window and are especially useful for PDT treatment.[24] In Chapter 4, the PS employed will be ZnTriMPyP (Figure 5), a

hydrophilic analogous of the well-known porphyrin photosensitizer ZnTPP, which was kindly provided by Professor Ross W. Boyle (University of Hull).[25]

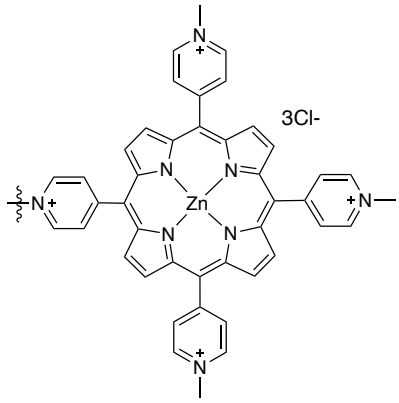

Figure 5. Chemical structure of ZnTriMPyP.

On the other hand, phthalocyanines (Pc) are a group of tetrapyrroles that are structurally close to porphyrins but have superior photophysical and photochemical properties. In comparison with porphyrins, the presence of benzene rings in the Pc derivatives conjugated to pyrrole rings at β-positions results in stronger absorption bands at longer wavelengths (670 – 780 nm) in the red region and low or even no absorption at 400 – 600 nm where the sun light intensity reaches highest; which means that the photodynamic process with Pc derivatives is more effective in deep tissue penetration with diminished skin photosensitization by daylight.[26] Moreover, complexes of Pcs with an appropriate central atom, such as silicon, aluminum or zinc, usually yield high $^1O_2$ generation efficacy with long-lived triplet states. In Chapter 5, two Pcs will be employed: i) a novel phthalocyanine synthesized by the laboratory of Anzhela Galstyan in Center for Soft Nanoscience, Westfälische Wihelms-Universität Münster in Münster, Germany. (Figure 6A) and ii) the commercially-available IRDye700DX (Figure 6B).

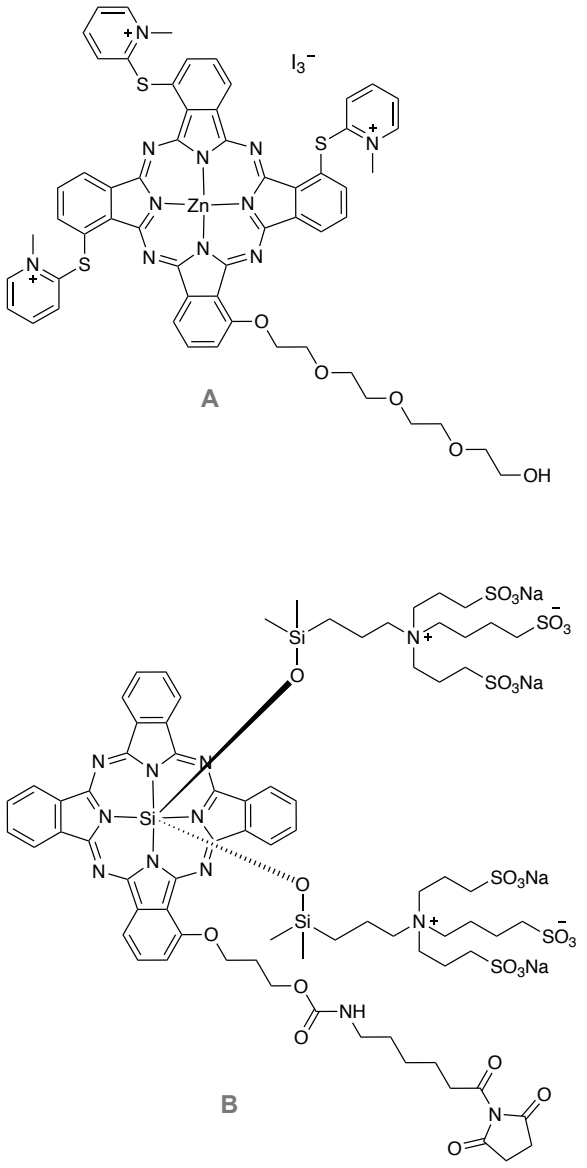

Figure 6. Chemical structure of A) ZnPcSMP and B) IRDye700DX-NHS

1.1.2.3 Oxygen

Molecular oxygen is unique in being a triplet in its ground state ($^3O_2$). Because of this particular spin multiplicity, its reaction with spin singlet reactants is forbidden in terms of the spin angular momentum, since the spins of the reactants are not conserved in the products.[27,28] In contrast, $^1O_2$ has the right spin to carry out the oxidation of organic compounds (Figure 7).

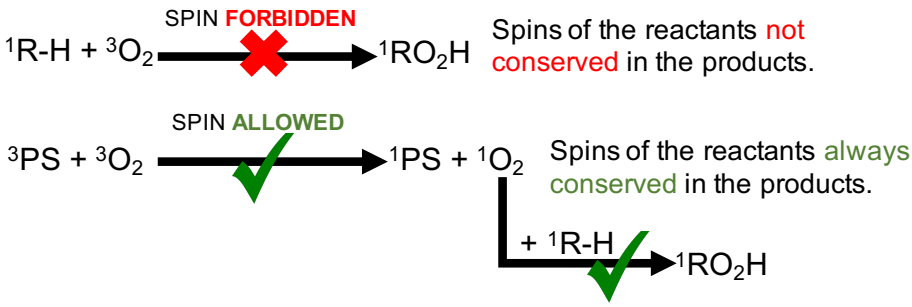

Figure 7. Reactivity of triplet and singlet state molecular oxygen.

The highly reactive $^1O_2$ can react towards a broad variety of molecules and biomolecules such as cellular proteins, lipids and nucleic acids. Their random and generalized oxidation is of utmost importance since it is the key factor by which treated cells find it much harder to develop resistance in comparison to traditional antibiotics or chemotherapeutic agents.

Since the diffusion constant of $^1O_2$ is pretty low, $^1O_2$ has a low sphere of action and, therefore, the primary cell damage is localized in the vicinity of where the PS is located, approximately about 10 – 30 nm in diameter.[29]

$^1O_2$ can be detected either directly taking advantage of its phosphorescent emission peaking at 1275 nm or by indirect methods. In the present work, its NIR phosphorescence is detected by a time-resolved detection system that is capable of confirm the presence of $^1O_2$ and also obtain information about its formation and decay kinetics. This topic will be discussed in detail in Chapter 3: *General Techniques and Methods*.

1.2 Photodynamic Therapy for Cancer Purposes

World Health Organization defines Cancer as *a large group of diseases that can start in almost any organ or tissue of the body when abnormal cells grow uncontrollably, go beyond their usual boundaries to invade adjoining part of the body and/or spread to other organs*. Cancer is the second leading cause of death globally, accounting for an estimated 9.6 million deaths, or one in six deaths, in 2018.[30] Great efforts are being made during decades to investigate and overcome this worldwide burden. Nowadays, the conventional cancer treatments such as chemotherapy, radiotherapy or surgery are still the first therapy choice. Nevertheless, the main issue when treating cancer patients with chemotherapy or radiotherapy is that these forms of treatment tend to have low selectivity for cancer cells and so are required to be administrated in high toxic drug loads to be considered effective. The high toxic dosage tends to affect normal body cells as well, often inducing severe unwanted side effects when patients undergo these forms of treatment. Thus, all this have placed a high demand on research and drug developers for more effective forms of treatment.

PDT is an alternative approach that has the potential to meet not only cancer, but many currently unmet medical needs. It can be used alone or either before or after conventional cancer treatments without compromising these therapeutic modalities. There are no significant changes in tissue temperature and the preservation of connective tissue leads to minimal fibrosis; allowing retention of functional anatomy and mechanical integrity of hollow organs undergoing PDT.[3] Although still emerging, PDT is already a successful and clinically approved therapeutic modality used for the management of neoplastic and non-malignant diseases.

In the 1960s, Lipson and colleagues initiated the modern era of PDT at the Mayo Clinic, studying the compound called hematoporphyrin derivative (HPD).[31,32] For the following years, different groups investigated this compound. A significant breakthrough occurred in 1975 when Dougherty and co-workers reported that the administration of HPD and red light completely eradicated breast tumor growth in mice.[33] In 1976, Kelly and co-workers initiated the first human trials with HPD in patients with bladder cancer.[34] During the following years a lot of studies showed promising responses in early-stage cancer patients, so PDT was recommended for patients with early-stage cancers that were inoperable. Patients with breast cancer, gynecological tumors, intraocular tumors, brain tumors, head and neck, colorectal cancer, cutaneous malignancies, intraperitoneal tumor and pancreatic cancer among others were subsequently treated with PDT.[2] In 1993, Photofrin®, a mixture of HPD, was approved to treat bladder cancer. Since then, although PDT was the first drug-device combination approved by the FDA, only a few PS has been approved for clinical use (Table 1).

Table 1. PDT agents in clinical use or in clinical trials.[35]

Class	PDT agent	Stage	λ_{exc} / nm	Area	Cancer type
Protoporphyrin IX precursor	5-Aminolevulinic acid (Levulan®)	FDA approved	635	Global	Skin, brain, oesophagus
	Methyl aminolevulinate (Metvix®)	FDA approved	635		Skin
	Hexyl 5-aminolevulinate (Hexvix®)	FDA approved	380–450 (diagnosis)		Bladder
Porphyrin derivatives	Porfimer sodium (Photofrin®)	FDA approved	630	Global	Lung, bladder, oesophagus, bile duct, brain
	Photogem	MHRF approved	660	Russia	Respiratory and digestive tracts, urogenital
Chlorin	Temoporfin	EMA	652	EU	Head and neck, bile

Class	PDT agent	Stage	λ_{exc} / nm	Area	Cancer type
derivatives	(Foscan®)	approved			duct, lung
	Ce6-PVP (Fotolon®)	Phase 2	660–670	Germany	Lung
	Radachlorin®	MHRF approved	662	Russia	Skin
	Talaporfin sodium (Laserphyrin®)	MHLW approved	664	Japan	Lung, brain
	HPPH (Photochlor®)	Phase 2	665	USA	Lung, oral cavity, oesophagus
Bacteriochlorin derivatives	Redaporfin	Phase 2	749	Portugal	Head and neck
Phthalocyanine derivatives	Silicon phthalocyanine (Pc4)	Phase 1	672	USA	Skin
Metal complex	Padoporfin (TOOKAD®)	Terminated	763	EU	Prostate
	Padeliporfin potassium (TOOKAD®Soluble)	EMA approved	753	EU	Prostate
	TLD-1433	Phase 2	520	Canada	Bladder, brain
	Motexafin lutetium (Antrin®)	Terminated	732	USA	Breast, prostate
	Rostaporfin (Purlytin®)	Phase 2/3	664	USA	Breast, bile duct, ovarian, colon

1.2.1 Anti-tumor Mechanisms of PDT

It is known that there are three main mechanism by which PDT mediates tumor destruction: direct tumor-cell killing, vascular damage and immune response.

In the first case, the ROS generated by PDT are responsible for the direct cell damage, which ultimately leads to apoptosis, necrosis or autophagy cell death.[36,37]

Second, PDT also damages the tumor-associates vasculature causing damage to the endothelial cells and ultimately blocking the blood flow in the vessels.[38] The viability of tumor cells depends on the amount of nutrients and oxygen supplied by the blood vessels. If vasculature alterations occur, evidenced as thrombus formation, blood vessel occlusion or vascular function shutdown, the growth of the tumor mass and metastasis are prevented.

Therefore, targeting the tumor vasculature is one promising approach to cancer treatment.[2]

Finally, PDT can activate an immune response in the host tissue in response to a PDT-induced oxidative stress.[39] The strong inflammatory reaction provoked by PDT will stimulate the proliferation of the immunocytes such as neutrophils, macrophages and lymphocytes. These cells can rapidly infiltrate into the tumor tissue to elicit specific immune responses against tumor cells.[40–43] Unlike surgery or chemotherapy that develop immunosuppression, PDT has shown immunostimulation which is reported to have implications in further destruction of remaining tumor cells and preventing tumor recurrence and metastasis.[44]

1.2.2 Photodynamic Combinational Therapy in Cancer Treatment

To improve the therapeutic effect of PDT, increasing numbers of attempts have been made to combine PDT with other traditional cancer therapies, including chemotherapy, immunotherapy, radiotherapy and enzyme inhibitors among others. In Chapter 5, an approach consisting in the combination of PDT with chemotherapy and immunotherapy will be investigated.

Following, a brief summary about the combination of PDT with chemotherapy and immunotherapy is introduced.

1.2.2.1 PDT Combined with Chemotherapy

The anti-tumor mechanism of chemotherapeutic drugs generally involves the binding to the DNA of tumor cells to inhibit the process of cell division and thereby prevent DNA replication, eventually leading to the death of the cancer cells.[45–47] Although this drug can kill cancer cells, chemotherapy has severed side effects, as explained in previous sections. To overcome the adverse effects, many attempts have been made to combine PDT with chemotherapy. This combination presents some advantages over the chemotherapy alone:[48]

- May result in a synergistic anti-tumor effect and reduce the therapeutic dose of the chemotherapeutic drugs. Numerous studies have demonstrated that combining PDT with chemotherapy can increase the therapeutic effect.[49–53]
- May overcome multidrug resistance produced during tumor treatment.[54]
- May improve treatment effects in late-stage patients. Some reports demonstrated that PDT combined with chemotherapy could improve the quality of life and improve the damage in patients with advanced cancer.[55]

1.2.2.1.1 Chemotherapeutic Agent of Interest: Doxorubicin

Doxorubicin (DOX) is an anthracycline antibiotic used clinically for a wide range of solid tumors and hematological malignances, including advanced breast cancer, small cell lung cancer, acute leukemia, lymphomas and myeloma, among others (Figure 8). DOX functions in several ways, including inhibiting DNA synthesis *via* intercalation, inhibition of topoisomerase II, free radical formation and lipid peroxidation. DOX is considered one of the most potent anti-cancer drugs, however, high cardiotoxicity is its main side effect.

DOX is the most frequently studied drug in combination with PDT and their combo usually achieves an enhancement in terms of toxicity. It can be administrated as single molecule with a PS[56,57] or, more interesting, by a single nanocarrier delivering both agents. Furthermore, its delivery from a drug delivery system can be modulated by the $^1O_2$ generated.[58–61] This strategy will be detailed discussed in following sections.

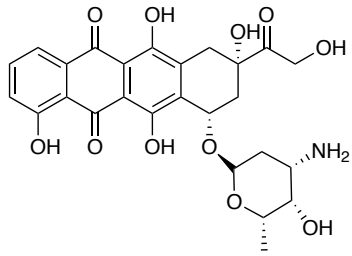

Figure 8. Doxorubicin chemical structure.

1.2.2.2 Photoimmunotherapy

Photoimmunotherapy (PIT) is a targeted form of conventional PDT, achieved through the combination of PS with monoclonal antibodies (mAbs) targeting specific cell surface receptors. The PS and mAb combo can improve the specificity of the PS and thus reduce its undesired side effects. PIT can also reduce other issues, such as dark toxicity and PS aggregation in aqueous media which reduce PDT efficacy.[62] This combinatorial strategy will be further explained in Section 1.4. *Targeted Photodynamic Therapy*.

In conclusion, the combination of PDT with other cancer therapies, such as chemotherapy and immunotherapy, produces greater effects than a single therapy. As will be explained below, nanocarriers are an optimal platform to deliver them since they can combine different treatments into a single administration.

1.3 Drug Delivery Systems for Photodynamic Therapy

Despite the elevated achievement levels of PDT in the treatment of different cancers, there is still room for improvement by enhancing its drug delivery and making the PS target specific. All this can be achieved by vehiculization of the PS into drug delivery systems. The main goal of drug vehiculization is to reduce therapy associated side effects and improve the drug bioavailability, thus leading to a higher efficacy of the drug with a decreased overall toxicity. During the last years, research in the utilization of nanocarriers within cancer PDT therapy as effective PS drug delivery systems has become very popular. This combo can overcome the limitations that conventional PS drug delivery methods experience: it increases the selectivity and stability of PSs, reduces unwanted side effects and limits dark toxicity.[63–66]

Nanoparticles (NPs) are a very advantageous drug delivery system for PDT:

- They are sub-micrometer size particles that can be easily accumulate in cells.
- Their surface chemistry usually allows for possible functionalization. Therefore, they can be designed as multifunctional nanoplatforms to carry multiple components together with the PS.
- Due to their large surface area to volume ratio, the covalent conjugation of their surface enables to construct nanocarriers with a high degree of payload.
- They protect the PS against enzymatic degradation.
- Sometimes, NP drug delivery system improves the solubility of the PS and therefore, its photophysical properties.[67] In other cases, the photosensitizing ability of the PS becomes reduced in the nanocarrier due to the high local concentration of the PS itself.[68]

In a NP drug delivery-based approach, a PS is either physically entrapped and so, loads within the vehicle core, or immobilized on the NPs surface using covalent or non-covalent interactions. The major advantage of drug loading nanocarriers is the great transfer of the drug from the NP vector to the cell. However, PS drug molecules absorbed to NPs are sometimes chemically or physically desorbed due to changes in their environment, leading to premature drug loss even before the cellular target site is reached. In contrast, covalently bound drugs ensure stability during transport to the cell.

Shape, size, material and surface nature are the main four physicochemical properties of a nanocarrier that can be modulated in order to design the optimal drug delivery system (Figure 9). These four properties govern the biological interactions of the nanocarrier, such as

intracellular uptake, blood circulation times or their clearance though reticuloendothelial system. Furthermore, the ability of nanocarriers to modify their surface is a key factor to modulate their biological interactions. One example is the surface modification with polyethylene glycol (PEG), NPs may be coated with a PEG shielding outer layer that allows for stability of the drug delivery system, as well as provides biocompatibility and thus allows NPs to have longer circulation times in the body. Moreover, targeting ligands can be added to the surface to specifically target cancerous cells. Therefore, the optimization of the nanocarriers surface by synthetic procedures can result in promising drug delivery systems.

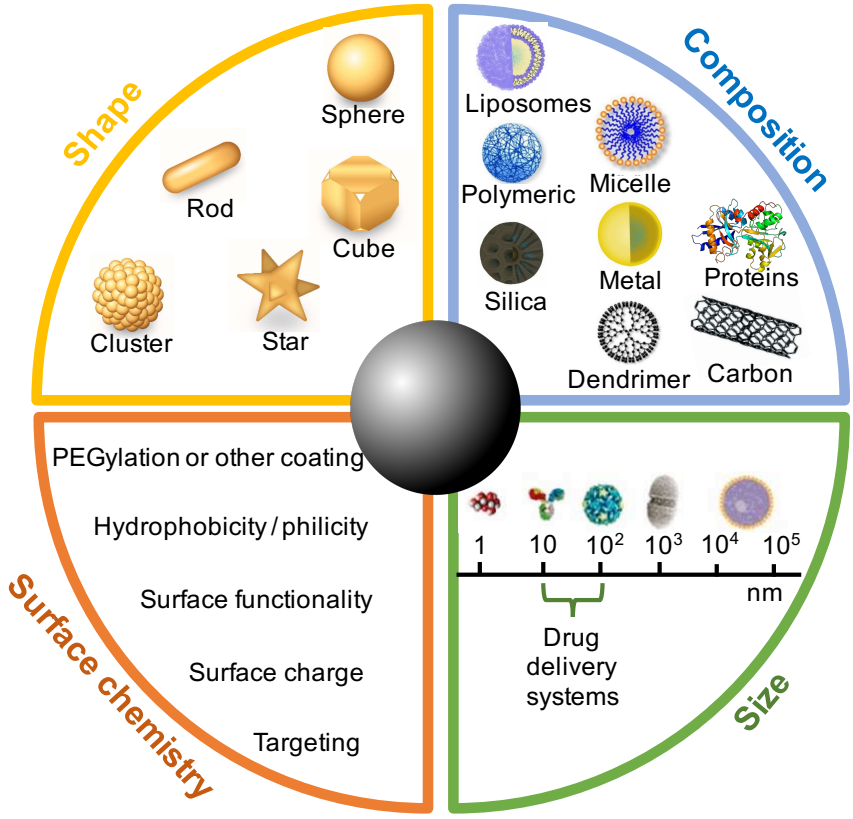

Figure 9. Schematic diagram of the main four physicochemical properties of a nanoparticle that could be tailored or modulated to obtain the desired drug delivery system.

A vast array of nanodelivery systems have been studied for PDT. On the one hand, organic NPs are solid particles composed of organic compounds such as lipids, proteins, polysaccharides or polymers. Examples of organic NP platforms for PDT include polymeric NPs (e.g., PLGA NPs, hydrogels and dendrimers), liposomes and protein-based NPs. On the other hand, there are inorganic NPs, such as silica NPs, metallic NPs and carbon-based NPs.

1.3.1 Nanocarriers of Interest: PLGA Nanoparticles and Mesoporous Silica Nanoparticles

In this thesis, two types of nanoparticles will be employed as nanodelivery systems for PDT: a biodegradable organic one, PLGA NPs (used in Chapter 4) and an inorganic non-biodegradable type, silica mesoporous NPs or MSNPs (employed in Chapter 5). Following, a summarized information about these particular nanocarriers is exposed.

1.3.1.1 PLGA Nanoparticles

Poly-(*D,L*-lactide-*co*-glycolide) (PLGA) and poly-(*D,L*-lactide) (PLA) are two of the most widely used biocompatible and biodegradable polymers for preparation of NPs. In addition, they are clinically validated by regulatory agencies for their use as delivery systems in the clinic, which makes them a desirable choice.[69]

Biodegradation of these polymers or its NPs *in vivo* is accomplished mainly by hydrolysis of the ester linkages, resulting in the building block monomers lactic acid and glycolic acid which are further eliminated by common metabolic pathways.

These polymeric NPs have excellent properties as nanoscale drug delivery vehicles: outstanding endocytosis ability, passive tumor-targeting, high encapsulation efficiency, high stability and, in addition, their surface can be modified with PEG and targeting moieties to design active-targeting nanovehicles.

1.3.1.2 Mesoporous Silica Nanoparticles

One type of silica based nanoparticles are mesoporous silica nanoparticles (MSNPs) which are characterized by the presence of pores. One of the major concerns when designing a drug nanocarrier is its biocompatibility. In the case of amorphous silica, the material is known to be, and has accordingly been listed as, “generally recognized as safe” by the FDA. In the specific case of MSNPs, while specific results differ by a number of variables including dosage, particle size, shape, cell lines used and so on, the general consensus is that MSNPs have a significantly lower cytotoxicity than non-mesoporous silica NPs.[70,71]

The key strengths of MSNPs for nanomedicine are as follows:[72,73]

i) Their porosity and consequent larger surface area. This fact enables the much higher drug loading/attachment and thus relieve patient’s sufferings *via* diminished overall dosage and frequency of nanomedicines, when compared with the most engineered carriers such as liposomes, micelles, hydrogels, etc.[74]

ii) The ease of surface modification. These nanocarriers, like PLGA NPs, can be designed as multifunctional platforms, but their surface modification is much easier than for PLGA NPs.

iii) The ability to control pore size and dimensions allowing for control of the drug release dynamics.

iv) The stability and tolerance over temperature and a variety of solvents. Thereby, MSNPs can tolerate various reaction conditions so that chemical modifications can be performed readily.

1.3.2 Drug-responsive Release Delivery Systems in Photodynamic Therapy

As previously mentioned, two different approaches can be followed for drug delivery by nanocarriers: the drug loading or the attachment of the drug to the surface of MSNPs. Covalent drug delivery requires direct breaking of the chemical bond between the drug and the NP platform. Careful design of this linker can afford site specific cleavage; selectivity which is not often available in a non-covalent system. The requirement for efficient but selective delivery has led to many different strategies to develop drug-responsive release systems using labile linkers.

Particularly in PDT, the drug responsive-release approach is generally investigated for the combination of PDT with chemotherapeutic drugs. The on-demand release of drugs can be achieved by environmental stimuli such as pH change, redox, temperature or light irradiation.[75–77] In this regard, as light is an essential component for PDT, the photoresponsive release of drugs is especially attractive and it is generally triggered by photothermal effect, photoconversion or by the singlet oxygen generated upon the photosensitization process:

- Photothermal effect. For instance, using NPs with NIR dyes whose irradiation triggers the temperature-responsive release of a drug.[78]
- Photoconversion. Under NIR irradiation, upconversion NPs convert NIR light into UV or visible light that can destroy sensitive moieties, allowing for on-demand drug release.[79,80]
- Singlet oxygen. When synergizing with PDT, the PS not only leads to light triggered $^1O_2$-induced drug release but also eliminate disease *via* the toxic effects of excessive $^1O_2$, resulting in improved therapeutic efficiency.

1.3.2.1 Singlet Oxygen-cleavable Linkers

By using $^1O_2$-cleavable linkers, PDT also has the function of controlling drug release in combinatorial treatment strategies.[81] Some authors explored the use of $^1O_2$-cleavable linkers to achieve the photoresponsive release of loaded drugs (not covalently attached) by degradation of the NPs or by un-blocking their pores.[82–92] However, much less reports are associated with the controlled release of covalently attached drugs to NPs by means of a $^1O_2$-sensitive linker.[61,93–98]

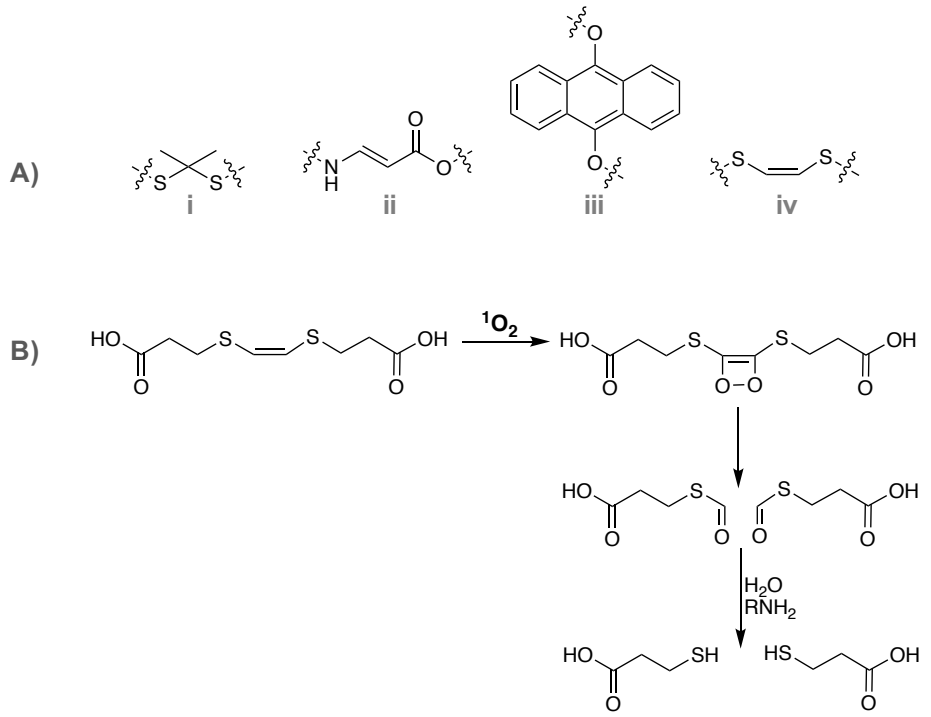

Figure 10. A) $^1O_2$-cleavable moieties used for covalent-bound of drugs to nanocarriers: i) dithioketal; ii) aminoacrylate; iii) alkoxyanthracene; and iv) bis-(alkylthio)alkene. B) Action of $^1O_2$ in the bis-(alkylthio)alkene linkage of study.

Several moieties such as dithioketal[97], diselenide bond[99,100], aminoacrylate group[95], alkoxyanthracene[61] and bis-(alkylthio)alkene scaffolds[58–60,83,86,93,101,102] are reported to cleave by action of $^1O_2$ (Figure 10A). Among them, bis-(alkylthio)alkene linkage will be employed in Chapter 5 to develop a $^1O_2$-responsive nanocarrier for on-demand Doxorubicin release. This was the cleavable moiety of choice due to its easy synthesis and good performing on a previous work of our laboratory.[98] The cleavage mechanism is based on a well-known property of the double bond to participate in a [2+2] cycloaddition with $^1O_2$, forming dioexetane ring intermediate, whose subsequent decomposition ultimately gives two aldehyde fragments (Figure 10B). The introduction of heteroatoms adjacent to the alkene moiety increases the relative reactivity of the linkage.

1.4 Targeted Photodynamic Therapy

One of the major limitations of PSs lies on the difficulties to precisely control the localization of the PS in the tumor tissue. Most PSs are randomly distributed, so they are often accumulated not only in cancerous cells, but also in healthy cells. Since ROS are intrinsically non-specific, both healthy and unhealthy cells will be damaged equally, resulting in non-specific phototoxic damage. Moreover, since light can diffuse through tissues, it is highly unlikely to specifically irradiate tumor and thus, healthy cells very proximal to the lesion are also irradiated. For these reasons, a targeted photosensitizer delivery system is highly desirable to increase the safety of PDT. High tumor-specific accumulation of PSs is required to improve efficacy and reduce system cytotoxicity. Drug delivery systems can target the PS by passive or active processes.

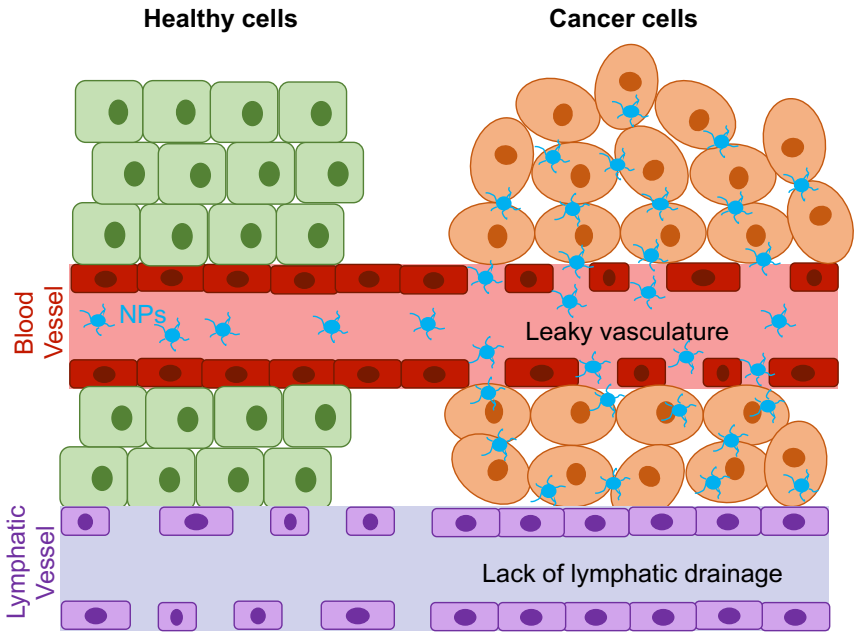

Figure 11. Schematic representation of the role of a passive tumor targeting. Unlike in normal tissue, in tumor tissue, the drug delivery system, smaller than the fenestrations between endothelial cells, can enter the interstitium and to be accumulated due to a poor lymphatic drainage.

On the one hand, passive targeting relies on the unique neovascularization of cancerous tissues. Unlike small molecules, NPs are not small enough to cross the tight junctions between endothelial cells on normal vascular linings. In contrast, the vessels inside a tumor region are well-known for their leaky walls, allowing NPs with the right sizes go through efficiently and be internalized into the tumor cells. This leaky vasculature together with a poor lymphatic drainage is known as enhanced permeability and retention (EPR) effect and makes the cancerous tissues more susceptible to NPs than healthy ones, resulting in a preferential

accumulation of NPs. Therefore, the drug uptake in tumor is increased, while reducing the overall toxicity in healthy cells. Passive targeting is a common strategy to increase the specific accumulation in target tissues by optimizing the physicochemical properties of the delivery system. Depending on the tumor type, the gaps in the tumor vasculature are typically in the size range of 100 – 800 nm, therefore, nanocarriers smaller than this range could preferentially accumulate by EPR effect (Figure 11). However, NPs with a size between 30 – 200 nm show most effective EPR.[103,104]

On the other hand, some authors reported that passive PS carrying NPs cannot exclusively differentiate between cancerous versus normal cells and so they are occasionally distributed in healthy tissues. For this reason, research has become focused on developing of active PDT NP drug carriage in which the PS is delivered to a specific targeted tumor site by means of a molecular recognition process. NPs grafted with targeting ligands can recognize and bind to surface receptor overexpressed by tumor cells and specifically be internalized *via* receptor-mediated endocytosis (Figure 12).[105]

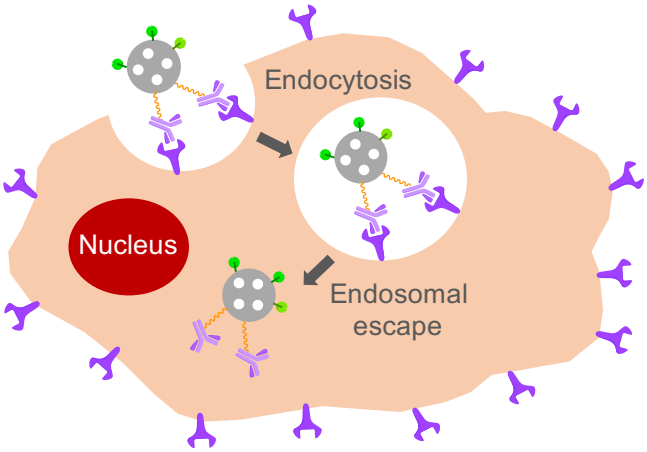

Figure 12. Schematic representation of active tumor targeting of nanocarriers *via* receptor-mediated endocytosis.

In terms of intracellular absorption of NPs, the receptor-mediated endocytosis pathway is known to be more efficient than the general endocytosis pathway. In this regard, various types of molecules, such antibodies, nucleic acids, proteins, peptides and small molecules, have been employed as highly specific molecular targeting moieties for the treatment of different types of cancer (Figure 13). Therefore, the surface functionalization of a drug delivery system with these targeting moieties facilitates a more effective, specific and active accumulation of PSs in tumor tissues or cells and so overall increases the efficacy of PDT without detrimental damage to normal healthy tissues.

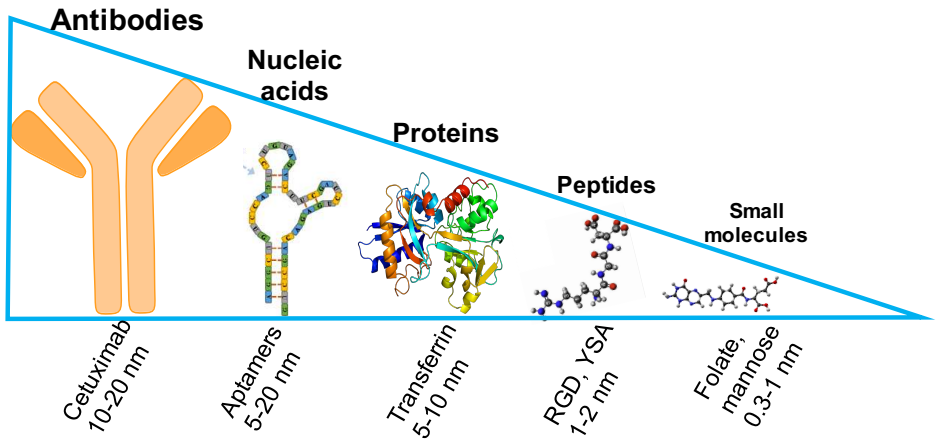

Figure 13. Classification by type of ligand and size of bioactive targeting moieties.

1.4.1 Targeting Moieties of Interest: c(RGDfK) Peptide and Cetuximab Monoclonal Antibody

In this thesis, two types of targeting moieties will be employed to improve the effectiveness and selectivity of PDT effect by active-targeting of nanodelivery systems. The first type (employed in Chapter 4) is the c(RGDfK) peptide. In collaboration with the Laboratory of Pharmaceutical Technology at the University of Geneva (Switzerland), supervised by Prof. Norbert Lange, this targeting peptide was previously attached to a PLA chain in order to further prepare polymeric nanoparticles. The second targeting moiety employed is the commercially available Cetuximab monoclonal antibody (used in Chapter 5). Following, a summarized information about these two is presented.

1.4.1.1 c(RGDfK) Peptide

Peptide-based targeting delivery systems exhibit several advantages compared to antibodies: lower molecular weight, resulting in a better tissue penetrating capacity, a wider range of targets, low immunogenicity and more stable.[106] Peptides however, have relatively lower affinity for their target site, and this deficiency is in-part mitigated through ligand avidity which is achieved by incorporating multiple peptides.[107]

Of specific interest are the RGD peptides, which specifically attach to $\alpha_v\beta_3$ integrin with a high binding affinity.[108] RGD-containing peptides have been widely used as targeting ligands for cancer diagnosis[109–112] and therapy[113–117], including PDT[118–122], since this integrin is known to be present on the neovasculature of cancer cells and is also overexpressed on glioblastoma, melanoma, lung, ovarian and breast cancer cells, but generally not in healthy cells.[123–125]

There are two types of RGD peptides classified by the structure of the sequence: linear and cyclic. Cyclic RGD (cRGD) peptides exhibit better *in vivo* behavior compared to linear ones since they are resistant to protease enzymes, more stable and have improved ability to interact towards integrin receptors with high affinity.[126] It is also known that multiple cRGD peptides can increase the affinity to $\alpha_v\beta_3$ integrin by multivalent and cluster effects.[127–130] In this sense, the use of nanocarriers as drug delivery system presents a great advantage since they can be conjugated to multiple peptides. The ability of multiple cRGD peptides conjugated to nanoscale systems to act as efficient drug targeting and delivery systems for cancer therapy has been demonstrated: the conjugation increases the cellular uptake efficiency *via* $\alpha_v\beta_3$ integrin receptor-mediated endocytosis and, consequently, enhances anticancer activity.[131–133]

Regarding the efficacy of the binding activity, it has been demonstrated that cyclic pentapeptides with a D-Phenylalanine amino acid following the Aspartic acid residue bind more efficiently to its receptor.[134] Furthermore, the type of amino acid in position 5 does not seem to have a significant influence on the selectivity towards the receptor, and therefore, an amino acid with a reactive functional group, such as the amino group in lysine, can be introduced in order to couple the peptide to the desired carrier. Thus, the cyclic pentapeptide c(RGDfK) is a promising sequence to target $\alpha_v\beta_3$ integrin in order to improve the selectivity of a photodynamic treatment.[118,135–137]

1.4.1.2 Cetuximab Monoclonal Antibody

In the recent years, the use of monoclonal antibodies for light therapies such as targeted-PDT and photoimmunotherapy have attracted much attention. mAbs are protein molecules made in the laboratory by recombinant DNA technology. mAbs have remained the preferred and most extensively used and investigated type of targeting moieties, due to the high affinity and specificity they render to the delivery system. The potential of mAbs in targeted cancer therapy led to the approval of a large number of this sort of macromolecules for clinical use, including Cetuximab, Trastuzumab and Rituximab, among others.

Epidermal growth factor receptor (EGFR) is a transmembrane glycoprotein with an intracellular tyrosine kinase domain that is significantly overexpressed on the surface of many types of cancer cells such as in glioblastomas, breast, colon, bladder, ovarian, prostate, renal, gastric, lung and pancreatic cancers. Because of this, EGFR has been utilized as an important target in actively-targeting cancer therapies. Epidermal growth factor (EGF), a protein produced in the body, attaches to its receptor (EGFR) to trigger cellular proliferation. Cetuximab, a chimeric mouse/human monoclonal antibody, is able to block the effect of EGF

by binding EGFR, resulting on inhibition of signaling of the downstream transduction, influencing the cell proliferation, angiogenesis, metastasis and apoptosis.[138–141] Cetuximab as single drug was approved by EMA and FDA for many types of cancer since 2004.

Recently, the construction of conjugates between PSs and mAbs is a very active topic. In this regard, the work of Kobayashi and co-workers is worth highlighting. They have reported that the conjugation between the PS IRDye700DX and mAbs targeting EGFR-cells leads to deeper tissue penetration and specific targeting, resulting in eradication of tumors.[142–146] Presently, their photoimmunotherapy approach is under the international phase III clinical trial against locoregional, recurrent head and neck cell carcinomas with FDA fast-track approval. Moreover, very recently, in September 2020, the Japanese government approved the Cetuximab Saratolacan (commercial name: Akalux®), that consists in a chemical conjugate of IRDye700DX and Cetuximab, for the treatment of these cancers.[147]

The importance of Kobayashi's studies in relation with this thesis is because in Chapter 5, a combination of IRDye700DX and Cetuximab will be investigated, but unlike their work, these compounds will be attached to a nanodrug delivery system.

CHAPTER 2: OBJECTIVES

The recent advances in nanotechnology permit the incorporation of various treatment components in a single nanoplatform. Thus, the main goal of this thesis is to explore the potential of enabling nanotechnologies in order to develop nanodevices that improve the effectiveness and safety of a photodynamic treatment by enhancing the drug accumulation in tumor cells, precluding damage to healthy cells, taking advantage of their selective delivery. This main goal will be achieved by the design of nanocarriers for actively-targeted photodynamic therapy and their evaluation for anticancer purposes.

The primary goal is further set to the following specific objectives:

I. Development of a PLGA nanocarrier with photosensitizing properties based on the photosensitizer ZnTriMPyP and grafted with the active-targeting moiety c(RGDfK) peptide. Study of its photoactivity and phototoxicity *in vitro*. This nanosystem will allow to study if the incorporation of c(RGDfK) peptide is an advantage in terms of cellular photodynamic efficacy and selectivity for the nanocarrier. In addition, we will explore if the covalent conjugation of the photosensitizer adds value to the formulation.

II. Preparation of immuno-photo-nanocarriers: mesoporous silica nanoparticles decorated with phthalocyanine and grafted with the active-targeting moiety Cetuximab antibody. Evaluation of their photophysics and biological effects. This system will enable to study whether the incorporation of Cetuximab improves the cellular selectivity of the nanoparticle formulation and enhances the accumulation in cancer cells.

III. Development of chemo-immuno-photo-nanocarriers: mesoporous silica nanoparticles grafted with phthalocyanine and Cetuximab that allow the on- demand release of covalent attached Doxorubicin by photo-cleavage of the linker that binds it to the nanoparticle. This release will be triggered by singlet oxygen generated in the photosensitization process. Characterization of their physicochemical and photophysical properties; and evaluation of their phototoxicity in cells. Through this new nanosystem, we will study whether covalent binding of the photoreleasable Doxorubicin onto the nanocarrier improves the safety of the treatment.

CHAPTER 3: GENERAL TECHNIQUES AND METHODS

This chapter describes the techniques and methods that have been employed in this thesis and their general aspects.

3.1 Synthetic Chemistry of Interest

3.1.1 Synthesis of PLGA Nanoparticles

Methods available for PLGA nanoparticle synthesis can be divided into two classes: bottom-up and top-down techniques. The bottom-up techniques employ a monomer as a starting point and involves the polymerization of these monomers. In contrast, in top-down techniques, the nanoparticles are synthesized from the pre-formed polymer. Some of the top-down techniques include emulsion evaporation, emulsion diffusion, solvent displacement and salting out. The advantage of this second class is that physicochemical features of the NPs, such as morphology, internal structure, size, drug loading and release kinetics, can be modulated more easily than using bottom-up techniques.[148]

In Chapter 4, PLGA NPs will be prepared by a modified nanoprecipitation method, also called solvent displacement method,[149,150] since this procedure is the more convenient in terms of length of time needed for NP preparation, simplicity of the methodology and obtaining of the smallest NPs. In this method, a hydrophobic polymer material is first dissolved in a water-miscible solvent. This polymeric dispersed organic phase is then added dropwise to an aqueous phase in continuous stirring (Figure 14). The solution resulting from the mixing of the polymeric phase with antisolvent (i.e., water) is a nonsolvent for the polymer solutes. As a consequence, hydrophobic polymer solutes become aggregated to form nanosized particles. Finally, the solvent is removed under reduced pressure.[148,151]

The general methodology followed in this work to synthesize PLGA NPs is the following: The PLGA polymers were dissolved in acetone (1 mL). This solution was injected dropwise to Milli-Q water (2 mL) under continuous stirring. Then, acetone was removed under reduced pressure. The suspension was centrifuged at 2,500 rpm for 15 min at 10 ºC. The pellet was discarded and the supernatant was stored at 4 ºC until use.

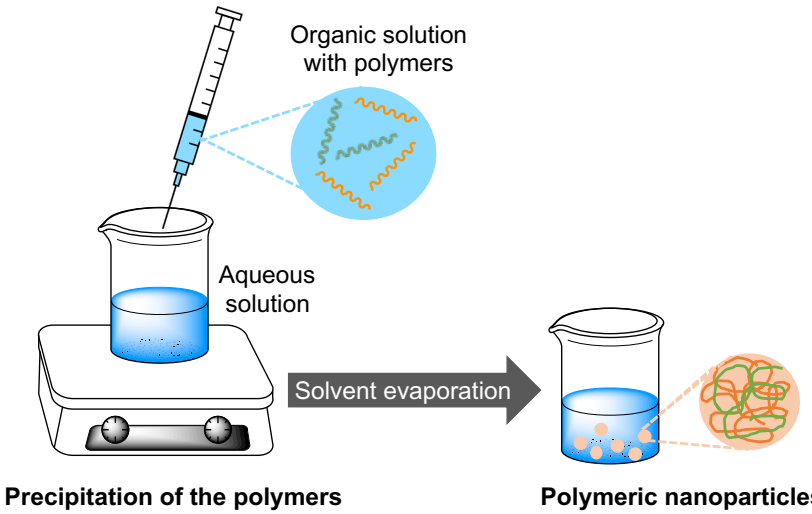

Figure 14. Schematic of PLGA nanoparticles synthesis process by nanoprecipitation, where PLGA in acetone is added dropwise to stirred beaker containing water.

3.1.2 *Synthesis of Mesoporous Silica Nanoparticles*

Silica nanoparticles (SiNPs) can be synthesized by a number of protocols yielding nanoparticles over a size range of 10-500 nm with a variety of shapes and physicochemical properties. The most commonly employed method for the synthesis of SiNPs are the Stöber process.[152] The Stöber method utilizes an inorganic silica precursor, tetraethyl orthosilicate (TEOS) which in the presence of EtOH and ammonia, undergoes hydrolysis followed by a polycondensation reaction to produce non-porous silica particles with sizes less than 200 nm. A modified Stöber's process with the incorporation of cationic surfactant such as cetyltrimethylammonium bromide or chloride (CTAB or CTAC) is widely used to synthesize mesoporous silica nanoparticles (MSNPs)[153,154] and it is the methodology followed in the present work to synthesize MSNPs. In solution, a self-assembly of organic surfactant molecules (CTAC, in this case) takes place at concentrations higher than the critical micellar concentration. Hydrolyzed TEOS in alkaline conditions arrange themselves around these micelles in order to form silica-template composites. After condensation of the composites, silica nanoparticles with mesoporous with a particular diameter are obtained after the removal of the organic surfactant molecules from the composites. Figure 15 shows the synthetic strategy for MSNPs.

The general methodology followed in this work to synthesize mesoporous silica nanoparticles is the following:

10.5 mL of CTAC (25 % wt in water) were added dropwise to 65 mL of MilliQ water under vigorous stirring. Later, the mixture was heated up to 80 °C. Once the temperature is

achieved, 12 mL of absolute EtOH and 120 µl of NH_3 (30 %) were added. Immediately after, 7.5 ml of TEOS were added dropwise and the reaction was left at 80 °C under stirring for 60 sec. The crude was cooled and centrifuged (30 min, 14000 rpm). In order to remove the CTAC, the pellet was suspended in 1% (wt/wt) NaCl in MeOH and was allowed to stir overnight. Then, it was washed two times, once with MeOH and the other with MeOH/water (50:50). The CTAC removal procedure was repeated twice. Finally, the MSNPs were kept in absolute EtOH at 4 ºC.

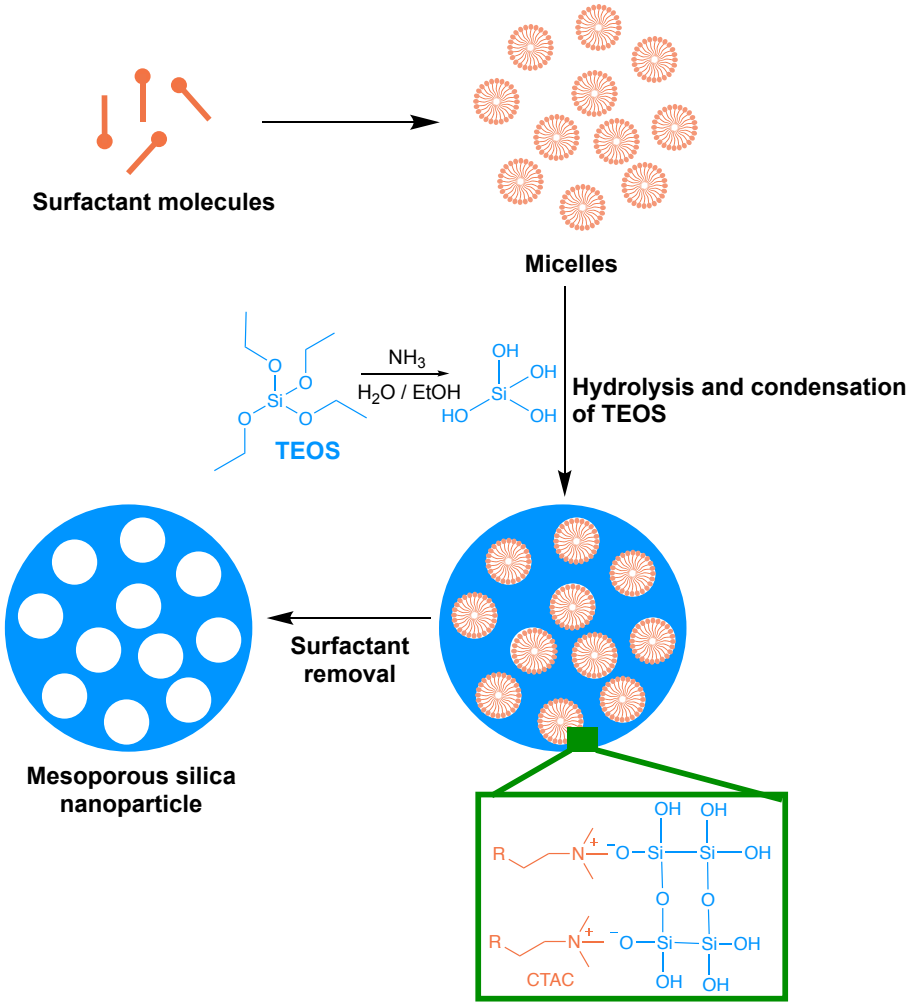

Figure 15. Schematic representation of the synthesis of MSNPs by Stöber-surfactant modified methodology.

3.1.3 Derivatization of Mesoporous Silica Nanoparticles with Silanes

Typically, the surface of MSNPs is rich in silanol groups that can be easily manipulated as the site of attachment for surface probes.[155] This covalent modification strategy involves either

co-condensation or post-synthetic grafting of organosilane coupling agents such as (3-aminopropyl)triethoxilane (APTES) onto the surface silanol groups. The post-synthetic option involves the conjugation of functional groups mostly on the surface of the MSNP. Whereas the co-condensation approach entails the presence of modified functional groups inside the pores of the MSNP.

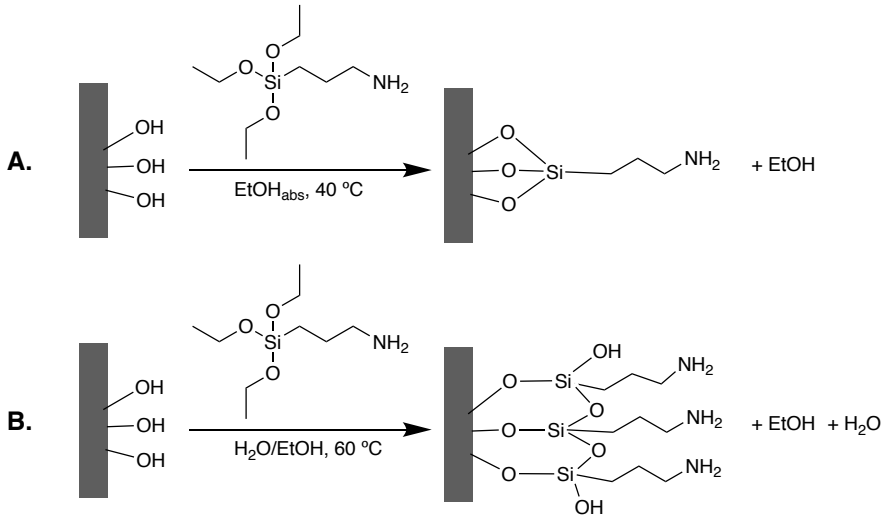

Figure 16. A) Silanization reaction between APTES and the hydroxylated surface yielding APTES functionalized surface. In anhydrous conditions, during heat treatment, condensation will occur between exposed ethoxy groups of APTES and the silanol groups on surface of MSNP. In case of long term treatment or high concentrated APTES solution, APTES is bonding to the MSNP with all ethoxy groups. B) In aqueous solution, horizontal polymerization occurs.

In the post-synthetic approach, the type of solvent strongly affects the density and conformation of the covalently attached organosilane layer.[156] Horizontal polymerization can occur when alkoxy groups are hydrolyzed due to water present in the system. The resulting silanol moieties can then react with each other *via* a condensation reaction to produce siloxane bonds.[157] Under anhydrous conditions, condensation between organosilane molecules attached to MSNPs surface will not occur, since there is no reaction occurring between the adjacent siloxane bonds (Figure 16).

3.1.4 N-acylation by NHS chemistry

A *N*-hydroxisuccinimide (NHS) ester is perhaps the most common activation chemistry for creating reactive acylating agents. Nowadays, the great majority of amine-reactive crosslinking or modification reagents commercially available utilize NHS esters. An NHS ester may be formed by the reaction of a carboxylate with NHS in the presence of a carbodiimide such as EDC (1-ethyl-3-(3-dimethylaminopropyl) carbodiimide hydrochloride). NHS ester-containing reagents react with nucleophiles with release of the NHS leaving group to form an

acylated product (Figure 17).

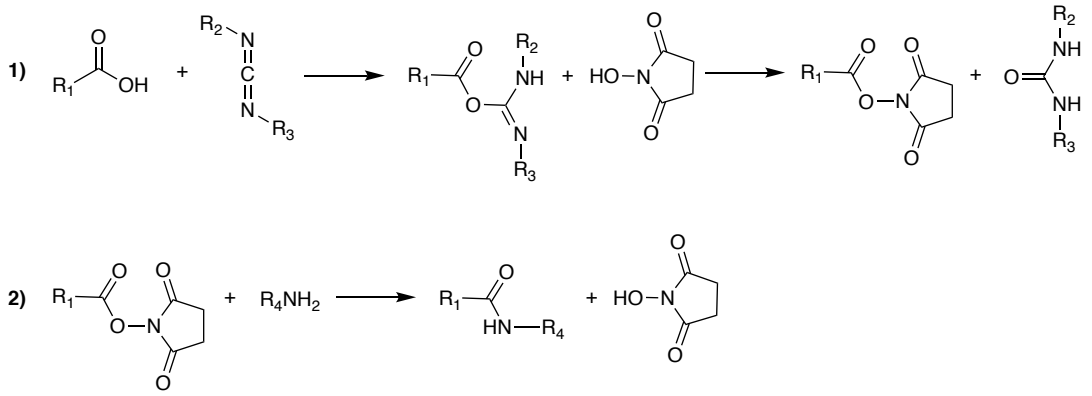

Figure 17. 1) *N*-substituted carbodiimides react with carboxylate group to form an active *O*-acylisourea intermediate. NHS reacts with *O*-acylisourea intermediate forming and NHS ester that is considerably more stable and reactive. 2) The attack of an amine nucleophile on the carbonyl group of the NHS ester results in the loss of the NHS and formation of an amide bond.

Carbodiimides can be used alone, without NHS, to mediate the formation of an amide linkage between a carboxylate group and an amine.[158–160] However, the resulting *O*-acylisourea reactive esters are extremely short-lived. EDC-esters are less stable intermediate in aqueous solution than the one formed with NHS, therefore, the subsequent coupling reaction with the amino group typically proceeds with lower yield values than also using NHS. In addition, by forming the secondary NHS esters, since the activate ester is more stable, excess EDC and NHS can be removed before adding the amino-reagent, thus preventing carbodiimides-mediated polymerization due to the presence of both amines and carboxylates on the reagent molecule.[161–163]

Sulfo-NHS esters present the same specificity and reactivity as NHS-esters with the advantage that are hydrophilic.[161] Unlike NHS-esters that are relatively water insoluble and must be first dissolved in organic solvent before being added to aqueous solutions, sulfo-NHS esters are water soluble. However, in aqueous solution, the hydrolysis of NHS-esters is the major competing reaction, both inactivating EDC and NHS itself and cleaving off the activated ester intermediate. In contrast, in organic solvents, the hydrolysis problem is eliminated.[164] For non-aqueous reactions, an organic base (proton acceptor) is typically added.

In protein molecules, NHS ester crosslinking reagents couple principally with the α-amines at the *N*-terminals and the ε-amines of lysine side chains. The reaction of such esters with a sulfhydryl or hydroxyl group may not yield stable conjugates, forming thioesters or esters linkages, respectively. Both bonds can potentially hydrolyze in aqueous environments or exchange with neighboring amines to form amide bonds.

3.1.5 Reactions with Isocyanates

Isocyanates can react with amine-containing molecules to form stable isourea linkages (Figure 18). Isocyanate-containing reagents can also be used to crosslink or label hydroxyl-containing molecules, forming a urethane (carbamate) linkage. The solvent used for this reaction must be of high purity and should be anhydrous since moisture decomposes isocyanates, releasing CO_2 and leaving an aromatic amine in its place.

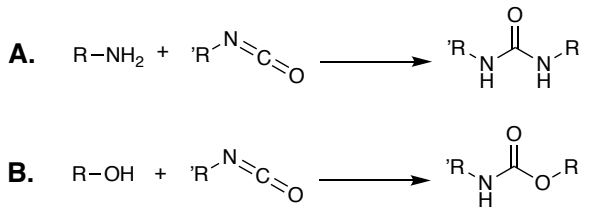

Figure 18. Isocyanate reaction with A) amine compound, forming isourea bond; and with B) hydroxyl compound, yielding carbamate linkage.

Isothiocyanates are similar to isocyanates, except a sulfur atom replaces the oxygen. The reactivity of isocyanates is greater than that of isothiocyanates, but for the same reason their stability is a problem.

3.2 Spectroscopic techniques

3.2.1 Steady-State Optical Techniques

In steady-state spectroscopies the samples are continuously irradiated with a beam of light at a very low intensity, creating and eliminating excited states in a continuous manner and reaching eventually a steady-state where their concentration remains constant. This facilitates the measurement of weak signal levels at the expense of losing kinetic information. Steady-state spectroscopies are best applied to the measurement of absorption and emission spectra.

3.2.1.1 Absorption

Absorption spectra were recorded on a double beam Varian Cary 600i UV-Vis-NIR spectrophotometer (Agilent Technologies, Santa Clara, CA, USA).

3.2.1.2 Fluorescence

Fluorescence excitation and emission spectra were registered in a *Fluoromax-4* spectrofluorometer (Horiba Jobin-Yvon, Edison, NJ, USA).

Fluorescence quantum yields (Φ_F) were determined by the comparative method of Williams *et al*., which involves the use of well characterized standard samples with known Φ_F values.[165] Essentially, solutions of the standard and test samples with identical absorbance at the same excitation wavelength can be assumed to be absorbing the same number of photons. Hence, a simple ratio of the integrated fluorescence intensities (this is, the area of the fluorescence spectrum) of the two solutions (recorded under identical conditions) will yield the ratio of the quantum yield values. Since Φ_F for the standard sample is known, it is trivial to calculate the Φ_F for the test sample. However, in practice, the measurement is slightly more complicated than this because it must take into account few considerations, such as the presence of concentration effects, e.g. self-quenching and inner filter effects, and the use of different solvents for standard and test samples. Therefore, it is important to work with a concentration range and acquiring data at a number of different absorbances (i.e. concentrations) and ensuring linearity across the concentration range for the standard and test samples. In order to minimize re-absorption effect, the absorbance should never exceed 0.1 (for cuvettes with 10 mm path length) at and above the excitation wavelength. Above this level, non-linear effect may be observed due to inner filter effects, and the resulting quantum yield values may be perturbed. Furthermore, standard samples should be chosen to ensure they absorb at the excitation wavelength of choice for the test sample and, if possible, emit in a similar region to the test sample.[166]

Fluorescence quantum yield is calculated from the acquired data following the Equation 1, where $Grad_x$ and $Grad_{ST}$ are the gradients from the plots of integrated fluorescence intensity *vs* absorbance of the test and standard samples respectively and η is the refractive index of the solvent.

$$\Phi_{F,x} = \Phi_{F,ST} \cdot \left(\frac{Grad_x}{Grad_{ST}}\right) \cdot \left(\frac{\eta_x^2}{\eta_{ST}^2}\right) \qquad \text{[Equation 1]}$$

3.2.2 *Time-Resolved Optical Techniques*

Time-resolved optical techniques enable the detection of excited states or other reaction intermediates generated upon pulsed irradiation of a sample with a light source whose intensity fluctuates as a function of time. In the techniques employed in the present work, fluorescence and phosphorescence spectroscopy, the monitoring of these species is achieved through photon emission as a function of time after excitation.[167,168] Time-resolved spectroscopies provide kinetic information at the expense of a lower sensitivity compared to steady-state techniques.

These techniques are usually coupled to photon counting detectors due to their better time

resolution, better sensitivity and lower interference compared to analog detectors. Photon counting mode was inspired by the principle behind the operation of photomultipliers tubes: the detection response is based on the initiation and amplification of a pulse of electrical current when a photon strikes their surface. There are three photon counting techniques, namely Gated Photon Counting (GPC), Time-Correlated Single Photon Counting (TCSPC) and Multichannel Scaling (MCS); the last two had been employed in the present work.[169]

3.2.2.1 Time-Correlated Single Photon Counting (TCSPC)

This method is commonly employed for time-resolved fluorescence measurements and it is based on the precisely timed registration of the first single photon arrival to the detector from the emitting sample.[170] Essentially, the sample is excited by a pulsed light source with a high repetition rate. When a photon is detected, the time of the corresponding detector pulse regarding the laser pulse is measured. The cumulative signal obtained from repetitive cycles is employed to address a histogram memory of photon arrivals per detection time which represents the time decay of a single excitation-emission cycle (see Figure 19).[171] This technique requires keeping a very low probability of registering more than one photon per cycle. To achieve this requisite, TCSPC makes use of the special properties of signals detected by a high-gain detector: if a sample is excited with very attenuated light, this is at a repetition rate in the MHz range, the detection rate of the fluorescence photons is lower than the pulse repetition rate of the excitation source. This means that the intensity of the emission of the sample is so low that the probability of detecting individual photons for each acquisitions period is less than 1. Consequently, the possibility of detecting several photons per acquisition period is extremely low. Therefore, to keep the count rate at the detector equal or below 1% of the excitation rate is needed.

Furthermore, when a high-resolution time is needed, TCSPC is the technique of choice among all photon-counting techniques since it provides the most accurate timing of the photon, below to a few picoseconds per channel. However, this implies that the histogram is built with shorter acquisition time, so with less data.[172]

The effective resolution of a TCSPC experiment is characterized by its instrument response function (IRF). IRF provides essential information about the setup employed: the pulse shape of the light source used, the temporal dispersion of the optical system, the transit time spread in the detector and the timing jitter in the recording electronics.[170] Measurement of IRF is typically achieved by collecting the scattered excitation light of a scattering medium. The deconvolution of the recorded fluorescence decay of the sample and the IRF, performed by a proper software for data analysis, is needed to recover the true signal of the time-resolved fluorescence measurement.

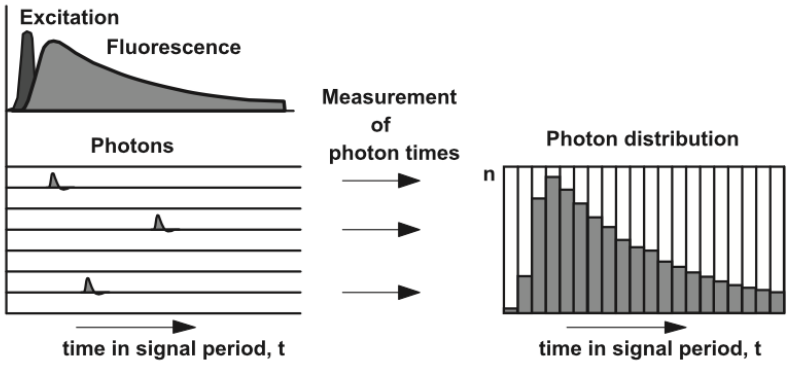

Figure 19. Principle of classic time-correlated single photon counting. The sample is excited by a pulsed laser source with a high repetition rate. Photons emitted by the sample are detected with a high-gain photomultiplier and the time with respect to the excitation pulse is measured. This information is used to build up a one-dimensional photon distribution over the time in the signal period.[171]

Time-resolved fluorescence measurements were carried out using a customized PicoQuant Fluotime 200 fluorescence lifetime system (PicoQuant GmbH, Berlin, Germany) and the FluoFit 5.0 software for data analysis. Excitation was achieved by means of pulsed LED sources emitting at 457 nm, 502 nm and 654 nm. Absorbance of the samples was kept below 0.1 at the excitation wavelength in all cases. The IRF signal was measured by placing a cuvette with a suspension of Ludox® in water.

3.2.2.2 Time-Resolved NIR Phosphorescence Detection

Time-resolved near-infrared phosphorescence detection (TRPD) is a technique that allows the direct and specific observation and monitoring of the $^1O_2$ formation and decay, and subsequently the measurement of its lifetime (τ_Δ) and the quantification of its photogeneration quantum yield (Φ_Δ). TRPD is based on the time-resolved detection of the weak phosphorescence of $^1O_2$ centered at 1275 nm. In this case, the photon-counting method employed is multichannel scaling, in which all detected photons are counted and sorted out in the different positions of a broad memory, thus the time distribution of the detected photons is obtained at once.[172]

Briefly, the setup of TRPD system is mainly composed by a light source to excite the sample, a NIR detector, a monochromator or bandpass filters to isolate the $^1O_2$ emission and a set of lenses to collect and focus the emitted photons onto the detector. Figure 20, reproduced from [173], illustrates schematically the typical TRPD system configuration.

The direct optical detection of $^1O_2$ is used for three main purposes: i) to demonstrate the generation of $^1O_2$ in a system, ii) to obtain kinetic information related to its production, diffusion

and decay, and iii) to quantify the amount of $^1O_2$ created.

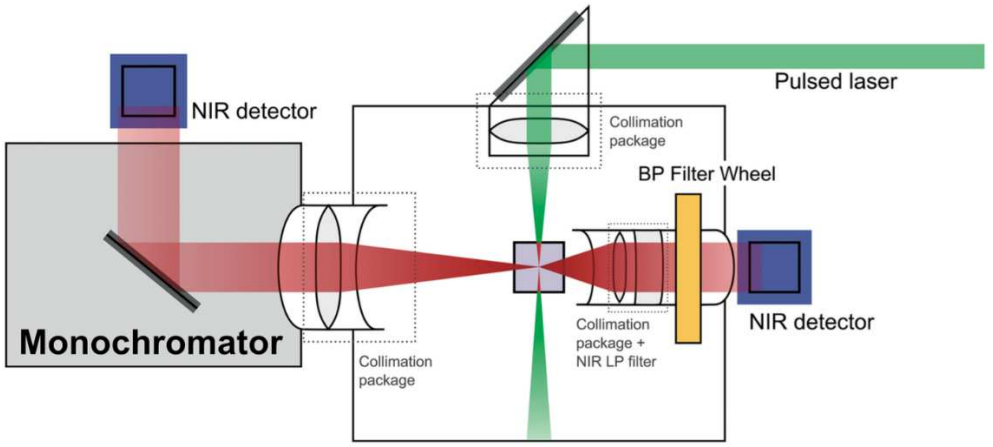

Figure 20. Generic scheme of the direct $^1O_2$ NIR phosphorescence detection system. Image from [173].

Regarding the second purpose, the formation and decay of $^1O_2$ is a bi-exponential process that, in most cases, can be analyzed by adjusting the Equation 2.[174] This process involves two species: a photosensitizer in its triplet state and molecular oxygen; τ_T and τ_Δ are the lifetimes of the ^{3}PS* and of $^1O_2$ respectively. S_0 is a quantity proportional to the concentration of $^1O_2$ created by the laser pulse. Thus, the transient signal obtained from direct optical detection of $^1O_2$ provides valuable information about the efficiency and kinetics of $^1O_2$ production.[174]

$$S(t) = S_0 \cdot \frac{\tau_\Delta}{\tau_\Delta - \tau_T} \cdot \left(e^{-\frac{t}{\tau_\Delta}} - e^{-\frac{t}{\tau_T}} \right) \quad \text{[Equation 2]}$$

In relation to the third purpose, the quantum yield of $^1O_2$ formation (Φ_Δ) is a parameter broadly used that describes the number of $^1O_2$ molecules generated per photon absorbed. Quantum yields were determined by comparative method using well characterized standard samples with known Φ_Δ values in the same solvent and same dose and intensity of excited light. It is possible to calculate Φ_Δ by comparing the fitted S_0 values for the test sample and for optically-matched solution of the standard sample (Equation 3). However, as explained for Φ_F, it is preferred to acquire data with a concentration range for the standard and test samples and ensuring linearity across the different concentrations by maintaining their absorbance below 0.1 at the excitation wavelength. Quantum yields of $^1O_2$ formation were calculated from the recorded data following the Equation 4, where $Grad_x$ and $Grad_{ST}$ are the gradients from the plots of S_0 *vs* $(1\text{-}10)^{-Abs}$ of the test and standard samples, respectively.

$$\Phi_{\Delta,x} = \Phi_{\Delta,ST} \frac{S_{0,x}}{S_{0,ST}} \quad \text{[Equation 3]}$$

$$\Phi_{\Delta,x} = \Phi_{\Delta,x} \cdot \left(\frac{\mathrm{Grad_x}}{\mathrm{Grad_{ST}}} \right) \quad \text{[Equation 4]}$$

Generation of $^1O_2$ was studied in the present work by time-resolved near-infrared phosphorescence using a customized PicoQuant Fluotime 200 lifetime system (PicoQuant GmbH, Berlin, Germany). The kinetic parameters governing the production and decay of $^1O_2$ were determined by fitting the Equation 2 to the time-resolved phosphorescence intensity at 1275 nm using the FluoFit 5.0 software. Excitation was achieved by means of laser sources emitting at 355 nm, 473 nm and 660 nm.

3.3 Confocal Microscopy

Confocal microscopy was employed in the present work to qualitatively study the internalization of nanoparticles in cells.

Confocal microscopy is a specific fluorescence microscopy technique that has been tremendously popular in recent years, due in part to the relative ease with which extremely high-quality images can be obtained. This technique allows imaging both fixed and living cells and tissues. As any fluorescence technique, confocal microscopy requires that the objects of interest fluoresce. However, most molecules in the cell are not very fluorescent and therefore, fluorophores must be incorporated into the specimen. This can be achieved either by the labeling with organic dyes or fluorescent probes or by the genetic introduction of fluorescent proteins. The current wide available options of fluorophores provide specific subcellular targeting as well as numerous color alternatives.[175,176]

Confocal microscopy provides higher resolution than conventional wide-field optical epifluorescence microscopy. This increase in the resolution is achieved due to three main factors. First, the use of lasers for illumination, which narrows the excitation range to 2-3 nm. This is around 10 times narrower than the range of wavelengths when using excitation filters.[177] Second, the focusing of the excitation light. Instead of illuminating the whole sample at once as happened in wide-field microscope, laser light is focused onto a defined spot at a specific depth within the sample. This leads to the emission of fluorescent light at exactly this point. The very specific optical path is achieved by adding a first pinhole placed in front of the excitation source. This excitation light is reflected from a dichroic mirror towards an objective lens which focusses the light to a spot in the sample.[178,179] Last but not least, the ability to exclude the “out-of-focus” light. When fluorescent specimens are imaged using a conventional wide-field fluorescence microscope, secondary fluorescence (out-of-focus light) emitted by the specimen that appears away from the region of interest often interferes with the resolution of those features that are in focus. Confocal microscopy removes this light and

significantly improves the imaging resolution. This improvement is achieved by placing a second pinhole in front of the detector to block out-of-focus light originated from above or below the plane of focus in the specimen from reaching the detector. The second pinhole has the same focus as the first pinhole mentioned before, the two are confocal.

The confocal microscope setup is shown in Figure 21. As mentioned before, confocal microscope has multiple laser excitation sources, whose light is focused by a first pinhole and objective lens. Fluorophores within the sample absorb the light and fluoresce. The objective lens collects the resulting fluorescent light which passes through a dichroic mirror. A second pinhole reject the out-of-focus light to reach the electronic detector, usually photomultipliers. Through a computer, the images are acquired, processed and analyzed.[180]

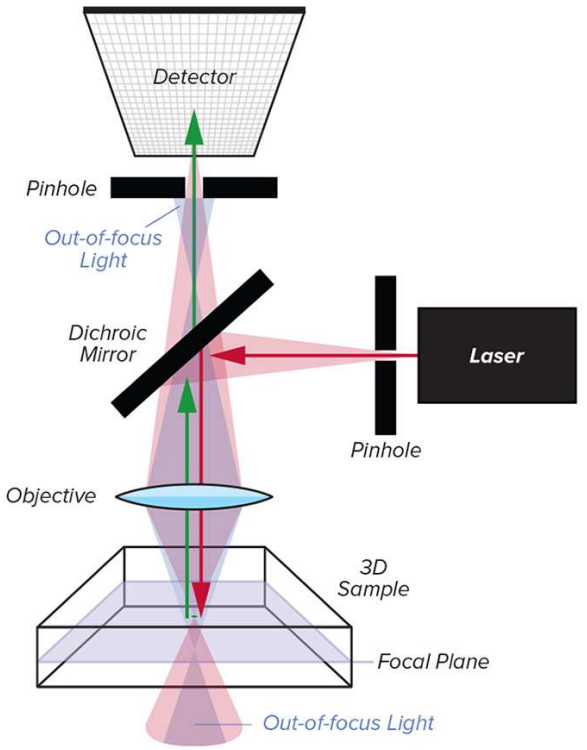

Figure 21. Generic scheme of a confocal microscope. Image from [179].

Qualitative uptake studies in cells were carried out by Leica TCS SP8 laser-scanning confocal spectral microscope (Leica Microsystems Heidelberg, Mannheim, Germany) with Argon and HeNe lasers attached to a Leica DMi8 S Platform inverted microscope. For visualization of the nanoparticles uptake, images were acquired using an APO 40 objective lens. Images were analyzed using ImageJ software.

3.4 Physicochemical Characterization of Nanoparticles

All the prepared nanoparticles were characterized in terms of their physicochemical properties, i.e. size, polydispersity index, zeta-potential and drug concentration.

3.4.1 Dynamic Light Scattering (DLS)

Nanoparticles size and polydispersity index were measured by Dynamic Light Scattering (DLS), also known as photon correlation spectroscopy. This is one of the most frequently used methods to obtain an average diameter of nanoparticles dispersed in liquids. This technique relies on Rayleigh scattering from the suspended nanoparticles that undergo Brownian motion. The nanoparticle suspension is illuminated with a laser source and as the incident light impinges on the particles, the direction and intensity of the light beam are both altered due to the scattering phenomena. Since the particles are in constant random motion due to their kinetic energy, the measurement over time of the fluctuations of the light intensity contains valuable information on that Brownian motion and can be used to determine the diffusion coefficient (D) of the particles, which is related to their hydrodynamic radius (Rh) through the Stokes-Einstein equation (Equation 5). Where κ_b is the Boltzmann constant, T is the absolute temperature, and η is the viscosity of the medium.DLS measures the hydrodynamic diameter of the particles which is defined as “the size of a hypothetical hard sphere that diffuses in the same fashion as that of the particle being measured”. Therefore, the hydrodynamic diameter is that of a sphere that has the same translational diffusion coefficient as the particle being measured, assuming a hydration layer surrounding the particle.

$$\mathrm{D} = \frac{k_b T}{6\pi\eta R_h} \qquad \text{[Equation 5]}$$

The determination of the diffusion coefficient is achieved by cumulant analysis, this is a method of analyzing the autocorrelation function obtained from the intensity fluctuation in the respective time frames. When the intensity is correlated at several time points, in the beginning, the scattered intensities are similar, losing this similarity over time due to particle’s movement. Then, for small particles, the diffusion is much faster and cause the intensity to fluctuate more rapidly than the large ones and thus, photon correlation is lost faster and the correlation decays at early time points of the measurement (Figure 22).[181,182]

DLs results are often expressed in terms of the Z-average. Z-average is defined in ISO 22412 as “the harmonic intensity averaged particle diameter”.[183] It is an intensity-based overall average size based on a specific fit to the raw correlation function data. The fitting, this is the

cumulant analysis, can be thought of as force-fitting the result to a simple Gaussian distribution where the Z-average is the mean. However, Z-average value should only be employed to provide the characteristic size of the particles if the sample is monomodal (i.e. only one peak), spherical and monodisperse. For a mixture of particles with obvious size difference (more than one peak), the calculated Z-average carries irrelevant information.[182]

Polydispersity index (PdI) is a dimensionless measure of the broadness of the size distribution. It informs about the monodispersity tendency of the sample.[183]

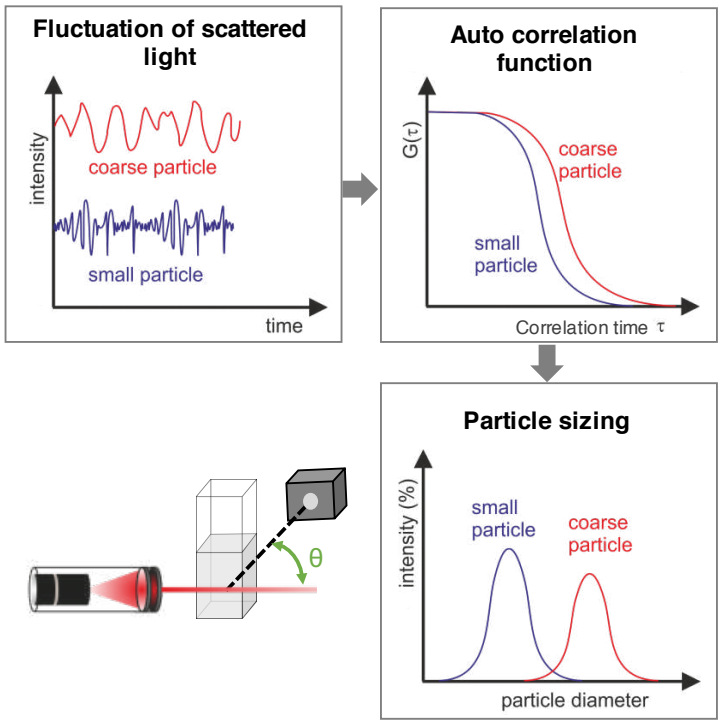

Figure 22. Analysis process of a DLS measurement and scheme of a typical DLS instrument.

Dynamic light scattering studies were performed using a Zetasizer-Malvern Nano ZS90 (Malvern Instruments Ltd., Worcestershire, UK).

3.4.2 *Zeta-Potential*

The net charge at the particle surface affects the ion distribution in the surrounding region, resulting in an increased concentration of counter ions close to the surface. Thus, an electrical double layer exists around each particle. This double layer consists of two parts: an inner region called the Stern layer, where the ions are strongly bound, and an outer, diffuse, region where they are less firmly attached. Zeta-potential reflects the potential that exists at the slipping plane, this is the potential at the hypothetical plane that acts as the interface between

the electric double layer and the layer of the surrounding dispersant (see Figure 23).[184]

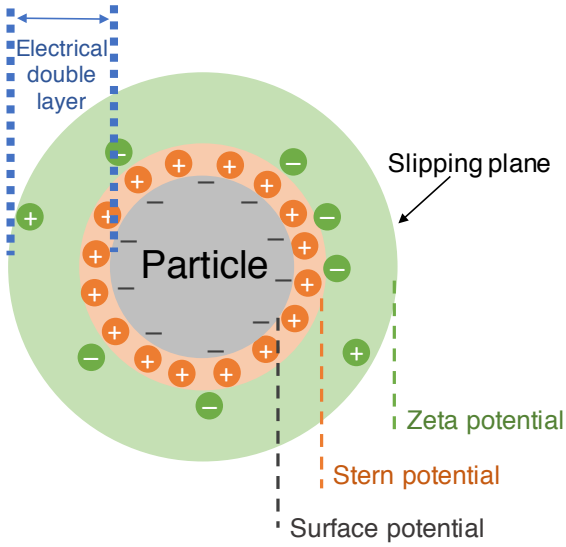

Figure 23. Schematic showing the electrical double layer that surrounds a particle in an aqueous medium. The potential at the slipping plane is the zeta-potential.

In this technique, a voltage is applied across a pair of electrodes at either end of a cell containing the particle dispersion. When an electric field is applied to the sample, charged particles suspended in the electrolyte are attracted towards the electrode of opposite charge. The particles move to the electrode with constant velocity, which is measured. The velocity of a particle in an electric field is referred to as its electrophoretic mobility. Zeta-potential is calculated by determining the electrophoretic mobility of the sample, obtained by performing an electrophoresis experiment and measuring the velocity of the particles under Laser Doppler Velocimetry. With this knowledge, the zeta-potential of the particle can be obtained by application of the Henry equation (Equation 6).[181,185] Where U_E is the measured electrophoretic mobility, ε is the relative permittivity/dielectric constant, ζ is the zeta-potential value, *f*(*Ka*) is the Henry's or Helmholtz-Smoluchowski function, and η is the viscosity at the experimental temperature.

$$U_E = \frac{2\varepsilon\zeta}{3\eta} f(Ka) \qquad \text{[Equation 6]}$$

Laser doppler velocimetry technique utilizes the Doppler effect to measure the velocity of the charged suspended particles. Briefly, the sample is irradiated and the light scattered is combined with the reference beam. This produces a fluctuating intensity signal where the rate of fluctuation is proportional to the speed of the particles. A digital signal processor is used to extract the characteristic frequencies in the scattered light.[184]

Laser Doppler micro-electrophoresis studies were carried out using a Zetasizer-Malvern Nano ZS90 (Malvern Instruments Ltd., Worcestershire, UK).

3.4.3 Drug Concentration

The reader is referred to the Experimental Section of each corresponding Chapter 4 or Chapter 5 for detailed explanation of the procedure in each particular case to calculate the drug concentration in the NPs suspension.

Entrapment efficiency (EE) is the percentage of drug that is successfully entrapped, or in this case covalently attached, to the nanoparticle in respect of the total drug added. EE is calculated as indicated in Equation 7.

$$\%\ \text{Entrapment efficiency} = \frac{\text{drug loading}}{\text{theoretical drug loading}} \cdot\ 100 \qquad \text{[Equation 7]}$$

Drug loading is the amount of drug loaded per unit weight of the nanoparticle and indicates the percentage off mass of the nanoparticle that is due to the encapsulated, or in this case covalently attached, drug. DL is calculated following the Equation 8.

$$\%\ \text{Drug loading} = \frac{\text{PS mass}}{\text{PLGA mass}} \cdot\ 100 \qquad \text{[Equation 8]}$$

3.5 *In Vitro* Biological Studies

3.5.1 Light Sources

For *in vitro* phototoxicity studies, two different light sources were employed in the present work. On the one hand, in Chapter 4, irradiation was carried out with the blue light from a LED Par 64 Short V2 lamp (λ_{em} = 463 ± 11 nm; irradiance = 12 mW·cm^{-2}; Showtec, Kerkrade, Netherlands). On the other hand, for both Doxorubicin cleavage and phototoxicities studies of Chapter 5, the red light from a Red 670 Device from RedLightMan (Greater Manchester, UK) composed by 42 red light LEDs (λ_{em} = 661 ± 10 nm; irradiance = 70 mW·cm^{-2}) was used.

The light dose received by the samples was calculated according to the Equation 9.

$$\text{Light dose}\ (\text{J} \cdot \text{cm}^{-2}) = \text{Irradiation}\ (\text{W} \cdot \text{cm}^{-2}) \cdot \text{Time}\ (\text{s}) \quad \text{[Equation 9]}$$

3.5.2 Uptake Studies

The cellular uptake of the nanoparticles was determined by recording the fluorescence intensity of the lysate treated cells normalized by their amount of protein. Cells were incubated

with fluorescence nanoparticles for various time periods up to 24 h. After incubation, the non-internalized nanoparticles were removed, cells were lysate with SDS to release the taken nanoparticles and their emission spectra were recorded in a Synergy H1 Hybrid microplate reader (BioTek Instruments, Inc., Winooski, VT, USA). The internalization level of the nanoparticles depends on the quantity of cells. Thus, each sample was normalized by the amount of protein present by means of the colorimetric bicinchoninic acid (BCA) assay.[186]

The chemistry behind BCA assay is a two-step color development reaction. In the first step, biuret reaction is performed, this is the reduction of Cu^{2+} to Cu^{+} by peptides with three or more amino acid residues in an alkaline medium containing sodium potassium tartrate, a chelating agent.[187] The formed Cu^{+} binds to peptides forming a Cu^{+}–peptide complex of purplish-violet color (Figure 24). In the second step, two molecules of BCA react with a Cu^{+} ion to yield purple-colored complex with higher absorption coefficient than Cu^{+}–peptide complex, thus increasing the sensitivity of the protein detection. Since the production of Cu^{+} in this assay is a function of protein concentration and incubation time, the protein content of unknown samples may be determined spectrophotometrically by comparison with known protein standards. BCA assay is generally not affected by a range of detergents and denaturing agents that tend to interfere with other colorimetric protein assays.

The reader is referred to the Experimental Section of Chapter 5 for detailed explanation of the procedure in each particular case to study the *in vitro* quantitative uptake of nanoparticles.

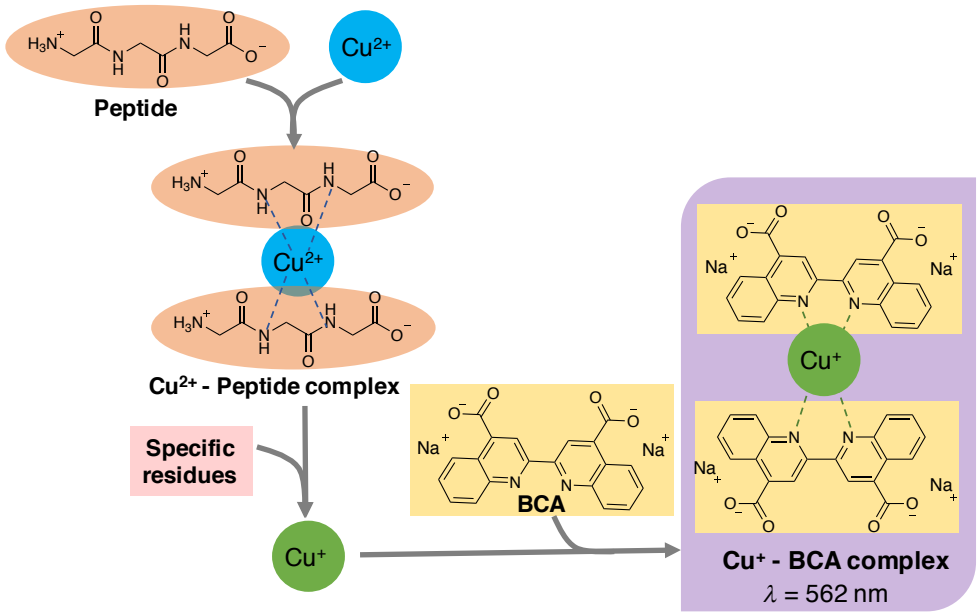

Figure 24. Schematic drawing to display the chemical species in a solution during the BCA protein assay. The peptide bonds and specific residues reduce cupric ions (Cu^{2+}) to cuprous ions (Cu^{+}), which form complexes with BCA.

3.5.3 Phototoxicity Studies

In order to examine the phototoxic effect of a photosensitizer, the colorimetric 3-(4,5-dimethylthiazol-2-yl)-2,5-diphenyltetrazolium bromide (MTT) assay[188] was performed. MTT assay is widely accepted and used as a reliable way to examine cell viability. The principle of the MTT assay is that for most viable cells, their mitochondrial activity is constant, therefore, an increase or decrease in the number of viable cells is linearly related to their mitochondrial activity. The mitochondrial activity of the cells is reflected by the conversion of the tetrazolium salt MTT into formazan crystals.[189,190] The yellow tetrazolium MTT is reduced by metabolically active cells, meanly by the action of dehydrogenase enzymes, to generate reducing equivalents such as NADH (

Figure 25).[191] The resulting insoluble purple formazan precipitate can be solubilized, in DMSO for example, and viable cell number can be detected by measuring its concentration reflected in its absorbance at 562 nm. For toxicity studies, the absorption values of the cells incubated with drugs are compared with the absorbance of not treated cells to determinate if the drug cause a decrease in the cell viability.

The reader is referred to the Experimental Sections of Chapter 4 and Chapter 5 for detailed explanation of the procedure in each particular case to study the *in vitro* phototoxicity of different drug formulations.

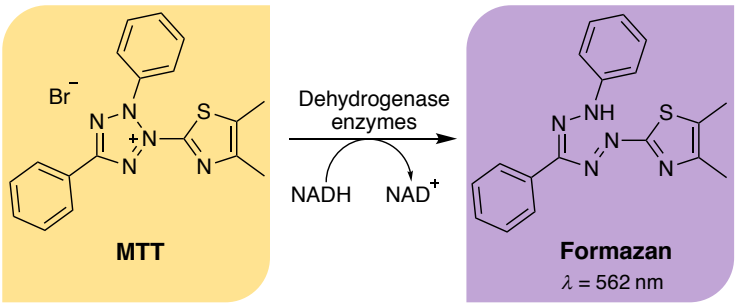

Figure 25. Enzymatic reduction of MTT to formazan.

CHAPTER 4: c(RGDfK) and ZnTrimPyP-Bound Polymeric Nanocarriers for Tumor-Targeted Photodynamic Therapy

4.1 Introduction

The major drawback of cancer therapies is still the lack of selectivity. In the recent years, great efforts are devoted to design selective drugs that potentiate the therapeutic effect in cancer cells while diminishing unwanted adverse effects to surrounding healthy cells. To achieve this goal, the active targeting strategy exploits the delivery of an agent to a specific targeted tumor site by means of a molecular recognition process.

The RGD-containing peptides are active-targeting moieties that specifically attach to $\alpha_v\beta_3$ integrin with a high binding affinity. They have been widely used as targeting ligands for cancer therapies[192,193], including photodynamic therapy (PDT)[118–122], since this integrin is known to be present on the neovasculature of cancer tissues and is also overexpressed on glioblastoma, melanoma, lung, ovarian and breast cancer cells, but generally not in healthy cells.[123–125] In the present research, we are motivated to investigate RDG-modified polymeric nanoparticles (NPs) as PDT delivery vehicles. The use of nanocarriers with RGD ligands as nanovehicles has two main advantages: i) more drug molecules can be delivered per internalized receptor; and ii) the carriers are more likely to be internalized *via* receptor mediated endocytosis than single RGD constructs owing to higher local ligand concentration and receptor cross-linking.

In a NP drug delivery-based approach, a PS is either physically entrapped or immobilized on the surface of NPs. Drug loading nanocarriers can greatly transfer their cargo from the NP vector to the cell. However, drug molecules absorbed to NPs are sometimes chemically or physically desorbed due to changes in their environment, leading to premature drug loss even before the cellular target site is reached. In contrast, covalently bound drugs ensure stability during transport to the cell. In this regard, our group previously described the synthesis and biological evaluation of physically entrapped zinc(II) tetraphenylporphyrin (ZnTPP) in PLGA-PEG nanoparticles[194] and, in addition, PLGA-PEG NPs with covalently-bound ZnTPP[25]. To our surprise, when ZnTPP was attached to the NP, the resulting nanoparticle formulation was essentially non-phototoxic, unlike when the PS was occluded. Photophysical studies revealed that the underlying reason for those results is that the hydrophobic ZnTPP is so deeply buried into the NPs that singlet oxygen ($^1O_2$) remains inside them and is unable to reach cellular targets. We thus hypothesized that a hydrophilic photosensitizer capable of remaining on the surface of NPs would be able to release $^1O_2$ and cause cellular damage. To this end, 5-[4-azidophenyl)-10,15,20-tri-(*N*-methyl-4-pyridinium)porphyrinato zinc (II) trichloride (ZnTriMPyP), the hydrophilic counterpart of ZnTPP, was covalently attached to the NP and we found that it was indeed able to release $^1O_2$ to the outer medium.[25]

The aim of the present research is to evaluate if the c(RGDfK) peptide active targeting

strategy could add value to the ZnTriMPyP nanoformulation. Moreover, we wish to assess whether locally concentrating the PS by covalently binding it to the NPs can enhance its phototoxicity.

4.2 Results and Discussion

4.2.1 Synthesis

4.2.1.1 Synthesis of Precursors of PLGA Nanoparticles

4.2.1.1.1 Synthesis of PLGA-ZnTriMPyP

Poly-(*D,L*-lactide-*co*-glycolide) (PLGA) was conjugated to the cationic porphyrin ZnTriMPyP as described by Boix-Garriga *et al.*[25] (Figure 26). This synthetic work was previously carried out in collaboration with the Photobiology and Photomedicine Group from the University of Hull (UK), supervised by Prof. Ross W. Boyle (see Figure A1 in Appendix A for its synthetic procedure). The conjugation of ZnTriMPyP to the polymeric chain of PLGA allowed a better control of the drug attachment in the NPs than *via* coupling it to previously prepared NPs.

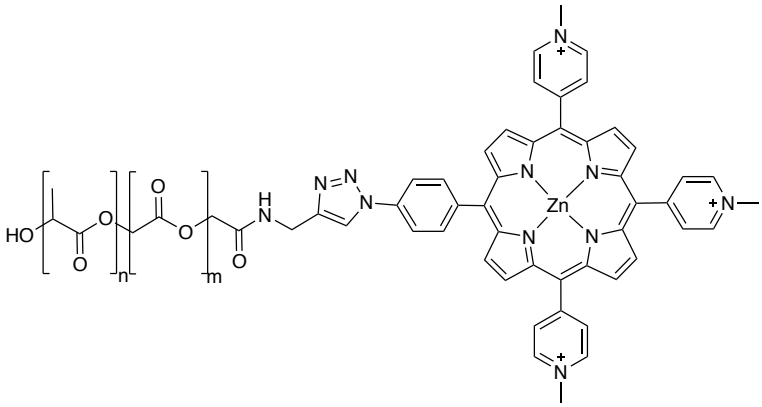

Figure 26. PLGA-ZnTriMPyP conjugate.

4.2.1.1.2 Synthesis of PLA-PEG-c(RGDfK)

Poly-(*D,L*-lactide) (PLA) was conjugated to polyethylene glycol (PEG) and c(RGDfK) peptide as described by de las Heras *et al.*[195] (Figure 27). This synthetic work was previously performed in collaboration with the Laboratory of Pharmaceutical Technology at the University of Geneva (Switzerland), supervised by Prof. Norbert Lange (see Figure A2 and Figure A3 in Appendix A for its synthetic procedure).

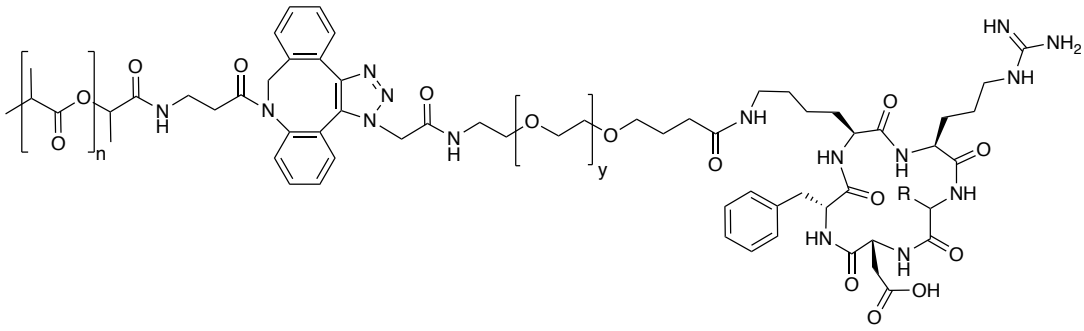

Figure 27. PLA-PEG-c(RGDfK) conjugate.

4.2.1.2 Synthesis of PLGA Nanoparticles

Three types of nanocarriers were prepared by a modified nanoprecipitation method[149]: PLGA-PEG (Blank), ZnTriMPyP-PLGA-PEG and ZnTriMPyP-PLGA-PLA-PEG-c(RGDfK) (Figure 28). Nanoprecipitation, also called solvent displacement method, is a simple method that produces smaller nanoparticles as compared to other methodologies, such as emulsification-solvent evaporation.[107,196] In order to obtain the desired formulations, different percentages of the polymers (i.e. PLGA-ZnTriMPyP, PLA-PEG-c(RGDfK), PLGA-mPEG and PLGA ester terminated) were employed (Table 2).

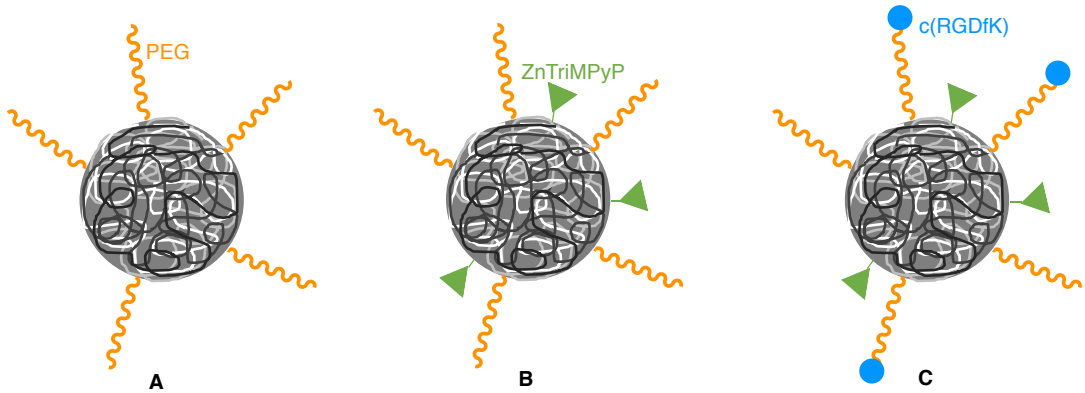

Figure 28. Illustrated scheme of the three types of prepared nanoparticles: PLA-PEG (Blank) (A), ZnTriMPyP-PLGA-PEG (B) and ZnTriMPyP-PLGA-PLA-PEG-c(RGDfK) (C).

Table 2. Percentages of the different polymeric formulations that constituted the desired nanoparticles.

Formulation	Blank NPs	ZnTriMPyP-PLGA-PEG NPs	ZnTriMPyP-PLGA-PLA-PEG-c(RGDfK) NPs
PLGA-ZnTriMPyP	-	10%	10%
PLA-PEG-c(RGDfK)	-	-	10%
PLGA-mPEG	70%	70%	70%
PLGA ester terminated	30%	20%	10%

Firstly, NPs could be recognized as foreign objects in the body and be cleared from systemic circulation by the cells of the mononuclear phagocyte system, precluding their accumulation in target cells and tissues. However, it is known that the presence of PEG on the surface of NPs protects them from aggregation, opsonization and phagocytosis, thereby increasing their circulation life-time.[197] The reason for this is because PEG provides steric stabilization and stealth properties against protein absorption and macrophage uptake.[198,199] In addition, PEG has been clinically validated in many different applications and is currently listed as "Generally Recognized as Safe" by the FDA. In the same way, previous research in our group demonstrated that 10% PEG coating confers high stability to PLGA NPs in the presence of serum proteins. In contrast, when 5% of PEG is used, PLGA NPs aggregate and precipitate; while increasing the PEG content to 15% leads to highly heterogeneous NP populations.[194] For this reason, in the present study, 10% PEG was kept constant in all the prepared PLGA NP formulations.

Secondly, a contribution of 10% PLGA-ZnTriMPyP was employed in ZnTriMPyP-PLGA-PEG and ZnTriMPyP-PLGA-PLA-PEG-c(RGDfK) NPs. We reported before that at the higher the percentage of PLGA-ZnTriMPyP in the NP, the greater the formation of aggregates due to dimerization between ZnTriMPyP molecules. However, the NPs suspensions need to have an adequate ZnTriMPyP concentration to achieve phototoxicity *in vitro*. To reach this compromise, we selected a contribution of 10% based on previous studies.[25]

Lastly, a contribution of 10% PLA-PEG-c(RGDfK) was employed to prepare the targeted NPs. Previous work on our laboratory demonstrated *in vitro* the cellular targeting ability of PLA NPs prepared with 10% of this conjugate against cells with high expression of $\alpha_v\beta_3$ integrin.[200] Since this former work is unpublished, the most relevant results of this investigation are summarized in Appendix A for a better comprehension of the present research.

4.2.2 Physicochemical Characterization of Nanoparticles

The prepared NPs were characterized in terms of their physicochemical properties: size, polydispersity index (PdI), zeta-potential, concentration of the photosensitizer ZnTriMPyP, drug loading and entrapment efficiency (Table 3).

The average size of blank, ZnTriMPyP-PLGA-PEG and ZnTriMPyP-PLGA-PLA-PEG-c(RGDfK) NPs was found to be ~75 nm, ~80 nm and ~94 nm, respectively. These values are similar to previously reported PLGA-PEG NPs prepared with this methodology.[25,196,201] Size is an important parameter in the passive targeting ability of NPs since it governs the biodistribution of the nanocarrier system. It is known that the optimal nanocarrier size for drug delivery is in the size range of 50 – 200 nm because the abnormal fenestrations between

adjacent endothelial cells in tumor tissues are typically 100 – 500 nm. Therefore, due to the small size of the prepared NPs, they could benefit from the enhanced permeability and retention (EPR) effect *in vivo.*[202] The PdI of the developed NPs was smaller than 0.2 in all the formulations, demonstrating a homogeneous distribution.

Moreover, ZnTriMPyP-PLGA-PLA-PEG-c(RGDfK) NPs exhibited a small increase in the zeta-potential as compared to ZnTriMPyP-PLGA-PEG NPs, due to the charge of arginine, as highlighted before.[203] The surface charge of NPs plays an important role in endocytic pathways. Negatively charged NPs are effective in evading the reticuloendothelial system and prolong blood circulation. However, when NPs have a very high negative charge, the cellular uptake efficiency could decrease due to electrostatic repulsion between them and the negatively charged cell membrane.[204,205] Thus, the ZnTriMPyP-PLGA-PEG-c(RGDfK) formulation, with small particle size and moderate negative zeta-potential value, could improve the circulatory half-life time while preserving the target affinity for tumor cells.

Both NP formulations, ZnTriMPyP-PLGA-PEG and ZnTriMPyP-PLGA-PEG-c(RGDfK), showed a notably high loading capacity and entrapment efficiency.

Table 3. Characterization of nanoparticles. PdI: polydispersity index. DL: drug loading. EE: entrapment efficiency.

NP formulation	Size / nm	PdI	Zeta-potential / mV	[PS] / μM	% DL	% EE
Blank PLGA-PEG	75 ± 3	0.07 ± 0.01	-32 ± 2	-	-	-
ZnTriMPyP-PLGA-PEG	80 ± 2	0.16 ± 0.02	-30 ± 1	18 ± 1	0.43 ± 0.03	89 ± 5
ZnTriMPyP-PLGA-PLA-PEG-c(RGDfK)	94 ± 2	0.17 ± 0.02	-25 ± 1	20 ± 1	0.47 ± 0.02	92 ± 3

In all, only minor differences in the studied physicochemical parameters were observed between ZnTriMPyP-PLGA-PEG and ZnTriMPyP-PLGA-PEG-c(RGDfK) formulations; thus, the conjugation of the NPs with c(RGDfK) does not affect markedly the physical characteristics of the nanocarrier.

4.2.3 Photophysical Characterization of Nanoparticles

The photophysical behavior of the synthesized nanoparticles were studied by UV-Vis, steady-state and time-resolved fluorescence spectroscopy, as well as time-resolved phosphorescence at 1275 nm to study the production of singlet oxygen.

4.2.3.1 Absorption and Steady-State Fluorescence

Absorption and emission spectra of aqueous suspensions of ZnTriMPyP-PLGA-PEG and ZnTriMPyP-PLGA-PLA-PEG-c(RGDfK) NPs were recorded (Figure 29A and B). In addition, the spectra were registered in DMSO, which disrupts the NPs, in order to compare the photophysical behavior of ZnTriMPyP when is covalently attached to the polymeric NPs and after their breakage (Figure 29C and D).

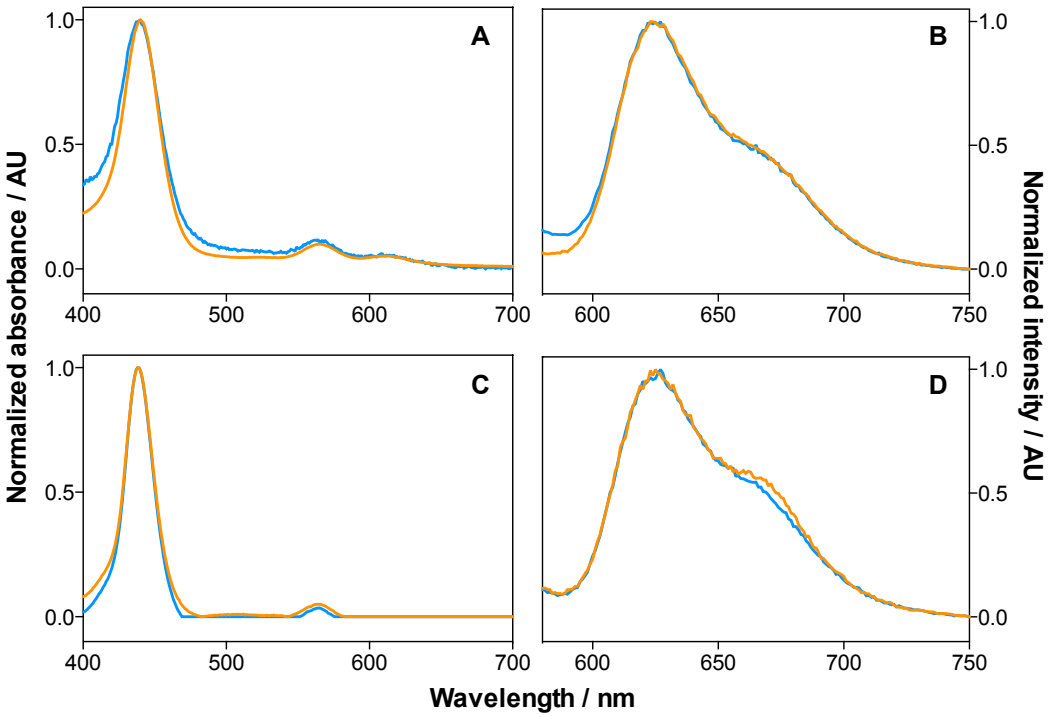

Figure 29. Normalized absorption (A) and normalized emission spectra (B) of aqueous suspensions of ZnTriMPyP-PLGA-PEG (in blue) and ZnTriMPyP-PLGA-PLA-PEG-c(RGDfK) (in orange) NPs and after disruption in DMSO, (normalized absorption in C and normalized emission spectra in D). λ_{exc} = 556 nm.

As mentioned in Boix-Garriga *et al.*[25], aqueous suspensions of both ZnTriMPyP-NPs showed a slight red shift in absorption spectra as compared to the spectra in organic solvent. Similarly, their emission spectra showed a reduced intensity of the Q (0,1) band when compared to the spectra in DMSO. These minor spectral differences can be attributed to differences in the local microenvironment of ZnTriMPyP in the NPs compared to that after the NPs disruption in DMSO. Likewise, scattering due to the NPs was observed in the absorption spectra of the aqueous suspensions of NPs, which was not appreciable in organic solvent. Therefore, despite these minor changes, the photosensitizer ZnTriMPyP seems to remain photophysical active in both NP formulations.

4.2.3.2 Time-Resolved Fluorescence

Time-resolved fluorescence spectra of aqueous suspensions of ZnTriMPyP-PLGA-PEG (Figure 30A) and ZnTriMPyP-PLGA-PLA-PEG-c(RGDfK) (Figure 30B) were recorded. To investigate the time-resolved emission of the photosensitizer ZnTriMPyP, their emission at 650 nm was monitored after excitation at 457 nm.

Both NP formulations showed biexponential decays (Table 4), whose main population of excited singlet state molecules decayed in 1.4 ns, which is very similar to free ZnTriMPyP in water (1.0 ns). Furthermore, they showed a smaller contribution of a very short component of 0.5 ns. These two populations observed are consistent with the values reported before for ZnTriMPyP-PLGA-PEG NPs.[25] In this previous publication, we attributed the 0.5 ns component to the presence of aggregates due to the dimerization of some neighboring ZnTriMPyP molecules at the surface of the NPs. Overall, the NP formulations did not exhibit appreciable differences since their singlet state lifetimes and contributions were very similar.

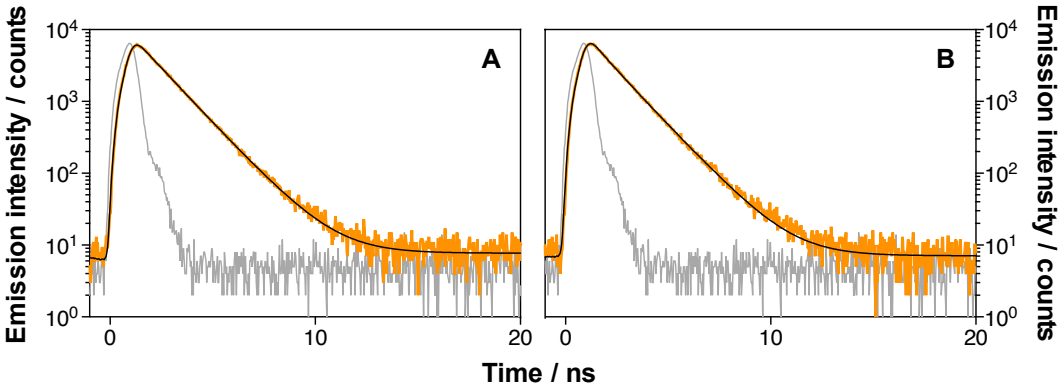

Figure 30. Time-resolved fluorescence decays of aqueous suspensions of ZnTriMPyP-PLGA-PEG (A) and ZnTriMPyP-PLGA-PLA-PEG-c(RGDfK) (B) NPs. λ_{exc} = 457 nm. λ_{em} = 650 nm. Grey line corresponds to instrumental response factor.

Table 4. Singlet state lifetimes (τ_s) and their relative amplitudes (A_s) for aqueous suspensions of ZnTriMPyP-PLGA-PEG and ZnTriMPyP-PLGA-PLA-PEG-c(RGDfK) NPs. [a]Data from Boix-Garriga *et al.*[25].

Sample	τ_s / ns	% A_s
ZnTriMPyP[a]	1.0 ± 0.1	100
ZnTriMPyP-PLGA-PEG NPs	1.4 ± 0.1	79 ± 10
	0.5 ± 0.2	21 ± 10
ZnTriMPyP-PLGA-PLA-PEG-c(RGDfK) NPs	1.4 ± 0.1	75 ± 5
	0.5 ± 0.1	25 ± 5

4.2.3.3 Singlet Oxygen Generation and Kinetics

Time-resolved NIR phosphorescence detection studies demonstrated the generation of $^1O_2$ in ZnTriMPyP-PLGA-PEG (Figure 31A) and ZnTriMPyP-PLGA-PLA-PEG-c(RGDfK) (Figure 31B) NPs suspended in water. Here, $^1O_2$ formation and decay were monitored by time-resolved detection of its weak NIR phosphorescence centered at 1275 nm after excitation at 473 nm. For both NP formulations, a monoexponential short rise and decay were shown. Results are summarized in Table 5.

Table 5. Kinetic parameters of $^1O_2$ phosphorescence (1275 nm) and ^{3}ZnTriMPyP* phosphorescence (1110 nm) of aqueous suspensions of ZnTriMPyP-PLGA-PEG and ZnTriMPyP-PLGA-PLA-PEG-c(RGDfK) NPs under saturated conditions of air or O_2; or with the addition of NaN_3 (10 mM). τ_Δ: $^1O_2$ lifetime. τ_T : ^{3}PS* lifetime.

NP formulation		Air		O_2		NaN_3
		1275 nm	1110 nm	1275 nm	1110 nm	1275 nm
ZnTriMPyP-PLGA-PEG	τ_Δ / μs	3.4 ± 0.2	-	4.0 ± 0.1	-	-
	τ_T / μs	7.1 ± 0.5	5.2 ± 0.6	1.4 ± 0.1	0.9 ± 0.5	5.1 ± 0.2
ZnTriMPyP-PLGA-PLA-PEG-c(RGDfK)	τ_Δ / μs	3.1 ± 0.5	-	4.1 ± 0.1	-	-
	τ_T / μs	7.3 ± 0.8	5.4 ± 1.1	1.5 ± 0.1	1.6 ± 0.3	5.9 ± 0.5

Firstly, in air saturated conditions, the rise presented a lifetime of ~3 μs, which corresponds to $^1O_2$ lifetime (τ_Δ) and is a typical value for this parameter in water. The decay showed a lifetime of ~7 μs, corresponding to $^1O_2$ formation, that is equivalent to that of the excited triplet state decay (τ_T) (^{3}PS* phosphorescence). Secondly, in O_2 saturated conditions, O_2 acts as a quencher of the triplet excited state and, as a consequence, τ_T was decreased to ~1 μs in both NP formulations. Thirdly, in order to unequivocally confirm the detection of $^1O_2$, the phosphorescence decay was recorded after the addition of a known $^1O_2$ quencher, sodium azide (NaN_3) (10 mM). This concentration of NaN_3 completely deactivated $^1O_2$, as observed in Figure 31 with the disappearance of the rise in the spectra.

Lastly, time-resolved phosphorescence at 1110 nm allowed the study of ^{3}PS* (Figure 32). Both NP formulations showed a monoexponential decay with a lifetime of ~5 μs in air saturated conditions and ~1 μs in O_2 saturated, values quite close to that at 1275 nm under the same conditions.

In all, non-relevant differences were shown for the prepared NPs, since they exhibited very similar lifetimes under the different conditions performed. Furthermore, the lifetimes observed are consistent with the values reported before for ZnTriMPyP-PLGA-PEG NPs.[25]

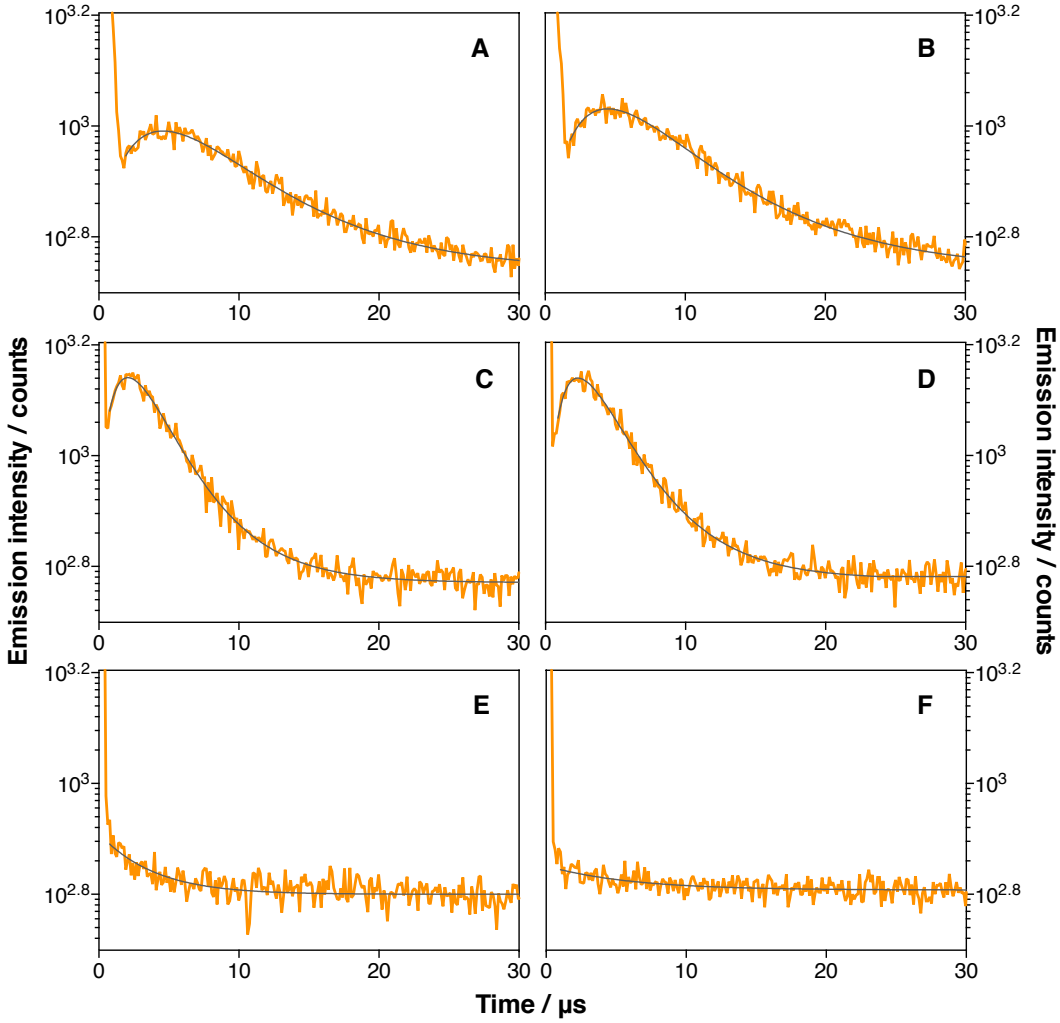

Figure 31. Time-resolved NIR phosphorescence at 1275 nm of aqueous suspensions of ZnTriMPyP-PLGA-PEG NPs in air (A), in O_2 saturated conditions (C) and with the addition of NaN_3 (E); and aqueous suspensions of ZnTriMPyP-PLGA-PLA-PEG-c(RGDfK) NPs in air (B), in O_2 saturated conditions (D) and with the addition of NaN_3 (C). λ_{exc} = 473 nm.

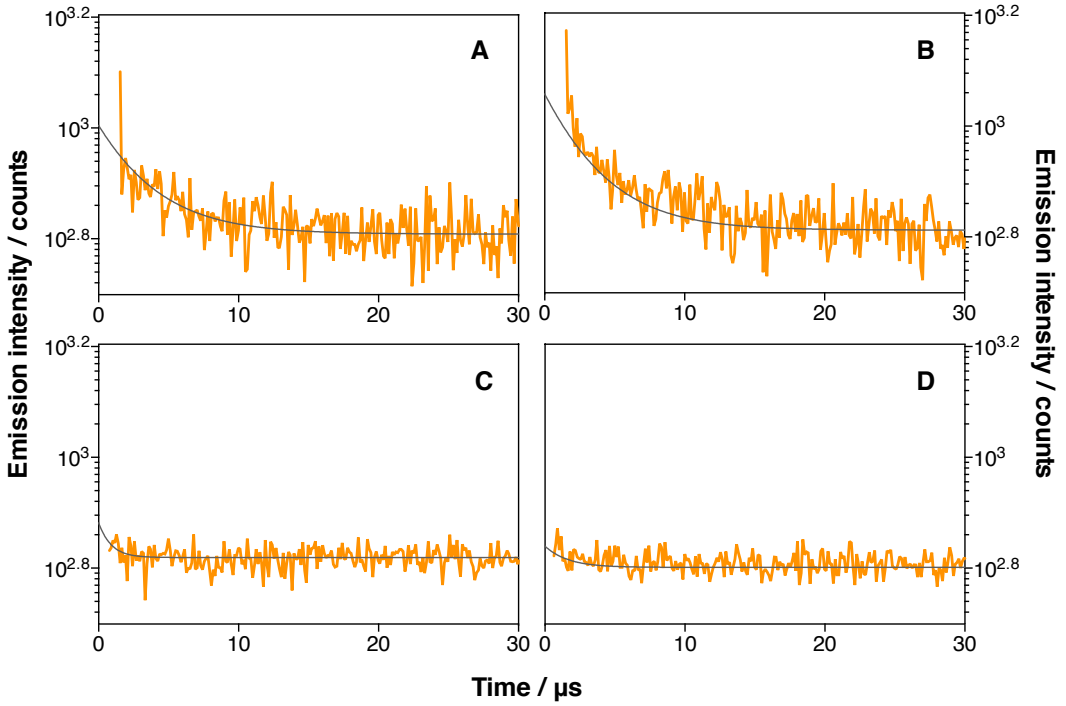

Figure 32. Time-resolved NIR phosphorescence at 1110 nm of aqueous suspensions of ZnTriMPyP-PLGA-PEG NPs in air (A), in O_2 saturated conditions (C) and with the addition of NaN_3 (E); and aqueous suspensions of ZnTriMPyP-PLGA-PLA-PEG-c(RGDfK) NPs in air (B), in O_2 saturated conditions (D) and with the addition of NaN_3 (C). λ_{exc} = 473 nm.

4.2.4 *Biological Study: In Vitro Phototoxicity*

The pentapeptide c(RGDfK) selectively binds to the $\alpha_v\beta_3$ integrin receptor, which is overexpressed in glioblastoma cells.[206] In order to evaluate *in vitro* the phototoxicity of the formulated nanoparticles, cell viability was assessed by the MTT assay[188] in two human cell lines: U-87 MG malignant glioblastoma and HeLa epithelioid cervix carcinoma. U-87 MG cells express a large number of $\alpha_v\beta_3$ integrin receptor[207,208], while other tumor cell lines, such as HeLa cells, express very few or no $\alpha_v\beta_3$ integrin receptors[209,210]. It was reported that the percentage of U-87 MG cells expressing $\alpha_v\beta_3$ integrin receptors is 99.98%, while for HeLa cells it is just 4.29%.[211]

The phototoxicity of the developed NPs was evaluated in both cell lines. The NPs were diluted in supplemented medium to achieve a range of ZnTriMPyP concentrations (0, 50, 100, 200, 300, 400 and 500 nM) and incubated in the cells for 2 h. Then, cells were irradiated with different light doses: 0 $J \cdot cm^{-2}$ (dark control), 10 $J \cdot cm^{-2}$ and 15 $J \cdot cm^{-2}$. The selection of 2 h of incubation time for this phototoxicity study was informed by uptake studies performed in the

above-mentioned previous work[200], in which the closely-related PLA-PEG-c(RGDfK) NPs exhibited maximum uptake after 2 h of the incubation of the NPs (Figure A4 in Appendix A).

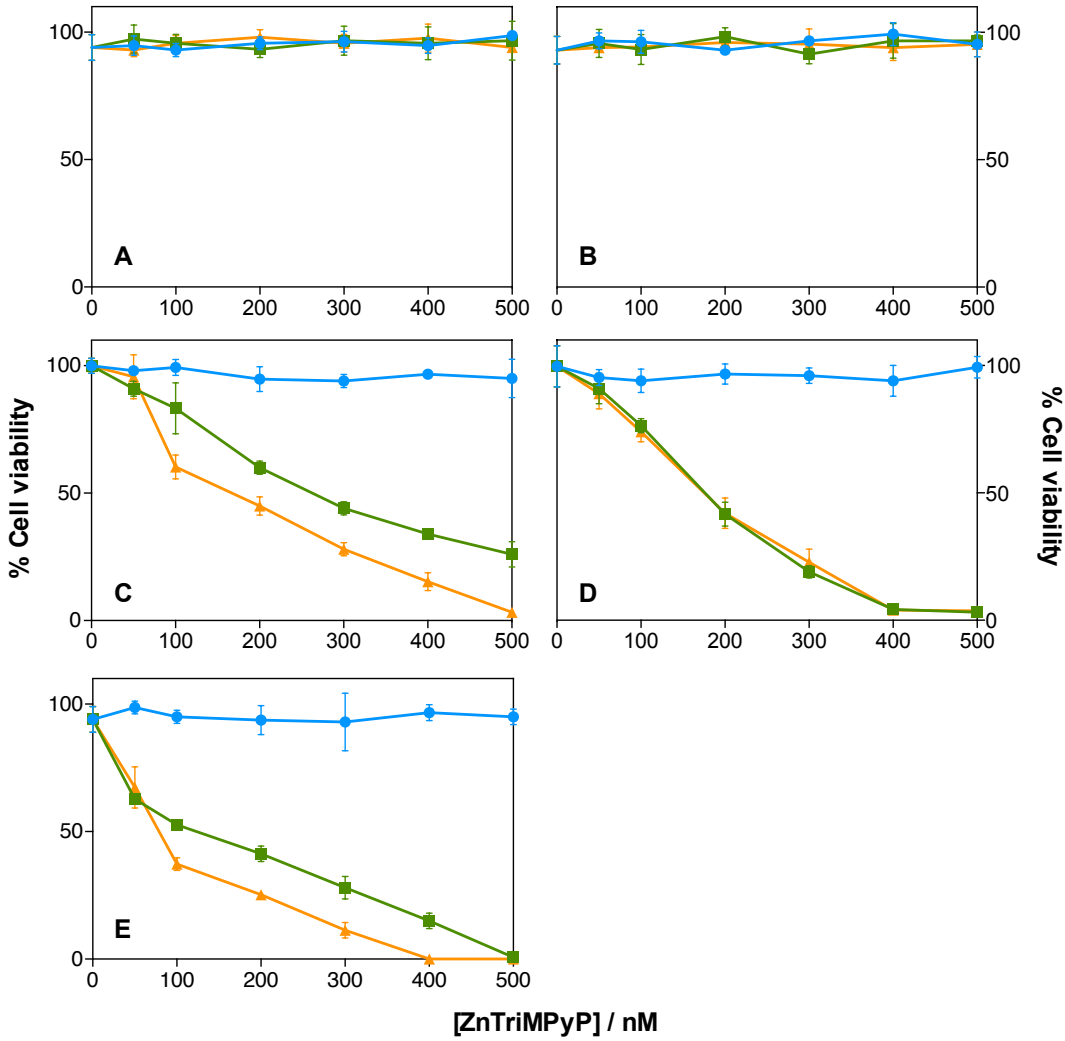

Figure 33. U-87 MG (A, C, E) and HeLa (B, D) cell viability (expressed as percentages) after incubation with: PLGA-PEG (Blank NPs) (blue circle), ZnTriMPyP-PLGA-PEG (green square) or ZnTriMPyP-PLGA-PLA-PEG-c(RGDfK) (orange triangle) NPs at various ZnTriMPyP concentrations (0, 50, 100, 200, 300, 400 and 500 nM) and at different light doses: 0 $J \cdot cm^{-2}$ i.e. dark (a, b), 10 $J \cdot cm^{-2}$ (c, d) or 15 $J \cdot cm^{-2}$ (e). Cells incubated with complete growth medium were used as 100% viability controls to calculate the cell viability of the cells treated at the different conditions. Values reported are the mean ± SD of at least three independent experiments.

As shown in Figure 33, cell viability was depended upon the light fluence and the concentration of the photosensitizer. With increasing concentrations of NPs, cell viability significantly decreased except in the case of PLGA-PEG (Blank) NPs, confirming that the cytotoxic effect of the formulation was mainly due to ZnTriMPyP and not to the nanocarrier itself. This phototoxicity study evidenced that the novel nanocarrier ZnTriMPyP-PLGA-PLA-

PEG-c(RGDfK) is effective at nanomolar concentrations of PS and devoid of dark toxicity. This is a major improvement compared to our previous nanosystems in which the related PS zinc(II) tetraphenyl porphyrin (ZnTPP) was occluded in PLGA-PEG NPs, which required longer incubation periods (24 h vs 2 h) and 10-fold higher PS concentrations to reach similar endpoints, albeit at lower light fluences. In addition, since the photosensitizer was occluded, its unwanted loss from the NPs occurred and as a consequence, the nanosystem showed dark cytotoxicity.[194] In the same way, if compared to the closely related previous nanosystem PLA-PEG-c(RGDfK) NPs with an occluded PS, pyropheophorbide *a* (PPa), similar improvements are evident since it required a 10-fold higher concentration to achieve a comparable phototoxicity to the novel ZnTriMPyP and c(RGDfK)-modified nanocarrier (Figure A5 in Appendix A). This suggests that the covalent binding of a hydrophilic photosensitizer to PEG-coated PLGA NPs exerts a positive influence on the overall phototoxicity.

Furthermore, the biological studies in U-87 MG cells demonstrated that c(RGDfK)-NPs exhibit higher phototoxicity than non-c(RGDfK)-NPs. The phototoxic effect of the targeted NPs was increased by 30-50% depending on the concentration when compared with the non-targeted NPs under the same conditions. Several PDT studies report the use of RGD-containing peptides for targeting nanoparticles, but only a few provide a comparison with non-targeted systems. In such cases, the results are consistent with our findings. For instance, Tang *et al*.[212] reported a novel near-infrared light activated NaScF4 up-conversion NPs with the PS chlorin e6 loaded and the peptide cRGDyK linked. *In vitro* studies in U-87 MG cells showed an increase in cell mortality by 70% on average. Yan *et al.*[213] reported that RGD-modified indocyanine-green liposomes achieved 2-70% higher mortality in 4T1 cells than non-targeted NPs. Wu *et al*.[214] showed that RGD-conjugation to gold nanoparticles delivering the protoporhyrin precursor ALA enhanced their phototoxic effect by 25-165% depending on the concentration. Finally, Zhang *et al.*[215] reported that RGD-conjugated PEG NPs containing chlorin e6 and Doxorubicin decreased the MDA-MB-231 cell viability by 20-40% compared to the non-targeted NPs. Therefore, non-targeted NPs, which are internalized into cells *via* endocytosis or phagocytosis non-specifically, are presumably accumulated to a lesser extent as compared to the targeted system.

Otherwise, the studies performed in HeLa cells showed no significant differences in cell viability between the targeted and non-targeted nanocarriers. Danhier *et al.*[193] reported before that the presence of the RGD peptide on PLGA-PEG nanoparticles does not influence the cell viability of HeLa cells. This fact is consistent with the remarkably low $\alpha_v\beta_3$ integrin expression in HeLa, suggesting the participation of receptor-mediated endocytosis in the uptake of c(RGDfK)-NPs in U-87 MG cells, resulting in an increased cytotoxicity, whereas non-targeted NPs may be internalized by normal passive uptake mechanisms only. However,

this strategy does not prevent non-specific damage in cells lacking this integrin, which limits the selectivity of this targeting approach.[193,216,217]

4.3 Experimental Section

4.3.1 Materials

Poly-(*D,L*-lactide-*co*-glycolide) (PLGA) RESOMER® RG 502 (ester terminated, lactide:glycolide 50:50, Mw 7,000-17,000 Da), Dulbecco's Phosphate Buffered Saline (PBS) and 3-(4,5-dimethylthiazol-2-yl)-2,5-diphenyltetrazolium bromide (MTT) were purchased from MilliporeSigma (St. Louis, MO, USA). Methoxy poly(ethyleneglycol)-*b*-poly(*D,L*-lactide-*co*-glycolide) copolymer (PLGA-mPEG) AK 102 (lactide:glycolide 50:50, Mw 30,000 and 5,000 Da for PLGA and PEG respectively) was purchased from PolySciTech®, Akina Inc. (West Lafayette, IN, USA). Dulbecco's Modified Eagle's Medium (DMEM) (with 4.5 g/L *D*-glucose and without sodium pyruvate or *L*-Glutamine), *L*-Glutamine solution (200 mM), Pencillin-Streptomycin solution, Trypsin EDTA solution (solution C (0.05%), EDTA (0.02%) and with phenol red) and certified Fetal Bovine Serum (FBS) were purchased from Biological Industries (Kibbutz Beit Haemek, Israel). Minimum Essential Medium (MEM) (with *L*-Glutamine) was purchased from Thermo Fisher Scientific (Waltham, MA, USA). All other chemicals were commercially available reagents of at least analytical grade. Milli-Q water (Millipore Bedford system, resistivity of 18 MΩ cm) was used.

4.3.2 Nanoparticles Preparation

In acetone (1 mL) was dissolved a mixture of different polymers, as indicated for each NP formulation in Table 6. This solution was injected dropwise to Milli-Q water (2 mL) under vigorous stirring. Then, acetone was removed under reduced pressure. The suspension was centrifuged at 2,500 rpm for 15 min at 10 ºC. The pellet was discarded and the supernatant was stored at 4 ºC until use.

Table 6. Amounts of the different polymeric formulations that constituted the desired nanoparticles.

Formulation	Blank NPs	ZnTriMPyP-PLGA-PEG NPs	ZnTriMPyP-PLGA-PLA-PEG-c(RGDfK) NPs
PLGA-ZnTriMPyP / mg	0	0.9	0.9
PLA-PEG-c(RGDfK) / mg	0	0	0.9
PLGA-mPEG / mg	6.3	6.3	6.3
PLGA ester terminated / mg	2.7	1.8	0.9

4.3.3 Determination of the Drug Concentration in the Nanoparticles

An aliquot of the different nanoparticle suspension was dissolved in a known volume of DMSO to disrupt the nanoparticle and dissolve both the photosensitizer and the polymers. Absorbance values were interpolated in a ZnTriMPyP calibration curve obtained under the same conditions. Drug loading and entrapment efficiency were calculated as indicated in Equations 7 and 8 in Chapter 3: *General Techniques and Methods*.

4.3.4 Cell Lines and Culture Conditions

In vitro studies were performed using Human HeLa adenocarcinoma cells (EUCELLBANK 0037-HBCK) and U-87 MG glioblastoma (ECACC-89081402). Both are adherent and grow in monolayer up to confluence after seeding. HeLa cells were cultured with Dulbecco's Modified Eagle's Medium (DMEM) (High Glucose) supplemented with 10% (v/v) FBS, 1% (v/v) *L*-Glutamine, 1% (v/v) Streptomycin and 1% (v/v) Penicillin. HeLa cells were seeded in T-25 flasks and allowed to grow up to 80% confluence before subculturing. U-87 MG cells were cultured with Minimum Essential Media (MEM) with *L*-Glutamine supplemented with 10% (v/v) FBS, 1% (v/v) Streptomycin and 1% (v/v) Penicillin, seeded in T-75 flasks and allowed to grow up to 80% confluence before subculturing. Both cell lines were maintained at 37 ºC in an incubator containing 5% CO_2.

4.3.5 In vitro Dark and Phototoxicity Assays

Quantities of 9,000 cells for HeLa and 17,000 cells for U-87 MG were seeded in 96-well plates and incubated at 37 ºC (5% CO_2) for 24 h to achieve 80% confluence. Then, the culture medium was removed and the suspended NPs in complete culture medium were added. ZnTriMPyP-NPs were employed at ranges of ZnTriMPyP between 0 and 500 nM. Also, blank NPs at equivalent concentrations of the loaded ones were used as controls. Cells without any treatment were taken as controls as well. Cells were incubated in darkness at 37 ºC for 2 h. Afterwards, the suspensions were removed, the wells were washed 3 times with PBS and then supplemented medium was added. Light-treated plates were irradiated with 10 and 15 $J \cdot cm^{-2}$. Dark controls were in darkness during irradiation time. For phototoxicity studies, the blue light from a LED Par 64 Short V2 lamp (λ_{em} = 463 ± 11 nm; irradiance = 12 $mW \cdot cm^{-2}$) was used. After irradiation, all the plates were incubated at 37 ºC for 24 h. Next, the medium was removed and the cell viability was determined by 3-(4,5-dimethylthiazol-2-yl)-2,5-diphenyltetrazolium bromide (MTT) assay. Concisely, remaining cells were incubated with 0.05 mg/mL MTT (HeLa) or 0.1 mg/mL (U-87 MG) in complete medium for 3 h. Then, medium was discarded and the purple crystals were solubilized with DMSO. Formazan concentration

was determined by absorption at λ = 562 nm. Absorbance was recorded in a Synergy H1 Hybrid microplate reader (BioTek Instruments, Inc., Winooski, VT, USA). Cell viability was calculated as the ratio between the absorbance of treated cells and that of non-treated cells.

4.4 Conclusions

The most relevant conclusions drawn from this chapter are the following:

I. The presence of c(RGDfK) peptide in the nanoparticle formulation does not alter its photoactivity in comparison with the corresponding nanosystem without the peptide.

II. In comparison with related nanosystems with the photosensitizer occluded instead of covalently attached, both ZnTriMPyP-bound nanocarriers show a substantial improvement in phototoxicity and dark cytotoxicity. Covalent binding of a hydrophilic photosensitizer to PEG-coated PLGA nanoparticles provides greater efficiency and safety to the nanosystem thanks to the higher local concentration of the photosensitizer achieved by keeping it attached to the nanocarrier, that also precludes the unwanted drug loss.

III. The novel ZnTriMPyP-PLGA-PLA-PEG-c(RGDfK) nanosystem is effective at submicromolar concentrations, is devoid of dark toxicity and enhances the photodynamic activity against tumor cells expressing the $\alpha_v\beta_3$ integrin receptor in comparison with the non-targeted nanocarrier. The presence of c(RGDfK) peptide in the nanoparticle formulation provides an additional 30-50% activity enhancement *in vitro*.

IV. However, functionalization of the PLGA nanoparticle with c(RGDfK) peptide does not prevent damage to cells lacking this integrin, which limits the selectivity of this targeting approach.

CHAPTER 5: MESOPOROUS SILICA NANOPARTICLES AS ON-DEMAND PHOTO-CHEMO-VEHICLES FOR CETUXIMAB-TARGETED PHOTODYNAMIC THERAPY

5.1 Introduction

The major drawback of cancer therapies, including PDT, is the lack of selectivity of the treatment, leading to serious side effects for the patients. This limitation lies on the difficulties to precisely control the localization of the drug (chemotherapeutic drug or photosensitizer, for instance) in only the tumor tissue. The combination of PDT with chemotherapy and immunotherapy can improve the effectiveness of the treatment and, more importantly, increase its selectivity and thus, its safety. The best strategy to deliver these three therapies at once is by nano-sized drug delivery systems. Among all the smart nanovehicles, mesoporous silica nanoparticles (MSNPs) are ideal nanocarriers for co-delivering different agents in desired locations due to their various advantageous properties including: i) the capability of co-delivering multiple therapeutic agents at high dosages; ii) the facile surface functionalization; and iii) the desired biological behavior. For these reasons, it seems that MSNPs are expected to be the ideal platform for combined chemo-immuno-phototherapy. Furthermore, to avoid unwanted release of the anti-cancer agents from the nanocarrier and thus improve even more the selectivity, the action of the chemotherapeutic agent can be modulated on-demand by the singlet oxygen generated by PDT. In this way, PDT also has the function of controlling drug release in this combinatorial treatment strategy. This control is achieved by the attachment of the antineoplastic agent to the nanocarrier by means of a singlet oxygen ($^1O_2$) cleavable linker.

Previously, our laboratory reported the spatial and temporally controlled delivery of Doxorubicin (DOX) from gold nanoclusters grafted with $^1O_2$-releseable DOX and the photosensitizer PpIX.[98] The present work wants to improve the mentioned past strategy. In this regard, firstly, the delivery system is changed to mesoporous silica nanoparticles for their above-mentioned advantages in combinatorial treatments. Secondly, the photosensitizer is also switched to a phthalocyanine that has red-shifted light absorption with higher extinction coefficient for optimal tissue penetration. Finally, nanoparticles are decorated with the active-targeting moiety Cetuximab to selectively kill EGFR-positive cells. For comparison purposes, phthalocyanine-grafted mesoporous silica nanoparticles with and without Cetuximab and with and without Doxorubicin are investigated.

The same design and approach are followed along the Chapter 5 to investigate the EGFR-selective photo-killing by $^1O_2$-modulated DOX release from MSNPs. However, this chapter is divided in two subchapters depending on the phthalocyanine employed. In Subchapter 5A, a novel hydrophilic phthalocyanine, ZnPcSMP, synthesized by the laboratory of Anzhela Galstyan (Center for Soft Nanoscience, Westfälische Wihelms-Universität Münster in Münster, Germany) is utilized. Similar phthalocyanines reported being efficient

photosensitizers.[218] On the other hand, in Subchapter 5B, the commercially available IRDye700DX is employed. IRDye700DX is a hydrophilic phthalocyanine that have little photodynamic efficacy due to poor localization and are therefore commonly used to form a conjugate with a targeting moiety.[219–222] In fact, a conjugate IRDye700DX-Cetuximab is clinically approved in Japan and sooner, worldwide. Nevertheless, to our knowledge, the delivery of IRDye700DX and Cetuximab by nanoparticles is still not investigated.

SUBCHAPTER 5A: ZnPcSMP as Photosensitizer

5.2 Results and Discussion

5.2.1 Synthesis

5.2.1.1 Synthesis of Precursors of Mesoporous Silica Nanoparticles

5.2.1.1.1 Conjugation Reaction Between ZnPcSMP and 3-(triethoxysilylpropyl)-isocyanate

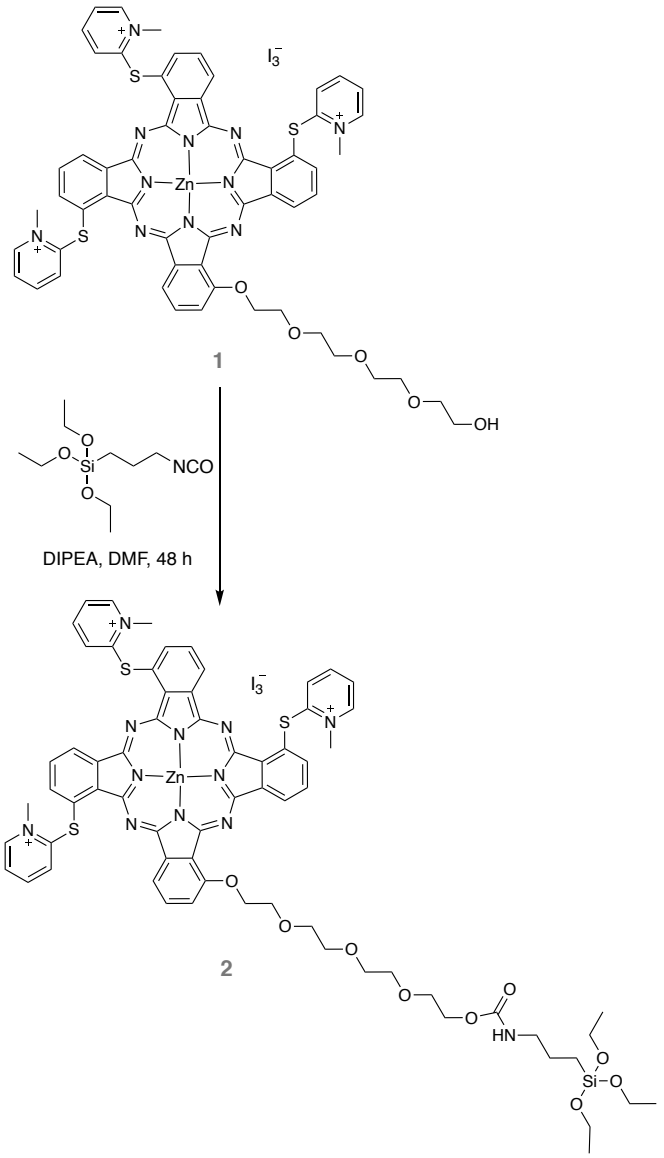

Figure 34. Conjugation reaction of ZnPcSMP with TESPIC by means of the formation of the carbamate.

The compound **1**, hereafter ZnPcSMP, was conjugated to 3-(triethoxysilylpropyl)-isocyanate (hereafter TESPIC) as shown in Figure 34. The reaction of the hydroxyl group of ZnPcSMP with the isocyanate of TESPIC gave the formation of the carbamate (or urethane) of interest. Isocyanates reactivity with alcohols is moderate, being usually catalyzed by molecules that greatly increase the rate of nucleophilic additions to the C=N bond. Tertiary amines, such as *N*,*N*-diisopropylethylamine (DIPEA), are common catalysts for this reaction. The tertiary amine and the isocyanate form an activated complex which facilitates the nucleophilic addition of the alcohol to the C=N double bond.[223]

The dark green conjugate **2** was not further purified since the non-reacted ZnPcSMP will not be covalently attached to the nanoparticle and subsequent washes of the MSNP will remove it.

5.2.1.1.2 Synthesis of the $^1O_2$-Cleavable Linker

The synthetic procedure of the $^1O_2$-sensitive linker (*Z*)-3,3'-(ethene-1,2-diylbis(sulfanediyl) dipropanoic acid (**4**) consisted of two steps (Figure 35): i) the formation of disodium salt of 3-mercaptopropionic acid (**3**; 3-MPA); and ii) the nucleophilic addition of both thiolate groups to the commercial *cis*-1,2-dichloroethylene. Although this procedure was previously described by Wang *et al.*[83], we performed some changes in the procedure. Firstly, when employing NaOMe as base for the deprotonation of 3-MPA, the overall yield was pretty low, only 10%. Changing the base to NaH, whose basify character is so much stronger, the overall yield was triplicate. Secondly, we observed that the addition of *cis*-1,2-dichloroethylene in EtOH led to a by-product instead of the corresponding diacid **4**. Thus, we were prompted to add directly the *cis*-1,2-dichloroethylene to the disodium salt solution.

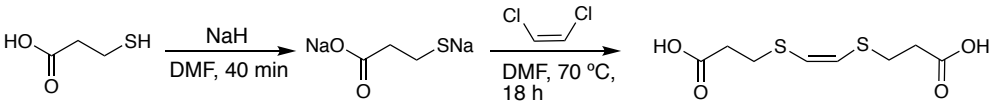

3 4

Figure 35. Synthetic procedure for $^1O_2$-sensitive linker, (*Z*)-3,3'-(ethene-1,2-diylbis(sulfanediyl) dipropanoic acid (**4**).

The physical and spectroscopic data of compound **4** were identical to those reported in the literature (spectra are shown in Figure B1 in Appendix B).[83]

5.2.1.1.3 Orthogonal Conjugation of Doxorubicin to the $^1O_2$-Cleavable Linker

With the required compound **4** in hand, we examined its mono-*N*-acylation with Doxorubicin (DOX, **5**) by a Steglich reaction (Figure 36). In order to selectively obtain the orthogonal product, equimolar amounts of DOX and the cleavable linker **4** were used. In the same way,

the addition dropwise of DOX over diacid **4** was performed in high-dilution conditions.

Compound **6** will be attached to amino-derivatized mesoporous silica nanoparticles. Thus, the orange reaction product obtained was not further purified since the non-reacted DOX and the diamide byproduct cannot react with the amino-MSNP and subsequent washes of the MSNPs will remove them.

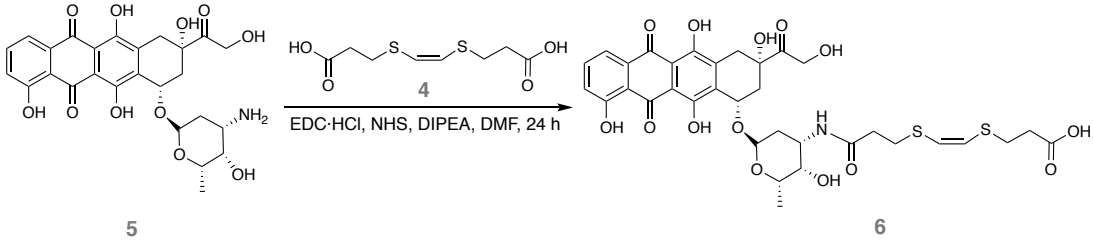

Figure 36. Synthetic procedure for the conjugate between Doxorubicin and the $^1O_2$-cleavable linker.

5.2.1.1.4 Conjugation Reaction Between Doxorubicin and 3-(triethoxysilylpropyl)-isocyanate

DOX was conjugated to TEPSIC as shown in Figure 37, forming the corresponding urea **7**. In isocyanate reactions, the rate of addition strongly depends on the type of nucleophile; typically, the reactivity decreases in the order: primary aliphatic amines > secondary aliphatic amines >> aromatic amines > primary alcohols > water > secondary alcohol >> carboxylic acid > ureas >> urethanes.[224] Here, unlike the previous reaction with a hydroxyl compound, the isocyanate group of the silane reacted more effectively with the amino group of DOX and a catalyst was not required. The orange conjugate **7** was not further purified.

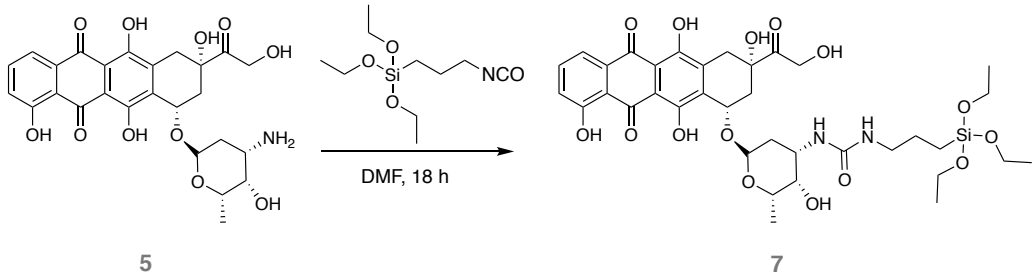

Figure 37. Conjugation reaction of Doxorubicin with TESPIC forming the corresponding urea conjugate.

5.2.1.1.5 Conjugation Reaction Cetuximab and PEG chains

The linkage of Cetuximab (Cet) to the PEG chains (**8**) was achieved *via* NHS *N*-acylation reaction in aqueous media (Figure 38). NHS ester-activated compounds react with primary amines in physiologic to slightly alkaline conditions (pH 7.2 to 9). The optimum pH range for

NHS coupling with proteins is pH 8.0 – 9.0. At this pH range, amino groups of proteins, i.e. the ε-amino groups of lysines, are unprotonated to a high degree and highly reactive towards the NHS-ester compound. Here, the pH of the reaction mixture was 8.0 prior to adding the amine reactant. This was the pH value of choice because of the compromise between amidation and hydrolysis: amidation is better facilitated at higher pH, however, as higher the pH, higher is the risk of hydrolyzing the NHS compound.[224] The conjugate **9** was purified using Amicon ultra 2 mL centrifugal unit.

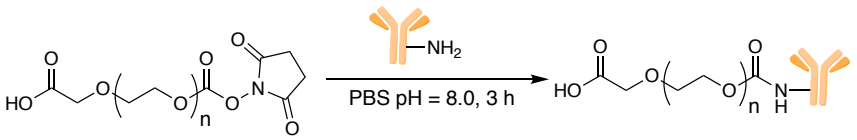

8 9

Figure 38. Conjugation reaction between PEG chain and Cetuximab.

Afterwards, a modification of a two-step protocol[225] for the activation of proteins with EDC/sufo-NHS and subsequent conjugation with amine-containing molecules were performed. The terminal carboxylic acid of PEG of compound **9** was activated with EDC/sulfo-NHS in PBS at pH 6.0 (Figure 39). It is known that carboxylate activation with EDC/NHS occurs most effectively at pH 3.5 to 4.5.[226] However, the maximal rate of hydrolysis of EDC occurs at acidic pH values, stability of the carbodiimides in solution increases at or above pH 6.0.[224] Therefore, in order to maximize the activation of the carboxylate but increasing the stabilization of the active ester intermediate, pH = 6.0 was employed. In addition, at pH 6.0, the amines on the protein will be protonated and thus be less reactive towards the sulfo-NHS esters.

Moreover, the active specie **10** can be isolated in a reasonable time frame without significant loss in conjugation potential. The hydrolysis rate of the sulfo-NHS esters is dramatically slower at slightly acid pH. Thanks to this fact, the conjugate **10** was purified using Amicon ultra 2 mL centrifugal unit. Nevertheless, the coupling-reaction with the amine-MSNPs was performed the same day in order to avoid the hydrolysis problem.

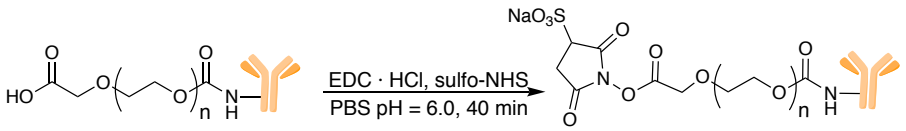

9 10

Figure 39. Reaction between the *N*-substituted carbodiimides (EDC) and sulfo-NHS with the carboxylic acid of compound **9** to form the NHS- derivative **10**.

5.2.1.2 Synthesis and Derivatization of Silica Mesoporous Nanoparticles

Six types of MSNPs were prepared. Table 7 summarizes the grafting elements of each synthesized MSNP formulation. In the present section, the synthesis and derivatization of each one is discussed in detail.

Table 7. Composition of each synthesized MSNP.

NP Formulation	ZnPcSMP	DOX	PEG	Cet
MSNP**A**	✓	✗	✓	✗
MSNP**A**-Cet	✓	✗	✓	✓
MSNP**B**	✓	✓, by means of a $^1O_2$-cleavable linker	✓	✗
MSNP**B**-Cet	✓	✓, by means of a $^1O_2$-cleavable linker	✓	✓
MSNP**C**	✓	✓, by means of a non-cleavable linker	✓	✗
MSNP**C**-Cet	✓	✓, by means of a non-cleavable linker	✓	✓

5.2.1.2.1 MSNPA-Cet: ZnPcSMP – Cetuximab – MSNP

The preparation of mesoporous silica nanoparticles with the photosensitizer ZnPcSMP and the antibody Cetuximab both covalently attached (MSNP**A**-Cet) was carried out in three synthetic steps (Figure 1):

i. Preparation of mesoporous silica nanoparticles with ZnPcSMP covalently attached (MSNP2). Blank MSNP was derivatized with the synthesized conjugate **2**. After the reaction took place, MSNPs were washed with DMF. This reaction was performed in DMF to allow the quantification of the ZnPcSMP in the supernatant of the washes. At first, we tested the strategy of modifying the surface of blank MSNP with isocyanate groups to allow the direct reaction with ZnPcSMP, however, the conjugation yield was lower than preparing the conjugate before.

ii. Modification of the surface of MSNPs with amino groups (MSNP3). High amount of APTES was employed in the reaction to ensure a high degree of surface's derivatization. Afterwards, MSNPs were washed with ethanol.

iii. Anchoring of the conjugate PEG-Cetuximab (compound **10**) *via* *N*-acylation to the nanoparticle (MSNP**A**-Cet). The intermediate NHS-ester **10** reacted with an amino

group on surface of MSNP joining the PEG-Cetuximab to the MSNP. Contrary to the previous steps, the final product of this reaction was not washed since the resuspension of the pellet required harsh sonication and this is not recommended when working with antibodies. Since this MSNP suspension will be employed to treat cells, PBS at physiological pH was chosen as the solvent for this reaction.

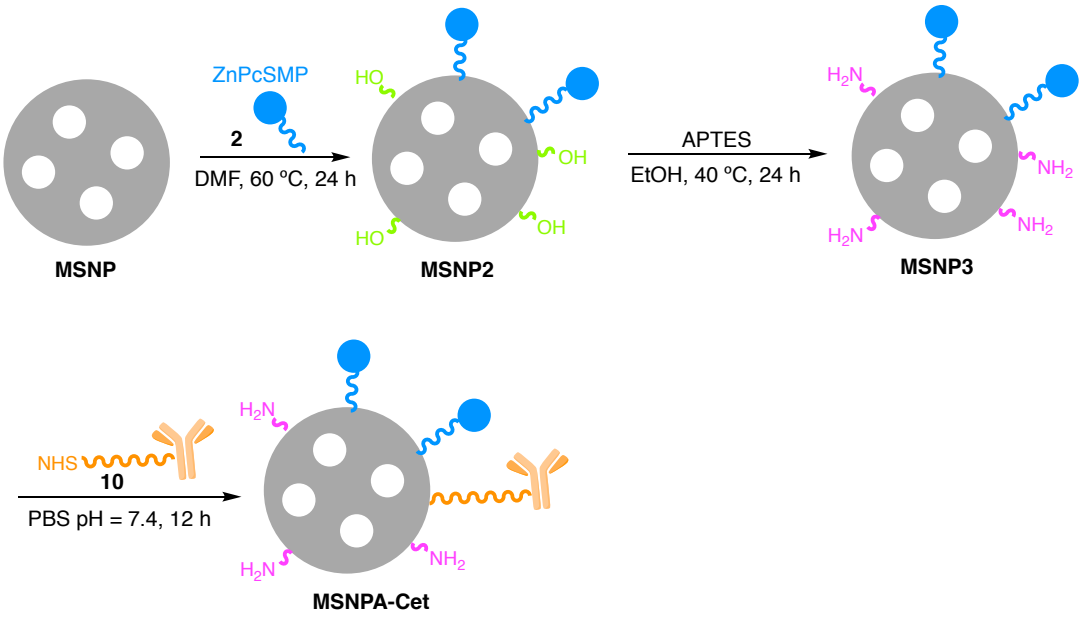

Figure 40. Preparation of the nanoparticle MSNP**A**-Cet.

Different strategies were followed to attach Cetuximab to the nanoparticles. First of all, we attempted to attach the PEG chains to the nanoparticle and further link the carboxylic acid groups of PEGs to the amino groups of the antibody. However, this strategy did not work due to the competition with the amino groups from the surface of MSNPs. Then, a second attempt was carried out blocking the amino groups with butyl isocyanate. Nevertheless, this molecule also reacted with carboxylic acid groups from PEGs and the further linkage with Cetuximab was not satisfactorily achieved. Because of these failed attempts, we designed the above-explained strategy where Cetuximab was previously linked to the PEG chains and the resulting conjugate was attached to the MSNP. This third approach yielded the effective conjugation of the antibody to the nanoparticles.

The overall preparation scheme of the non-targeted analogous, MSNP**A**, is shown in Figure B2 in Appendix B. The synthetic route is the same as for MSNP**A**-Cet except the last step, in which NHS-PEG-COOH is attached to the nanoparticles without its prior conjugation with Cetuximab.

Furthermore, analogs of MSNP**A** and MSNP**A**-Cet labeled with FITC were also carried out.

The overall preparation schemes are shown in Figure B5 and Figure B6 in Appendix B. Briefly, the procedure is the same as for MSNP**A** and MSNP**A**-Cet except for the reaction of MSNP3 with FITC before the PEGylation step.

5.2.1.2.2 MSNPB: ZnPcSMP – Cetuximab – DOX (releasable by $^1O_2$) – MSNP

The preparation of mesoporous silica nanoparticles with the photosensitizer ZnPcSMP and the antibody Cetuximab both covalently attached; and the chemotherapeutic agent DOX bond by means of the $^1O_2$-cleavable linker (MSNP**B**-Cet) was carried out in four steps (Figure 41):

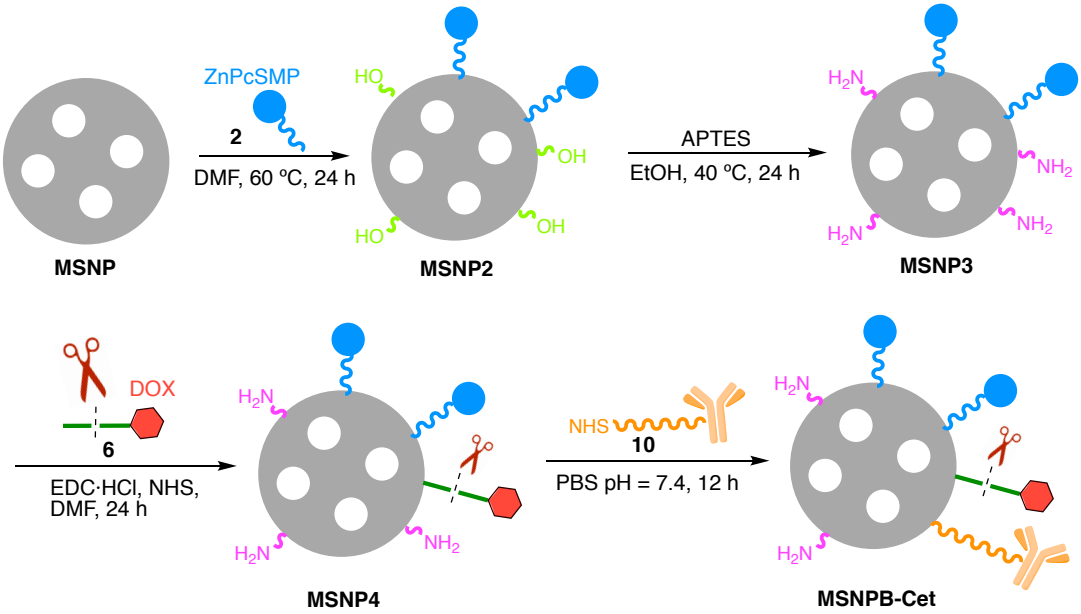

Figure 41. Preparation of the nanoparticle MSNP**B**-Cet.

i. Preparation of mesoporous silica nanoparticles with ZnPcSMP covalently attached (MSNP2).

ii. Modification of the surface of MSNPs with amino groups (MSNP3).

iii. Derivatization of the nanoparticle with the conjugate **6** (formed by DOX and the $^1O_2$-cleavable linker) *via N*-acylation with EDC/NHS chemistry (MSNP4). The activated NHS-ester of the conjugate **6** reacted with an amino group on surface of MSNP. After the reaction took place, MSNPs were washed with DMF to discard the unreacted compound **6**.

iv. Anchoring of PEG-Cetuximab to MSNP4 nanoparticles (MSNP**B-Cet**).

The overall preparation scheme of the non-targeted analogous, MSNP**B**, is shown in Figure

B3 in Appendix B.

5.2.1.2.3 MSNPC: ZnPcSMP – Cetuximab – DOX (not releasable) – MSNP

The preparation of mesoporous silica nanoparticles with the photosensitizer ZnPcSMP, the antibody Cetuximab and the chemotherapeutic agent DOX, all of them covalently attached and non-cleavable, (MSNP**C**-Cet) was carried out in four steps (Figure 42):

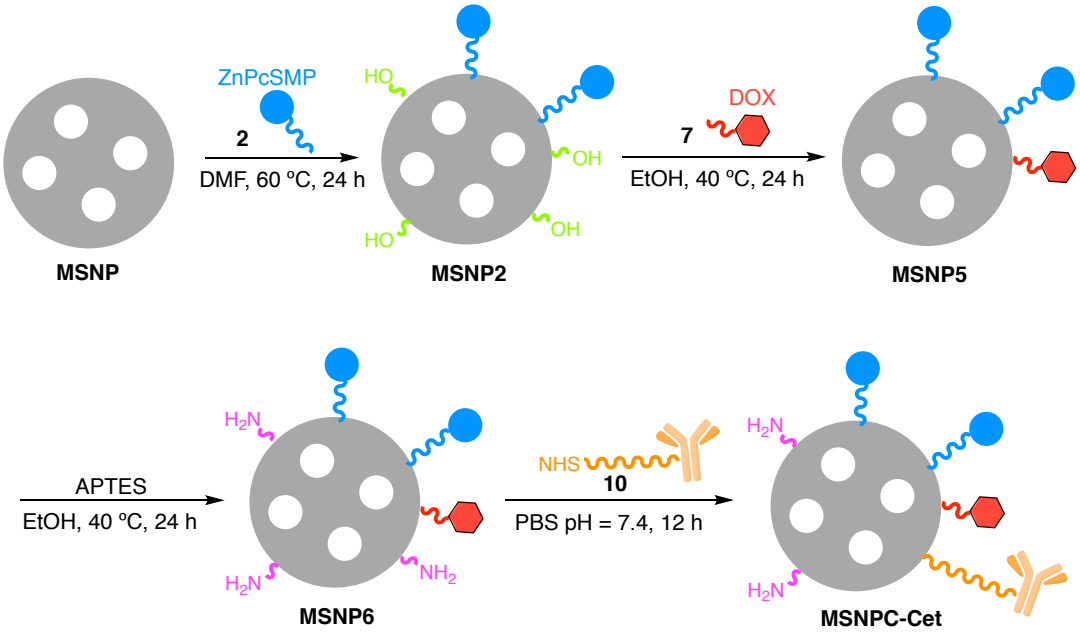

Figure 42. Preparation of the nanoparticle MSNP**C**-Cet.

i. Preparation of mesoporous silica nanoparticles with ZnPcSMP covalently attached (MSNP2).

ii. Preparation of non-cleavable and covalently attached DOX-modified nanoparticles (MSNP5). MSNP2 was derivatized with the synthesized conjugate **7**. After the reaction took place, MSNPs were washed with EtOH. Additionally, we tested a different approach: the modification of the surface of blank MSNPs with isocyanate groups to allow the direct reaction with Doxorubicin. However, the conjugation yield of this second strategy was lower than firstly preparing the conjugate followed by its reaction with the MSNP.

iii. Modification of the surface of MSNPs with amino groups (MSNP6).

iv. Anchoring of PEG-Cetuximab to MSNP6 nanoparticles (MSNP**C**-Cet).

The overall preparation scheme of the non-targeted analogous, MSNP**C**, is shown in Figure

B4 in Appendix B.

5.2.2 Physicochemical Characterization of Nanoparticles

The prepared mesoporous silica nanoparticles were characterized in terms of their physicochemical properties: size, polydispersity index (PdI), zeta-potential and concentrations of the photosensitizer ZnPcSMP and the chemotherapeutic agent DOX (Table 8).

Size, polydispersity and zeta-potential were measured by dynamic light scattering (DLS). After each preparation step for the three nanoparticle formulations (MSNP**A**-Cet, **B**-Cet and **C**-Cet), an increase in their size and changes in zeta-potential were shown. These differences were a good indication that the reactions in the nanoparticles had been successfully accomplished.

The average size of MSNP**A**-Cet, MSNP**B**-Cet and MSNP**C**-Cet in aqueous suspension was found to be ~398 nm, ~412 nm and ~422 nm respectively. These values are pretty higher compared to their analogs without antibody (~228 nm, ~243 nm and ~241 nm for MSNP**A**, MSNP**B** and MSNP**C** respectively). This increment in size can be explained by two different reasons. First, the attachment of a bulky element, as it is the antibody, obviously increased the MSNPs size. Second, the targeted and non-targeted MSNPs were measured in different solvents. The Cetuximab-MSNPs were measured in water since the antibody disrupts in organic media; mesoporous silica nanoparticles tend to aggregate in aqueous suspension. Contrarily, the non-Cetuximab-MSNPs were measured in ethanol, solvent in which nanoparticles are non-aggregated and thus smaller.

The polydispersity index of the prepared formulations was smaller than 0.4 in all the non-Cetuximab-MSNPs, demonstrating a homogeneous distribution. However, for the Cetuximab-MSNPs, this value was higher, surely due to the two reasons mentioned above.

The zeta-potential of the nanoparticles was changing depending on the moiety introduced. The preparation of MSNP2 showed an increase in the zeta-potential compared to blank MSNP, consistent with the presence of the cationic charges from the ZnPcSMP. In the same way, the introduction of amino groups on the surface of MSNPs (MSNP3 and MSNP6) yielded to a large increase in the surface charge of the MSNPs.

On the other hand, the ZnPcSMP and DOX concentrations in the MSNPs suspensions were calculated as the difference between the incorporated amount and the amount present in the washing supernatants. The concentrations of the photosensitizer ZnPcSMP and the chemotherapeutic agent DOX in the formulations were calculated for 1 mg MSNP / 1 mL of

suspension. The entrapment efficiency for compound **2** was 70%, for compound **6** was 48%, and for the compound **7**, 41%.

Table 8. Characterization of nanoparticles. PdI: polydispersity index. EE: entrapment efficiency.

	NP formulation	Size / nm	PdI	Zeta-potential / mV	[ZnPcSMP] / μM	[Dox] /μM	EE
	Blank	119 ± 3	0.13 ± 0.05	-25	-	-	
With ZnPcSMP and without DOX	MSNP2	150 ± 7	0.23 ± 0.07	-17 ± 2	11.9	-	70%
	MSNP3	179 ± 4	0.22 ± 0.10	6 ± 2	"	-	-
	MSNP**A**	228 ± 5	0.18 ± 0.05	8 ± 1	"	-	-
	MSNP**A**-Cet	398 ± 43	0.85 ± 0.13	-	"	-	-
With ZnPcSMP and with releasable DOX	MSNP4	194 ± 3	0.27 ± 0.06	9 ± 2	"	21.6	48%
	MSNP**B**	243 ± 8	0.34 ± 0.05	6 ± 2	"	"	-
	MSNP**B**-Cet	412 ± 31	0.91 ± 0.23	-	"	"	-
With ZnPcSMP and with non-releasable DOX	MSNP5	162 ± 3	0.20 ± 0.05	-10 ± 2	"	18.6	41%
	MSNP6	192 ± 5	0.23 ± 0.11	11 ± 2	"	"	-
	MSNP**C**	241 ± 5	0.34 ± 0.08	7 ± 2	"	"	-
	MSNP**C**-Cet	422 ± 26	0.89 ± 0.10	-	"	"	-

5.2.3 Photophysical Characterization of Nanoparticles

The photophysical behavior of free ZnPcSMP and the synthesized nanoparticles were studied by UV-Vis, steady-state and time-resolved fluorescence spectroscopy, as well as time-resolved phosphorescence at 1275 nm to study the production of singlet oxygen.

5.2.3.1 Absorption and Steady-State Fluorescence

5.2.3.1.1 Free ZnPcSMP

UV-Vis spectra of ZnPcSMP were recorded in DMF and purified water. Monomeric form of ZnPcSMP in DMF was evidenced by single well-defined Q-bands peaking at 695 nm (Figure 43A). Nevertheless, the absorption spectrum of ZnPcSMP in aqueous media differed remarkably in comparison. Spectra in milliQ water at similar concentrations showed a broadening and decrease of the molar absorption coefficients in the Q-band, as well as the

rising of a new band at 646 nm. All these mentioned differences are indicative of H-type aggregation, common phenomena of substituted phthalocyanines in aqueous media.[227] The formation of aggregates in water can be rationalized by the determinant role of the solvophobic forces, which have a stronger contribution than the ionic repulsion between the *N*-methylpyridinium moieties. Absorption spectra were registered in a range of concentrations (between 8.9 x 10^{-7} and 5.0 x 10^{-6} M). For the verification of the Lambert-Beer law, an analysis of linear regression between the intensity of the Q-band and the concentration was performed with R^2 values of ~0.999 in DMF and in water (Figure B7 in Appendix B).

Table 9. Photophysical properties of ZnPcSMP in DMF and in water. [a] Matched absorbances at λ_{exc} = 610 nm. [b] ZnPc in DMF as a reference (Φ_F = 0.28).

Solvent	λ_{abs} / nm ($\log_{10}\varepsilon$)	λ_{em} / nm [a]	Φ_F [b]
DMF	695 (5.20); 327 (4.85)	702	0.04
H_2O	646 (4.84); 327 (4.82)	704	0.001

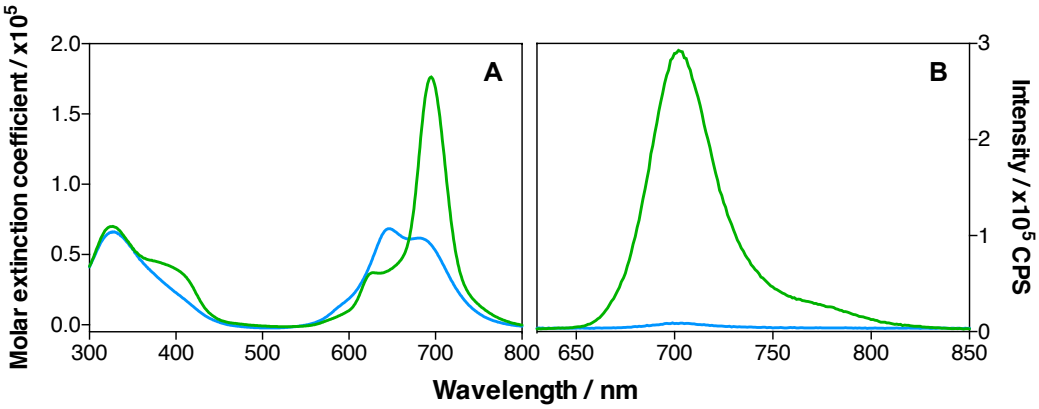

Figure 43. Absorption spectra expressed as molar extinction coefficient (A) and emission spectra (B) of ZnPcSMP in DMF (green line) or in purified water (blue line). λ_{exc} = 610 nm.

On the other hand, emission spectra of ZnPcSMP were acquired in DMF and purified water (Figure 43B). Fluorescence quantum yields of ZnPcSMP were determined by comparative method (Table 9) (Figure B8 in Appendix B). The emission of ZnPcSMP was also affected by the aggregation phenomena. The fluorescence of ZnPcSMP in water was considerably quenched in comparison with that in the organic media. Nevertheless, the Φ_F value of ZnPcSMP in DMF (0.04), although was greater than in water, was pretty low compared with other phthalocyanines such as ZnPc (Φ_F = 0.28 in DMF[228]).

5.2.3.1.2 The Prepared Mesoporous Silica Nanoparticles

The UV-Vis absorbance and emission spectra of MSNP3, MSNP4 and MSNP6 nanoparticles

dispersed in DMF were recorded (Figure 44). These nanoparticles are the precursors of MSNP**A**-Cet, MSNP**B**-Cet and MSNP**C**-Cet. In the absorbance spectra, the near-infrared region band corresponding to ZnPcSMP was shown for all the prepared MSNP formulations, as well as its emission after excitation at 610 nm. These results demonstrated the effectively conjugation of the photosensitizer ZnPcSMP to the MSNPs. However, the absorption spectra of ZnPcSMP in the MSNPs showed different shape and intensity for the Q-bands in comparison with free ZnPcSMP in DMF. The presence of a second peak (~649 nm) in the NIR infrared region and the decrease in absorption indicated the presence of ZnPcSMP aggregates in the nanoparticles.

Likewise, the absorption spectrum of MSNP4 showed three peaks at 500 – 600 nm, which evidenced the presence of DOX in its basic form in the MSNPs. In addition, DOX emission was shown for MSNP4 and MSNP6 after excitation at 475 nm, confirming the conjugation of DOX in both formulations. MSNP4 showed higher DOX emission intensity than MSNP6, when the same concentration of nanoparticles was measured, which is coherent with the higher concentration of DOX in MSNP4 formulation.

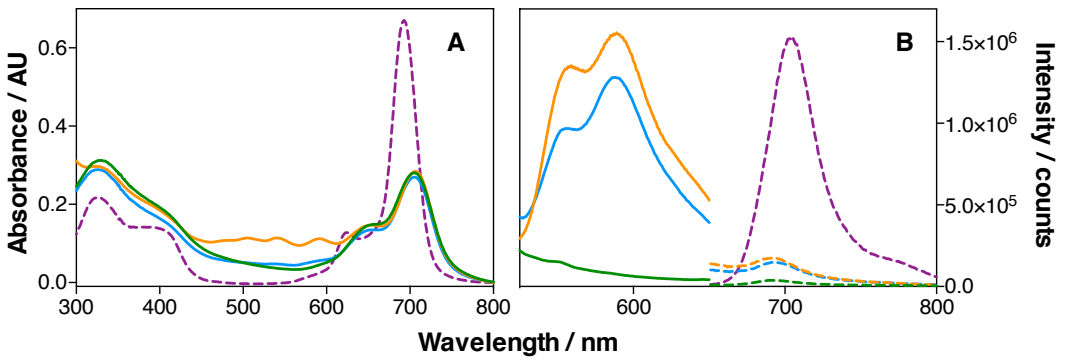

Figure 44. Absorption (A) and emission spectra (B) in DMF of MSNP3 (green line), MSNP4 (orange line) and MSNP6 (blue line). Continuous and dotted lines in B are emission spectra for λ_{exc} = 475 nm and λ_{exc} = 610 nm respectively. Free ZnPcSMP in DMF is showed (in dotted purple lines) for comparison.

Moreover, the absorption and emission spectra of MSNP**A**-Cet, MSNP**B**-Cet and MSNP**C**-Cet nanoparticles in PBS were acquired (Figure 45). The characteristic absorption and emission of ZnPcSMP and DOX were shown in the targeted-nanoparticles. Therefore, the conjugation of the compound **10** (PEG chain attached to Cetuximab) did not alter the presence of the photosensitizer and the chemotherapeutic agent in the MSNPs. Nevertheless, a broadening and decrease of the absorbance in the Q-bands of ZnPcSMP were shown for all the MSNP formulations, as well as the rising of the band at 646 nm, indicating that ZnPcSMP was forming aggregates. Therefore, the covalent conjugation of PEG-Cet (**10**) to MSNPs did not prevent their aggregation in aqueous media.

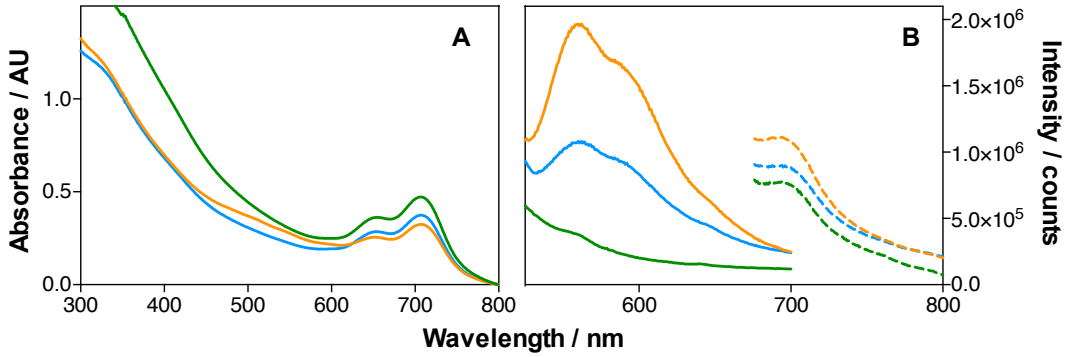

Figure 45. Absorption (A) and emission spectra (B) in water of MSNP**A**-Cet (green line), MSNP**B**-Cet (orange line) and MSNP**C**-Cet (blue line). Continuous and dotted lines in B are emission spectra for λ_{exc} = 475 nm (slits = 6) and λ_{exc} = 610 nm (slits = 11) respectively.

5.2.3.2 Time-Resolved Fluorescence

Time-resolved fluorescence spectra of free ZnPcSMP, MSNP3, MSNP4 and MSNP6 were recorded in DMF (Figure 46 and Table 10). To investigate the time-resolved fluorescence of the photosensitizer, their emission at 698 nm was monitored after excitation at 654 nm. Free ZnPcSMP showed a monoexponential decay with a lifetime of 2.12 ns, corresponding to excited singlet state lifetime of ZnPcSMP (τ_s). MSNP3, MSNP4 and MSNP6 showed biexponential decays. This fact implies that two molecular species were present in the solution. In MSNP3 nanoparticles, the main population (75%) of excited singlet state molecules decayed in 0.50 ns and the smaller contribution (25%) in 2.09 ns. 67% of the molecules in MSNP4 decayed in 0.83 ns and 33% in 2.21 ns. Similar values were shown for MSNP6, the main and minor components showed lifetimes of 0.73 ns (66%) and 2.21 ns (34%). To sum up, all the MSNP formulations presented a minor population with lifetime of ~2 ns which corresponds with the lifetime of free ZnPcSMP in DMF solution. However, a major population with shorter lifetime was also present in all the MSNP suspensions. Therefore, these results indicated the existence of ZnPcSMP in its monomeric form but also the presence of aggregates in the MSNPs suspended in DMF. This is consistent with the evidence observed in the absorbance study.

Likewise, to study the time-resolved fluorescence of DOX, the emission of MSNP4 and MSNP6 at 590 nm was monitored after excitation at 502 nm. Both MSNP formulations showed bioexponential decays with lifetimes of 0.67 ns (74%) and 2.25 (26%) for MSNP4 and 0.85 ns (68%) and 2.97 ns (32%) for MSNP6. Here again, the major population of excited singlet state of DOX had shorter lifetimes surely due to the formation of aggregates.

Table 10. Singlet state lifetimes (τ_s) and their relative amplitudes (A_s) for DMF and aqueous suspensions of free ZnPcSMP, free DOX and MSNP3, MSNP4, MSNP6, MSNP**A**-Cet, MSNP**B**-Cet and MSNP**C**-Cet.

Sample	Solvent	ZnPcSMP		DOX	
		τ_s / ns	% A_s	τ_s / ns	% A_s
ZnPcSMP	DMF	2.12	100	-	-
	PBS	1.98	100	-	-
DOX	DMF	-	-	1.46	100
	PBS	-	-	1.03	100
MSNP3	DMF	0.50 2.09	75 25	-	-
MSNP4	DMF	0.83 2.21	67 33	0.67 2.25	74 26
MSNP6	DMF	0.73 2.19	66 34	0.83 2.97	68 32
MSNP**A**-Cet	PBS	0.28 2.05	95 5	-	-
MSNP**B**-Cet	PBS	0.28 2.21	98 2	0.14 1.03	97 3
MSNP**C**-Cet	PBS	0.32 2.08	92 8	0.35 1.44	80 20

On the other hand, the time-resolved fluorescence of free ZnPcSMP, MSNP**A**-Cet, MSNP**B**-Cet and MSNP**C**-Cet were recorded in PBS (Figure 47 and Table 10). As above-mentioned, to investigate the time-resolved fluorescence of the photosensitizer, their emission at 698 nm was monitored after excitation at 654 nm. Free ZnPcSMP showed a monoexponential decay with a lifetime of 1.98 ns, corresponding to τ_s of ZnPcSMP. However, the fluorescence decay profiles of aqueous suspensions of MSNP**A**-Cet, MSNP**B**-Cet and MSNP**C**-Cet were characterized by biexponential decay processes. Their minor contribution had a lifetime of ~2 ns, same value as the free photosensitizer in PBS (5%, 2%, 8% for MSNP**A**-Cet, MSNP**B**-Cet and MSNP**C**-Cet respectively). The main population in all the MSNP formulations presented a lifetime of ~0.3 ns (95%, 98% and 92% for MSNP**A**-Cet, MSNP**B**-Cet and MSNP**C**-Cet respectively). Therefore, for MSNPs suspensions in PBS, almost all the ZnPcSMP molecules presented a very short lifetime due to the formation of aggregates.

Similarly, the time-resolved fluorescence of DOX was studied for DOX, MSNP**B**-Cet and MSNP**C**-Cet. The emission of MSNP4 and MSNP6 at 590 nm was monitored after excitation at 502 nm. The fluorescence decay profiles of both MSNP formulations were characterized by biexponential decay processes with a τ_s of 0.14 ns (97%) and 1.03 ns (3%) for MSNP**B**-Cet and 0.35 (80%) and 1.44 ns (20%) for MSNP**C**-Cet.

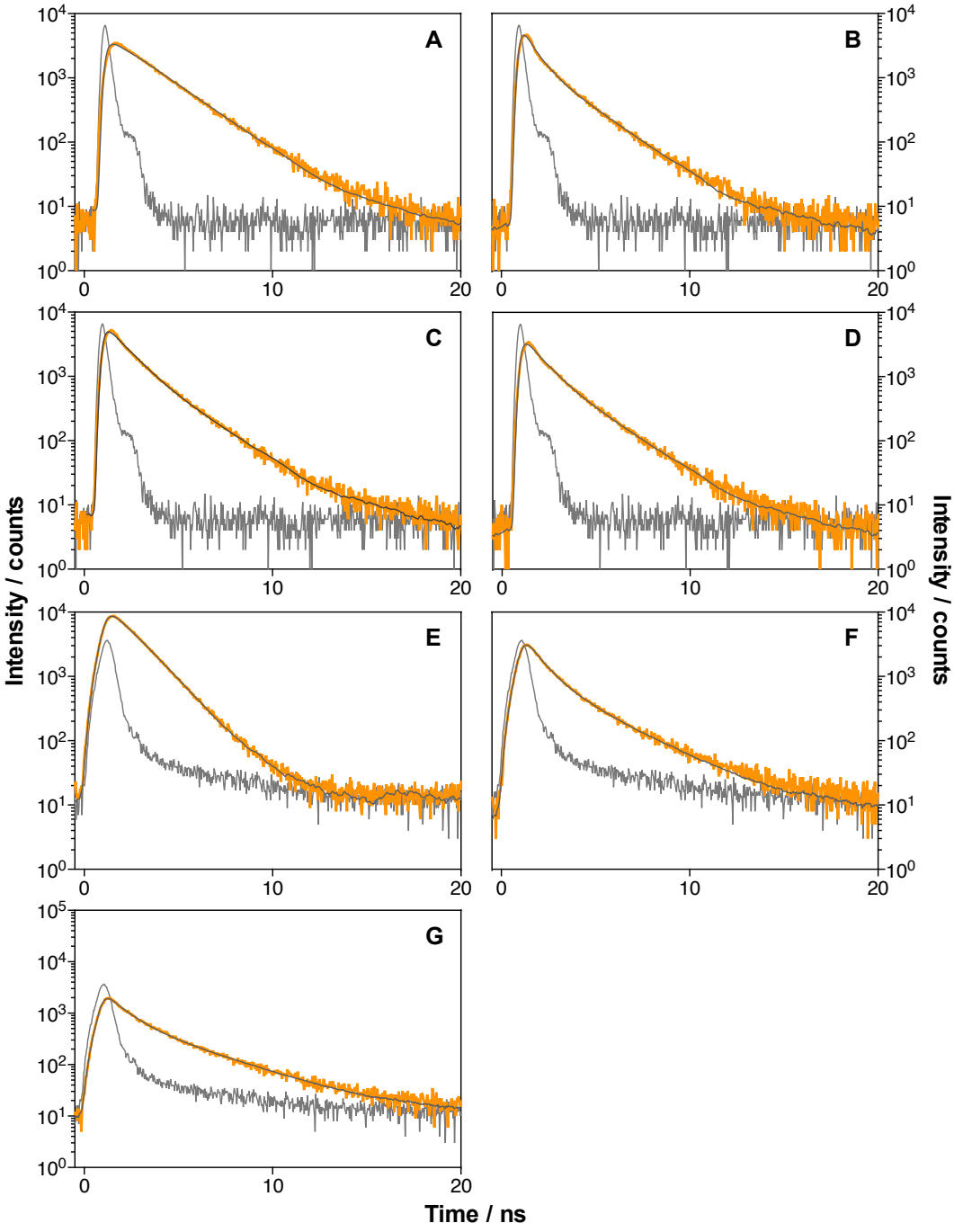

Figure 46. Time-resolved fluorescence decays (λ_{exc} = 654 nm. λ_{em} = 698 nm) of suspensions in DMF of ZnPcSMP (A), MSNP3 (B), MSNP4 (C) and MSNP6 (D). Time-resolved fluorescence decays (λ_{exc} = 502 nm. λ_{em} = 590 nm) of suspensions in DMF of DOX (E), MSNP4 (F) and MSNP6 (G). Instrumental response factor (IRF) in grey.

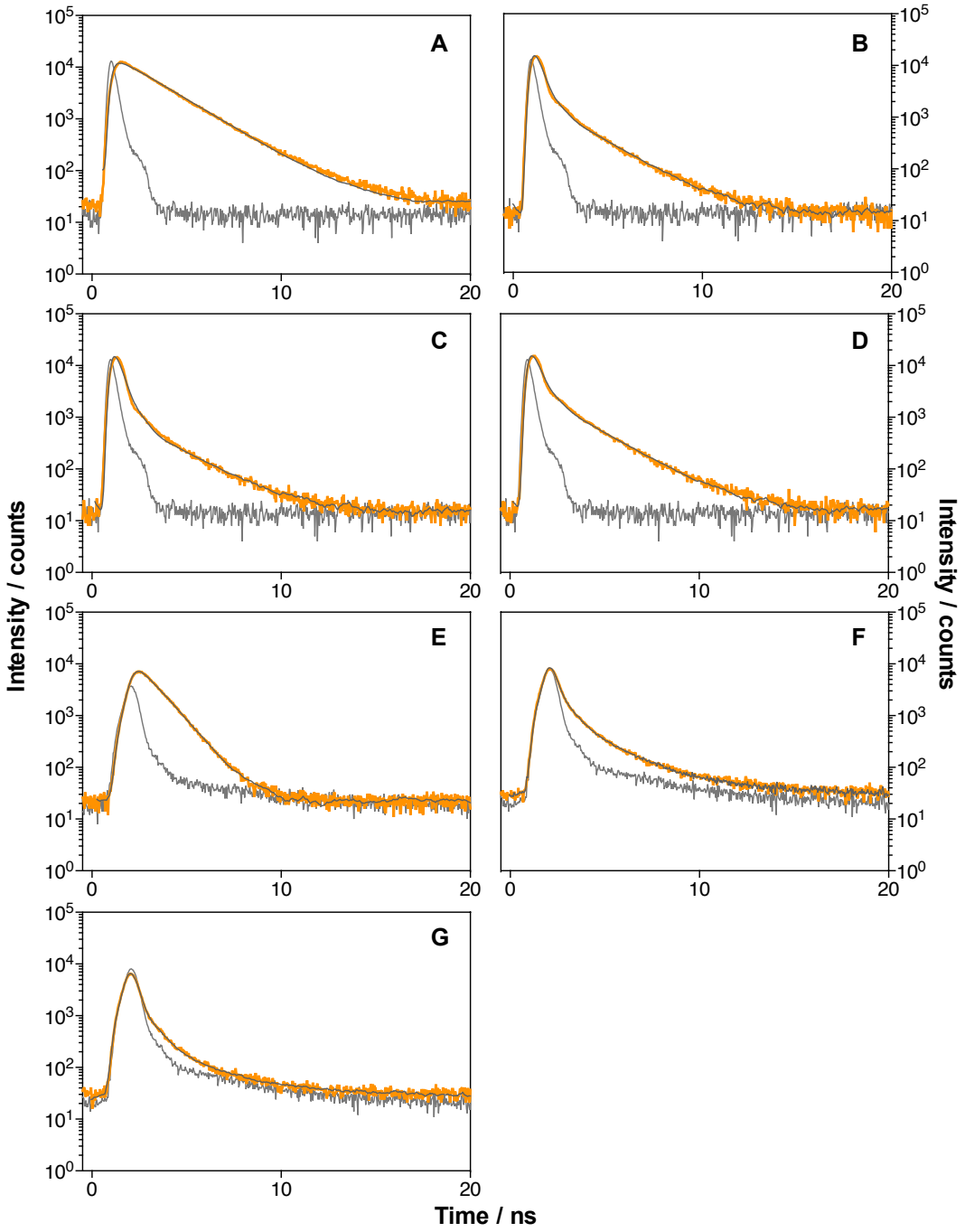

Figure 47. Time-resolved fluorescence decays (λ_{exc} = 654 nm. λ_{em} = 698 nm) of suspensions in PBS of ZnPcSMP (A), MSNP**A**-Cet (B), MSNP**B**-Cet (C) and MSNP**C**-Cet (D). Time-resolved fluorescence decays (λ_{exc} = 502 nm. λ_{em} = 590 nm) of suspensions in PBS of DOX (E), MSNP**B**-Cet (F) and MSNP**C**-Cet (G). Instrumental response factor (IRF) in grey.

5.2.3.3 Singlet Oxygen Generation and Kinetics

5.2.3.3.1 Free ZnPcSMP

Time-resolved NIR phosphorescence detection was performed to study the generation and kinetics of singlet oxygen ($^1O_2$) by free ZnPcSMP in DMF (Figure 48A) and in D_2O (Figure 48B). Their singlet oxygen quantum yields (Φ_Δ) were determined by direct observation of the $^1O_2$ phosphorescence at 1275 nm after excitation at 355 nm using ZnPc in DMF as reference (Φ_Δ = 0.56[229]) and PNS in D_2O (Φ_Δ = 0.98[230,231]) (Table 11). In addition, the triplet ZnPcSMP phosphorescence was recorded at 1110 nm after excitation at 355 nm (Figure 48C and D).

Table 11. Singlet oxygen generation yield and kinetic values of ZnPcSMP in DMF and D_2O.

Solvent	Φ_Δ	τ_T / µs	τ_Δ / µs
DMF	0.16	0.89	17.4
D_2O	0.06	2.6	68.9

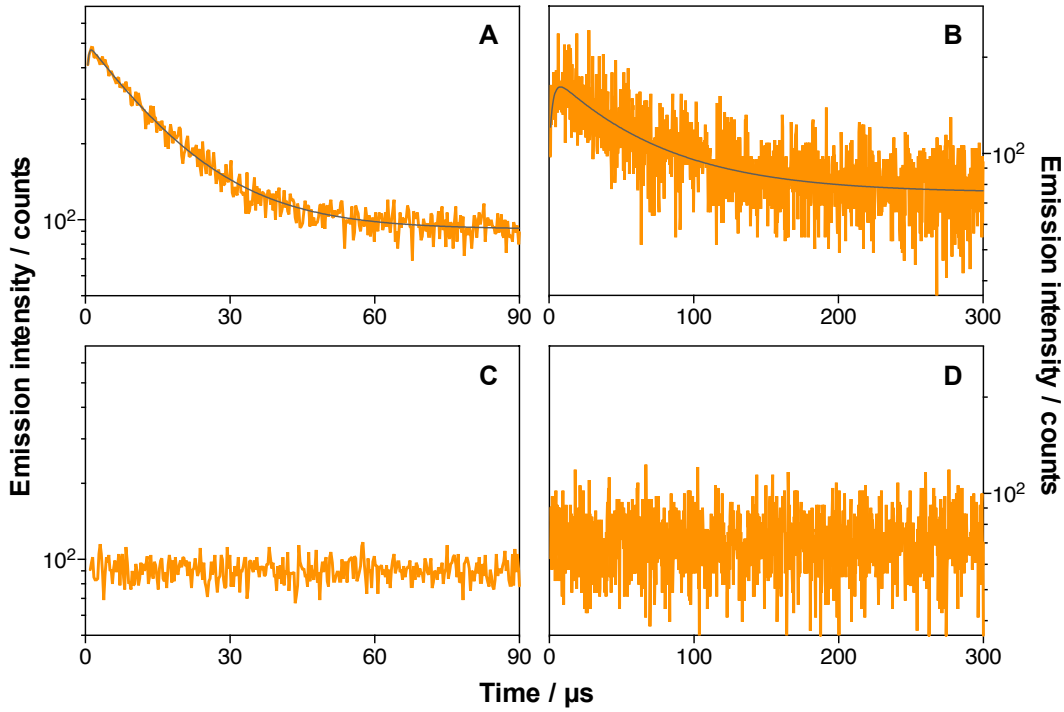

Figure 48. Time-resolved phosphorescence decays of free ZnPcSMP in DMF at 1275 nm (A) and 1110 nm (C) and in D_2O at 1275 nm (B) and 1110 nm (D). λ_{exc} = 1275 nm. λ_{em} = 355 nm.

Firstly, for ZnPcSMP in DMF, unequivocal $^1O_2$ production was demonstrated by the observation of a rise-and decay signal at 1275 nm, while at 1110 nm no signal was observed. The decay presented a lifetime of 17.4 µs, which corresponds to $^1O_2$ lifetime (τ_Δ) and is a typical value for this parameter in DMF (Table 11).[232] The rise showed a very short lifetime of

0.89 µs, corresponding to excited triplet state lifetime (τ_T). The calculated quantum yield of $^1O_2$ production by ZnPcSMP in DMF was 0.16 (Figure B9 and Figure B10 in Appendix B).

Secondly, the generation of $^1O_2$ by ZnPcSMP in D_2O was evidenced by the observation of a rise-and decay signal at 1275 nm with values of τ_Δ and τ_T of 68.9 µs and 2.6 µs, respectively. However, its production in this solvent was much lower than in DMF: the Φ_Δ found was only 0.06 (Figure B9 and Figure B10 in Appendix B). This fact can be rationalized by the formation of ZnPcSMP aggregates in aqueous media.

5.2.3.3.2 The Prepared Mesoporous Silica Nanoparticles

Time-resolved NIR phosphorescence detection studies were performed for MSNP3, MSNP4 and MSNP6, precursors of the targeted-MSNPs. In this study, $^1O_2$ generation was monitored by time-resolved detection of its phosphorescence at 1275 nm after excitation at 355 nm (Figure 49 and Table 12).

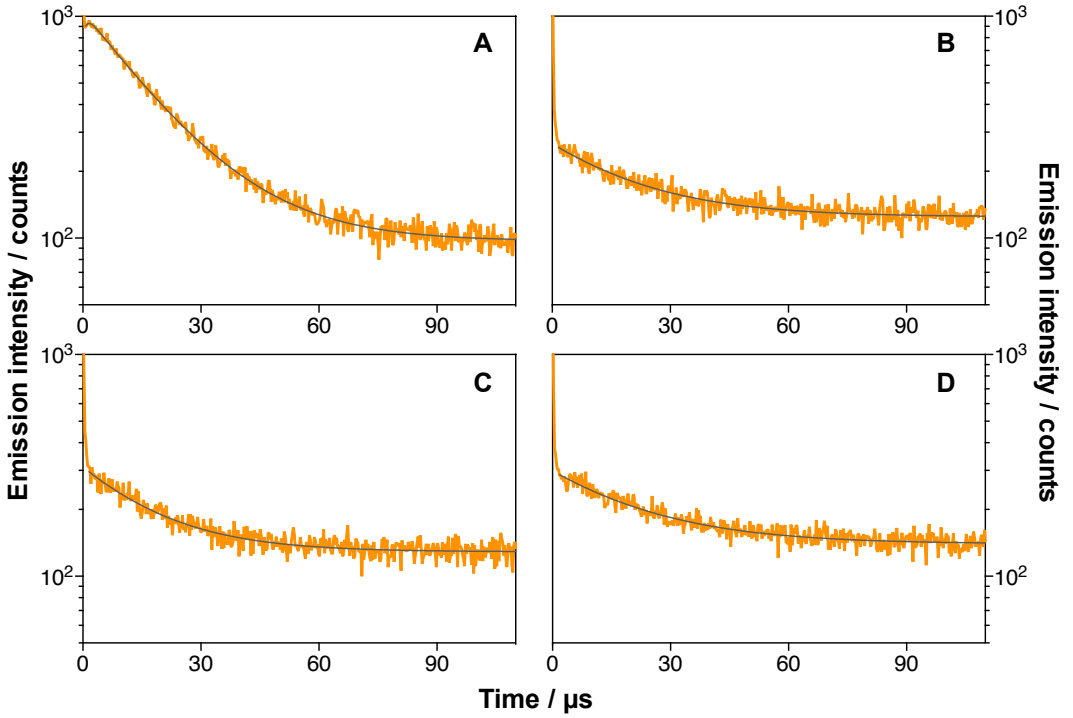

Figure 49. Time-resolved phosphorescence decays of free ZnPcSMP(A), MSNP3 (B), MSNP4 (C) and MSNP6 (D) suspensions in DMF. λ_{em} = 1275 nm. λ_{exc} = 355 nm.

The three types of MSNPs generated $^1O_2$. MSNP3 and MSNP6 formulations in DMF showed a decay of ~21 µs, which corresponds to $^1O_2$ lifetime (τ_Δ). However, MSNP4 showed a shorter decay of 18 µs. The shortening in the lifetime of MSNP4 formulation may be due to the

presence of the $^1O_2$-cleavable linker. The generation of $^1O_2$ by concentration-matched free ZnPcSMP in DMF was much higher than that for all the MSNP formulations. Comparing their amplitudes of singlet oxygen lifetimes, MSNPs decreased the production of $^1O_2$ by ~85% in comparison with free ZnPcSMP.

Table 12. Singlet oxygen kinetic values of ZnPcSMP, MSNP3, MSNP4 and MSNP6 suspensions in DMF. A_Δ: amplitude of singlet oxygen lifetime. A_T: amplitude of triplet lifetime. λ_{em} = 1275 nm. λ_{exc} = 355 nm.

Sample	τ_Δ / µs	A_Δ	τ_T / µs	A_T
Free ZnPcSMP	17.4	920	0.9	-114
MSNP3	21.7	132	-	-
MSNP4	18.1	167	-	-
MSNP6	21.4	147	-	-

The same study was performed after excitation at 660 nm, in the Q-band region (Figure 50 and Table 13). Very similar lifetimes were found for the different MSNP formulations in comparison with the values obtained after excitation at 355 nm. However, in this case, MSNPs decreased the generation of $^1O_2$ by ~93%, an even more pronounced difference than before.

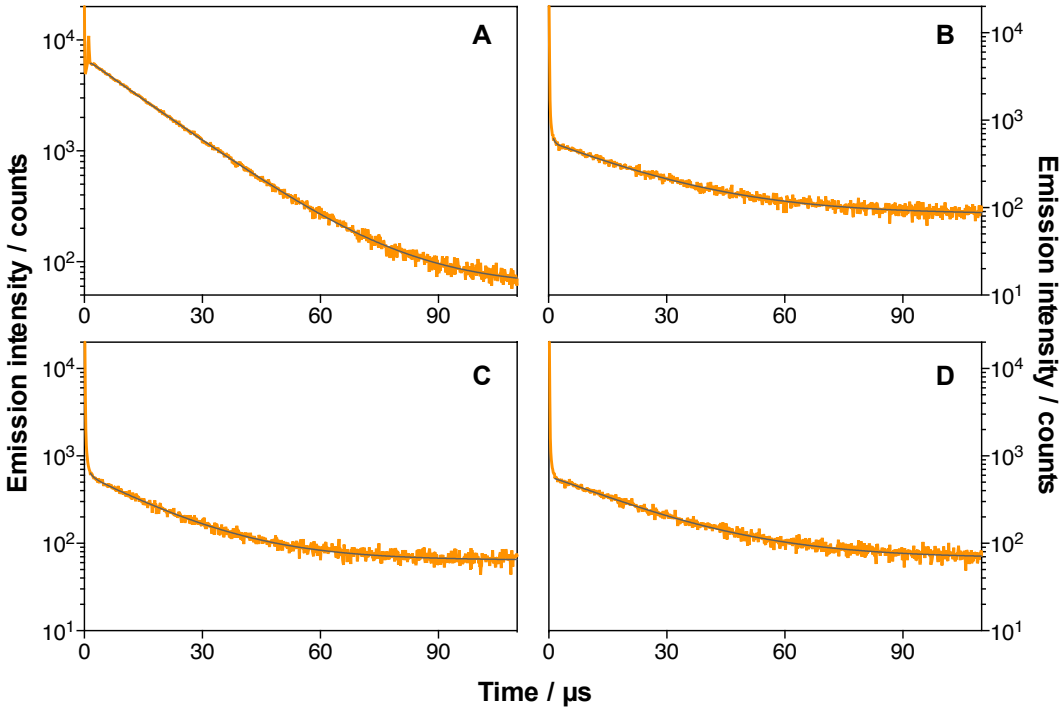

Figure 50. Time-resolved phosphorescence decays of free ZnPcSMP(A), MSNP3 (B), MSNP4 (C) and MSNP6 (D) suspensions in DMF. λ_{em} = 1275 nm. λ_{exc} = 660 nm.

Table 13. Singlet oxygen kinetic values of ZnPcSMP, MSNP3, MSNP4 and MSNP6 suspensions in DMF. A_Δ: amplitude of singlet oxygen lifetime. A_T: amplitude of triplet lifetime. λ_{em} = 1275 nm. λ_{exc} = 660 nm.

Sample	τ_Δ / µs	A_Δ
ZnPcSMP	17.2	6253
MSNP3	21.6	462
MSNP4	17.9	506
MSNP6	21.0	509

Therefore, ZnPcSMP showed a remarkably lower $^1O_2$ generation when it was attached to the MSNPs. Consistent with the evidence showed in absorption, emission and TRF studies, ZnPcSMP is surely majority aggregated in the MSNPs and because of this, it has a minor photoactivity.

5.2.3.4 Photobleaching of ZnPcSMP

To gain insights into the stability of the photosensitizer ZnPcSMP in DMF and H_2O, its photobleaching (photodegradation) was assessed upon illumination with λ_{exc} = 661 ± 10 nm and 70 mW·cm^{-2} irradiance at increasing light doses (Figure 51).

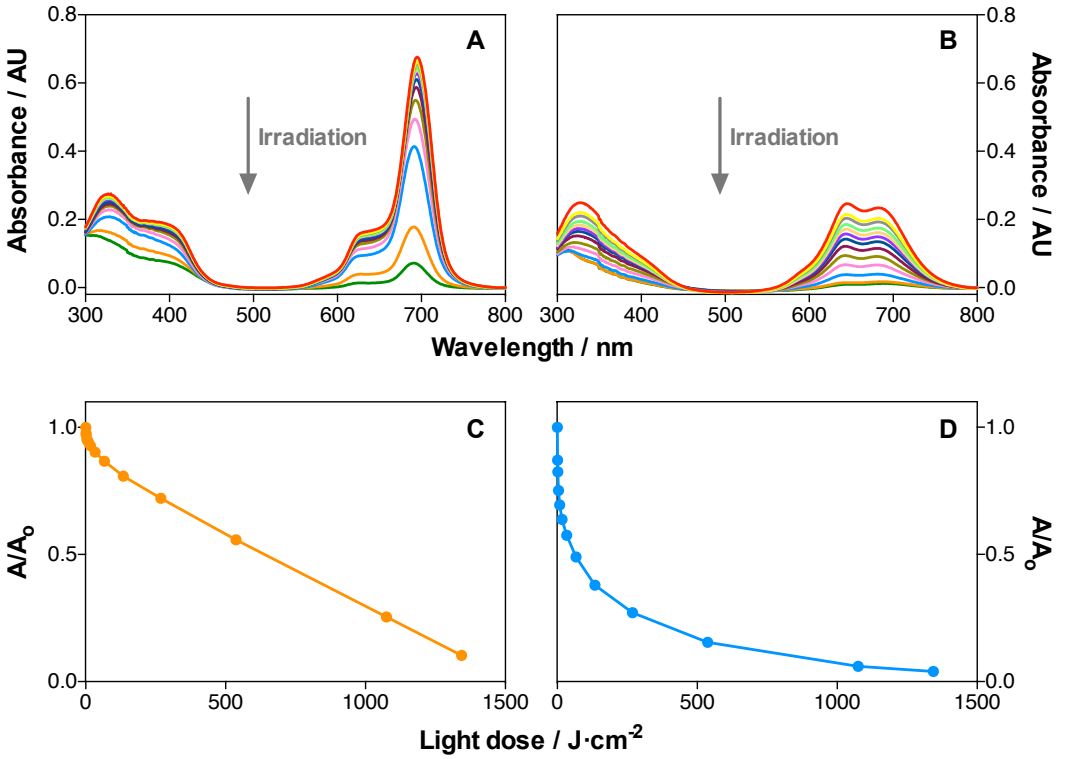

Figure 51. Absorption spectra of ZnPcSMP after irradiation at each light dose in DMF (A) and in PBS (B). Changes in absorbance of ZnPcSMP at the absorption maximum wavelength during irradiation in DMF (C) and in PBS (D).

The absorption spectrum was recorded for each studied light dose, showing a decrease in the absorbance upon higher irradiation. Figure 51C and D shows the decrease in the Q-band of the UV-vis spectra relative to the non-irradiated absorbance value upon increased light doses.

5.2.3.5 Photo-responsive Doxorubicin Release in Solution

The efficiency of the cleavage of the $^1O_2$-sensitive linker and the subsequent release of DOX from MSNP4 nanoparticles was investigated by irradiating them with increasing red light doses. MSNP4 formulation has the photosensitizer ZnPcSMP covalently immobilized and the DOX covalently attached by means of a $^1O_2$-sensitive linker; this formulation is the precursor of MSNP**B**-Cet nanoparticles. In order to unequivocally study the photo-responsive release of Doxorubicin from MSNP4, dark controls were performed following the same procedure as the irradiated ones but keeping them in dark conditions during the irradiation periods. As shown in Figure 52, illuminated MSNP4 dispersed in DMF released DOX in a similar cumulative emission intensity as compared with the dark controls. The percentage of Doxorubicin released compared to that present in the MSNP4 formulation was determined calculating the cumulative concentration of released Doxorubicin at each light dose by interpolating the cumulative emission values in a Doxorubicin calibration curve obtained under the same conditions. After 540 J·cm^{-2} of irradiation, MSNP4 dispersed in DMF only released 0.20 % of the total DOX, comparable with the value of its dark control, 0.18% (Figure 54A).

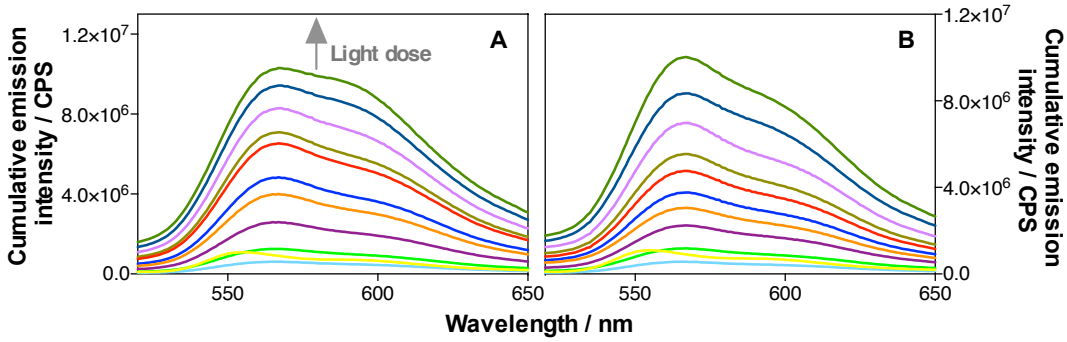

Figure 52. Cumulative emission spectra of DOX upon illumination of MSNP4 nanoparticles in DMF with increasing light doses (A) and dark controls (B). λ_{exc} = 475 nm.

On the other hand, the same photo-responsive study was performed for MSNP6, in which, DOX is attached to the nanoparticles *via* $^1O_2$-insensitive linker. MSNP6 formulation is the precursor of MSNP**C**-Cet nanoparticles. As happened with MSNP4, the cumulative emission intensity of irradiated MSNP6 was comparable with that for the dark control (Figure 53). A

suspension of MSNP6 nanoparticles in DMF released 0.17% of its total DOX after 540 J·cm^{-2} irradiation and 0.19% in darkness (Figure 54B).

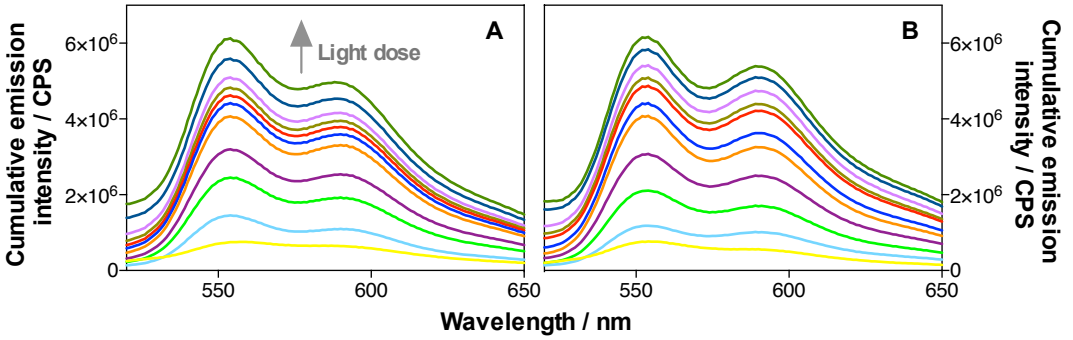

Figure 53. Cumulative emission spectra of DOX upon illumination of MSNP6 nanoparticles in DMF with increasing light doses (A) and dark controls (B). λ_{exc} = 475 nm.

Taking all these results together, MSNP4 nanoparticles only showed a negligible release of DOX, not light-dependent and comparable with that for the nanoparticles with the DOX attached by means of the $^1O_2$-insentive linker (MSNP6). Two different explanations might be the answer to these results: i) DOX was not properly attached to the nanoparticle by the $^1O_2$-sensitive linker, or ii) the generated $^1O_2$ by MSNP4 was not enough to cleave the linker and release the DOX.

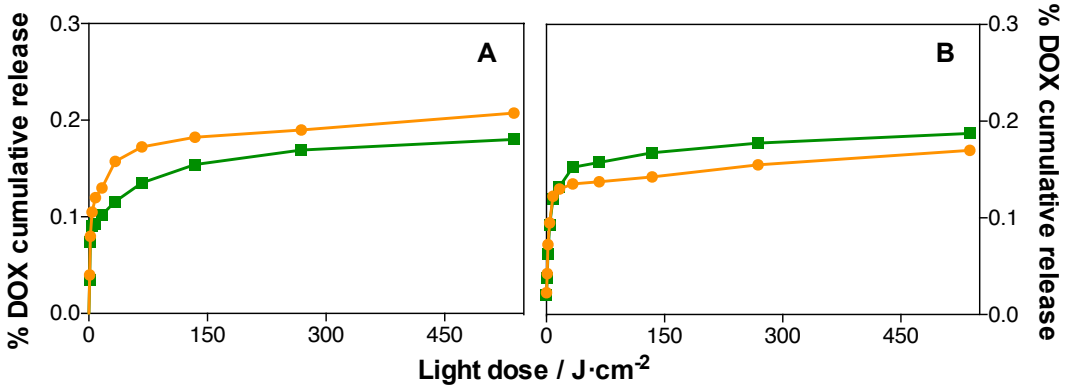

Figure 54. Percentage of DOX released of suspensions in DMF of MSNP4 (A) and MSNP6 (B). Light-treated samples are shown in orange circles and dark control samples in green squares.

In order to elucidate which one of the hypothesis was correct, an additional photo-responsive DOX release experiment was performed. This time, MSNP4 nanoparticles were suspended in DMF with 10 μM of methylene blue (MB). Methylene blue is a well-known photosensitizer, which absorbs red light and is soluble in DMF, thus MB would definitely generate $^1O_2$ upon irradiation in the current experiment. In contrast to the results seen previously, here, kinetic analysis of the released DOX emission showed a huge increase in fluorescence upon

irradiation of MSNP4 nanoparticles (Figure 55). In contrast, dark controls showed a remarkably low DOX emission. Therefore, the photo-responsive release of DOX from MSNP4 was achieved satisfactorily, which implies that DOX was undoubtedly attached to the nanoparticle by means of the $^1O_2$-sensitive linker. Nevertheless, this last experiment also indicated that MSNP4 nanoparticles themselves did not generate enough $^1O_2$ to cleave the linker and release the Doxorubicin.

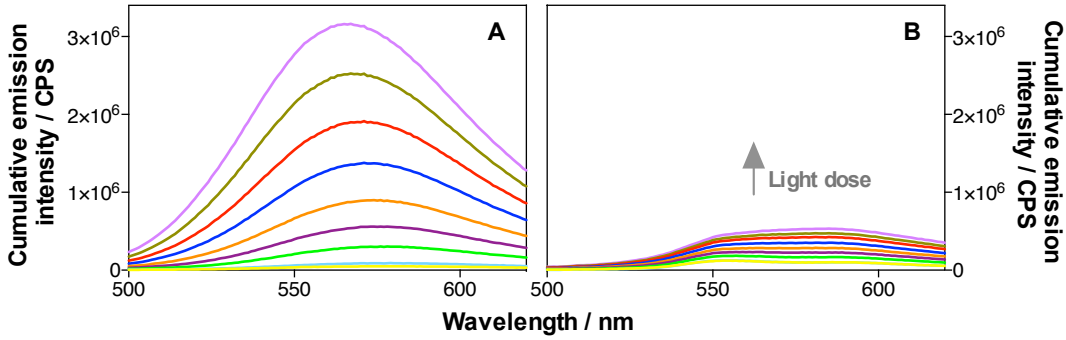

Figure 55. Cumulative emission spectra of DOX upon illumination of MSNP4 with increasing light doses in DMF with 10 μM of methylene blue (A). Dark controls (B) were also performed. λ_{exc} = 475 nm.

5.2.4 Biological Studies

Biological studies were performed in two different pancreatic cell lines: AsPC-1 and MIA PaCa-2. AsPC-1 cells express higher levels of EGFR than MIA PaCa-2 cells.[233] Cetuximab is a monoclonal antibody that binds to the extracellular domain of EGFR molecule.

5.2.4.1 *In vitro* Uptake of MSNPA Labeled with FITC

5.2.4.1.1 Qualitative Uptake via Confocal Microscopy

In order to ascertain the targeting ability of Cetuximab-nanoparticles, AsPC-1 and MIA-PaCa-2 cells were incubated with MSNP**A**-FITC and MSNP**A**-FITC-Cet nanoparticles at 1 μM of FITC at different incubation times (1 h, 2 h, 4 h, 8 h and 24 h). After incubation, nanoparticles still present in the culture medium were removed by washing. The internalization of the MSNPs was investigated by studying their FITC fluorescence *via* confocal microscopy (λ_{exc} = 488 nm). The results are summarized in Figure 57.

On the one hand, for AsPC-1 cells, MSNP**A**-FITC-Cet nanoparticles were effectively internalized. AsPC-1 cells showed more FITC emission as higher the incubation time. At short incubation times (1 h and 2 h), targeted-MSNPs were shown in a lesser quantity but also as isolated spots in the cells, so the cell shape was not shown. In contrast, with higher incubation

times, the cytosolic distribution of MSNP**A**-FITC-Cet nanoparticles in the cells was more evidenced. Otherwise, cells incubated with non-targeted nanoparticles only showed emission by large isolated aggregates. In addition, the emission intensity was not dependent of the incubation time. Therefore, non-targeted nanoparticles were apparently not internalized in the cells. It is known that monoclonal antibodies allow the internalization of nanoparticles by receptor mediated endocytosis, improving their capability of being internalized. Nevertheless, in this case, Cetuximab also plays an important role in the aqueous solubility of the nanoparticles. MSNPs have a great tendency to form large aggregates of nanoparticles in water that are barely internalized in cells due to their large size. Thereby, despite the presence of PEG in MSNP**A**-FITC, this formulation was not soluble enough in aqueous media without the presence of the antibody to avoid the formation of aggregates (Figure 56).

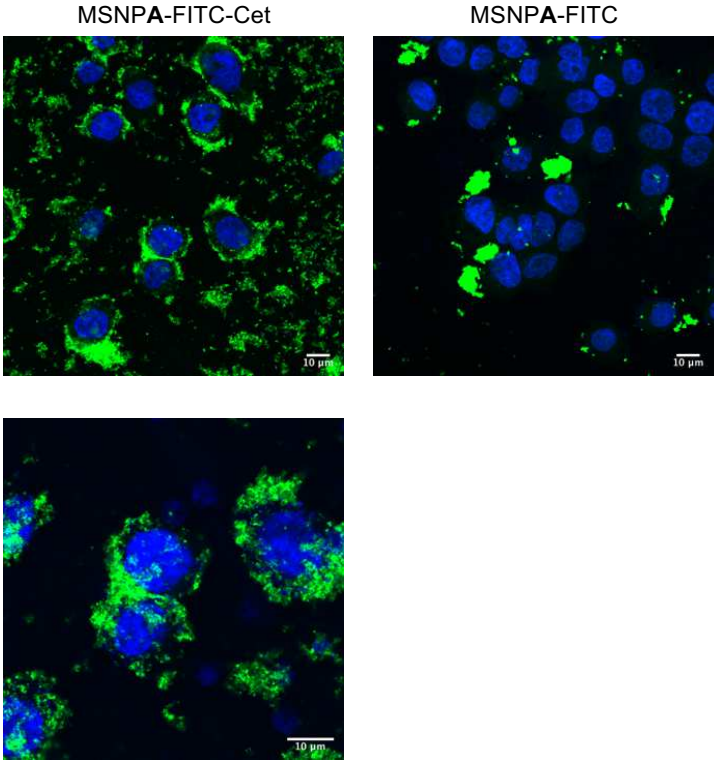

Figure 56. Confocal microscope images of AsPC-1 cells after 24 h incubation with MSNP**A**-FITC-Cet or MSNP**A**-FITC nanoparticles. The same amount of MSNPs were incubated. FITC is shown in green and Hoechst in blue.

On the other hand, for MIA PaCa-2 cells. As higher the incubation time, the FITC emission from MSNP**A**-FITC-Cet nanoparticles was more intense. However, the intensity was lower than for AsPC-1 cells, despite the cells were treated with the same concentration of nanoparticles. In addition, even at the largest incubation time, the clearly cell-shape distribution of MSNP**A**-FITC-Cet showed in AsPC-1 cells was not appreciable in MIA PaCa-

2. Therefore, targeted-nanoparticles were presumably internalized in a lesser manner in MIA PaCa-2 in comparison with AsPC-1 cells. As above-explained for AsPC-1, non-targeted nanoparticles were also shown in MIA PaCa-2 cells as large aggregates whose emission was not dependent of the incubation time.

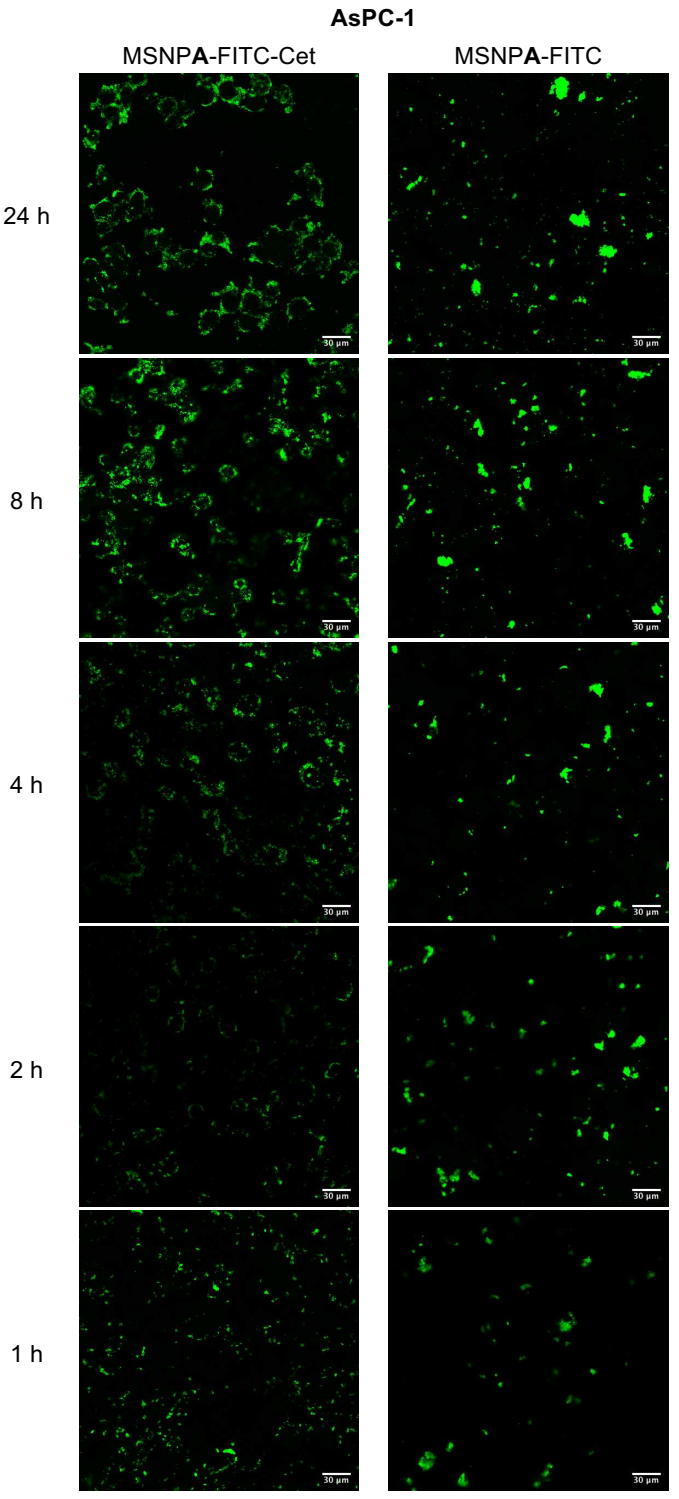
AsPC-1
MSNP**A**-FITC-Cet
MSNP**A**-FITC
24 h
8 h
4 h
2 h
1 h
30 µm

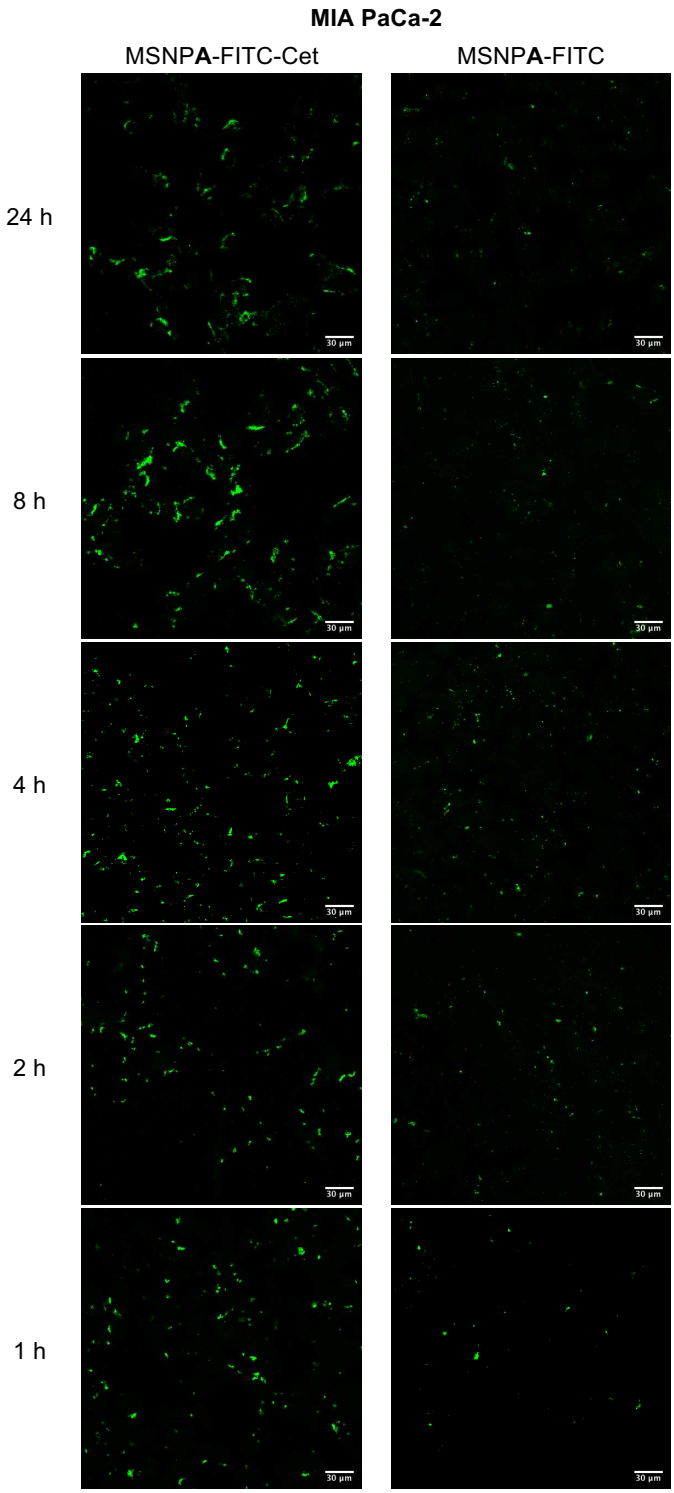

Figure 57. Qualitative cellular uptake of MSNP**A** labeled with FITC conjugated to Cetuximab and non-conjugated to Cetuximab on AsPC-1 and MIA PaCa-2 cells.

5.2.4.1.2 Quantitative Uptake

Before testing the nanoparticles for the photodynamic activity, it is important to determine quantitatively their targeting efficacy. Thus, the cellular uptake of MSNP**A**-FITC-Cet by AsPC-1 and MIA PaCa-2 cells was investigated at different incubation times. Both cell lines were incubated with MSNP**A**-FITC and MSNP**A**-FITC-Cet nanoparticles at 1 μM of FITC at different incubation times (1 h, 2 h, 4 h, 8 h and 24 h). After incubation, nanoparticles still present in the culture medium were removed by washing. The internalization of the MSNPs was investigated by studying their fluorescence at λ_{exc} = 440 nm and λ_{em} = 520 nm. Fluorescence was normalized by the amount of protein present in each sample. The results are summarized in Figure 58.

First, for AsPC-1 cells, as higher the incubation time, the emission intensity of FITC from the targeted-nanoparticles was increased. This fact is in consonance with a previous publication employing Cetuximab-targeted MSNPs in this cell line.[234] In contrast, FITC emission was almost negligible for cells treated with MSNP**A**-FITC. Thereby, unlike the non-targeted nanoparticles, the targeted ones were effectively internalized by the cells. All these results were consistent with the evidence showed in the confocal microscopy studies.

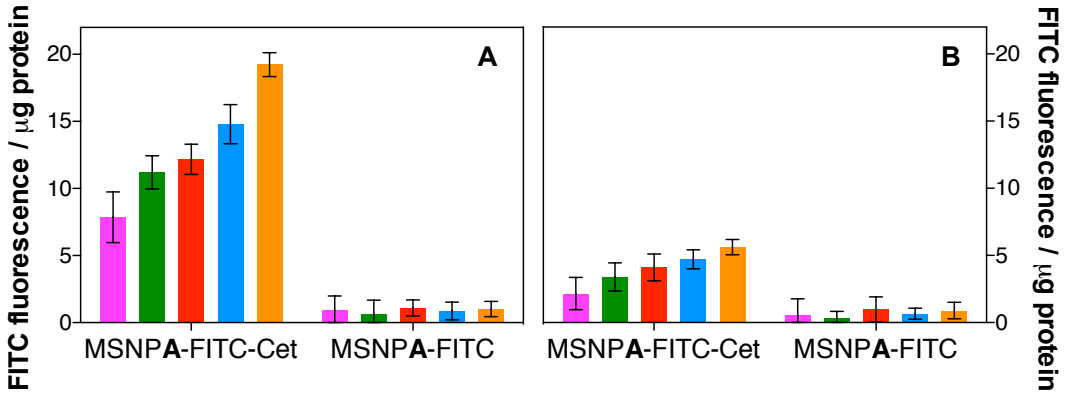

Figure 58. Cellular uptake of MSNP**A**-FITC and MSNP**A**-FITC-Cet nanoparticles in AsPC-1 (A) and MIA PaCa-2 (B) cells at different incubation times: 1 h (pink), 2 h (green), 4 h (red), 8 h (blue) and 24 h (orange). Cells were treated with the same concentration of FITC and MSNPs. Values reported are the mean ± SD of at least three independent experiments.

Second, the emission intensity of FITC from MSNP**A**-FITC-Cet nanoparticles was increased as increased the incubation time of the MSNPs in MIA PaCa-2 cells as well. However, despite both cell lines were treated with the same FITC concentration, MIA PaCa-2 showed much lesser FITC fluorescence. Therefore, targeted-nanoparticles were lesser internalized in this cell line which is consistent with its minor EGFR expression. Here again, the FITC emission from the non-targeted nanoparticles was negligible and non-dependent of the incubation time;

demonstrating their lack of uptake by the cells.

5.2.4.2 *In vitro* Phototoxicity Studies

The phototoxicity of the targeted nanoparticles (MSNP**A**-Cet, MSNP**B**-Cet and MSNP**C**-Cet) and the non-targeted ones (MSNP**A**, MSNP**B** and MSNP**C**) was investigated in AsPC-1 cells. In addition, free ZnPcSMP was studied as a control. The nanoparticles were diluted in supplemented medium to achieve a ZnPcSMP concentration of 2 μM. Then, they were incubated during 24 h in the cells. Afterwards, cells were washed and irradiated with 30 J·cm^{-2} and 60 J·cm^{-2} of red light. The cell viability test MTT was performed 24 h after the irradiation. The results are summarized in Figure 59 for 60 J·cm^{-2} of light dose; and in Figure B11 in Appendix B for 30 J·cm^{-2}.

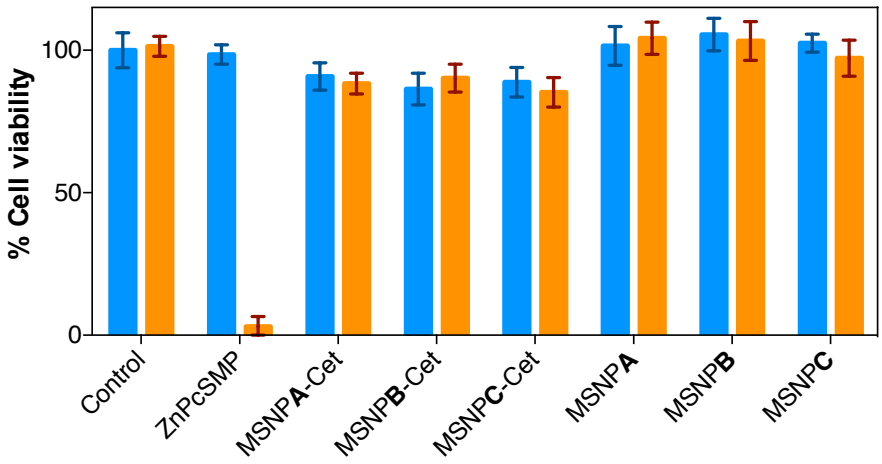

Figure 59. Phototoxicity studies in AsPC-1 of MSNP**A**-Cet MSNP**B**-Cet and MSNP**C-Cet** nanoparticles and their non-targeted analogs. Cells were irradiated with 60 J·cm^{-2} (in orange). Dark controls were also performed for each sample (in blue). Non-treated cells were used as control. Values reported are the mean ± SD of at least three independent experiments.

Firstly, any nanoparticle formulation did not show significant phototoxic effect since they did not decrease the cell viability in comparison with their corresponding dark control. Non-targeted MSNPs were expected to be non-toxic due to their lack of uptake by cells. In contrast, targeted MSNPs did show an effectively uptake with 24 h of incubation, however they demonstrated being non-phototoxic as well. The low or null generation of $^1O_2$ by the MSNPs is surely the reason of the lack of photodynamic action by the nanoparticles.

Secondly, the mortality showed in dark controls of treated cells with targeted-nanoparticles is surely due to their intrinsic cytotoxicity. Cetuximab binds to the extracellular domain of the EGFR molecule, which is overexpressed in many cancers. This competitively binding inhibits

the binding of epidermal growth factor (EGF) and other ligands resulting in inhibition of cell growth and the induction of apoptosis *in vitro*[235,236] and in xenograft models[237,238]. Cytotoxicity was not shown in cells treated with non-targeted nanoparticles.

Nevertheless, free ZnPcSMP at the same concentration as the MSNPs achieved a reduction in cell viability to 4% when irradiated with 60 $J \cdot cm^{-2}$. The toxicity effect of free ZnPcSMP was all due to its photodynamic activity since it was devoid of dark toxicity. Therefore, these results confirmed that when ZnPcSMP is attached to the MSNPs, it loses its photoactivity and thereby, its phototoxic effect *in vitro*.

5.3 Experimental Section

5.3.1 Materials

TESPIC, 3-MPA, *cis*-1,2-dichloroethylene, DOX·HCl, NHS, sulfo-NHS, APTES, CTAC, TEOS, FITC, Hoechst 33258, PBS and MTT were purchased from MilliporeSigma (St. Louis, MO, USA). DIPEA and EDC·HCl were purchased from Tokyo Chemical Industry Co., Ltd. (Tokyo, Japan). DMEM (with 4.5 g/L *D*-glucose and without sodium pyruvate or *L*-Glutamine), *L*-Glutamine solution (200 mM), Pencillin-Streptomycin solution, Trypsin EDTA solution (solution C (0.05%), EDTA (0.02%) and with phenol red) and FBS were purchased from Biological Industries (Kibbutz Beit Haemek, Israel). RPMI 1640 medium was purchased from Fisher Scientific (Waltham, Massachusetts, USA). Cetuximab was purchased from Carbosynth Ltd. (Compton, United Kingdom). COOH-PEG_{5k}-NHS was purchased from Laysan Bio Inc. (Arab, Alabama, USA). All other chemicals were commercially available reagents of at least analytical grade. Milli-Q water (Millipore Bedford system, resistivity of 18 MΩ cm) was used.

5.3.2 Synthesis of Precursors of Mesoporous Silica Nanoparticles

5.3.2.1 Conjugation Reaction Between ZnPcSMP and 3-(triethoxysilylpropyl)-isocyanate

The 3-(triethoxysilylpropyl) – ZnPcSMP conjugate was synthesized reacting (triethoxysilylpropyl)isocyanate (TESPIC) (0.98 µmols, 3 eq) and ZnPcSMP (0.5 mg, 0.33 µmols, 1 eq) in anhydrous DMF (200 µL) with the presence of DIPEA (5 µL). The mixture was stirred for 48 h in darkness and at RT. After, **2** was collected without further purification. (Quantities for 20 mg of blank MSNPs).

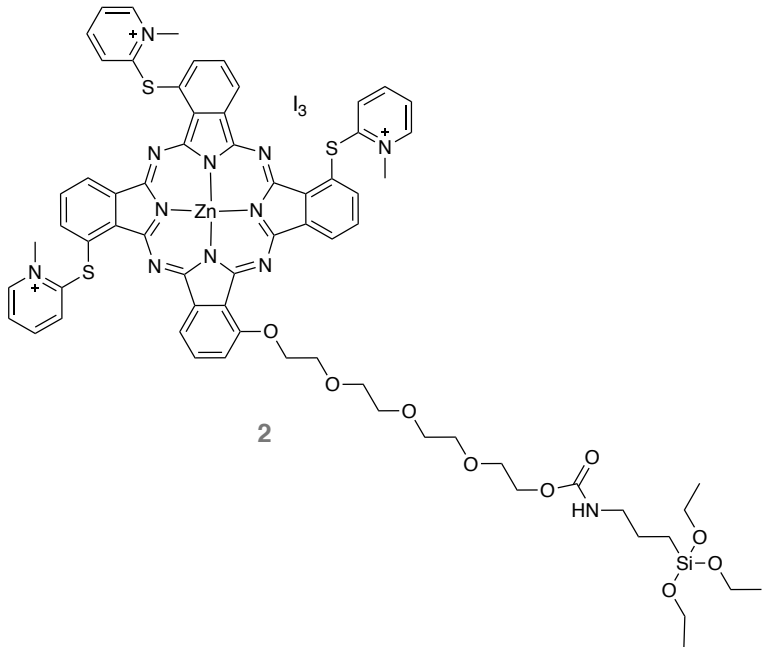

2

5.3.2.2 Synthesis of the $^1O_2$-Cleavable Linker

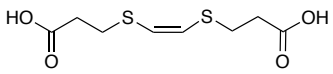

4

3-MPA (4.4 mL, 50.5 mmol, 1.9 eq.) was added dropwise to a solution of NaH (60% dispersion in mineral oil) (4.36 g, 109 mmol) in anhydrous DMF (200 mL) at 0°C for 10 min and 30 min at RT. Then, *cis*-1,2-dichloroethylene (2.0 mL, 26.5 mmol, 1 eq.) was added dropwise. The resulting mixture was stirred for 20 min at RT. Afterwards, the reaction was heated up to 70 ^oC for 18 h. Next, the crude was diluted with water (100 mL) and acidified to pH = 2 with $KHSO_4$ 1M. The mixture was extracted with EtOAc (200 mL x3) and the combined organic layers were washed with brine (200 mL), dried over anhydrous $MgSO_4$ and evaporated under reduced pressure. The concentrated residue in diethyl ether (50 mL) was extracted with water (40 mL x3); the organic layer was washed with brine (40 mL), dried over anhydrous $MgSO_4$ and concentrated under reduced pressure. Then, the product was recrystallized with EtOAc/hexane and dried under vacuum to afford the desired diacid (*Z*)-3, 3'-(ethene-1,2-diylbis(sulfanediyl)dipropanoic acid (**4**). Compound was isolated in 30% (1.4279 g, 6.1 mmol) yield. The correct synthesis of the desired product was checked by ^{1}H-NMR and ^{13}C-NMR.

The physical and spectroscopic data of (*Z*)-3,3'-(ethene-1,2-diylbis(sulfanediyl)dipropanoic acid were identical to those reported in the literature[83] (the spectra are shown in Figure B1 in Appendix B).

TLC: 0.32 (EtOAc:hexane; 1:1)

^{1}H NMR (CD_3OD): δ 6.20 (s, 2H), 2.93 (td, J = 7.0, 0.5 Hz, 4H), 2.61 (td, J = 7.0, 0.5 Hz, 4H).

^{13}C NMR (CD_3OD): δ 175.4 (C), 124.9 (CH), 36.2 (CH_2), 29.9 (CH_2).

IR (KBr) spectroscopy: υ, cm^{-1} 3431 (st O-H free), 3300-2500 (st O-H bonded), 3026 (st C-H), 2760 and 2588 (st C-H_2), 1639 (st C=O), 1554 (st C=C), 1409 (δ C-H_2), 1198 (st C-O) 642 (*cis* C=C).

MS (EI): *m/z* (abundance) $C_8H_{12}O_4S_2$ 236.1 (100).

5.3.2.3 Orthogonal Conjugation of Doxorubicin to the $^1O_2$-Cleavable Linker

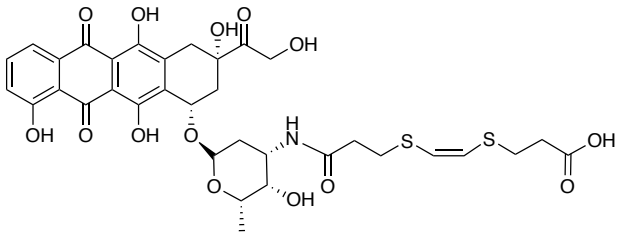

6

A mixture of the cleavable linker (**4**) (0.3 mg, 0.9 µmol, 1 eq), EDC·HCl (0.7 mg, 3.6 µmol, 4 eq) and NHS (0.4 mg, 3.6 µmol, 4 eq) in anhydrous DMF (500 µL) was stirred for 2 h at RT. Then, the mixture was treated dropwise with a solution of DOX (0.5 mg, 0.9 µmol, 1 eq) with DIPEA (1.6 µL) in anhydrous DMF. The resulting reaction mixture was allowed to stir at RT for 24 h. After, the orange product **6** was collected without further purification.

5.3.2.4 Conjugation Reaction Between Doxorubicin and 3-(triethoxysilylpropyl)-isocyanate

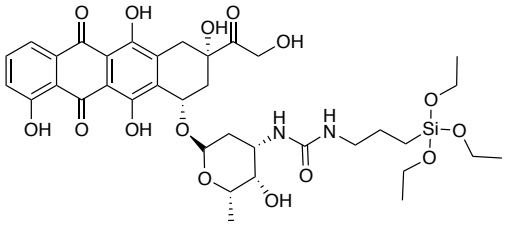

7

To a solution of DOX (0.5 mg, 0.8 µmols, 1 eq) in anhydrous DMF (400 µL), TESPIC (2.6 µmols, 3 eq) was added. The mixture was stirred for 18 h at RT. After, the conjugate **7** was collected without further purification. (Quantities for 20 mg of MSNP).

5.3.2.5 Conjugation Reaction Between COOH-PEG-NHS and Cetuximab

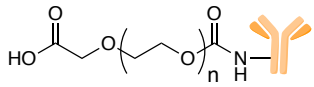

9

To a solution of NHS-PEG-COOH in PBS pH = 8.0, Cetuximab was added (1:1 wt NHS-PEG-COOH:Cet). The mixture was stirred for 3 h at RT. After, it was purified using Amicon ultra 2 mL centrifugal units. Briefly, the mixture was centrifuged (15 min, 7,500 g). Then, a wash was performed adding 1 mL of PBS pH = 7.4 and centrifuging (15 min, 7,500 g). Two washes were performed in total. Afterwards, the conjugate **9** was collected by flipping the centrifuge unit and centrifuging (4 min, 1,000 g).

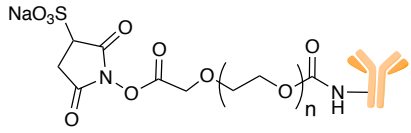

10

Immediately before of the preparation of Cetuximab-nanoparticles, a mixture was prepared with all the compound **9**, EDC·HCl (1:1 wt with PEG) and sulfo-NHS (1:1 wt with PEG) in PBS pH = 6.0. The mixture was stirred for 40 min at RT. After, it was purified using using Amicon ultra 2 mL centrifugal units. Briefly, the mixture was centrifuged (15 min, 7,500 g). Then, a wash was performed adding 1 mL of PBS pH = 6.0 and centrifuging (15 min, 7,500 g). Two washes were performed in total. Afterwards, the conjugate **10** was collected by flipping the centrifuge unit and centrifuging (4 min, 1,000 g).

5.3.3 *Derivatization of Silica Mesoporous Nanoparticles*

5.3.3.1 MSNPA-Cet: ZnPcSMP – Cetuximab – MSNP

- MSNP2: functionalization of blank MSNPs with compound **2**. All of the synthesized **2** was added to 20 mg of blank mesoporous silica nanoparticles dispersed in anhydrous DMF (20 mL). The mixture was closed and kept in dark under stirring for 24 h at 60 ºC. Afterwards, the reaction mixture was centrifuged (60 min, 14000 rpm, 15 ºC) and washed three times with DMF to remove the non-conjugated **2**. MSNP2 nanoparticles were kept in EtOH at 4 ºC.

- MSNP3: reaction between MSNP2 and APTES. APTES (15 µL) was added to all of the MSNP2 nanoparticles prepared and dispersed in absolute EtOH (20 mL). The mixture was closed and under stirring overnight at 40 ºC. Afterwards, the reaction mixture was centrifuged (60 min, 14000 rpm, 15 ºC) and washed three times with

EtOH. MSNP3 nanoparticles were kept in EtOH at 4 ºC.

- MSNP**A**: PEGylation of MSNP3. NHS-PEG-COOH (20 mg, 5.8 µmols) (5:2 wt ratio of MSNP:PEG) was added to all the prepared MSNP3 nanoparticles dispersed in DMF (20 mL). The mixture was stirred for 24 h in darkness and at RT. Then, the reaction mixture was centrifuged (60 min, 14000 rpm, 15 ºC) and washed three times with DMF. MSNP**A** nanoparticles were kept in EtOH at 4 ºC.

  *For the FITC-labeled MSNP**A**, prior to the PEGylation, 0.5 mg of FITC were added 20 mg of prepared MSNP3 nanoparticles dispersed in EtOH (20 mL). The mixture was allowed to stir overnight at RT. Afterwards, the mixture was centrifuged (60 min, 14000 rpm, 15 ºC) and washed three times with EtOH.

- MSNP**A**-Cet: Conjugation of compound **10** to MSNP**A**. Compound **10** was added to a dispersion of MSNP3 nanoparticles in the same volume of PBS pH = 7.4 (5:2:2 wt MSNPs:PEG:Cetuximab) and stirred overnight at RT. Finally, MSNP**A**-Cet nanoparticles were collected without further purification.

5.3.3.2 MSNPB: ZnPcSMP – Cetuximab – Doxorubicin (covalently attached, releasable) – MSNP

- MSNP2 and MSNP3 were prepared as described before.

- MSNP4: functionalization of MSNP3 with the orthogonal conjugate cleavable linker – Doxorubicin, compound **6**. All of the synthesized **6**, EDC·HCl (1 eq) and NHS (1 eq) were added to MSNP3 dispersed in DMF (20 mL). The mixture was allowed to react for 24 h at 40 ºC. Afterwards, the reaction mixture was centrifuged (60 min, 14000 rpm, 20 ºC) and washed three times with DMF to remove the non-conjugated **6**. MSNP4 nanoparticles were left in EtOH at 4 ºC.

- Synthesis of MSNP**B** and MSNP**B**-Cet. To obtain MSNP**B** nanoparticles, MSNP4 nanoparticles were PEGylated as described before for MSNP**A**. Finally, the conjugation of PEG-Cetuximab to MSNP4 nanoparticles was performed as explained for MSNP**A**-Cet.

5.3.3.3 MSNPC: ZnPcSMP – Cetuximab – Doxorubicin (covalently attached, not releasable) – MSNP

- MSNP2 was prepared as described before.

- MSNP5: functionalization of MSNP2 with the conjugate **7**. All of the synthesized **7**

was added to MSNP2 nanoparticles dispersed in absolute EtOH (20 mL). The mixture was allowed to stir for 24 h at 40 ºC. Afterwards, the reaction mixture was centrifuged (60 min, 14000 rpm, 15 ºC) and washed three times with EtOH to remove the non-conjugated **7**. MSNP7 nanoparticles were kept in DMF at 4 ºC.

- Synthesis of MSNP6, MSNP**C** and MSNP**C**-Cet. To obtain MSNP6 nanoparticles, APTES was introduced on the surface of MSNP5 nanoparticles following the same procedure as described for MSNP3. Next, the PEGylation of MSNP6 nanoparticles with NHS-PEG-COOH was carried out as described before for MSNP**A**. Finally, the conjugation of PEG-Cetuximab to MSNP6 nanoparticles was performed as mentioned for MSNP**A**-Cet.

5.3.4 Measurement of the Physicochemical Parameters

Size, polydispersity index and zeta-potential measurements were carried out for all the synthesized nanoparticles. On the one hand, for non-Cetuximab attached nanoparticles, size and PdI were carried out using a mixture of 240 µL of nanoparticles (1 mg/mL) with 2 mL EtOH. For Cetuximab linked nanoparticles, they were performed employing a mixture of 240 µL nanoparticles (1 mg/mL) with 2 mL milliQ water. On the other hand, zeta-potential was measured using 240 µL nanoparticles and 2 mL milliQ water for all the nanoparticles.

5.3.5 Determination of the Drug Concentration in the Nanoparticles

The concentrations of the photosensitizer ZnPcSMP and the chemo-drug DOX in the nanoparticle formulations were calculated as the difference between the amount of ZnPcSMP or DOX incorporated and the amount recovered from supernatant collected upon centrifugation of the nanoparticles (1 h, 14,000 rpm). The ZnPcSMP concentration from supernatant was determined by comparison with absorbance standard curves obtained in the same conditions. The DOX concentration from supernatant was determined by comparison with emission standard curves obtained employing the same experimental conditions.

5.3.6 Determination of the Photophysical Parameters

Fluorescence quantum yields were determined by the comparative method. For ZnPcSMP, ZnPc in DMF was used as the standard (Φ_F = 0.28).

Singlet oxygen quantum yields were determined using the comparative method. For ZnPcSMP in DMF, ZnPc in DMF was used as the standard (Φ_Δ = 0.56). For ZnPcSMP in D_2O,

PNS in D_2O was used as the reference (Φ_Δ = 0.98).

5.3.7 Photo-responsive Release of Doxorubicin from MSNP4

In order to evaluate the photo-responsive drug release from MSNP4, DMF and water suspensions of MSNP4 nanoparticles were irradiated with red light from Red 670 Device (RedLightMan) (λ_{em} = 661 ± 10 nm; irradiance = 70 mW·cm^{-2}) at increasing light doses. After irradiation, the released DOX from MSNP4 was isolated by centrifugation (20 min, 28,000 rpm). The concentration of DOX from the supernatant was studied by fluorescence (λ_{exc} = 475 nm). MSNP4 nanoparticles were also incubated in darkness (negative control). For control experiment, MSNP6 was assessed by the same procedure.

5.3.8 Cell Lines and Culture Conditions

In vitro studies were performed using AsPC-1 (human pancreatic adenocarcinoma) and MIA PaCa-2 (human pancreas carcinoma) cell lines. Both are adherent and grow in monolayer up to confluence after seeding. AsPC-1 cells were cultured in RPMI 1640 medium supplemented with 10% (v/v) FBS, 1% (v/v) *L*-Glutamine and 1% (v/v) Streptomycin-Penicillin. MIA PaCa-2 cells were cultured in Dulbecco's Modified Eagle's Medium (DMEM) (High Glucose) supplemented with 10% (v/v) FBS, 1% (v/v) *L*-Glutamine, 1% (v/v) Streptomycin-Penicillin. Both cell lines were seeded in T-75 flask and were maintained at 37 ºC in an incubator containing 5% CO_2.

5.3.9 Cellular Uptake Assays

5.3.9.1 Quantitative

A quantity of 12,000 cells were seeded in black 96-well plates and incubated at 37 ºC (5% CO_2) for 24 h to achieve 80% confluence (for 96-well plates, the working volume is 100 µL). Then, the culture medium was removed and the suspended MSNPs in complete culture medium were added. FITC-labeled ZnPcSMP nanoparticles with and without Cetuximab were employed at 1 µM FITC. After the corresponding incubation times at 37 ºC, the suspensions were removed, the wells were washed 3 times with PBS. Then, 100 µL of SDS (2%) were added and incubated for 30 min more at 37 ºC. Afterwards, the plates were shaken and FITC fluorescence was read in a Synergy H1 Hybrid microplate reader (BioTek Instruments, Inc., Winooski, VT, USA) (λ_{exc} = 440 nm; λ_{em} = 520 nm). The BCA protein kit (Micro BCA™ Protein Assay Kit from Thermo Scientific™) was used for protein correlation after reading the FITC fluorescence. Thus, 50 µL from each well was transferred to a clear 96 well plate. 50 µL of

the BCA working reagent was added to each well. The plates were shaken for 30 secs and incubated at 37 ºC for 1 h. After, the plates were cooled to RT and the absorbance of each well was measured at 562 nm with the microplate reader. The amount of protein was calculated by using a standard curve of BSA in the same conditions. Then, the fluorescence of the wells was divided with their correlated BSA concentration. Thus, the cellular uptake of nanoparticles was determined as FITC fluorescence / protein amount (µg).

5.3.9.2 Qualitative

A quantity of 100,000 AsPC-1 cells and 80,000 MIA PaCa-2 cells were seeded in glass cover-slips (keeping them in 12-well plates) and incubated at 37 ºC (5% CO_2) for 24 h to achieve 80% confluence. Then, the culture medium was removed and the suspended MSNPs in complete culture medium were added. FITC-labeled ZnPcSMP nanoparticles (MSNP**A**-FITC) with and without Cetuximab were employed at 1 µM FITC. After the corresponding incubation times at 37 ºC, the suspensions were removed and the wells were washed 3 times with PBS. Then, cells were incubated at 37 ºC with complete medium with Hoechst (1 mg/mL stock was diluted 1:5,000 in PBS) for 60 min. Afterwards, washes with PBS were performed and cells were fixed adding 400 µL of 4% paraformaldehyde (pH = 7.4) for 30 min. Next, the suspensions were removed and washed 2 times with PBS. Then, the cover-slips were transferred to glass microscope slides adding a drop of Fluoromount solution (Fluoromount™ Aqueous Mounting Medium) and allowing to dry for 30 min. Intracellular fluorescence of FITC was observed by confocal microscope with excitation at 488 nm and false-imaged as green. Hoechst was excited at 405 nm and false-imaged as blue. For all the samples, the same measuring conditions were used.

5.3.10 In vitro Dark and Phototoxicity Assays

A quantity of 12,000 and 10,000 AsPC-1 and MIA PaCa-2 cells respectively were seeded in 96-well plates and incubated at 37 ºC (5% CO_2) for 24 h to achieve 80% confluence. Then, the culture medium was removed and the compounds in complete culture medium were added. The nanoparticles were diluted in supplemented medium to achieve a ZnPcSMP concentration of 2 µM. Cells without any treatment were taken as controls. Cells were incubated in darkness at 37 ºC for 24 h. Afterwards, the suspensions were removed, the wells were washed 3 times with PBS and then supplemented medium was added. Light-treated plates were irradiated with 30 or 60 $J \cdot cm^{-2}$. Dark controls were in darkness during irradiation time. For phototoxicity studies, the red light from Red 670 Device (RedLightMan) (λ_{em} = 661 ± 10 nm; irradiance = 70 $mW \cdot cm^{-2}$ was used). After irradiation, all the plates were incubated at 37 ºC for 24 h. Next, the medium was removed and the cell viability was determined by 3-

(4,5-dimethylthiazol-2-yl)-2,5-diphenyltetrazolium bromide (MTT) assay. Concisely, remaining cells were incubated with 0.1 mg/mL MTT in complete medium for 3 h. Then, medium was discarded and the purple crystals were solubilized with DMSO. Formazan concentration was determined by absorption at λ = 562 nm. Absorbance was recorded in the microplate reader. Cell viability was calculated as the ratio between the absorbance of treated cells and that of non-treated cells.

5.4 Conclusions

The most relevant conclusions drawn from this subchapter are the following:

I. The tri-cationic phthalocyanine ZnPcSMP is strongly aggregated when it is covalently attached to mesoporous silica nanoparticles, even in organic media, and thus, its photosensitizing ability is remarkably quenched.

II. Doxorubicin can be effectively released from mesoporous silica nanoparticles by singlet oxygen-mediated cleavage of its linker in a light-dose dependent manner. However, the prepared nanoparticles do not generate singlet oxygen enough to induce the photo-responsive release.

III. Conjugation of Cetuximab antibody to the PEG-coated mesoporous silica nanoparticles improves the aqueous dispersibility of the nanocarrier and enables its internalization in EGFR-expressing cells according to their expression level of this receptor. As incremented the incubation time of the targeted-nanoparticles in cells, the uptake is increased.

IV. Despite free ZnPcSMP is phototoxic against AsPC-1 cells, the prepared nanoparticles at the same ZnPcSMP concentration do not show photodynamic activity. When ZnPcSMP is attached to mesoporous silica nanoparticles, it loses its phototoxic effect due to the low generation of $^1O_2$.

SUBCHAPTER 5B: IRDye700DX as Photosensitizer

5.5 Introduction

The results obtained in Subchapter 5A demonstrated that ZnPcSMP-bound MSNPs did not generate $^1O_2$ with a good yield due to the formation of aggregates when the photosensitizer is covalently attached to the MSNP. Therefore, in the present Subchapter 5B, the photosensitizer is changed in order to increase the production of $^1O_2$ from the MSNPs and thus, exert the photoresponsive release of DOX and achieve phototoxicity *in vitro*.

The photosensitizer of choice is IRDye700DX, a commercially available phthalocyanine. IRDye700DX has great hydrophilic properties thanks to the nature of its axial substituents that avoid its aggregation even in water.

5.6 Results and Discussion

5.6.1 Synthesis and Derivatization of Mesoporous Silica Nanoparticles

Four types of MSNPs were prepared. Table 14 summarizes the grafting elements of each synthesized MSNP formulation. In the present section, the synthesis and derivatization of each one is explained.

Table 14. Composition of each synthesized MSNP formulation.

Formulation	IRDye700DX	DOX	PEG	Cet
MSNP**D**	✓	✗	✓	✗
MSNP**D**-Cet	✓	✗	✓	✓
MSNP**E**	✓	✓, by means of a $^1O_2$-cleavable linker	✓	✗
MSNP**E**-Cet	✓	✓, by means of a $^1O_2$-cleavable linker	✓	✓

5.6.1.1 MSNPD IRDye700DX – Cetuximab – MSNP

The preparation of mesoporous silica nanoparticles with the photosensitizer IRDye700DX and the antibody Cetuximab both covalently attached (MSNP**D**-Cet) was carried out in three synthetic steps (Figure 60):

i. Modification of the surface of blank MSNPs with amino groups (MSNP7). High amount of APTES was employed in the reaction to ensure a high degree of

surface's derivatization.

ii. Attachment of IRDye700DX-NHS to MSNP7 nanoparticles *via* *N*-acylation (MSNP8). The NHS group from IRDye700DX reacted with an amino group on surface of MSNP joining the IRDye700DX to the MSNP.

iii. Anchoring of PEG-Cetuximab (compound **10**) *via* *N*-acylation to MSNP8 nanoparticles. The activated carboxyl of PEG reacted with an amino group on surface of MSNP. Contrary to the previous steps, the final product of this reaction was not washed since the resuspension of the pellet required harsh sonication and this is not recommended when working with antibodies.

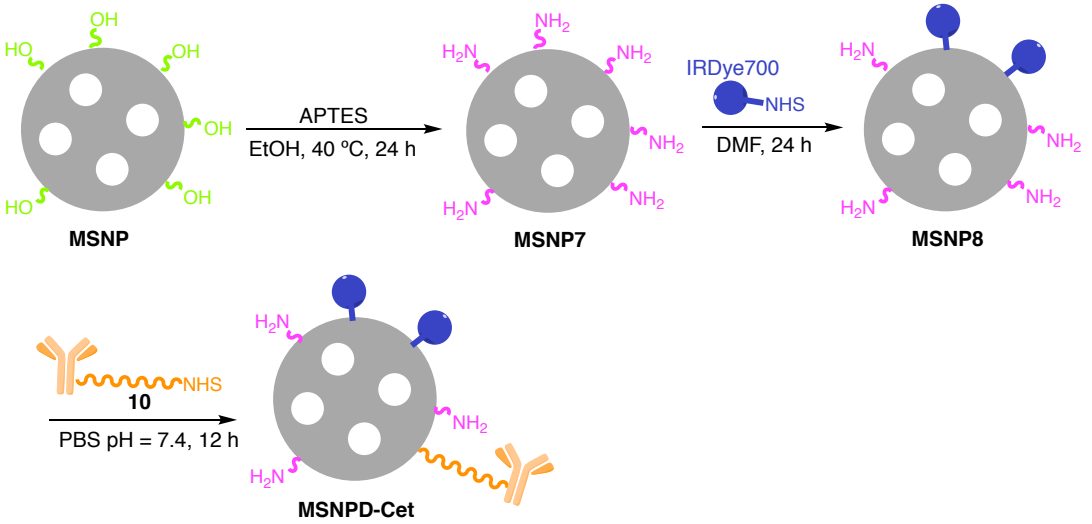

Figure 60. Preparation of the nanoparticle MSNP**D**-Cet.

The overall preparation scheme of the non-targeted analogous, MSNP**D**, is shown in Figure B12 in Appendix B. The synthetic route is the same as MSNP**D**-Cet except the last step, in which NHS-PEG-COOH is attached to the nanoparticles without its prior conjugation with Cetuximab.

5.6.1.2 MSNPE-Cet: IRDye700DX – Cetuximab – DOX (releasable by $^1O_2$) – MSNP

The preparation of mesoporous silica nanoparticles with the photosensitizer IRDye700DX and the antibody Cetuximab covalently attached, and the chemotherapeutic agent DOX covalently bound by means of the $^1O_2$-cleavable linker (MSNP**E**-Cet) was carried out in four steps (Figure 61):

i. Modification of the surface of blank MSNPs with amino groups (MSNP7).

ii. Attachment of IRDye700DX-NHS to MSNP7 nanoparticles *via* *N*-acylation

(MSNP8).

iii. Derivatization of MSNP8 nanoparticles with the conjugate **6** (between DOX and the $^1O_2$-cleavable linker) *via* *N*-acylation (MSNP9). The activated carboxyl of the conjugate **6** reacts with an amino group on surface of MSNP.

iv. Anchoring of PEG-Cetuximab (compound **10**) *via* *N*-acylation to MSNP9 nanoparticles (MSNP**E**-Cet).

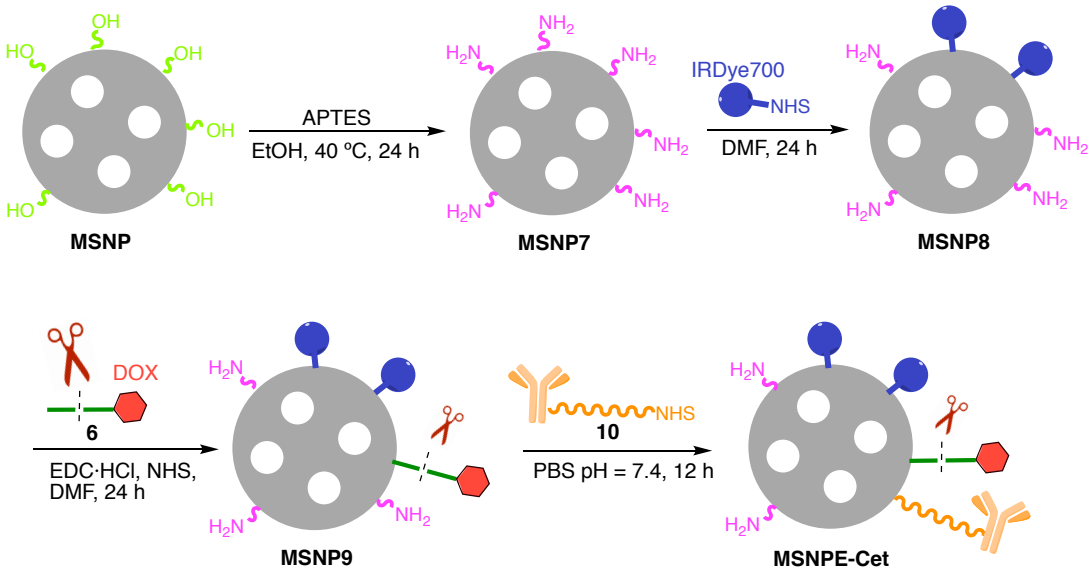

Figure 61. Preparation of the nanoparticle MSNP**E**-Cet.

The overall preparation scheme of the non-targeted analogous, MSNP**E**, is shown in Figure B13 in Appendix B.

5.6.2 *Physicochemical Characterization of Nanoparticles*

The prepared mesoporous silica nanoparticles were characterized in terms of their physicochemical properties: size, polydispersity index (PdI), zeta-potential and concentration of the photosensitizer IRDye700DX and the chemotherapeutic agent DOX (Table 15).

On the one hand, size, polydispersity and zeta-potential were measured by dynamic light scattering (DLS). After each preparation step, an increase in their size and changes in zeta-potential were shown. These changes are a good indication that the reactions in the nanoparticles had been successfully accomplished.

Table 15. Characterization of nanoparticles. PdI: polydispersity index. EE: entrapment efficiency.

	NP formulation	Size / nm	PdI	Zeta-potential / mV	[IRDye700DX] / μM	[Dox] /μM	EE
	Blank	165 ± 3	0.07 ± 0.04	-22 ±1	-	-	-
With IRDye700DX and without DOX	MSNP7	165 ± 1	0.03 ± 0.03	6 ± 1	-	-	-
	MSNP8	172 ± 2	0.13 ± 0.02	6 ± 1	9.2	-	100%
	MSNP**D**	243 ± 4	0.11 ± 0.09	10 ± 1	"	-	-
	MSNP**D**-Cet	410 ± 38	0.95 ± 0.10	-	"	-	-
With IRDye700DX and with releasable DOX	MSNP9	196 ± 3	0.10 ± 0.05	8 ± 1	"	18.7 21.7 134.4	68% 59% 29%
	MSNP**E**	255 ± 6	0.12 ± 0.04	6 ± 1	"	"	-
	MSNP**E**-Cet	430 ± 52	0.89 ± 0.04	-	"	"	-

The average size of MSNP**D**-Cet and MSNP**E**-Cet in aqueous suspension was found to be ~410 nm, and ~430 nm respectively. These values are pretty higher compared to their analogs without antibody (~243 nm MSNP**D** and ~255 nm MSNP**E**) due to, firstly, the attachment of a bulky element as an antibody, and, secondly, due to the different solvent employed to suspend them. The Cetuximab-nanoparticles were measured in water since the antibody disrupts in organic media; MSNPs tend to aggregate in aqueous suspension. Contrarily, the non-Cetuximab-nanoparticles were measured in ethanol, a solvent in which nanoparticles are non-aggregated and thus smaller.

The polydispersity index of the prepared formulations was smaller than 0.3 in all the non-Cetuximab-nanoparticles, demonstrating a homogeneous distribution. However, for the Cetuximab-nanoparticles, this value was higher, surely due to the two reasons mentioned above.

The zeta-potential of the nanoparticles was changing depending on the moiety introduced. The preparation of MSNP7 showed a huge increase in the zeta-potential compared to blank MSNP, due to the introduction of amino groups in the surface of MSNPs.

On the other hand, the IRDye700DX and DOX concentrations in the MSNP suspensions were calculated as the difference between the incorporated amount and the amount present in the washing supernatants. Firstly, the photosensitizer concentration in the washing supernatants was negligible (Figure 62). Thereby, the drug attachment of IRDye700DX was 100%, since all the IRDye700DX was satisfactory attached to MSNPs.

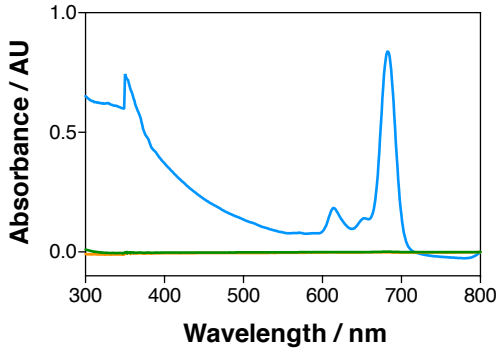

Figure 62. Absorption spectra in DMF of MSNP8 nanoparticles (in blue) and the supernatant washes of MSNP8 (in green and orange). Negligible absorption was shown for both supernatants.

Secondly, MSNP9 nanoparticles with different concentration of DOX were prepared. As shown in

Figure 63, with low concentration of DOX in the MSNP formulation, the MSNP suspension turned out to be purple; with high concentration of DOX, it was orange. The entrapment efficiency of compound **6** decreases as increases its amount as reactant.

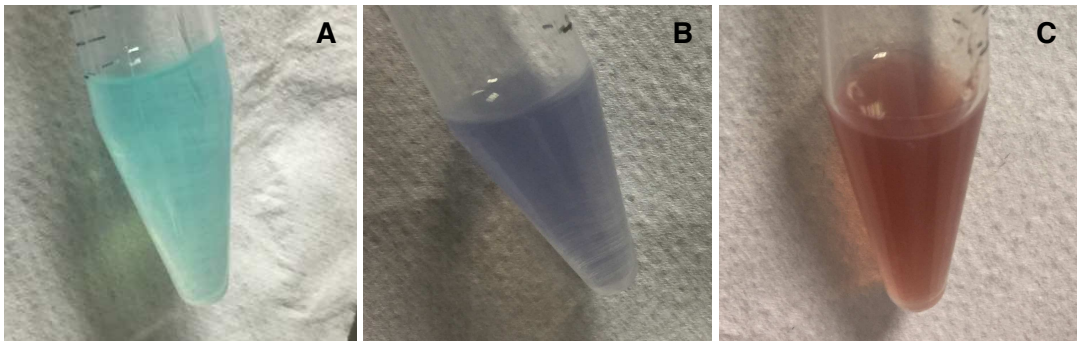

Figure 63. MSNP8 (A), MSNP9 18 μM (B) and MSNP9 134 μM (C) nanoparticles suspensions in DMF.

5.6.3 *Photophysical Characterization of Nanoparticles*

The Photophysical behavior of free IRDye700DX and the synthesized nanoparticles were studied by UV-Vis, steady-state fluorescence spectroscopy and time-resolved phosphorescence at 1275 nm to study the production of singlet oxygen.

5.6.3.1 Absorption and Steady-State Fluorescence

5.6.3.1.1 Free IRDye700DX

UV-Vis and emission spectra of IRDye700DX were recorded in DMF, MeOH and purified

water (Figure 64). In contrast with the absorption spectra of ZnPcSMP seen in the previous subchapter 5A, here the monomeric form of IRDye700DX was evidenced in all the employed solvents since sharp Q-band peaking at ~690 nm and the B-band transition were shown. The absorption and emission photophysical parameters studied are summarized in Table 16.

Table 16. Absorption and emission photophysical properties of IRDye700DX in DMF, MeOH and water. *IRDye700DX absorption coefficient data in MeOH and water are extracted from literature.[239]

Solvent	λ_{abs} / nm ($\log_{10}\varepsilon$)	λ_{em} / nm
DMF	684 (5.57)	691
MeOH	680 (5.32)*	686
H_2O	689 (5.22)*	696

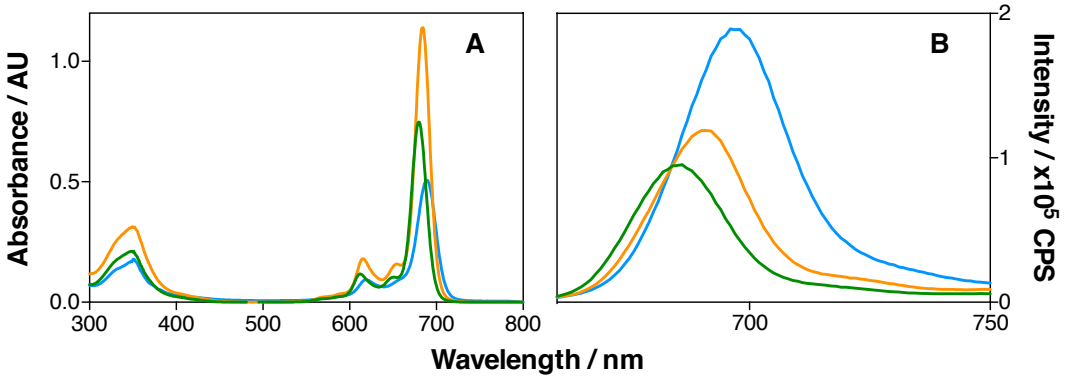

Figure 64. Absorption (A) and emission spectra (B) of IRDye700DX in DMF (orange line), MeOH (green line) or in purified water (blue line). Same IRDye700DX concentration in all the measurements. λ_{exc} = 610 nm.

5.6.3.1.2 Nanoparticles

On the one hand, the UV-Vis spectra of MSNP8, MSNP9 (18 μM DOX) and MSNP9 (134 μM DOX) nanoparticles dispersed in ethanol were recorded (Figure 65A). In the spectra, the near-infrared region band (693 nm) corresponding to IRDye700DX is shown for all the prepared MSNP formulations, demonstrating the successful conjugation of IRDye700DX to the nanoparticles. Unlike happened with ZnPcSMP, absorption spectra of the prepared MSNPs showed that IRDye700DX was not aggregated when it was covalently attached to the nanoparticles. In addition, MSNP9 showed a broad peak centered at 483 nm, which evidences the presence of DOX in the nanoparticle formulation.

Likewise, the absorption spectra of MSNP**D**-Cet, MSNP**E**-Cet (18 μM DOX) and MSNP**E**-Cet (134 μM DOX) nanoparticles in dPBS were acquired (Figure 65B). The conjugation of the compound **10** (PEG-Cetuximab) did not alter the presence of IRDye700DX and DOX in the

nanoparticles, since their peaks (centered at 690 nm and ~480 nm respectively) were still shown. However, IRDye700DX seemed to be more aggregated than when the MSNPs were suspended in ethanol, probably due to the aggregation of the MSNPs in aqueous medium. The existence of the Cetuximab in these nanoparticle formulations was evidenced by the peak at ~280 nm due to the tryptophan molecules of the protein. An increase in scattering was shown in dPBS for MSNP**E**-Cet in comparison with MSNP**D**-Cet. The nanoparticles with the highest concentration of DOX showed the most scattered spectrum.

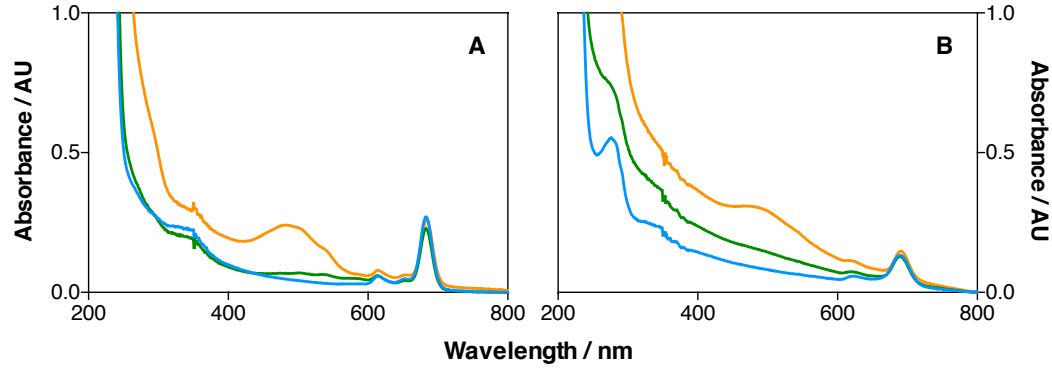

Figure 65. A) Absorption spectra in EtOH of MSNP8 (blue), MSNP9 (18 μM of DOX) (green) and MSNP9 (134 μM of DOX) (orange). B) Absorption spectra in dPBS of MSNP**D**-Cet (blue), MSNP**E**-Cet (18 μM of DOX) (green) and MSNP**E**-Cet (134 μM of DOX) (orange).

On the other hand, the emission spectra of MSNP8 and MSNP9 (134 μM DOX) nanoparticles in ethanol were recorded. The presence of DOX in MSNP9 nanoparticles was also proved by its emission after excitation at 475 nm (Figure 66A). As expected, MSNP8 did not exhibit DOX fluorescence. Despite both formulations had matched concentrations of IRDye700DX, the emission intensity of the photosensitizer is higher for MSNP8 than MSNP9 (Figure 66B). Therefore, the emission of IRDye700DX in MSNP9 nanoparticle formulation is considerably quenched.

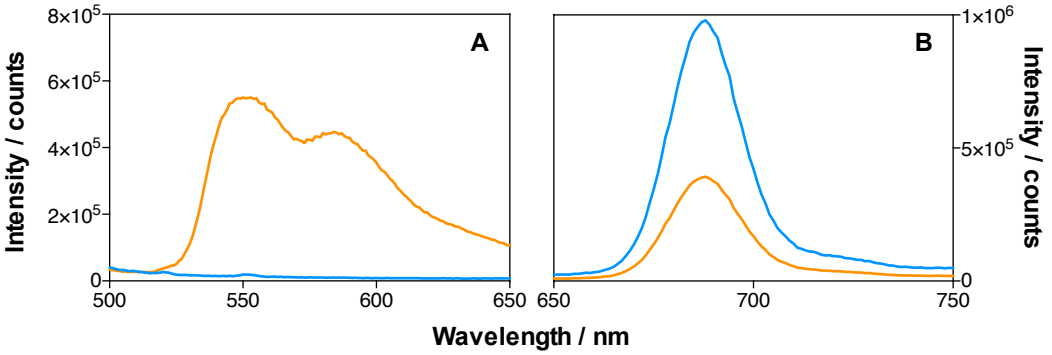

Figure 66. Emission spectra in EtOH of MSNP8 (blue) and MSNP9 (134 μM of DOX) (orange). Same concentration of IRDye700DX in all the MSNP formulations. A) λ_{exc} = 475 nm. B) λ_{exc} = 610 nm.

Furthermore, the emission spectra of MSNP**D**-Cet, MSNP**E**-Cet (18 μM DOX) and MSNP**E**-Cet (134 μM DOX) nanoparticles in dPBS were also recorded. All of the MSNP formulations had the same concentration of IRDye700DX, however, their emission spectra showed lesser emission intensity of IRDye700DX (peak centered at 696 nm) when the concentration of DOX in the formulation increases (Figure 67B). In addition, DOX emission intensity also decreases in MSNP**E**-Cet (134 μM DOX) compared with the lesser concentrated one (Figure 67A).

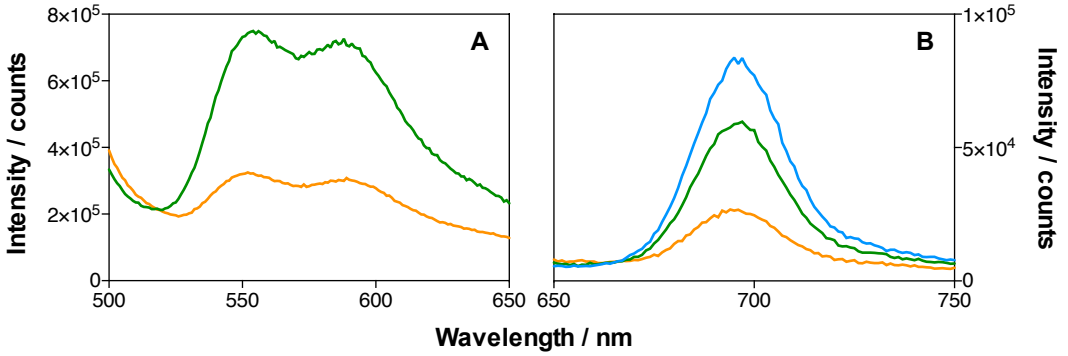

Figure 67. Emission spectra in dPBS of MSNP**D**-Cet (blue), MSNP**E**-Cet (18 μM of DOX) (green) and MSNP**E**-Cet (134 μM of DOX) (orange). Same concentration of IRDye700DX in all the MSNP formulations. A) λ_{exc} = 475 nm. B) λ_{exc} = 610 nm.

5.6.3.2 Singlet Oxygen Generation

5.6.3.2.1 MSNP8 and MSNP9 nanoparticles

Time-resolved NIR phosphorescence detection studies demonstrated the generation of singlet oxygen by MSNP8 and MSNP9, precursor nanoparticles of MSNP**D**-Cet and MSNP**E**-Cet (Figure 68). In this study, $^1O_2$ formation and decay were monitored by time-resolved detection of their phosphorescence at 1275 nm after excitation at 660 nm. Ethanolic suspensions of MSNP8 and MSNP9 nanoparticles showed a monoexponential short rise and decay. The decay presented a lifetime of ~14 μs, which corresponds to $^1O_2$ lifetime (τ_Δ) and is a typical value for this parameter in ethanol (Table 17). The rise showed a lifetime of ~1 μs, corresponding to excited triplet state lifetime (τ_T). No remarkable differences were shown for the kinetic values of MSNP8, MSNP9 (18 μM DOX) and MSNP9 (134 μM DOX) nanoparticles in ethanol. However, MSNP8 nanoparticles showed more $^1O_2$ generation than MSNP9 perhaps their IRDye700DX concentrations were matched. This fact is consistent with the minor photoactivity of MSNP9 nanoparticles in the emission studies. Comparing the amplitudes of singlet oxygen lifetimes, both MSNP9 formulations decreased the production of $^1O_2$ by ~50% in comparison with MSNP8 nanoparticles, despite of the different concentration of DOX in the MSNP9 formulations. Therefore, the conjugation of DOX by

means of the $^1O_2$-cleavable linker decreases the production of $^1O_2$.

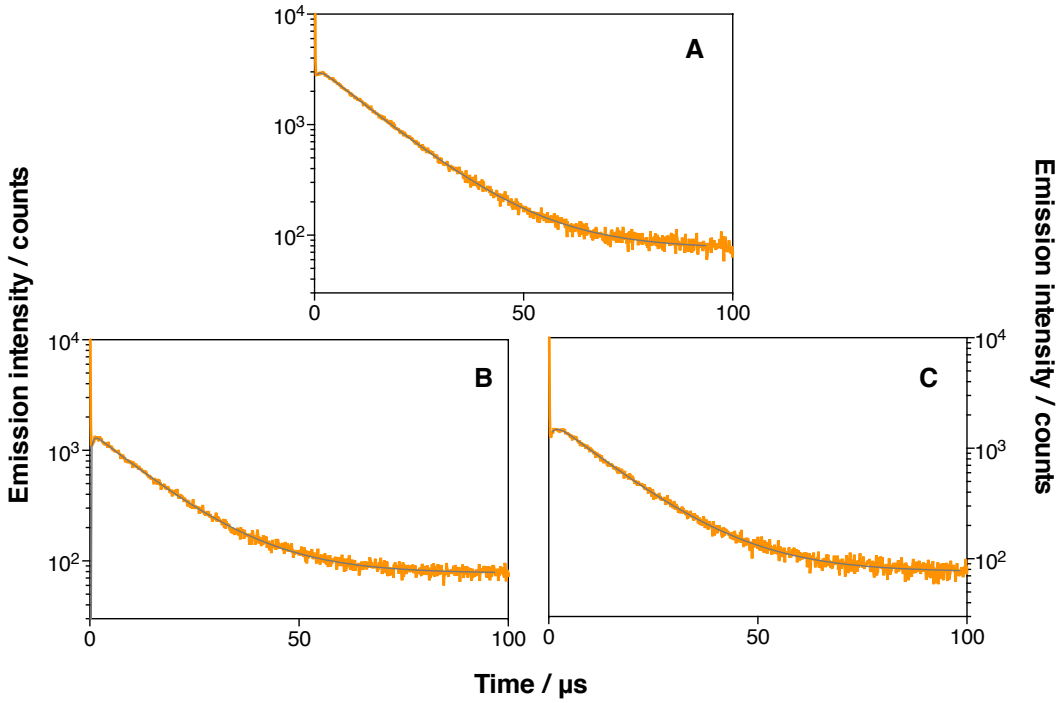

Figure 68. Time-resolved phosphorescence decays of free MSNP8 (A), MSNP9 (18 µM DOX) (B) and MSNP9 (134 µM DOX) (C) in EtOH. λ_{em} = 1275 nm. λ_{exc} = 660 nm.

Table 17. Singlet oxygen kinetic values of MSNP8, MSNP9 (18 µM DOX) and MSNP9 (134 µM DOX) suspensions in EtOH. A: amplitude.

Sample	τ_T / µs	A_T	τ_Δ / µs	A_Δ
MSNP8	1.0	-468	14.2	3236
MSNP9 (18 µM of DOX)	0.9	-359	14.0	1558
MSNP9 (134 µM of DOX)	1.2	-333	14.5	1664

5.6.3.2.2 MSNPD-Cet and MSNPE-Cet nanoparticles

The generation of singlet oxygen by MSNP**D**-Cet and MSNP**E**-Cet nanoparticles suspended in dPBS was investigated (Figure 69). For all the samples studied, a monoexponential short rise and decay were shown, the kinetic values are summarized in Table 18. Firstly, free IRDye700DX in dPBS presented a τ_Δ of 64 µs, which is a typical value for this parameter in this deuterated solvent; and the τ_T was 2.6 µs. Secondly, MSNP**D**-Cet nanoparticles suspended in dPBS showed a decrease in its τ_Δ (54.7 µs) and increase in τ_T (7.2 µs) in comparison with free IRDye700DX. Secondly, MSNP**E**-Cet (18 µM DOX) presented a similar value of τ_Δ (53.6 µs) as MSNP**D**-Cet, however, its τ_T decreased (2.9 µs) compared with the

non-Doxorubicin MSNP. Lastly, MSNP**E**-Cet (134 μM DOX) exhibited the lowest lifetimes (τ_Δ: 42.5 μs and τ_T: 0.3 μs). Furthermore, despite all the MSNPs studied here had the same concentration of IRDye700DX, the generation of singlet oxygen by MSNP**D**-Cet is much higher than MSNP**E**-Cet, as seen for MSNP8 and MSNP9 nanoparticles in ethanol. However, in this case, as higher the concentration of DOX in the nanoparticles formulation, more remarkable are the changes in $^1O_2$ generation and its kinetic parameters, unlike in ethanol. An aggregation phenomenon of MSNP**E**-Cet in dPBS could give a possible explanation for these differences.

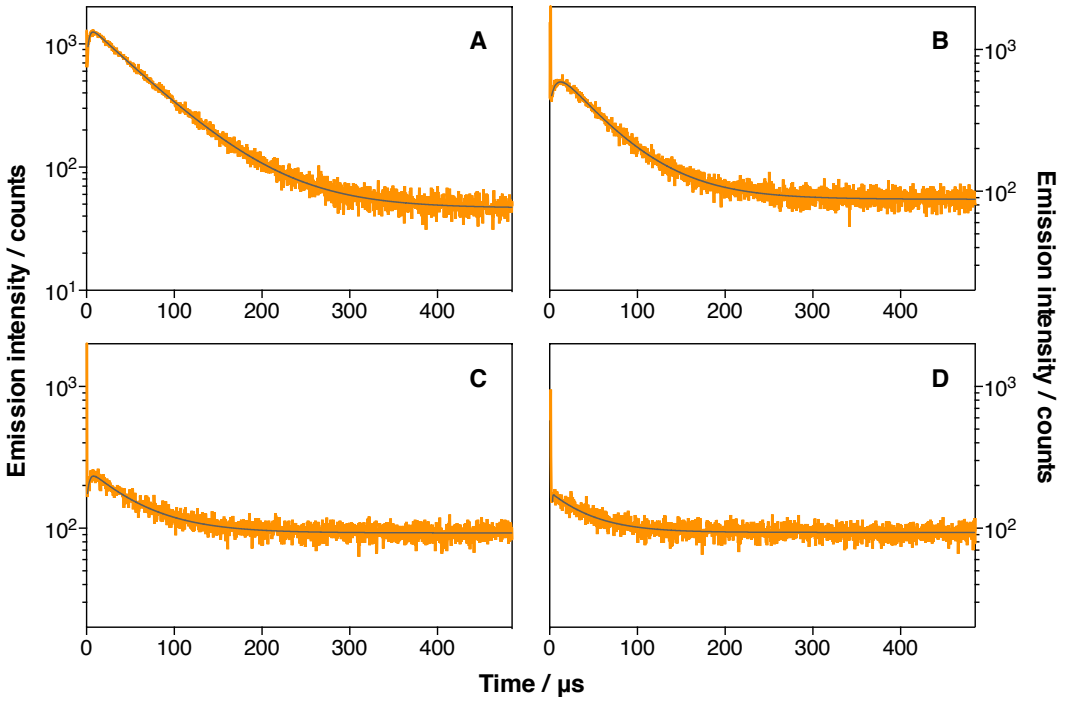

Figure 69. Time-resolved phosphorescence decays of free IRDye700DX (A), MSNP**D**-Cet (B), MSNP**E**-Cet (18 μM DOX) (C) and MSNP**E**-Cet (134 μM DOX) (D) in dPBS. λ_{em} = 1275 nm. λ_{exc} = 660 nm.

Table 18. Singlet oxygen kinetic values of IRDye700DX, MSNP**D**-Cet, MSNP**E**-Cet (18 μM DOX) and MSNP**E**-Cet (134 μM DOX) suspensions in dPBS.

Sample	τ_T / μs	A_T	τ_Δ / μs	A_Δ
IRDye700DX	2.6	-468	63.8	1372
MSNP**D**-Cet	7.2	-313	54.7	698
MSNP**E**-Cet (18 μM of DOX)	2.9	-85	53.6	169
MSNP**E**-Cet (134 μM of DOX)	0.3	-20	42.5	81

In order to study a possible aggregation effect in the targeted nanoparticles in dPBS, the phosphorescence at 1275 nm of MSNP**D**-Cet and MSNP**E**-Cet were recorded in DMF, solvent in which MSNPs do not aggregate (Figure 70). As shown in Table 19, no significant

differences in lifetimes were shown for MSNP**D**-Cet and MSNP**E**-Cet. Therefore, all the changes in lifetimes showed in dPBS were due to the aggregation of MSNP**E**-Cet. As more compound **6** in the nanoparticle formulation, i.e. more DOX attached by means of the $^1O_2$-cleavable linker, their tendency to aggregate in aqueous media is higher, so the lifetimes are reduced. This fact is coherent with the more scattering showed in the absorbance spectra as higher was the content of DOX in the MSNP formulation. In addition, emission spectra showed a decrease in fluorescence when more DOX was present in the MSNPs, which could be due to the aggregation of the MSNPs in water.

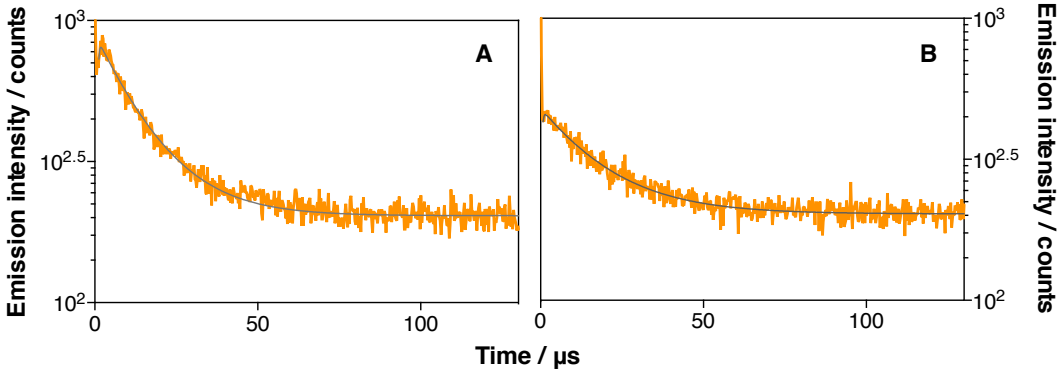

Figure 70. Time-resolved phosphorescence decays of MSNP**D**-Cet (A) and MSNP**E**-Cet (134 µM DOX) (B) in DMF. λ_{em} = 1275 nm. λ_{exc} = 660 nm.

Table 19. Singlet oxygen kinetic values of MSNP**D**-Cet and MSNP**E**-Cet (134 µM DOX) suspensions in DMF.

Sample	τ_T / µs	A_T	τ_Δ / µs	A_Δ
MSNP**D**-Cet	0.23	-110	17.5	635
MSNP**E**-Cet (134 µM of DOX)	0.29	-39	18.3	267

Nevertheless, although the aggregation of the nanoparticles in water explains the differences in lifetimes shown in dPBS for MSNP**D**-Cet and MSNP**E**-Cet formulations, this phenomenon cannot answer the differences in $^1O_2$ production between the nanoparticles with and without DOX in the organic solvent.

5.6.3.2.3 Far-away-Doxorubicin Nanoparticles

It had been demonstrated that the generation of $^1O_2$ was remarkably decreased when DOX was attached to the MSNP through the $^1O_2$-clevable linker. However, the reason of this fact was unclear. At this point, we wondered if DOX was quenching the photoactivity of IRDye700DX. In order to clarify what was happening, a novel MSNP formulation was synthesized with IRDye700DX covalently attached to the MSNP as usual, but with the DOX covalently bound to the nanoparticle by means of a large PEG (the scheme and synthesis of

this new MSNP formulation is shown in Figure B15 in Appendix B). By moving the DOX away from the IRDye700DX, it was possible to find out if there was indeed a quenching between both molecules.

The generation of $^1O_2$ was monitored for ethanolic suspensions of MSNP8, MSNP9 and the new MSNP formulation with the DOX far away (MSNP10) (Figure 71 and Table 20). To be able to compare, all the MSNP suspensions had the same concentration of nanoparticles and IRDye700DX. MSNP9 and MSNP10 had also very similar concentration of DOX (MSNP10 a bit less concentrated).

The results again evidenced that MSNP8 produces much more $^1O_2$. However, the production of this species is very similar for both DOX-MSNP formulations, despite the distance of the DOX from the nanocarrier and thus, from the IRDye700DX. This fact would seem to indicate that it is not the DOX or the cleavable linker that reduces the $^1O_2$ production, but rather the fact of decorating the nanoparticle.

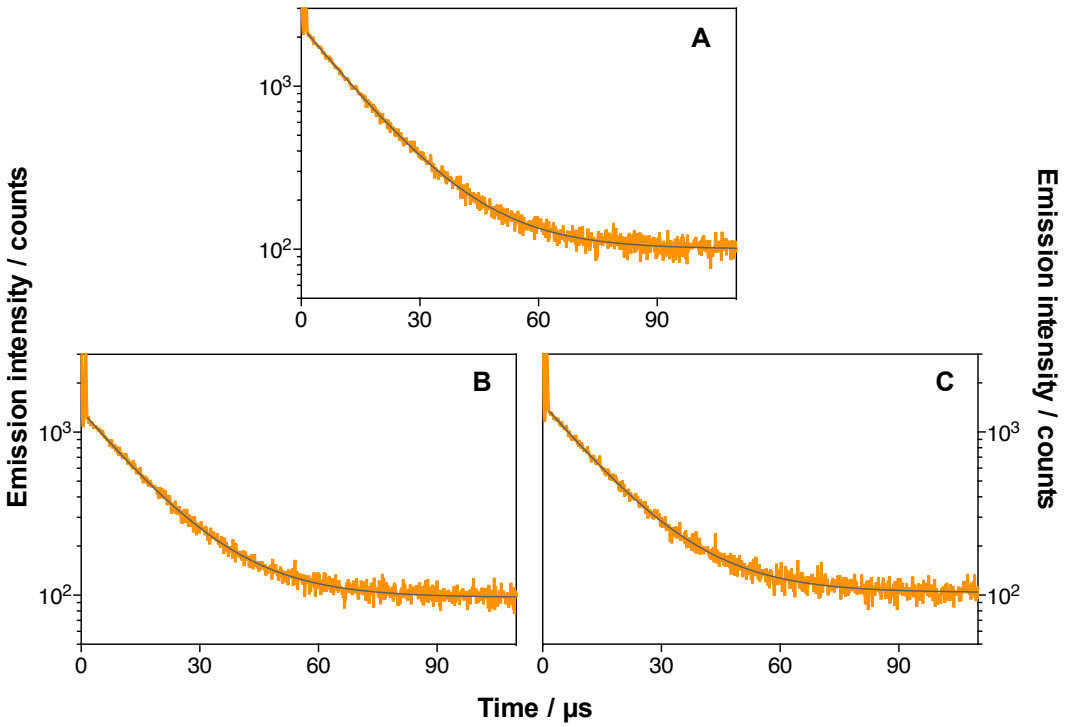

Figure 71. Time-resolved phosphorescence decays of MSNP8 (A), MSNP9 (B) and MSNP10 (C) in EtOH. Same concentration of nanoparticles and IRDye700DX. λ_{em} = 1275 nm. λ_{exc} = 660 nm.

Table 20. Singlet oxygen kinetic values of MSNP8, MSNP9 and MSNP10 suspensions in EtOH.

Sample	τ_Δ / μs	A_Δ
MSNP8	14.4	2014
MSNP9	14.6	1129
MSNP10	14.6	1232

5.6.3.3 Photo-responsive Doxorubicin Release

In Section 5.2.3.5, the ability of the $^1O_2$-cleavable linker to release its DOX attached upon light in the presence of a good photosensitizer was probed. Here, the photorelease of DOX was tested for the MSNP**E**-Cet nanoparticles. Both MSNP**E**-Cet (18 μM and 134 μM of DOX) nanoparticles suspended in PBS were irradiated with 30 J·cm^{-2} red light (the light dose used for the biological studies). After irradiation, nanoparticles were centrifuged and the emission spectra of the supernatants were recorded. DOX was detected in the supernatant of both nanoparticle formulations, thereby, the photorelease of DOX was demonstrated (Figure 72).

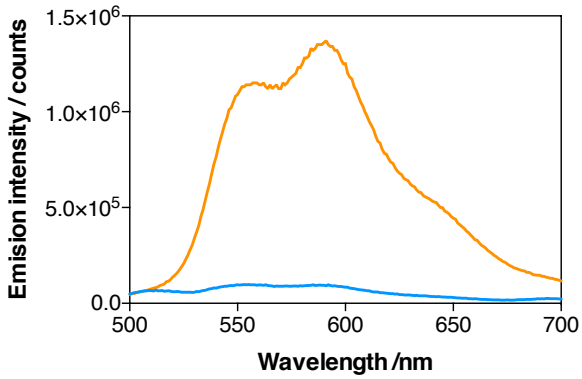

Figure 72. Emission spectra in PBS of MSNP**E**-Cet (18 μM of DOX) (in blue) and MSNP**E**-Cet (134 μM of DOX) (in orange). λ_{exc} = 475 nm.

In order to investigate the concentration of DOX released, their emission was interpolated in a fluorescence calibration curve of DOX in the same experimental conditions. The percentages of DOX photoreleased in respect of the total DOX attached to the MSNP**E**-Cet nanoparticles were 2% for MSNP**E**-Cet (18 μM of DOX) and 12% for MSNP**E**-Cet (134 μM of DOX). As the concentration of DOX in the formulation is increased, more DOX is liberated although the production of $^1O_2$ is more affected by the aggregation phenomena. This fact could be rationalized considering that in the same range of action, $^1O_2$ finds more molecules to cleave in MSNP**E**-Cet with 134 μM of DOX than with 18 μM.

5.6.3.3.1 Effect of DOX release on singlet oxygen generation

Once the successful cleavage and release of DOX from nanoparticles upon irradiation was demonstrated, the following step was the investigation of the behavior of MSNP9 nanoparticles when they were treated with increasing light doses.

A suspension of MSNP9 nanoparticles in EtOH were irradiated at increasing red light doses (0, 15, 31, 46, 61, 77 and 92 J·cm^{-2}). After each irradiation treatment, the absorbance and emission spectra (λ_{exc} = 475 nm and λ_{exc} = 610 nm) were recorded, as well as the time-resolved phosphorescence at 1275 nm to study the $^1O_2$ generation and kinetics. Figure 73, Figure 74 and Table 21 summarize all the results obtained.

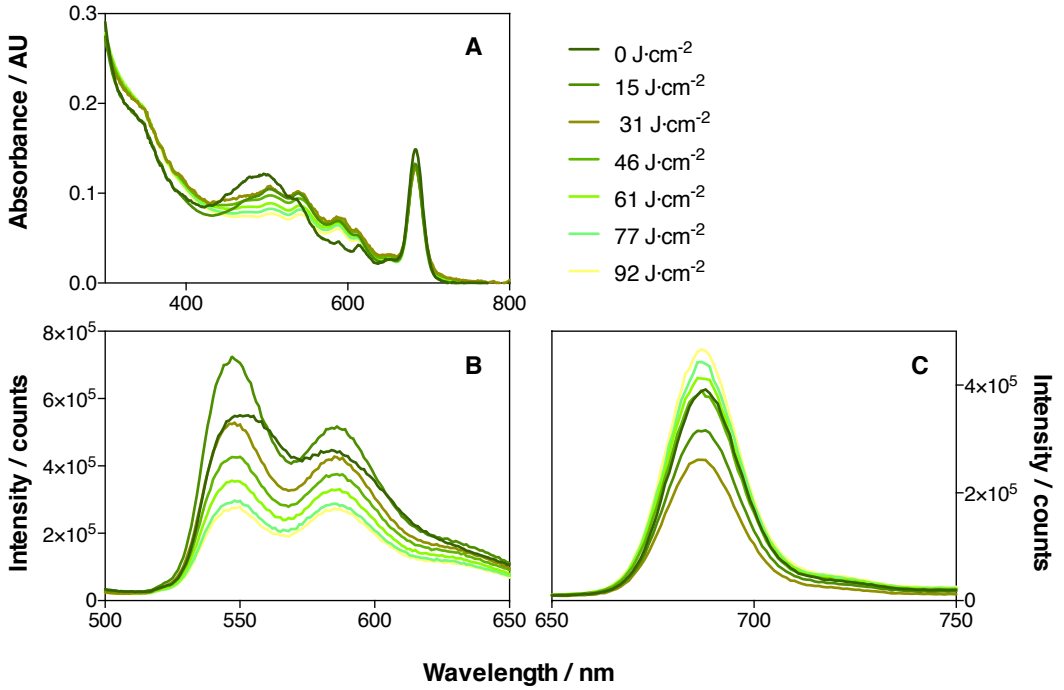

Figure 73. Absorption spectra in EtOH of MSNP9 after irradiation with 0, 15, 31, 46, 61, 77, 92 J·cm^{-2} light dose (A) and their emission spectra B) λ_{exc} = 475 nm and C) λ_{exc} = 610 nm.

Table 21. Singlet oxygen kinetic values of MSNP9 nanoparticles in EtOH after each irradiation treatment.

Sample	Light Dose / J·cm^{-2}	τ_Δ / μs	A_Δ
MSNP9	0	13.92	87
	15	13.90	66
	31	6.20	51
	46	6.37	84
	61	6.21	89
	77	6.49	100
	92	6.63	110

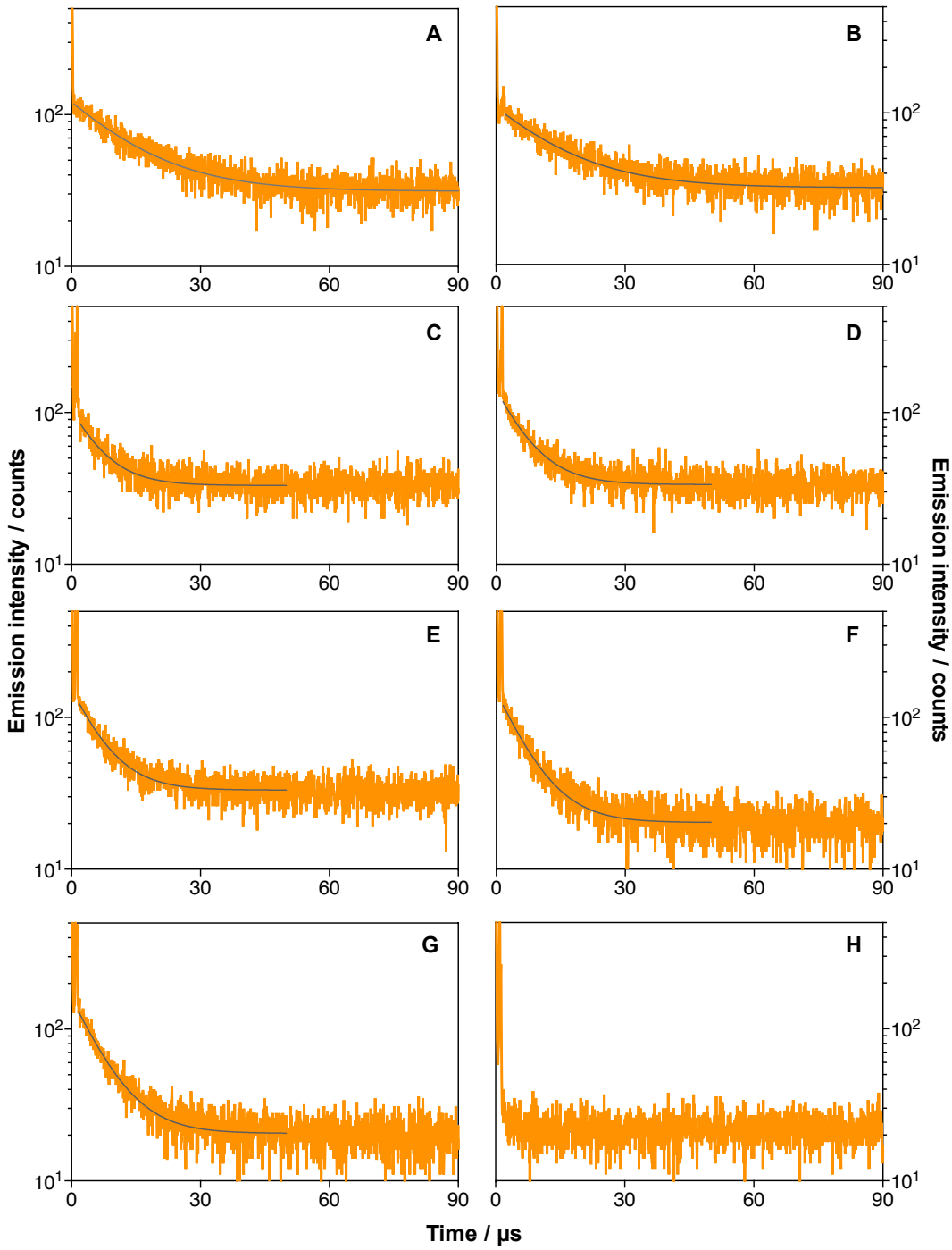

Figure 74. Time-resolved phosphorescence decays of MSNP9 nanoparticles in EtOH after irradiation treatment with A) 0 J·cm^{-2}, B) 15 J·cm^{-2}, C) 31 J·cm^{-2}, D) 46 J·cm^{-2}, E) 61 J·cm^{-2}, F) 77 J·cm^{-2} and G) 92 J·cm^{-2} at λ_{em} = 1275 nm. H) decay of MSNP9 nanoparticle in EtOH after 92 J·cm^{-2} treatment at λ_{em} = 1110 nm. All the samples were excited at 660 nm.

Firstly, after the irradiation with the lowest light dose (15 J·cm^{-2}), MSNP9 nanoparticles showed remarkable changes in their absorbance spectrum. The DOX bands in the absorption spectrum variated and new bands at ~500 – 650 nm raised. The emission intensity of DOX (λ_{exc} = 475 nm) was increased in comparison with the non-irradiated ones. In contrast, the emission intensity of IRDye700DX (λ_{exc} = 610 nm) was reduced, which is consistent with the lesser absorbance showed for its Q-band, surely due to the photobleaching phenomenon. Furthermore, the $^1O_2$ generation was also decreased and the $^1O_2$ lifetime was similar to that for 0 J·cm^{-2}, ~14 μs, a typical value of τ_Δ in EtOH.

Secondly, 31 J·cm^{-2} red light irradiation did not change the shape of the absorbance spectrum but the DOX bands (500-600 nm) showed higher absorbance than after 15 J·cm^{-2} light treatment. In contrast, the DOX emission intensity was reduced, as well as the IRDye700DX emission. The production of $^1O_2$ was reduced again. Nevertheless, τ_Δ was remarkably decreased to ~6 μs, which indicates than once $^1O_2$ is generated, some specie is arresting it.

Next, as the light dose increased, the absorbance was reduced as well as the DOX emission intensity. In contrast, IRDye700DX emission was intensifying. Moreover, the $^1O_2$ generation by nanoparticles was also increasing. The short $^1O_2$ lifetime value did not change significantly.

Therefore, despite IRDye700DX from nanoparticles was photodegrading as the light dose was increased, at light doses equal or greater than 31 J·cm^{-2}, its emission and $^1O_2$ production were intensifying. Above this light dose value, the photoactivity recovered by IRDye700DX was greater than that lost by photodegradation. This fact demonstrated that as DOX was releasing, IRDye700DX was recovering its fluorescence and $^1O_2$ generation. Nevertheless, the $^1O_2$-mediated cleavage of DOX seems to be quenching $^1O_2$, since τ_Δ was markedly reduced after 31 J·cm^{-2} of irradiation.

The previous experiment with the nanoparticles that had DOX far away from the surface evidenced that the loss of photoactivity by IRDye700DX is surely due to the decoration of the MSNP and not to quenching between DOX and IRDye700DX. These results are consistent with the evidences shown in the present study. As the moieties that graft the nanoparticle are released, IRDye700DX recovers its photoactivity.

5.6.4 Biological Studies

5.6.4.1 In vitro Uptake of MSNPD-Cet

5.6.4.1.1 Qualitative Uptake *via* Confocal Microscopy

In order to ascertain the targeting ability of Cetuximab-decorated nanoparticles, AsPC-1 and

MIA PaCa-2 cells were incubated with MSNP**D** and MSNP**D**-Cet at 2 μM of IRDye700DX for 24 h. After incubation, nanoparticles still present in the culture medium were removed by washing. The internalization of the nanoparticles was investigated by studying their fluorescence *via* confocal microscopy (λ_{exc} = 638 nm; λ_{em} = 650-700 nm).

As shown in Figure 75, AsPC-1 and MIA PaCa-2 cells showed an apparently cytosolic distribution of targeted-nanoparticles within the cells with a black background where cells were not present. In contrast, for non-targeted nanoparticles, all the background was shown red, so nanoparticles were everywhere in the sample. Confocal images demonstrated that non-Cetuximab nanoparticles were not internalized by the cells, instead of that, the silica nanoparticles were widely attached to the cover glass.

The huge difference in uptake between MSNP**D** and MSNP**D**-Cet can be rationalized by two factors: the ability of targeting and solubilize the nanoparticles by Cetuximab. First, Cetuximab allows the internalization of nanoparticles by receptor-mediated endocytosis; improving their capability to being internalized by the cells compared with the non-targeted ones, which can be internalized only by non-specific pathways. Second, the conjugation of Cetuximab remarkably improves the aqueous solubility of nanoparticles. MSNP**D** have a greater tendency to form aggregates of nanoparticles in water than MSNP**D**-Cet. The aggregates are barely internalized in cells due to their high size. The all red background observed for non-targeted nanoparticles, may be silica aggregates that precipitated at the bottom of the cover slip and attached to the glass, so the washes did not remove them.

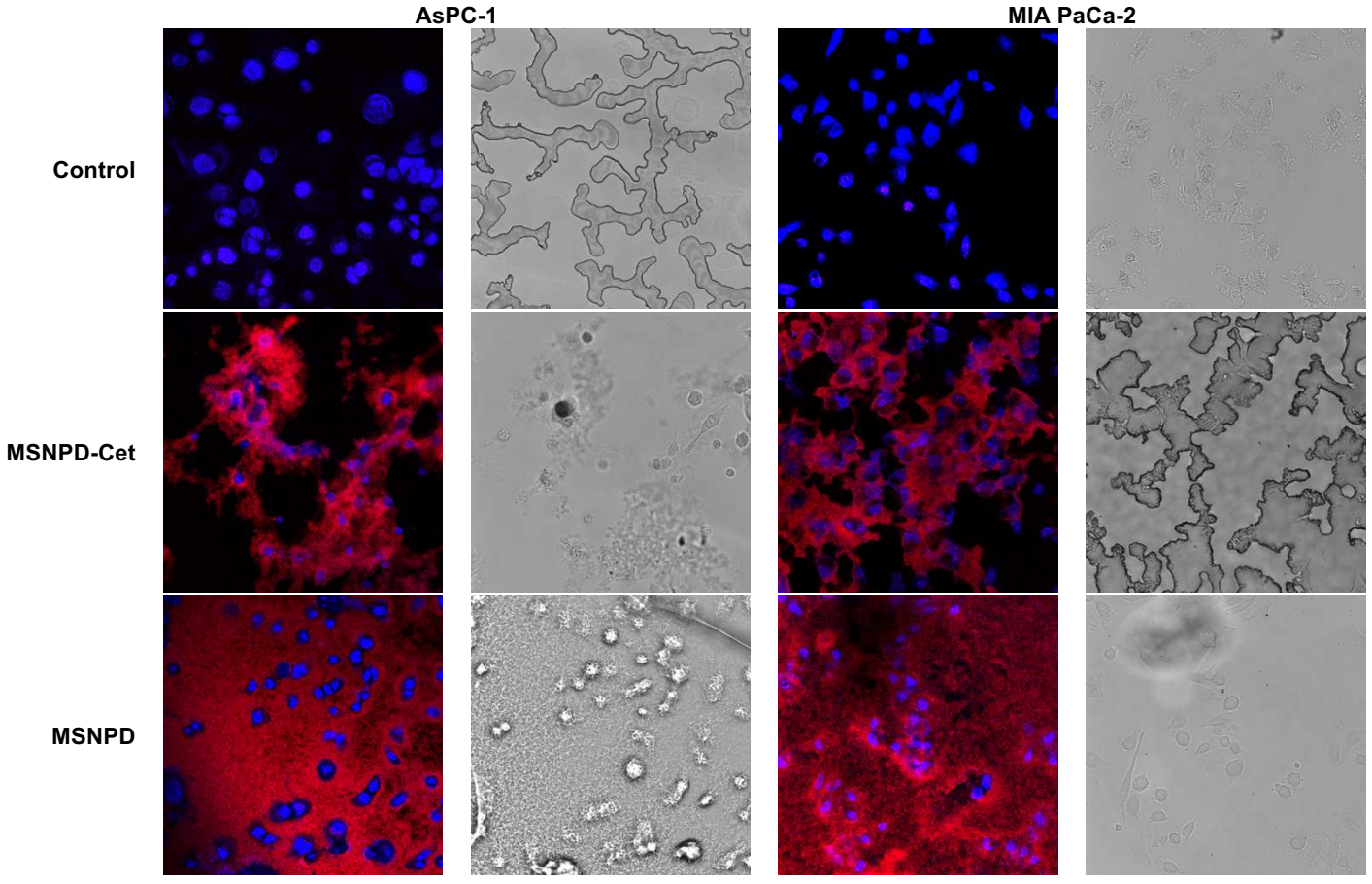

Figure 75. Confocal images of AsPC-1 and MIA PaCa-2 cells after 24 h incubation with MSNP**D** or MSNP**D**-Cet (2 μM of IRDye700DX) (the same concentration of nanoparticles was incubated). IRDye700DX is shown in red and Hoechst in blue. Wild-field images are shown. Non-treated cells were performed as controls.

5.6.4.1.2 Quantitative Uptake

In the previous Subchapter 5A, a quantitative uptake study demonstrated that Cetuximab-nanoparticles were greater internalized in AsPC-1 than in MIA PaCa-2 cells which was consistent with the major EGFR expression of AsPC-1 cell line. Here, the uptake study was performed for MSNP**D**-Cet nanoparticles in both cell lines. The internalization of MSNPs was investigated at only one incubation time, 24 h, since in the previous uptake it was demonstrated that this incubation time achieved the greater uptake among the times studied. Both cell lines were incubated with MSNP**D**-Cet nanoparticles at 2 μM of IRDye700DX. After incubation, MSNPs still present in the culture medium were removed by washing. The internalization of the nanoparticles was investigated by studying their fluorescence at λ_{exc} = 630 nm and λ_{em} = 699 nm. Fluorescence was normalized by the amount of protein present in each sample. The results are summarized in Figure 76.

As demonstrated before with the analogous MSNP system with ZnPcSMP, MSNP**D**-Cet nanoparticles were greater internalized by AsPC-1 cells than by MIA PaCa-2. Furthermore, the difference in uptake by both cell lines is pretty similar to that showed previously, which is reasonable since both MSNP systems despite have different phthalocyanine, are very similar nanocarriers.

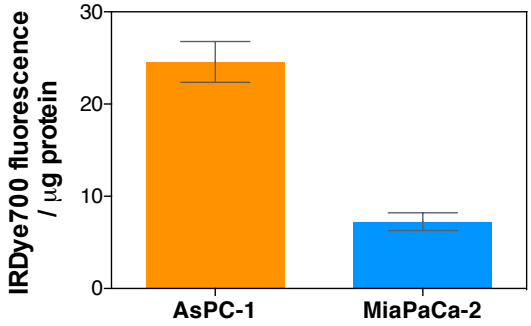

Figure 76. Cellular uptake of MSNP**D**-Cet in AsPC-1 and MIA PaCa-2 cells after 24 h of incubation. Cells were treated with the same concentration of IRDye700DX and MSNPs. Values reported are the mean ± SD of at least three independent experiments.

5.6.4.2 *In vitro* Singlet Oxygen Generation

To assure the generation of singlet oxygen by MSNP**D**-Cet in cells, MSNP**D**-Cet treated cells were studied by time-resolved NIR phosphorescence detection. AsPC-1 and MIA PaCa-2 cells were incubated 24 h with MSNP**D**-Cet. After the incubation time, cells were washed twice with PBS in order to discard the non-internalized nanoparticles. Then, cells were trypsinized and resuspended in complete culture medium. Afterwards, $^1O_2$ formation and

decay were monitored by time-resolved detection of their phosphorescence at 1275 nm after excitation at 355 nm (Figure 77).

Cellular suspensions showed a monoexponential rise and decay. The decay presented a lifetime of ~4 µs which corresponds to $^1O_2$ lifetime (τ_Δ) and is a typical value for this parameter in water (Table 22). The rise showed a lifetime of ~1 µs, corresponding to excited triplet state lifetime (τ_T). This study demonstrated that MSNP**D**-Cet nanoparticle formulation generates singlet oxygen with good yield once they are internalized in AsPC-1 and MIA PaCa-2 cells. In addition, perhaps the same concentration of MSNP**D**-Cet was incubated in both cell lines, the production of $^1O_2$ is higher in AsPC-1 cells than in MIA PaCa-2. By comparison of the amplitudes of τ_Δ, the generation of $^1O_2$ in MIA PaCa-2 was decreased by 30% in comparison with AsPC-1 cells. This decrease is consistent with the lower uptake of MSNP**D**-Cet nanoparticles by MIA PaCa-2 cells in comparison with AsPC-1.

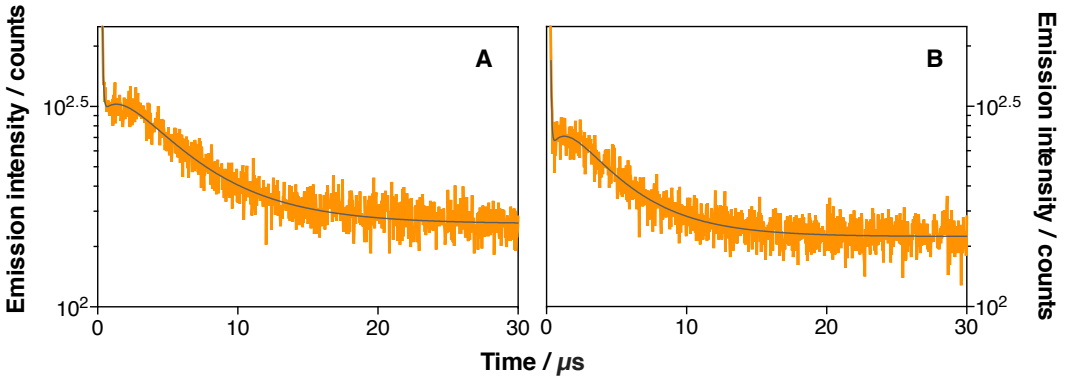

Figure 77. Time-resolved phosphorescence decays for MSNP**D**-Cet-treated cells suspensions of AsPC-1 (A) and MIA PaCa-2 (B) cells. λ_{exc} = 1275 nm. λ_{em} = 355 nm.

Table 22. Singlet oxygen kinetic values for AsPC-1 and MIA-PaCa-2 cells suspensions treated with MSNP**D**-Cet nanoparticles. For comparison, IRDye700DX in water was measured. A: amplitude.

Sample	Cells	τ_T / µs	A_T	τ_Δ / µs	A_Δ
IRDye700DX	-	1.8	-	4.1	-
MSNP**D**-Cet	AsPC-1	1.5	-129	4.5	274
	MIA-PaCa-2	1.1	-105	4.0	205

5.6.4.3 *In vitro* Phototoxicity Studies

The phototoxic effect of the synthesized nanoparticles and the free compounds IRDye700DX and DOX was studied *in vitro* by analyzing cell proliferation after photodynamic treatment by MTT assay.

5.6.4.3.1 Free IRDye700DX and DOX

The phototoxicity *in vitro* of the free compounds IRDye700DX and DOX was tested in AsPC-1 and MIA PaCa-2 cells.

On the one hand, the phototoxic effect of IRDye700DX was studied at different drug concentrations (0.05, 0.1, 0.25, 0.5 and 1 μM) and upon 30 J·cm^{-2} of red light irradiation. IRDye700DX-NHS was previously dissolved in Tris buffer in order to hydrolyze the highly reactant NHS group. This solution was diluted in supplemented media at the corresponding IRDye700DX concentration and later incubated for 24 h. As shown in Figure 78A and Figure 78B, IRDye700DX did not show phototoxicity in AsPC-1 and MIA PaCa-2 cells. Furthermore, IRDye700DX was not cytotoxic in the concentration range studied.

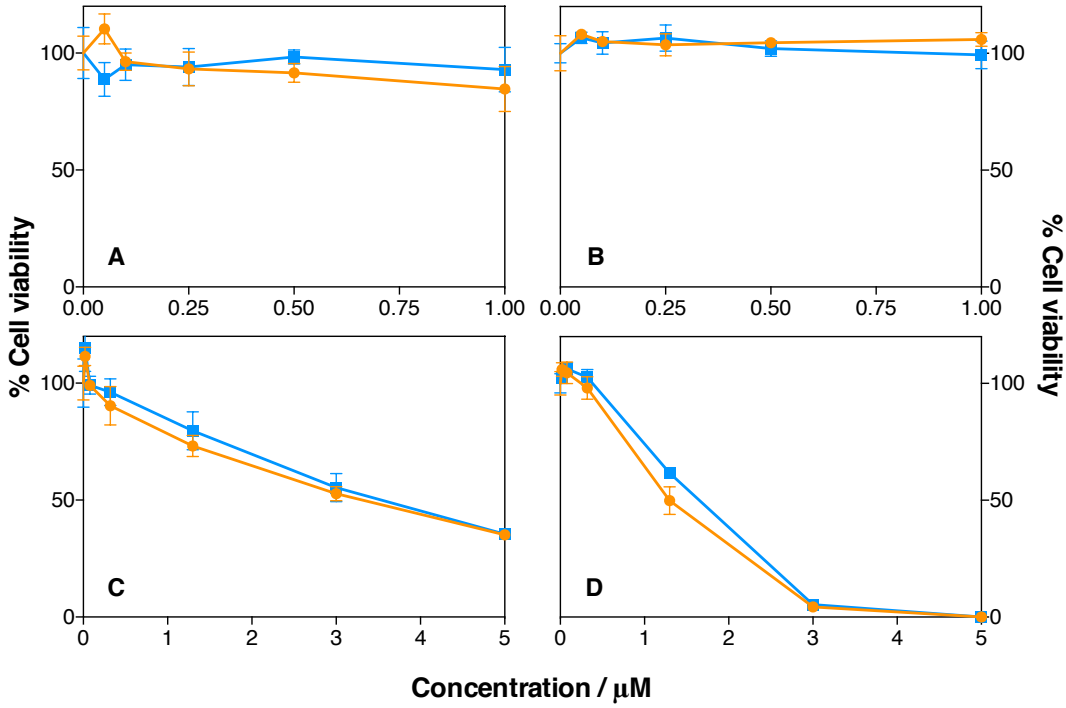

Figure 78. Phototoxicity studies of IRDye700DX (A, B) and Doxorubicin (C, D) in AsPC-1 (A, C) and MIA PaCa-2 cells (B, D). IRDye700DX was studied at different drug concentrations (0.05, 0.1, 0.25, 0.5 and 1 μM) and DOX as well (0.02, 0.08, 0.32, 1.3, 3 and 5 μM). Light treated cells in orange (30 J·cm^{-2}, λ_{exc} = 661 ± 10 nm) and dark controls in blue. Values reported are the mean ± SD of at least three independent experiments.

On the other hand, the phototoxicity of DOX was investigated. A wide range of DOX concentrations (0.02, 0.08, 0.32, 1.3, 3 and 5 μM) was tested in AsPC-1 and MIA PaCa-2 cells (Figure 78C and Figure 78B, respectively) with or without the irradiation treatment (30 J·cm^{-2} of red light). DOX showed higher cytotoxic effect in MIA PaCa-2 cells than in AsPC-1. This chemotherapeutic agent was not phototoxic since no significant differences were shown

between the irradiated and non-irradiated samples.

5.6.4.3.2 MSNPD-Cet Nanoparticles

The phototoxicity of MSNP**D** and MSNP**D**-Cet nanoparticles was investigated in AsPC-1 and MIA PaCa-2 cells. The nanoparticles were diluted in supplemented medium to achieve a range of IRDye700DX concentrations (0.25, 0.5, 0.75, 1 and 1.5 μM) and incubated in the cells for 24 h. Then, cells were irradiated with 30 J·cm^{-2} of red light. The selection of a 24 h incubation for phototoxicity studies was informed by uptake studies of alike Cetuximab-nanoparticles, which showed maximal fluorescence signal after 24 h of incubation (Section 5.2.4.1.2 in Subchapter 5A).

As shown in Figure 79, targeted-nanoparticles showed concentration-dependent phototoxic effect against both cell lines, unlike non-Cetuximab nanoparticles that were not phototoxic. While a 30 J·cm^{-2} light dose in AsPC-1 cells treated with 1 μM of MSNP**D** did not kill the cells, the cell viability was dramatically reduced to <15% by the targeted-nanoparticles. This is in agreement with the confocal studies that demonstrated the lack of internalization by MSNP**D** in both cell lines. Therefore, the conjugation of the antibody is essential to achieve photodynamic activity by the nanoparticles.

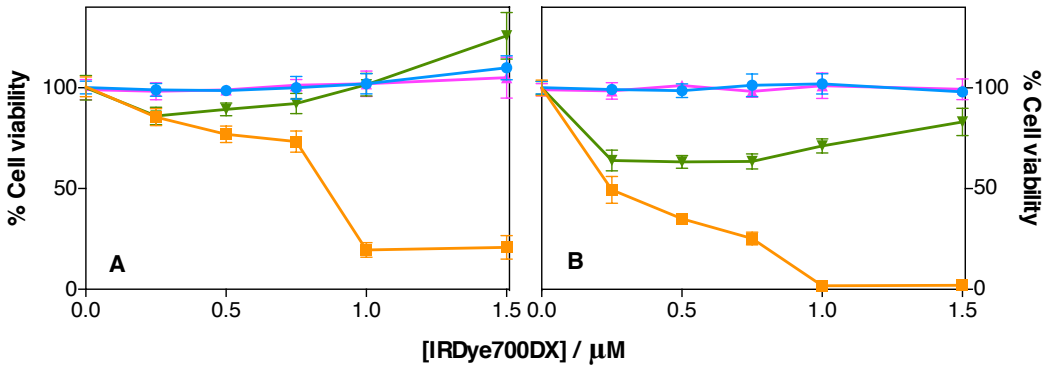

Figure 79. Phototoxicity studies of MSNP**D** (irradiated in blue and non-irradiated in pink) and MSNP**D**-Cet (irradiated in orange, non-irradiated in green) in AsPC-1 (A) and MIA PaCa-2 cells (B). A range of IRDye700DX concentrations (0.25, 0.5, 0.75, 1 and 1.5 μM) were incubated in the cells for 24 h. Cells were irradiated with 30 J·cm^{-2} (λ_{exc} = 661 ± 10 nm). Values reported are the mean ± SD of at least three independent experiments.

Similarly, the enhancement of phototoxicity activity by MSNP**D**-Cet nanoparticles, compared with the non-targeted ones, was reflected in MIA PaCa-2 cells. MIA PaCa-2 cells showed greater sensitivity upon photodynamic treatment than AsPC-1 cells despite their lesser uptake. The variation of sensitivity to the treatment in individual cancer cell lines may indicate that the effectiveness of the targeted-PDT may depend not only upon the EGFR expression of cells, but also upon intrinsic biological properties of individual tumor cell lines.

Nevertheless, MSNP**D**-Cet nanoparticles showed dark toxicity. MIA PaCa-2 cells were again more sensible to MSNP**D**-Cet in dark conditions than AsPC-1. The same concentrations of free Cetuximab with regard to each concentration of MSNP**D**-Cet studied did not show cytotoxicity in both cell lines (Figure B16 in Appendix B). Therefore, the action of Cetuximab alone is not enough to achieve the cytotoxic effect shown in darkness for MSNP**D**-Cet formulation. Nevertheless, it is possible that the vehiculization of the antibody makes it more lethal.

In conclusion, we designed a novel PEG-coated mesoporous silica nanoparticle with the photosensitizer IRDye700DX and the antibody Cetuximab covalently attached that demonstrated being phototoxic. IRDye700DX itself has not photodynamic efficacy due to a poor cellular localization and because of this, it is commonly used to form a conjugate with a targeting molecule. Conjugates between IRDye700DX and Cetuximab are extensively investigated, however, to our knowledge, until today no research has been published about the combination of these two moieties in nanoparticles. Only few reports studied the combination of IRDye700DX and a targeting moiety in nanocarriers.[130,240,241]

5.6.4.3.3 MSNPE-Cet Nanoparticles

The photodynamic activity of MSNP**E**-Cet was investigated *in vitro*. Three MSNP**E**-Cet nanoparticles with different DOX concentration (1.5, 2 and 12 μM of DOX) were studied, as well as MSNP**D**-Cet for comparison. The concentration of IRDye700DX and nanoparticles were kept constant in all the MSNP formulations. A concentration of 0.8 μM of IRDye700DX was chosen since this is approximately the concentration that achieved 50% inhibition in AsPC-1 cell viability by MSNP**D**-Cet. The nanoparticles were diluted in supplemented medium and incubated for 24 h in AsPC-1 and MIA PaCa-2 cells. Then, cells were irradiated with 30 $J \cdot cm^{-2}$ of red light. After 24 h or 48 h, the cell proliferation was analyzed by MTT assay.

On the one hand, MTT assay results for AsPC-1 cells are shown in Figure 80A and Figure 80C. MSNP**E**-Cet (1.5 μM of DOX) showed much lesser phototoxicity in comparison with MSNP**D**-Cet. This can be rationalized by the reduction of $^1O_2$ generation by MSNP**E**-Cet in comparison with its analog without DOX. In addition, the formulation with 2 μM of DOX exhibited less photodynamic action that the one with 1.5 μM, fact that is coherent with the singlet oxygen studies that demonstrated that $^1O_2$ production is more affected by increasing the concentration of DOX in the formulation. Nevertheless, MSNP**E**-Cet with 12 μM of DOX showed a noteworthy decrease in cell viability. The phototoxic effect of MSNP**E**-Cet (12 μM of DOX) is due to the photoreleased DOX since the $^1O_2$ generated by MSNP**E**-Cet formulation was not enough to achieve that percentage of mortality at lower DOX concentrations.

On the other hand, *in vitro* phototoxicity study was also performed in MIA PaCa-2 cells (Figure 80B and Figure 80D). As seen for AsPC-1 cells, MSNP**E**-Cet formulations with 1.5 and 2 μM of DOX showed lesser phototoxicity than MSNP**D**-Cet. However, cell viability did not decrease for MSNP**E**-Cet nanoparticles with 12 μM of DOX, but it even increased. Thereby, the photoreleased DOX had not effect on MIA PaCa-2 cells despite this cell line demonstrated being more sensitivity to DOX than AsPC-1. The lesser uptake of Cetuximab-MSNPs by MIA PaCa-2 cells may be the explanation for this difference. Due to the minor internalization, the concentration of photoreleased DOX was not enough to exhibit cytotoxicity, so the cells were killed only by action of $^1O_2$; as it was for MSNP**E**-Cet with 1.5 and 2 μM of DOX.

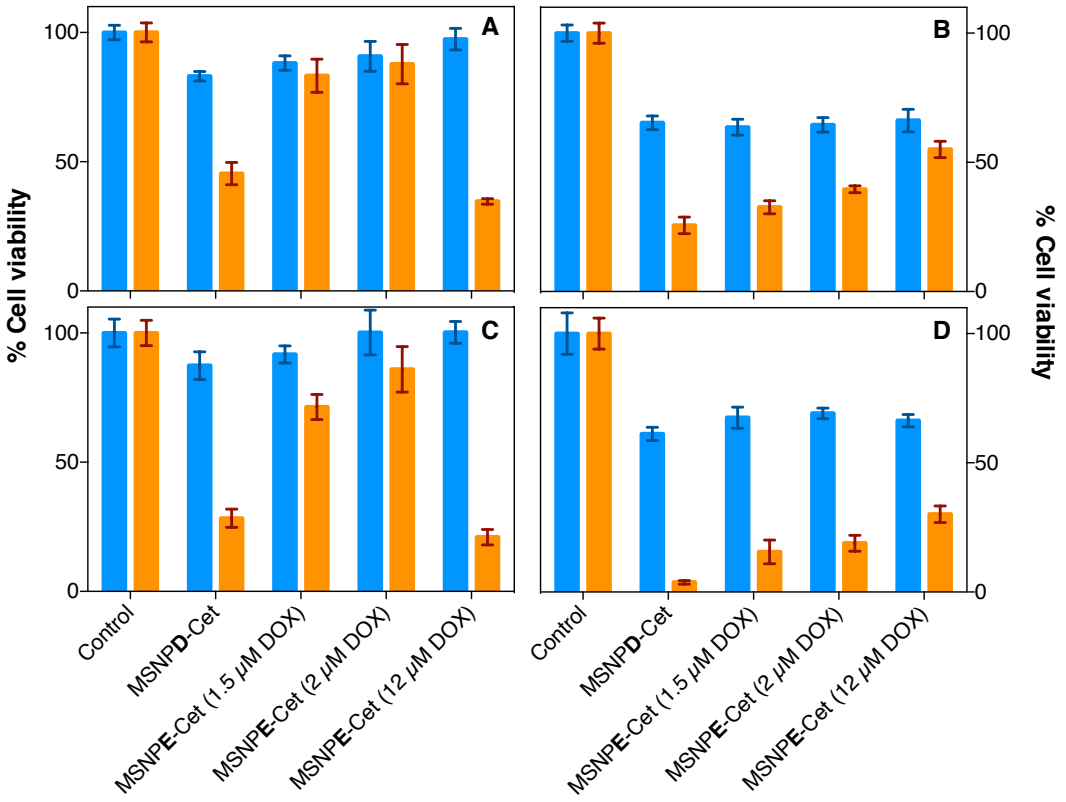

Figure 80. Phototoxicity studies of MSNP**D**-Cet and MSNP**E**-Cet (irradiated in orange and non-irradiated in blue) in AsPC-1 (A, C) and MIA PaCa-2 cells (B, D); 24 h post-irradiation incubation (A, B) and 48 h incubation post-irradiation (C, D). The concentration of IRDye700DX was constant (0.8 μM) for all the nanoparticles formulations, as well as the number of MSNPs. Three concentration of DOX in the nanoparticles was studies, 1.5, 2 and 12 μM. Cells were irradiated with 30 J·cm^{-2}. For 48 h post-irradiation incubation, half quantities of cells were seeded than for 24 h. Values reported are the mean ± SD of at least three independent experiments.

Therefore, the photokilling achieved by MSNP**D**-Cet is due only to the direct action of $^1O_2$ against cells. In contrast, MSNP**E**-Cet formulation kills cells majority by action of the photoreleased DOX. In Section 5.6.3.3, the percentage of DOX released after this specific

irradiation treatment was calculated. Only 12% of the total DOX was photoreleased, which means that ~1.4 μM of DOX was available to kill cells in the present experiment if all the MSNPs had been internalized, which surely is not the case. 1.3 μM of free DOX (incubated in the same number of AsPC-1 cells for 24 h and performing the MTT assay after 24 h of the irradiation treatment) decreased cell viability to 75% (Section 5.6.4.3.1). In contrast, here, the photoreleased DOX from MSNP**E**-Cet nanoparticles reduced the cell viability to 34%.

Wong *et al.*[61] reported a similar nanosystem in which the release of DOX was triggered by $^1O_2$ thanks to its attachment to the MSNP by means of a $^1O_2$-cleavable linker, a 9,10-dialkoxyanthracene moiety. The generation of $^1O_2$ by ZnPc and posterior release of DOX did not increase the phototoxic effect *in vitro*; since both nanosystems with and without DOX showed no significant differences in cell viability in HepG2 cells. Moreover, the dark toxicity of this nanosystem was very significant, since the cell viability decreased to 40%. Therefore, MSNP**E**-Cet formulation presents great improvements in comparison with this published nanosystem.

Likewise, Yue *et al*.[96] reported the formulation of a ROS-triggered theranostic platform based on Ce6-CPT-UCNPs for chemo-photodynamic combined therapy. In this case, camptothecin (CPT) is covalently immobilized to upconversion NPs (UCNPs) by means of a $^1O_2$-cleavable moiety, a dithioketal. The introduction of CPT to the NP formulation decreased the cell viability by 10% in comparison with the formulation without the chemotherapeutic agent; a difference smaller than the achieved in our work with MSNP**E**-Cet related to MSNP**D**-Cet.

In a previous publication from our laboratory, Tabero *et al.*[98], about dual-functionalized gold nanoclusters with PPIX and DOX attached through the same $^1O_2$-cleavable linker; the difference in the treatment outcomes between the nanosystems with and without DOX was much more significant, a decrease in cell viability by 60%. There, the DOX concentration in the nanocarrier used to perform the MTT assay was 10 times higher than the IC_{50} of DOX in that cell line. In contrast, in the present work, the concentration of DOX is approximately 4 times higher than the IC_{50} of DOX in AsPC-1 cells. Since our results show a tendency that the higher the DOX concentration in the nanoformulation, the lower the cell viability; if we increased the DOX content to that extent, we would very likely see a more pronounced decrease in cell viability and thus a greater difference between the formulations with and without DOX. However, we cannot load the MSNPs with that much DOX since, additionally, we graft an antibody to the MSNPs to achieve active targeting.

In conclusion, the novel MSNP**E**-Cet nanoparticle formulation is a drug delivery system that successfully achieves the killing of high expressing-EGFR cells majority by action of DOX at lower doses than the free drug only when the system is illuminated. Thereby, through this

nanocarrier, the treatment gains in efficacy and selectivity, and thus in safety, thanks to two factors: i) the attachment of the antibody Cetuximab that increases the uptake according to the EGFR expression of cells; and ii) the modulation on-demand of the release of the antineoplastic agent.

5.7 Experimental Section

5.7.1 Materials

Sulfo-NHS, APTES, CTAC, TEOS, Hoechst 33258, PBS and MTT were purchased from Sigma-Aldrich Chemical Co. (St. Louis, MO, USA). EDC·HCl were purchased from Tokyo Chemical Industry Co., Ltd. (Tokyo, Japan). DMEM (with 4.5 g/L *D*-glucose and without sodium pyruvate or *L*-Glutamine), *L*-Glutamine solution (200 mM), Pencillin-Streptomycin solution, Trypsin EDTA solution (solution C (0.05%), EDTA (0.02%) and with phenol red) and FBS were purchased from Biological Industries (Kibbutz Beit Haemek, Israel). RPMI 1640 medium was purchased from Fisher Scientific (Waltham, Massachusetts, USA). Cetuximab was purchased from Carbosynth Ltd. (Compton, United Kingdom). COOH-PEG_{5k}-NHS was purchased from Laysan Bio Inc. (Arab, Alabama, USA). IRDye700DX-NHS was purchased from Li-COR (Lincoln, NE, USA) through Bonsai Lab (Alcobendas, Madrid, Spain) All other chemicals were commercially available reagents of at least analytical grade. Milli-Q water (Millipore Bedford system, resistivity of 18 MΩ cm) was used.

5.7.2 Derivatization of Silica Mesoporous Nanoparticles

5.7.2.1 MSNPD-Cet: IRDye700DX – Cetuximab – MSNP

- MSNP7: reaction between blank MSNP nanoparticles and APTES. APTES (15 µL) was added to blank mesoporous nanoparticles (22.5 mg) prepared and dispersed in absolute EtOH (22.5 mL). The mixture was closed and under stirring overnight at 40 ºC. Afterwards, the reaction mixture was centrifuged (60 min, 14000 rpm, 15 ºC) and washed three times with EtOH. MSNP7 nanoparticles were kept in DMF at 4 ºC.
- MSNP8: introduction of IRDye700DX-NHS to MSNP7 nanoparticles. IRDye700DXNHS (0.2 mg) were added to all the prepared MSNP7 nanoparticles dispersed in anhydrous DMF (22.5 mL). The mixture was closed and stirred overnight. Then, the reaction mixture was centrifuged and the supernatant discarded. Pellet was washed three times with DMF. MSNP8 nanoparticles were kept in DMF at

4 ºC and darkness.

- MSNP**D**: PEGylation of MSNP8. NHS-PEG-COOH (5:2 wt ratio of MSNP:NHS-PEG-COOH) was added to all the prepared MSNP8 nanoparticles dispersed in DMF (20 mL). The mixture was stirred for 24 h in darkness and at RT. Then, the reaction mixture was centrifuged (60 min, 14000 rpm, 15 ºC) and washed three times with DMF. MSNP**D** nanoparticles were kept in DMF at 4 ºC.
- MSNP**D**-Cet: conjugation of compound **10** to MSNP8. Compound **10** was added to a dispersion of MSNP8 nanoparticles in the same volume of PBS pH = 7.4 (5:2:2 wt MSNPs:PEG:Cetuximab) and stirred overnight at RT. Finally, MSNP**D**-Cet nanoparticles were collected without further purification.

5.7.2.2 MSNPE-Cet: IRDye700DX – Cetuximab – Doxorubicin (covalently attached, releasable) – MSNP

- MSNP7 and MSNP8 were prepared as described before.
- MSNP9: functionalization of MSNP8 with the orthogonal conjugate cleavable linker – Doxorubicin, compound **6**. All of the synthesized **6** was added to MSNP3 dispersed in DMF (20 mL). The mixture was allowed to react for 24 h at 40 ºC. Afterwards, the reaction mixture was centrifuged (60 min, 14000 rpm, 20 ºC) and washed three times with DMF to remove the non-conjugated **6**. MSNP9 nanoparticles were left in DMF at 4 ºC.
- Synthesis of MSNP**E** and MSNP**E**-Cet. To obtain MSNP**E** nanoparticles, MSNP9 nanoparticles were PEGylated as described before for MSNP**D**. Finally, the conjugation of PEG-Cetuximab to MSNP9 nanoparticles was performed as explained for MSNP**D**-Cet.

5.7.3 Determination of the Drug Concentration in the Nanoparticles

The concentration of the photosensitizer IRDye700DX and the chemo-drug DOX in the nanoparticle formulations was calculated as the difference between the amount of IRDye700DX or DOX incorporated and the amount recovered from supernatant collected upon centrifugation of the nanoparticles (14,000 rpm, 1 h). The photosensitizer concentration from supernatant was determined by comparison with absorbance standard curves obtained in the same conditions. The DOX concentration from supernatant was determined by comparison with emission standard curves obtained employing the same experimental

conditions.

5.7.4 Singlet Oxygen Generation in Cell Culture

A quantity of 100,000 AsPC-1 cells and 80,000 MIA PaCa-2 cells were seeded in 12-well plates and incubated at 37 ºC (5% CO_2) for 24 h to achieve 80% confluence. Then, the culture medium was removed and the suspended MSNPs in complete culture medium were added. MSNP**D**-Cet nanoparticles were employed at 2 μM of IRDye700DX. After 24 h of incubation, the suspensions were removed and the wells were washed 3 times with PBS. Then, cells were trypsinized. Supplemented culture medium (2 mL) was added and the cells were centrifuged (1,100 rpm, 5 min). The pellet was suspended in 1 mL of complete culture medium without phenol red. Afterwards, $^1O_2$ formation and decay were monitored by time-resolved detection of their phosphorescence at 1275 nm after excitation at 355 nm.

5.8 Conclusions

The most relevant conclusions drawn from this subchapter are the following:

I. Unlike the phthalocyanine ZnPcSMP, IRDye700DX maintains its ability to generate singlet oxygen with good yield at the same conditions, and as a consequence, Doxorubicin is released from the nanoparticle.

II. MSNP**D**-Cet is the first reported nanocarrier that has covalently attached IRDye700DX and Cetuximab and, unlike the free photosensitizer, achieves photodynamic activity at sub-micromolar concentrations against EGFR-expressing cells.

III. The further decoration of IRDye700DX-bound mesoporous silica nanoparticles reduces their singlet oxygen production ability. Their additional grafting with small amounts of Doxorubicin leads to a decrease in their photodynamic activity.

IV. In contrast, mesoporous silica nanoparticles loaded with the photosensitizer IRDye700DX, decorated with Cetuximab and grafted with higher concentrations of Doxorubicin, show efficient and selective photokilling of EGFR-expressing cells, mainly through singlet oxygen-induced cleavage of the Doxorubicin linker.

CHAPTER 6: GENERAL CONCLUSIONS

The conclusions of the present thesis are highlighted in this chapter. A detailed analysis of the conclusions derived from each of the works presented in this thesis is outlined at the end of the corresponding Chapters 4 and 5.

I. Covalent binding of the hydrophilic ZnTriMPyP to the surface of PEG-coated PLGA nanoparticles improves the phototoxicity and dark toxicity of the nanosystem compared to related nanocarriers with the photosensitizer occluded. PLGA nanoparticles with surface-bound hydrophilic photosensitizers are valuable nanosystems for photodynamic therapy.

II. Functionalization of the PLGA nanoparticle surface with the c(RGDfK) peptide enhances the photodynamic activity against tumor cells expressing the $\alpha_v\beta_3$ integrin receptor but does not prevent damage to cells lacking this integrin, which limits the selectivity of this targeting approach.

III. Conjugation of Cetuximab antibody to the PEG-coated mesoporous silica nanoparticles improves the aqueous dispersibility of this nanocarrier and enables its internalization in EGFR-expressing cells according to their expression level of this receptor.

IV. The tri-cationic phthalocyanine ZnPcSMP is strongly aggregated and its photosensitizing ability is quenched when it is covalently attached to the surface of mesoporous silica nanoparticles. In contrast, the tetra-anionic phthalocyanine IRDye700DX maintains its ability to generate singlet oxygen when grafted at the same concentration. Consequently, mesoporous silica nanoparticles loaded with ZnPcSMP are not phototoxic *in vitro* while those carrying IRDye700DX show high photodynamic activity against AsPC-1 and MIA PaCa-2 cancer cells.

V. Doxorubicin can be effectively released from PEG-coated mesoporous silica nanoparticles by singlet oxygen-mediated cleavage of its linker in a light-dose dependent manner.

VI. PEG-coated mesoporous silica nanoparticles loaded with the photosensitizer IRDye700DX and decorated with Cetuximab suffer an unexpected reduction in their singlet oxygen production ability and photodynamic activity upon additional grafting of small amounts of Doxorubicin onto their surface.

VII. In contrast, PEG-coated mesoporous silica nanoparticles loaded with the photosensitizer IRDye700DX, decorated with Cetuximab and grafted with higher concentrations of Doxorubicin, show efficient and selective photokilling of EGFR-expressing cells without any dark toxicity, mainly through singlet oxygen-induced

cleavage of the Doxorubicin linker. Therefore, this novel triply functionalized nanosystem is an effective and safe nanodevice for light-triggered on-demand Doxorubicin delivery.

LIST OF PUBLICATIONS

Papers

- **de las Heras, E**.; Boix-Garriga, E.; Bryden, F.; Agut, M.; Mora, M.; Sagristá, M. L.; Boyle, R. W.; Lange, N.; Nonell, S. C(RGDfK)- and ZnTriMPyP-Bound Polymeric Nanocarriers for Tumor-Targeted Photodynamic Therapy. *Photochem. Photobiol.* 2020, *96* (3), 570–580.
- Revuelta-Maza, M.Á.; **de las Heras, E**.; Agut, M.; Nonell, S.; Torres, T.; de la Torre, G. Self-Assembled Binaphthyl-Bridged Amphiphilic AABB Phthalocyanines: Nanostructures for Efficient Antimicrobial Photodynamic Therapy. *Chemistry*. 2021, 27 (15), 4955–4963.

Additional papers are at different stages of publication:

- **de las Heras, E**; Sagristá M. L.; Agut M.; Nonell S. Mesoporous Silica Nanoparticles as On-Demand Photo-chemo-vehicles for Cetuximab-Targeted Photodynamic Therapy.

Communications in Congresses

- **de las Heras, E**; Nieves, I.; Agut, M.; Nonell, S. Gentamicin-Based Photo-Antimicrobials, 5th European Society for Photobiology (ESP) School, Bressanone (Italy), June 10th – 17th, 2018.
- **de las Heras, E**; Nieves, I.; Agut, M.; Nonell, S. Gentamicin-Based Photo-Antimicrobials, Photodynamic Therapy and Photodiagnosis Uptade 2018 Conference, Kochel am See (Germany), September 18th – 22nd, 2018.
- **de las Heras, E**.; Boix-Garriga, E.; Bryden, F.; Agut, M.; Mora, M.; Sagristá, M. L.; Boyle, R. W.; Lange, N.; Nonell, S. c(RGD) and ZnTriMPyP-Modified Polymeric Nanocarriers for Tumor-Targeted Photodynamic Therapy. 17th Congress of the International Union of Photobiology and 18th Congress of the European Society for Photobiology, Barcelona (Spain), August 25th – 30th, 2019.

REFERENCES

(1) Daniell, M. D.; Hill, J. S. A History of Photodynamic Therapy. *ANZ J. Surg.* **1991**, *61* (5), 340–348.

(2) Dolmans, D. E. J. G. J.; Fukumura, D.; Jain, R. K. Photodynamic Therapy for Cancer. *Nat. Rev. Cancer* **2003**, *3* (5), 380–387.

(3) Agostinis, P.; Berg, K.; Cengel, K. A.; Foster, T. H.; Girotti, A. W.; Gollnick, S. O.; Hahn, S. M.; Hamblin, M. R.; Juzeniene, A.; Kessel, D.; et al. Photodynamic Therapy of Cancer: An Update. *CA. Cancer J. Clin.* **2011**, *61* (4), 250–281.

(4) Obaid, G.; Broekgaarden, M.; Bulin, A.-L.; Huang, H.-C.; Kuriakose, J.; Liu, J.; Hasan, T. Photonanomedicine: A Convergence of Photodynamic Therapy and Nanotechnology. *Nanoscale* **2016**, *8* (25), 12471–12503.

(5) Wainwright, M.; Maisch, T.; Nonell, S.; Plaetzer, K.; Almeida, A.; Tegos, G. P.; Hamblin, M. R. Photoantimicrobials—Are We Afraid of the Light? *Lancet Infect. Dis.* **2017**, *17* (2), e49–e55.

(6) McCaughan, J. S. Photodynamic Therapy. *Drugs Aging* **1999**, *15* (1), 49–68.

(7) Krammer, B. Vascular Effects of Photodynamic Therapy. *Anticancer Res.* **2001**, *21* (6B), 4271–4277.

(8) van Straten, D.; Mashayekhi, V.; de Bruijn, H. S.; Oliveira, S.; Robinson, D. J. Oncologic Photodynamic Therapy: Basic Principles, Current Clinical Status and Future Directions. *Cancers (Basel).* **2017**, *9* (2), 1–54.

(9) Plaetzer, K.; Krammer, B.; Berlanda, J.; Berr, F.; Kiesslich, T. Photophysics and Photochemistry of Photodynamic Therapy: Fundamental Aspects. *Lasers Med. Sci.* **2009**, *24* (2), 259–268.

(10) Brown, S. B.; Brown, E. A.; Walker, I. The Present and Future Role of Photodynamic Therapy in Cancer Treatment. *Lancet Oncol.* **2004**, *5* (8), 497–508.

(11) Martinez De Pinillos Bayona, A.; Mroz, P.; Thunshelle, C.; Hamblin, M. R. Design Features for Optimization of Tetrapyrrole Macrocycles as Antimicrobial and Anticancer Photosensitizers. *Chem. Biol. Drug Des.* **2017**, *89* (2), 192–206.

(12) Stolik, S.; Delgado, J. A.; Pérez, A.; Anasagasti, L. Measurement of the Penetration Depths of Red and near Infrared Light in Human ″ex Vivo″ Tissues. *J. Photochem. Photobiol. B* **2000**, *57* (2–3), 90–93.

(13) Douplik, A.; Saiko, G.; Schelkanova, I.; Tuchin, V. V. The Response of Tissue to Laser Light. In *Lasers for Medical Applications: Diagnostics, Therapy and Surgery*; 2013; pp 47–109.

(14) Star, W. M. Light Dosimetry in Vivo. *Phys. Med. Biol.* **1997**, *42* (5), 763–787.

(15) Jori, G. Far-Red-Absorbing Photosensitizers: Their Use in the Photodynamic Therapy of Tumours. *J. Photochem. Photobiol. A* **1992**, *62* (3), 371–378.

(16) Juzeniene, A.; Peng, Q.; Moan, J. Milestones in the Development of Photodynamic Therapy and Fluorescence Diagnosis. *Photochem. Photobiol. Sci.* **2007**, *6* (12), 1234–1245.

(17) Triesscheijn, M.; Baas, P.; Schellens, J. H. M.; Stewart, F. A. Photodynamic Therapy in Oncology. *Oncologist* **2006**, *11* (9), 1034–1044.

(18) Rai, P.; Mallidi, S.; Zheng, X.; Rahmanzadeh, R.; Mir, Y.; Elrington, S.; Khurshid, A.; Hasan, T. Development and Applications of Photo-Triggered Theranostic Agents. *Adv. Drug Deliv. Rev.* **2010**, *62* (11), 1094–1124.

(19) Hsu, C. Y.; Chen, C. W.; Yu, H. P.; Lin, Y. F.; Lai, P. S. Bioluminescence Resonance Energy Transfer Using Luciferase-Immobilized Quantum Dots for Self-Illuminated Photodynamic Therapy. *Biomaterials* **2013**, *34* (4), 1204–1212.

(20) Xu, X.; An, H.; Zhang, D.; Tao, H.; Dou, Y.; Li, X.; Huang, J.; Zhang, J. A Self-Illuminating Nanoparticle for Inflammation Imaging and Cancer Therapy. *Sci. Adv.* **2019**, *5* (1), eaat2953.

(21) Sun, W.; Zhou, Z.; Pratx, G.; Chen, X.; Chen, H. Nanoscintillator-Mediated X-Ray Induced Photodynamic Therapy for Deep-Seated Tumors: From Concept to Biomedical Applications. *Theranostics* **2020**, *10* (3), 1296–1318.

(22) Castano, A. P.; Demidova, T. N.; Hamblin, M. R. Mechanisms in Photodynamic Therapy: Part One - Photosensitizers, Photochemistry and Cellular Localization. *Photodiagnosis Photodyn. Ther.* **2004**, *1* (4), 279–293.

(23) Rodríguez-Amigo, B.; Planas, O.; Bresolí-Obach, R.; Torra, J.; Ruiz-González, R.; Nonell, S. Photosensitisers for Photodynamic Therapy: State of the Art and Perspectives. In *Photodynamic Medicine: From Bench to Clinic*; Kostron, H., Hasan, T., Eds.; The Royal Society of Chemistry, 2016; pp 23–62.

(24) Ethirajan, M.; Chen, Y.; Joshi, P.; Pandey, R. K. The Role of Porphyrin Chemistry in Tumor Imaging and Photodynamic Therapy. *Chem. Soc. Rev.* **2011**, *40* (1), 340–362.

(25) Boix-Garriga, E.; Bryden, F.; Savoie, H.; Sagristá, M. L.; Mora, M.; Boyle, R. W.; Nonell, S. Poly(D,L-Lactide-Co-Glycolide) Nanoparticles with Covalently-Bound Porphyrins for Efficient Singlet Oxygen Photosensitization. *J. Porphyr. Phthalocyanines* **2016**, *20* (08n11), 1306–1318.

(26) Sobotta, L.; Skupin-Mrugalska, P.; Piskorz, J.; Mielcarek, J. Porphyrinoid Photosensitizers Mediated Photodynamic Inactivation against Bacteria. *Eur. J. Med. Chem.* **2019**, *175*, 72–106.

(27) Kasha, M.; Khan, A. U. Physics, Chemistry, and Biology of Singlet Molecular Oxygen. *Ann. N. Y. Acad. Sci.* **1970**, *171* (1), 5–23.

(28) Kearns, D. R. Physical and Chemical Properties of Singlet Molecular Oxygen. *Chem. Rev.* **1971**, *71* (4), 395–427.

(29) Macdonald, I. J.; Dougherty, T. J. Basic Principles of Photodynamic Therapy. *J. Porphyr. Phthalocyanines* **2001**, *05* (02), 105–129.

(30) World Health Organization. Cancer. https://www.who.int/health-topics/cancer#tab=tab_1 (accessed December 27, 2020).

(31) Lipson, R. L.; Baldes, E. J. The Photodynamic Properties of a Particular Hematoporphyrin Derivative. *Arch. Dermatol.* **1960**, *82* (4), 508–516.

(32) Lipson, R. L.; Baldes, E. J.; Olsen, A. M. Hematoporphyrin Derivative - a New Aid for Endoscopic Detection of Malignant Disease. *J. Thorac. Cardiovasc. Surg.* **1961**, *42* (5), 623-.

(33) Dougherty, T. J.; Grindey, G. B.; Fiel, R.; Weishaupt, K. R.; Boyle, D. G. Photoradiation Therapy. II. Cure of Animal Tumors with Hematoporphyrin and Light. *J. Natl. Cancer Inst.* **1975**, *55* (1), 115–121.

(34) Kelly, J. F.; Snell, M. E. Hematoporphyrin Derivative: A Possible Aid in the Diagnosis and Therapy of Carcinoma of the Bladder. *J. Urol.* **1976**, *115* (2), 150–151.

(35) Shi, H.; Sadler, P. J. How Promising Is Phototherapy for Cancer? *Br. J. Cancer* **2020**, *123* (6), 871–873.

(36) Mroz, P.; Yaroslavsky, A.; Kharkwal, G. B.; Hamblin, M. R. Cell Death Pathways in Photodynamic Therapy of Cancer. *Cancers (Basel).* **2011**, *3* (4), 2516–2539.

(37) Chiaviello, A.; Postiglione, I.; Palumbo, G. Targets and Mechanisms of Photodynamic Therapy in Lung Cancer Cells: A Brief Overview. *Cancers (Basel).* **2011**, *3* (1), 1014–1041.

(38) Chen, B.; Pogue, B. W.; Luna, J. M.; Hardman, R. L.; Hoopes, P. J.; Hasan, T. Tumor Vascular Permeabilization by Vascular-Targeting Photosensitization: Effects, Mechanism, and Therapeutic Implications. *Clin. Cancer Res.* **2006**, *12* (3), 917–923.

(39) Yamamoto, N.; Homma, S.; Sery, T. W.; Donoso, L. A.; Hoober, J. K. Photodynamic Immunopotentiation: In Vitro Activation of Macrophages by Treatment of Mouse Peritoneal Cells with Haematoporphyrin Derivative and Light. *Eur. J. Cancer* **1991**, *27* (4), 467–471.

(40) Canti, G.; De Simone, A.; Korbelik, M. Photodynamic Therapy and the Immune System in Experimental Oncology. *Photochem. Photobiol. Sci.* **2002**, *1* (1), 79–80.

(41) Reginato, E.; Wolf, P.; Hamblin, M. R. Immune Response after Photodynamic Therapy Increases Anti-Cancer and Anti-Bacterial Effects. *World J. Immunol.* **2014**, *4* (1), 1–11.

(42) Wachowska, M.; Muchowicz, A.; Demkow, U. Immunological Aspects of Antitumor Photodynamic Therapy Outcome. *Cent. Eur. J. Immunol.* **2015**, *40* (4), 481–486.

(43) Anzengruber, F.; Avci, P.; De Freitas, L. F.; Hamblin, M. R. T-Cell Mediated Anti-Tumor Immunity after Photodynamic Therapy: Why Does It Not Always Work and How Can We Improve It? *Photochem. Photobiol. Sci.* **2015**, *14* (8), 1492–1509.

(44) Dąbrowski, J. M.; Arnaut, L. G. Photodynamic Therapy (PDT) of Cancer: From Local to Systemic Treatment. *Photochem. Photobiol. Sci.* **2015**, *14* (10), 1765–1780.

(45) Faber, M.; Coudray, C.; Hida, H.; Mousseau, M.; Favier, A. Lipid Peroxidation Products, and Vitamin and Trace Element Status in Patients with Cancer before and after Chemotherapy, Including Adriamycin - A Preliminary Study. *Biol. Trace Elem. Res.* **1995**, *47* (1–3), 117–123.

(46) Sederholm, C.; Hillerdal, G.; Lamberg, K.; Kölbeck, K.; Dufmats, M.; Westberg, R.;

Gawande, S. R. Phase III Trial of Gemcitabine plus Carboplatin versus Single-Agent Gemcitabine in the Treatment of Locally Advanced or Metastatic Non-Small-Cell Lung Cancer: The Swedish Lung Cancer Study Group. *J. Clin. Oncol.* **2005**, *23* (33), 8380–8388.

(47) Morabito, A.; Longo, R.; Gattuso, D.; Carillio, G.; Massaccesi, C.; Mariani, L.; Bonginelli, P.; Amici, S.; De Sio, L.; Fanelli, M.; et al. Trastuzumab in Combination with Gemcitabine and Vinorelbine as Second-Line Therapy for HER-2/Neu Overexpressing Metastatic Breast Cancer. *Oncol. Rep.* **2006**, *16* (2), 393–398.

(48) Zhang, Q.; Li, L. Photodynamic Combinational Therapy in Cancer Treatment. *J. BUON* **2018**, *23* (3), 561–567.

(49) Canti, G.; Nicolin, A.; Cubeddu, R.; Taroni, P.; Bandieramonte, G.; Valentini, G. Antitumor Efficacy of the Combination of Photodynamic Therapy and Chemotherapy in Murine Tumors. *Cancer Lett.* **1998**, *125* (1–2), 39–44.

(50) Crescenzi, E.; Chiaviello, A.; Canti, G.; Reddi, E.; Veneziani, B. M.; Palumbo, G. Low Doses of Cisplatin or Gemcitabine plus Photofrin/Photodynamic Therapy: Disjointed Cell Cycle Phase-Related Activity Accounts for Synergistic Outcome in Metastatic Non-Small Cell Lung Cancer Cells (H1299). *Mol. Cancer Ther.* **2006**, *5* (3), 776–785.

(51) Habiba, K.; Encarnacion-Rosado, J.; Garcia-Pabon, K.; Villalobos-Santos, J. C.; Makarov, V. I.; Avalos, J. A.; Weiner, B. R.; Morell, G. Improving Cytotoxicity against Cancer Cells by Chemo-Photodynamic Combined Modalities Using Silver-Graphene Quantum Dots Nanocomposites. *Int. J. Nanomedicine* **2015**, *11*, 107–119.

(52) De Pinillos Bayona, A. M.; Moore, C. M.; Loizidou, M.; MacRobert, A. J.; Woodhams, J. H. Enhancing the Efficacy of Cytotoxic Agents for Cancer Therapy Using Photochemical Internalisation. *Int. J. Cancer* **2016**, *138* (5), 1049–1057.

(53) Cheng, Y. S.; Peng, Y. B.; Yao, M.; Teng, J. P.; Ni, D.; Zhu, Z. J.; Zhuang, B. F.; Yang, Z. Y. Cisplatin and Photodynamic Therapy Exert Synergistic Inhibitory Effects on Small-Cell Lung Cancer Cell Viability and Xenograft Tumor Growth. *Biochem. Biophys. Res. Commun.* **2017**, *487* (3), 567–572.

(54) Khdair, A.; Di Chen; Patil, Y.; Ma, L.; Dou, Q. P.; Shekhar, M. P. V.; Panyam, J. Nanoparticle-Mediated Combination Chemotherapy and Photodynamic Therapy Overcomes Tumor Drug Resistance. *J. Control. Release* **2010**, *141* (2), 137–144.

(55) Kimura, M.; Miyajima, K.; Kojika, M.; Kono, T.; Kato, H. Photodynamic Therapy (PDT) with Chemotherapy for Advanced Lung Cancer with Airway Stenosis. *Int. J. Mol. Sci.* **2015**, *16* (10), 25466–25475.

(56) Casas, A.; Fukuda, H.; Riley, P.; del C Batlle, A. M.; Caro, R.; Straight, R.; Kopecek, J.; Funayama, Y.; Ogasawara, H.; Ohiro, T.; et al. Enhancement of Aminolevulinic Acid Based Photodynamic Therapy by Adriamycin. *Cancer Lett.* **1997**, *121* (1), 105–113.

(57) Kirveliene, V.; Grazeliene, G.; Dabkeviciene, D.; Micke, I.; Kirvelis, D.; Juodka, B.; Didziapetriene, J. Schedule-Dependent Interaction between Doxorubicin and MTHPC-Mediated Photodynamic Therapy in Murine Hepatoma in Vitro and in Vivo. *Cancer Chemother. Pharmacol.* **2006**, *57* (1), 65–72.

(58) Saravanakumar, G.; Lee, J.; Kim, J.; Kim, W. J. Visible Light-Induced Singlet Oxygen-Mediated Intracellular Disassembly of Polymeric Micelles Co-Loaded with a Photosensitizer and an Anticancer Drug for Enhanced Photodynamic Therapy. *Chem. Commun.* **2015**, *51* (49), 9995–9998.

(59) Yang, G.; Sun, X.; Liu, J.; Feng, L.; Liu, Z. Light-Responsive, Singlet-Oxygen-Triggered On-Demand Drug Release from Photosensitizer-Doped Mesoporous Silica Nanorods for Cancer Combination Therapy. *Adv. Funct. Mater.* **2016**, *26* (26), 4722–4732.

(60) Lee, J.; Lee, Y. M.; Kim, J.; Kim, W. J. Doxorubicin/Ce6-Loaded Nanoparticle Coated with Polymer via Singlet Oxygen-Sensitive Linker for Photodynamically Assisted Chemotherapy. *Nanotheranostics* **2017**, *1* (2), 196–207.

(61) Wong, R. C. H.; Ng, D. K. P.; Fong, W. P.; Lo, P. C. Glutathione- And Light-Controlled Generation of Singlet Oxygen for Triggering Drug Release in Mesoporous Silica Nanoparticles. *J. Mater. Chem. B* **2020**, *8* (20), 4460–4468.

(62) Sandland, J.; Boyle, R. W. Photosensitizer Antibody-Drug Conjugates: Past, Present, and Future. *Bioconjug. Chem.* **2019**, *30* (4), 975–993.

(63) Lim, C. K.; Heo, J.; Shin, S.; Jeong, K.; Seo, Y. H.; Jang, W. D.; Park, C. R.; Park, S. Y.; Kim, S.; Kwon, I. C. Nanophotosensitizers toward Advanced Photodynamic Therapy of Cancer. *Cancer Lett.* **2013**, *334* (2), 176–187.

(64) Debele, T. A.; Peng, S.; Tsai, H. C. Drug Carrier for Photodynamic Cancer Therapy. *Int. J. Mol. Sci.* **2015**, *16* (9), 22094–22136.

(65) Kruger, C. A.; Abrahamse, H. Utilisation of Targeted Nanoparticle Photosensitiser Drug Delivery Systems for the Enhancement of Photodynamic Therapy. *Molecules* **2018**, *23* (10), 2628.

(66) Mokwena, M. G.; Kruger, C. A.; Ivan, M. T.; Heidi, A. A Review of Nanoparticle Photosensitizer Drug Delivery Uptake Systems for Photodynamic Treatment of Lung Cancer. *Photodiagnosis Photodyn. Ther.* **2018**, *22*, 147–154.

(67) Konan, Y. N.; Gurny, R.; Allémann, E. State of the Art in the Delivery of Photosensitizers for Photodynamic Therapy. *J. Photochem. Photobiol. B* **2002**.

(68) Vargas, A.; Lange, N.; Arvinte, T.; Cerny, R.; Gurny, R.; Delie, F. Toward the Understanding of the Photodynamic Activity of M-THPP Encapsulated in PLGA Nanoparticles: Correlation between Nanoparticle Properties and in Vivo Activity. *J. Drug Target.* **2009**.

(69) Acharya, S.; Sahoo, S. K. PLGA Nanoparticles Containing Various Anticancer Agents and Tumour Delivery by EPR Effect. *Adv. Drug Deliv. Rev.* **2011**, *63* (3), 170–183.

(70) Asefa, T.; Tao, Z. Biocompatibility of Mesoporous Silica Nanoparticles. *Chem. Res. Toxicol.* **2012**, *25* (11), 2265–2284.

(71) Tarn, D.; Ashley, C. E.; Xue, M.; Carnes, E. C.; Zink, J. I.; Brinker, C. J. Mesoporous Silica Nanoparticle Nanocarriers: Biofunctionality and Biocompatibility. *Accounts Chem. Res.* **2013**, *46* (3), 792–801.

(72) Hong, S. ho; Choi, Y. Mesoporous Silica-Based Nanoplatforms for the Delivery of

Photodynamic Therapy Agents. *J. Pharm. Investig.* **2018**, *48* (1), 3–17.

(73) Manzano, M.; Vallet-Regí, M. Mesoporous Silica Nanoparticles for Drug Delivery. *Adv. Funct. Mater.* **2020**, *30* (2), 1902634.

(74) Cheng, Y. J.; Hu, J. J.; Qin, S. Y.; Zhang, A. Q.; Zhang, X. Z. Recent Advances in Functional Mesoporous Silica-Based Nanoplatforms for Combinational Photo-Chemotherapy of Cancer. *Biomaterials* **2020**, *8*, 598722.

(75) Wong, R. C. H.; Ng, D. K. P.; Fong, W. P.; Lo, P. C. Encapsulating PH-Responsive Doxorubicin–Phthalocyanine Conjugates in Mesoporous Silica Nanoparticles for Combined Photodynamic Therapy and Controlled Chemotherapy. *Chem. Eur. J.* **2017**, *23* (65), 16505–16515.

(76) Liu, Y.; Liu, X.; Xiao, Y.; Chen, F.; Xiao, F. A Multifunctional Nanoplatform Based on Mesoporous Silica Nanoparticles for Imaging-Guided Chemo/Photodynamic Synergetic Therapy. *RSC Adv.* **2017**, *7*, 31133–31141.

(77) Yang, B.; Wei, L.; Wang, Y.; Li, N.; Ji, B.; Wang, K.; Zhang, X.; Zhang, S.; Zhou, S.; Yao, X.; et al. Oxidation-Strengthened Disulfide-Bridged Prodrug Nanoplatforms with Cascade Facilitated Drug Release for Synergetic Photochemotherapy. *Asian J. Pharm. Sci.* **2020**, *15* (5), 637–645.

(78) Shi, C. E.; You, C. Q.; Pan, L. Facile Formulation of Near-Infrared Light-Triggered Hollow Mesoporous Silica Nanoparticles Based on Mitochondria Targeting for on-Demand Chemo/Photothermal/Photodynamic Therapy. *Nanotechnology* **2019**, *30* (32), 325102.

(79) He, S.; Krippes, K.; Ritz, S.; Chen, Z.; Best, A.; Butt, H. J.; Mailänder, V.; Wu, S. Ultralow-Intensity near-Infrared Light Induces Drug Delivery by Upconverting Nanoparticles. *Chem. Commun.* **2015**, *51* (2), 431–434.

(80) Xu, J.; Kuang, Y.; Lv, R.; Yang, P.; Li, C.; Bi, H.; Liu, B.; Yang, D.; Dai, Y.; Gai, S.; et al. Charge Convertibility and near Infrared Photon Co-Enhanced Cisplatin Chemotherapy Based on Upconversion Nanoplatform. *Biomaterials* **2017**, *130*, 42–55.

(81) Wang, X.; Xuan, Z.; Zhu, X.; Sun, H.; Li, J.; Xie, Z. Near-Infrared Photoresponsive Drug Delivery Nanosystems for Cancer Photo-Chemotherapy. *J. Nanobiotechnology* **2020**, *18* (1), 108.

(82) Yang, S.; Li, N.; Liu, Z.; Sha, W.; Chen, D.; Xu, Q.; Lu, J. Amphiphilic Copolymer Coated Upconversion Nanoparticles for Near-Infrared Light-Triggered Dual Anticancer Treatment. *Nanoscale* **2014**, *6* (24), 14903–14910.

(83) Wang, H.; Han, R. L.; Yang, L. M.; Shi, J. H.; Liu, Z. J.; Hu, Y.; Wang, Y.; Liu, S. J.; Gan, Y. Design and Synthesis of Core-Shell-Shell Upconversion Nanoparticles for NIR-Induced Drug Release, Photodynamic Therapy, and Cell Imaging. *ACS Appl. Mater. Interfaces* **2016**, *8* (7), 4416–4423.

(84) Huang, L.; Chen, X.; Bian, Q.; Zhang, F.; Wu, H.; Wang, H.; Gao, J. Photosensitizer-Stabilized Self-Assembling Nanoparticles Potentiate Chemo/Photodynamic Efficacy of Patient-Derived Melanoma. *J. Control. Release* **2020**, *328*, 325–338.

(85) Kim, K.; Lee, C. S.; Na, K. Light-Controlled Reactive Oxygen Species (ROS)-Producible Polymeric Micelles with Simultaneous Drug-Release Triggering and

Endo/Lysosomal Escape. *Chem. Commun.* **2016**, *52* (13), 2839–2842.

(86) Chai, S.; Guo, Y.; Zhang, Z.; Chai, Z.; Ma, Y.; Qi, L. Cyclodextrin-Gated Mesoporous Silica Nanoparticles as Drug Carriers for Red Light-Induced Drug Release. *Nanotechnology* **2017**, *28* (14), 145101.

(87) Su, J.; Sun, H.; Meng, Q.; Zhang, P.; Yin, Q.; Li, Y. Enhanced Blood Suspensibility and Laser-Activated Tumor-Specific Drug Release of Theranostic Mesoporous Silica Nanoparticles by Functionalizing with Erythrocyte Membranes. *Theranostics* **2017**, *7* (3), 523–537.

(88) Saravanakumar, G.; Park, H.; Kim, J.; Park, D.; Pramanick, S.; Kim, D. H.; Kim, W. J. Miktoarm Amphiphilic Block Copolymer with Singlet Oxygen-Labile Stereospecific β-Aminoacrylate Junction: Synthesis, Self-Assembly, and Photodynamically Triggered Drug Release. *Biomacromolecules* **2018**, *19* (6), 2202–2213.

(89) Brega, V.; Scaletti, F.; Zhang, X.; Wang, L. S.; Li, P.; Xu, Q.; Rotello, V. M.; Thomas, S. W. Polymer Amphiphiles for Photoregulated Anticancer Drug Delivery. *ACS Appl. Mater. Interfaces* **2019**, *11* (3), 2814–2820.

(90) Zhu, Y.; Chen, C.; Cao, Z.; Shen, S.; Li, L.; Li, D.; Wang, J.; Yang, X. On-Demand PEGylation and DePEGylation of PLA-Based Nanocarriers via Amphiphilic MPEG-TK-Ce6 for Nanoenabled Cancer Chemotherapy. *Theranostics* **2019**, *9* (26), 8312–8320.

(91) Sun, X.; Cao, Z.; Mao, K.; Wu, C.; Chen, H.; Wang, J.; Wang, X.; Cong, X.; Li, Y.; Meng, X.; et al. Photodynamic Therapy Produces Enhanced Efficacy of Antitumor Immunotherapy by Simultaneously Inducing Intratumoral Release of Sorafenib. *Biomaterials* **2020**, *240*, 119845.

(92) Yu, H.; Jin, F.; Liu, D.; Shu, G.; Wang, X.; Qi, J.; Sun, M.; Yang, P.; Jiang, S.; Ying, X.; et al. ROS-Responsive Nano-Drug Delivery System Combining Mitochondria-Targeting Ceria Nanoparticles with Atorvastatin for Acute Kidney Injury. *Theranostics* **2020**, *10* (5), 2342–2357.

(93) Lee, J.; Park, J.; Singha, K.; Kim, W. J. Mesoporous Silica Nanoparticle Facilitated Drug Release through Cascade Photosensitizer Activation and Cleavage of Singlet Oxygen Sensitive Linker. *Chem. Commun.* **2013**, *49* (15), 1545–1547.

(94) Yuan, Y.; Liu, J.; Liu, B. Conjugated-Polyelectrolyte-Based Polyprodrug: Targeted and Image-Guided Photodynamic and Chemotherapy with on-Demand Drug Release upon Irradiation with a Single Light Source. *Angew. Chem. Int. Ed. Engl.* **2014**, *53* (28), 7163–7168.

(95) Bio, M.; Rajaputra, P.; Nkepang, G.; You, Y. Far-Red Light Activatable, Multifunctional Prodrug for Fluorescence Optical Imaging and Combinational Treatment. *J. Med. Chem.* **2014**, *57* (8), 3401–3409.

(96) Yue, C.; Zhang, C.; Alfranca, G.; Yang, Y.; Jiang, X.; Yang, Y.; Pan, F.; de la Fuente, J. M.; Cui, D. Near-Infrared Light Triggered Ros-Activated Theranostic Platform Based on Ce6-Cpt-Ucnps for Simultaneous Fluorescence Imaging and Chemo-Photodynamic Combined Therapy. *Theranostics* **2016**, *6* (4), 456–469.

(97) Li, J.; Cui, D.; Jiang, Y.; Huang, J.; Cheng, P.; Pu, K. Near-Infrared Photoactivatable Semiconducting Polymer Nanoblockaders for Metastasis-Inhibited Combination

Cancer Therapy. *Adv. Mater.* **2019**, *31* (46), 1905091.

(98) Tabero, A.; Planas, O.; Gallavardin, T.; Nieves, I.; Nonell, S.; Villanueva, A. Smart Dual-Functionalized Gold Nanoclusters for Spatio-Temporally Controlled Delivery of Combined Chemo- and Photodynamic Therapy. *Nanomaterials (Basel)* **2020**, *10* (12), 2474.

(99) Han, P.; Li, S.; Cao, W.; Li, Y.; Sun, Z.; Wang, Z.; Xu, H. Red Light Responsive Diselenide-Containing Block Copolymer Micelles. *J. Mater. Chem. B* **2013**, *1* (6), 740–743.

(100) Tian, Y.; Zheng, J.; Tang, X.; Ren, Q.; Wang, Y.; Yang, W. Near-Infrared Light-Responsive Nanogels with Diselenide-Cross-Linkers for on-Demand Degradation and Triggered Drug Release. *Part. Part. Syst. Charact.* **2015**, *32* (5), 547–551.

(101) Ruebner, A.; Yang, Z.; Leung, D.; Breslow, R. A Cyclodextrin Dimer with a Photocleavable Linker as a Possible Carrier for the Photosensitizer in Photodynamic Tumor Therapy. *Proc. Natl. Acad. Sci. U. S. A.* **1999**, *96* (26), 14692–14693.

(102) Liu, J.; Yang, G.; Zhu, W.; Dong, Z.; Yang, Y.; Chao, Y.; Liu, Z. Light-Controlled Drug Release from Singlet-Oxygen Sensitive Nanoscale Coordination Polymers Enabling Cancer Combination Therapy. *Biomaterials* **2017**, *146*, 40–48.

(103) Rojnik, M.; Kocbek, P.; Moret, F.; Compagnin, C.; Celotti, L.; Bovis, M. J.; Woodhams, J. H.; Macrobert, A. J.; Scheglmann, D.; Helfrich, W.; et al. In Vitro and in Vivo Characterization of Temoporfin-Loaded PEGylated PLGA Nanoparticles for Use in Photodynamic Therapy. *Nanomedicine (Lond).* **2012**, *7* (5), 663–677.

(104) Nakamura, H.; Jun, F.; Maeda, H. Development of Next-Generation Macromolecular Drugs Based on the EPR Effect: Challenges and Pitfalls. *Expert Opin. Drug Deliv.* **2015**, *12* (1), 53–64.

(105) Danhier, F.; Feron, O.; Préat, V. To Exploit the Tumor Microenvironment: Passive and Active Tumor Targeting of Nanocarriers for Anti-Cancer Drug Delivery. *J. Control. Release* **2010**, *148* (2), 135–146.

(106) Asati, S.; Pandey, V.; Soni, V. RGD Peptide as a Targeting Moiety for Theranostic Purpose: An Update Study. *Int. J. Pept. Res. Ther.* **2019**, *25* (1), 49–65.

(107) Kamaly, N.; Xiao, Z.; Valencia, P. M.; Radovic-Moreno, A. F.; Farokhzad, O. C. Targeted Polymeric Therapeutic Nanoparticles: Design, Development and Clinical Translation. *Chem. Soc. Rev.* **2012**, *41* (7), 2971–3010.

(108) Schottelius, M.; Laufer, B.; Kessler, H.; Wester, H.-J. Ligands for Mapping Alphavbeta3-Integrin Expression in Vivo. *Acc. Chem. Res.* **2009**, *42* (7), 969–980.

(109) Shi, J.; Jin, Z.; Liu, X.; Fan, D.; Sun, Y.; Zhao, H.; Zhu, Z.; Liu, Z.; Jia, B.; Wang, F. PET Imaging of Neovascularization with 68Ga-3PRGD2 for Assessing Tumor Early Response to Endostar Antiangiogenic Therapy. *Mol. Pharm.* **2014**, *11* (11), 3915–3922.

(110) Hernandez, R.; Valdovinos, H. F.; Yang, Y.; Chakravarty, R.; Hong, H.; Barnhart, T. E.; Cai, W. 44Sc: An Attractive Isotope for Peptide-Based PET Imaging. *Mol. Pharm.* **2014**, *11* (8), 2954–2961.

(111) Hu, H.; Li, D.; Liu, S.; Wang, M.; Moats, R.; Conti, P. S.; Li, Z. Integrin Alpha2beta1

Targeted GdVO4: Eu Ultrathin Nanosheet for Multimodal PET/MR Imaging. *Biomaterials* **2014**, *35* (30), 8649–8658.

(112) Tan, M.; Lu, Z.-R. Integrin Targeted MR Imaging. *Theranostics* **2012**, *1* (1), 83–101.

(113) Yoon, H. Y.; Shin, M. L.; Shim, M. K.; Lee, S.; Na, J. H.; Koo, H.; Lee, H.; Kim, J. H.; Lee, K. Y.; Kim, K.; et al. Artificial Chemical Reporter Targeting Strategy Using Bioorthogonal Click Reaction for Improving Active-Targeting Efficiency of Tumor. *Mol. Pharm.* **2017**, *14* (5), 1558–1570.

(114) Chen, Y.; Feng, S.; Liu, W.; Yuan, Z.; Yin, P.; Gao, F. Vitamin E Succinate-Grafted-Chitosan Oligosaccharide/RGD-Conjugated TPGS Mixed Micelles Loaded with Paclitaxel for U87MG Tumor Therapy. *Mol. Pharm.* **2017**, *14* (4), 1190–1203.

(115) Chen, L.; Liu, Y.; Wang, W.; Liu, K. Effect of Integrin Receptor-Targeted Liposomal Paclitaxel for Hepatocellular Carcinoma Targeting and Therapy. *Oncol. Lett.* **2015**, *10* (1), 77–84.

(116) Xiao, D.; Jia, H. Z.; Ma, N.; Zhuo, R. X.; Zhang, X. Z. A Redox-Responsive Mesoporous Silica Nanoparticle Capped with Amphiphilic Peptides by Self-Assembly for Cancer Targeting Drug Delivery. *Nanoscale* **2015**, *7* (22), 10071–10077.

(117) Malamas, A. S.; Jin, E.; Gujrati, M.; Lu, Z. R. Dynamic Contrast Enhanced MRI Assessing the Antiangiogenic Effect of Silencing HIF-1α with Targeted Multifunctional ECO/SiRNA Nanoparticles. *Mol. Pharm.* **2016**, *13* (7), 2497–2506.

(118) Frochot, C.; Stasio, B. Di; Vanderesse, R.; Belgy, M. J.; Dodeller, M.; Guillemin, F.; Viriot, M. L.; Barberi-Heyob, M. Interest of RGD-Containing Linear or Cyclic Peptide Targeted Tetraphenylchlorin as Novel Photosensitizers for Selective Photodynamic Activity. *Bioorg. Chem.* **2007**, *35*, 205–220.

(119) Srivatsan, A.; Ethirajan, M.; Pandey, S. K.; Dubey, S.; Zheng, X.; Liu, T. H.; Shibata, M.; Missert, J.; Morgan, J.; Pandey, R. K. Conjugation of CRGD Peptide to Chlorophyll a Based Photosensitizer (HPPH) Alters Its Pharmacokinetics with Enhanced Tumor-Imaging and Photosensitizing (PDT) Efficacy. *Mol. Pharm.* **2011**, *8*, 1186–1197.

(120) Zhao, Z.; Qiu, K.; Liu, J.; Hao, X.; Wang, J. Two-Photon Photodynamic Ablation of Tumour Cells Using an RGD Peptide-Conjugated Ruthenium(Ii) Photosensitiser. *Chem. Commun.* **2020**, *56* (83), 12542–12545.

(121) Cheng, Y. J.; Qin, S. Y.; Liu, W. L.; Ma, Y. H.; Chen, X. S.; Zhang, A. Q.; Zhang, X. Z. Dual-Targeting Photosensitizer-Peptide Amphiphile Conjugate for Enzyme-Triggered Drug Delivery and Synergistic Chemo-Photodynamic Tumor Therapy. *Adv. Mater. Interfaces* **2020**, *7* (19), 2000935.

(122) Li, Y.; Zhou, R.; Xiao, D.; Shi, S.; Peng, S.; Wu, S.; Wu, P.; Lin, Y. Polypeptide Uploaded Efficient Nanophotosensitizers to Overcome Photodynamic Resistance for Enhanced Anticancer Therapy. *Chem. Eng. J.* **2021**, *403*, 126344.

(123) Shimaoka, M.; Xiao, T.; Liu, J. H.; Yang, Y.; Dong, Y.; Jun, C. D.; McCormack, A.; Zhang, R.; Joachimiak, A.; Takagi, J.; et al. Structures of the AlphaL I Domain and Its Complex with ICAM-1 Reveal a Shape-Shifting Pathway for Integrin Regulation. *Cell* **2003**, *112* (1), 99–111.

(124) Wang, Y.; Xiao, W.; Zhang, Y.; Meza, L.; Tseng, H.; Takada, Y.; Ames, J. B.; Lam,

K. S. Optimization of RGD-Containing Cyclic Peptides against Alphavbeta3 Integrin. *Mol. Cancer Ther.* **2016**, *15* (2), 1–9.

(125) Weis, S. M.; Cheresh, D. A. Tumor Angiogenesis: Molecular Pathways and Therapeutic Targets. *Nat. Med.* **2011**, *17* (11), 1359–1370.

(126) Wang, F.; Li, Y.; Shen, Y.; Wang, A.; Wang, S.; Xie, T. The Functions and Applications of RGD in Tumor Therapy and Tissue Engineering. *Int. J. Mol. Sci.* **2013**, *14* (7), 13447–13462.

(127) Dijkgraaf, I.; Kruijtzer, J. A. W.; Liu, S.; Soede, A. C.; Oyen, W. J. G.; Corstens, F. H. M.; Liskamp, R. M. J.; Boerman, O. C. Improved Targeting of the Alphavbeta3 Integrin by Multimerisation of RGD Peptides. *Eur. J. Nucl. Med. Mol. Imaging* **2007**, *34* (2), 267–273.

(128) Lucie, S.; Elisabeth, G.; Stéphanie, F.; Guy, S.; Amandine, H.; Corinne, A. R.; Didier, B.; Catherine, S.; Alexeï, G.; Pascal, D.; et al. Clustering and Internalization of Integrin Alphavbeta3 with a Tetrameric RGD-Synthetic Peptide. *Mol. Ther.* **2009**, *17* (5), 837–843.

(129) Miura, Y.; Takenaka, T.; Toh, K.; Wu, S.; Nishihara, H.; Kano, M. R.; Ino, Y.; Nomoto, T.; Matsumoto, Y.; Koyama, H.; et al. Cyclic RGD-Linked Polymeric Micelles for Targeted Delivery of Platinum Anticancer Drugs to Glioblastoma through the Blood-Brain Tumor Barrier. *ACS Nano* **2013**, *7* (10), 8583–8592.

(130) Dou, X.; Nomoto, T.; Takemoto, H.; Matsui, M.; Tomoda, K.; Nishiyama, N. Effect of Multiple Cyclic RGD Peptides on Tumor Accumulation and Intratumoral Distribution of IRDye 700DX-Conjugated Polymers. *Sci. Rep.* **2018**, *8* (1), 8126.

(131) Liu, Y.; Ran, R.; Chen, J.; Kuang, Q.; Tang, J.; Mei, L.; Zhang, Q.; Gao, H.; Zhang, Z.; He, Q. Paclitaxel Loaded Liposomes Decorated with a Multifunctional Tandem Peptide for Glioma Targeting. *Biomaterials* **2014**, *35* (17), 4835–4847.

(132) Jiang, X.; Sha, X.; Xin, H.; Xu, X.; Gu, J.; Xia, W.; Chen, S.; Xie, Y.; Chen, L.; Chen, Y.; et al. Integrin-Facilitated Transcytosis for Enhanced Penetration of Advanced Gliomas by Poly(Trimethylene Carbonate)-Based Nanoparticles Encapsulating Paclitaxel. *Biomaterials* **2013**, *34* (12), 2969–2979.

(133) Ganipineni, L. P.; Ucakar, B.; Joudiou, N.; Riva, R.; Jérôme, C.; Gallez, B.; Danhier, F.; Préat, V. Paclitaxel-Loaded Multifunctional Nanoparticles for the Targeted Treatment of Glioblastoma. *J. Drug Target.* **2019**, *27* (5–6), 614–623.

(134) Kantlehner, M.; Schaffner, P.; Finsinger, D.; Meyer, J.; Jonczyk, A.; Diefenbach, B.; Nies, B.; Hölzemann, G.; Goodman, S. L.; Kessler, H. Surface Coating with Cyclic RGD Peptides Stimulates Osteoblast Adhesion and Proliferation as Well as Bone Formation. *Chembiochem* **2000**, *1* (2), 107–114.

(135) Conway, C. L.; Walker, I.; Bell, A.; Roberts, D. J. H.; Brown, S. B.; Vernon, D. I. In Vivo and in Vitro Characterisation of a Protoporphyrin IX-Cyclic RGD Peptide Conjugate for Use in Photodynamic Therapy. *Photochem. Photobiol. Sci.* **2008**.

(136) Wu, J.; Feng, S.; Liu, W.; Gao, F.; Chen, Y. Targeting Integrin-Rich Tumors with Temoporfin-Loaded Vitamin-E-Succinate-Grafted Chitosan Oligosaccharide/D-α-Tocopheryl Polyethylene Glycol 1000 Succinate Nanoparticles to Enhance Photodynamic Therapy Efficiency. *Int. J. Pharm.* **2017**, *528* (1–2), 287–298.

(137) Chen, H.; He, C.; Chen, T.; Xue, X. New Strategy for Precise Cancer Therapy: Tumor-Specific Delivery of Mitochondria-Targeting Photodynamic Therapy Agents and: In Situ O2-Generation in Hypoxic Tumors. *Biomater. Sci.* **2020**, *8* (14), 3994–4002.

(138) Baselga, J. The EGFR as a Target for Anticancer Therapy - Focus on Cetuximab. *Eur. J. Cancer* **2001**, *37* (Suppl 4), 16–22.

(139) Graham, J.; Muhsin, M.; Kirkpatrick, P. Cetuximab. *Nat. Rev. Drug Discov.* **2004**, *3* (7), 549–550.

(140) Ross, J. S.; Gray, K. E.; Webb, I. J.; Gray, G. S.; Rolfe, M.; Schenkein, D. P.; Nanus, D. M.; Millowsky, M. I.; Bander, N. H. Antibody-Based Therapeutics: Focus on Prostate Cancer. *Cancer Metastasis Rev.* **2005**, *24* (4), 521–537.

(141) Cathomas, R.; Rothermundt, C.; Klingbiel, D.; Bubendorf, L.; Jaggi, R.; Betticher, D. C.; Brauchli, P.; Cotting, D.; Droege, C.; Winterhalder, R.; et al. Efficacy of Cetuximab in Metastatic Castration-Resistant Prostate Cancer Might Depend on EGFR and PTEN Expression: Results from a Phase II Trial (SAKK 08/07). *Clin. Cancer Res.* **2012**, *18* (21), 6049–6057.

(142) Mitsunaga, M.; Ogawa, M.; Kosaka, N.; Rosenblum, L. T.; Choyke, P. L.; Kobayashi, H. Cancer Cell-Selective in Vivo near Infrared Photoimmunotherapy Targeting Specific Membrane Molecules. *Nat. Med.* **2011**, *17* (12), 1685–1691.

(143) Mitsunaga, M.; Nakajima, T.; Sano, K.; Choyke, P. L.; Kobayashi, H. Near-Infrared Theranostic Photoimmunotherapy (PIT): Repeated Exposure of Light Enhances the Effect of Immunoconjugate. *Bioconjug. Chem.* **2012**, *23* (3), 604–609.

(144) Ishida, M.; Kagawa, S.; Shimoyama, K.; Takehara, K.; Noma, K.; Tanabe, S.; Shirakawa, Y.; Tazawa, H.; Kobayashi, H.; Fujiwara, T. Trastuzumab-Based Photoimmunotherapy Integrated with Viral HER2 Transduction Inhibits Peritoneally Disseminated HER2-Negative Cancer. *Mol. Cancer Ther.* **2016**, *15* (3), 402–411.

(145) Ito, K.; Mitsunaga, M.; Nishimura, T.; Kobayashi, H.; Tajiri, H. Combination Photoimmunotherapy with Monoclonal Antibodies Recognizing Different Epitopes of Human Epidermal Growth Factor Receptor 2: An Assessment of Phototherapeutic Effect Based on Fluorescence Molecular Imaging. *Oncotarget* **2016**, *7* (12), 14143–14152.

(146) Kobayashi, H.; Choyke, P. L. Near-Infrared Photoimmunotherapy of Cancer. *Accounts Chem. Res.* **2019**, *52* (8), 2332–2339.

(147) Kobayashi, H.; Furusawa, A.; Rosenberg, A.; Choyke, P. L. Near-Infrared Photoimmunotherapy of Cancer: A New Approach That Kills Cancer Cells and Enhances Anti-Cancer Host Immunity. *Int. Immunol.* **2021**, *33* (1), 7–15.

(148) Astete, C. E.; Sabliov, C. M. Synthesis and Characterization of PLGA Nanoparticles. *J. Biomater. Sci. Polym. Ed.* **2006**, *17* (3), 247–289.

(149) Barichello, J. M.; Morishita, M.; Takayama, K.; Nagai, T. Encapsulation of Hydrophilic and Lipophilic Drugs in PLGA Nanoparticles by the Nanoprecipitation Method. *Drug Dev. Ind. Pharm.* **1999**, *25* (4), 471–476.

(150) Yallapu, M. M.; Gupta, B. K.; Jaggi, M.; Chauhan, S. C. Fabrication of Curcumin Encapsulated PLGA Nanoparticles for Improved Therapeutic Effects in Metastatic

Cancer Cells. *J. Colloid Interface Sci.* **2010**, *351* (1), 19–29.

(151) Govender, T.; Stolnik, S.; Garnett, M. C.; Illum, L.; Davis, S. S. PLGA Nanoparticles Prepared by Nanoprecipitation: Drug Loading and Release Studies of a Water Soluble Drug. *J. Control. Release* **1999**, *57* (1), 171–185.

(152) Stöber, W.; Fink, A.; Bohn, E. Controlled Growth of Monodisperse Silica Spheres in the Micron Size Range. *J. Colloid Interface Sci.* **1968**, *26*, 62–69.

(153) Grün, M.; Lauer, I.; Unger, K. K. The Synthesis of Micrometer- and Submicrometer-Size Spheres of Ordered Mesoporous Oxide MCM-41. *Adv. Mater.* **1997**, *9*, 254–256.

(154) Yano, K.; Fukushima, Y. Synthesis of Mono-Dispersed Mesoporous Silica Spheres with Highly Ordered Hexagonal Regularity Using Conventional Alkyltrimethylammonium Halide as a Surfactant. *J. Mater. Chem.* **2004**, *14*, 1579–1584.

(155) Sterman, S.; Marsden, J. G. Silane Coupling Agents. *Ind. Eng. Chem.* **1966**, *58* (3), 33–37.

(156) Chiang, C. H.; Liu, N. I.; Koenig, J. L. Magic-Angle Cross-Polarization Carbon 13 NMR Study of Aminosilane Coupling Agents on Silica Surfaces. *J. Colloid Interface Sci.* **1982**, *86* (1), 26–34.

(157) Vandenberg, E. T.; Bertilsson, L.; Liedberg, B.; Uvdal, K.; Erlandsson, R.; Elwing, H.; Lundström, I. Structure of 3-Aminopropyl Triethoxy Silane on Silicon Oxide. *J. Colloid Interface Sci.* **1991**, *147* (1), 103–118.

(158) Hoare, D. G.; Koshland, D. E. A Procedure for the Selective Modification of Carboxyl Groups in Proteins. *J. Am. Chem. Soc.* **1966**, *88* (9), 2057–2058.

(159) Chu, B. C. F.; Kramer, F. R.; Orgel, L. E. Synthesis of an Amplifiable Reporter RNA for Bioassays. *Nucleic Acids Res.* **1986**, *14* (14), 5591–5603.

(160) Ghosh, S. S.; Kao, P. M.; McCue, A. W.; Chappelle, H. L. Use of Maleimide-Thiol Coupling Chemistry for Efficient Syntheses of Oligonucleotide-Enzyme Conjugate Hybridization Probes. *Bioconjug. Chem.* **1990**, *1* (1), 71–76.

(161) Staros, J. V. N-Hydroxysulfosuccinimide Active Esters: Bis(N-Hydroxysulfosuccinimide) Esters of Two Dicarboxylic Acids Are Hydrophilic, Membrane-Impermeant, Protein Cross-Linkers. *Biochemistry* **1982**, *21* (17), 3950–3955.

(162) Borque, L.; Maside, C.; Rus, A.; Del Cura, J. Latex Immunoassay of B2-Microglobulin in Serum and Urine. *J. Clin. Immunoassay* **1994**, *17* (3), 160–165.

(163) Bonfield, T. L.; John, N.; Barna, B. P.; Kavuru, M. S.; Thomassen, M. J.; Yen-Lieberman, B. Multiplexed Particle-Based Anti-Granulocyte Macrophage Colony Stimulating Factor Assay Used as Pulmonary Diagnostic Test. *Clin. Diagn. Lab. Immunol.* **2005**, *12* (7), 821–824.

(164) Gilles, M. A.; Hudson, A. Q.; Borders, C. L. Stability of Water-Soluble Carbodiimides in Aqueous Solution. *Anal. Biochem.* **1990**, *184* (2), 244–248.

(165) Rhys Williams, A. T.; Winfield, S. A.; Miller, J. N. Relative Fluorescence Quantum

Yields Using a Computer-Controlled Luminescence Spectrometer. *Analyst* **1983**, *108* (1290), 1067–1071.

(166) Horiba. A Guide to Recording Fluorescence Quantum Yields. https://static.horiba.com/fileadmin/Horiba/Application/Materials/Material_Research/Quantum_Dots/quantumyieldstrad.pdf (accessed March 25, 2020).

(167) Nonell, S.; Viappiani, C. Basic Spectroscopy. In *Photobiological Sciences Online*; Lee, J., Smith, K. C., Eds.; American Society for Photobiology, 2007.

(168) Abbruzzetti, S.; Bruno, S.; Faggiano, S.; Grandi, E.; Mozzarelli, A.; Viappiani, C. Time-Resolved Methods in Biophysics. 2. Monitoring Haem Proteins at Work with Nanosecond Laser Flash Photolysis. *Photochem. Photobiol. Sci.* **2006**, *5* (12), 1109–1120.

(169) Jiménez-Banzo, A.; Ragàs, X.; Kapusta, P.; Nonell, S. Time-Resolved Methods in Biophysics. 7. Photon Counting vs. Analog Time-Resolved Singlet Oxygen Phosphorescence Detection. *Photochem. Photobiol. Sci.* **2008**, *7* (9), 1003.

(170) Becker, W. *Advanced Time-Correlated Single Photon Counting Techniques*; Castleman, A. W., Toennies, J. P., Zinth, W., Eds.; Springer Series in Chemical Physics; Springer Berlin Heidelberg: Berlin, Heidelberg, 2005; Vol. 81.

(171) Becker, W.; Bergmann, A.; Biscotti, G.; Rück, A. Advanced Time-Correlated Single Photon Counting Technique for Spectroscopy and Imaging in Biomedical Systems. *Springer* **2004**, *5340*, 1–9.

(172) Jiménez-Banzo, A.; Ragàs, X.; Kapusta, P.; Nonell, S. Time-Resolved Methods in Biophysics. 7. Photon Counting vs. Analog Time-Resolved Singlet Oxygen Phosphorescence Detection. *Photochem. Photobiol. Sci.* **2008**, *7* (9), 1003–1010.

(173) Nonell, S.; Flors, C. Chapter 25. Steady-State and Time-Resolved Singlet Oxygen Phosphorescence Detection in the Near-IR. In *Singlet Oxygen: Applications in Biosciences and Nanosciences*; Nonell, S., Flors, C., Eds.; Royal Society of Chemistry, 2016; pp 7–26.

(174) Nonell, S.; Braslavsky, S. E. Time-Resolved Singlet Oxygen Detection. *Methods Enzymol.* **2000**, *319*, 37–49.

(175) Tsien, R. Y.; Waggoner, A. Fluorophores for Confocal Microscopy. In *Handbook of Biological Confocal Microscopy*; Springer, Boston, MA, 1995; pp 267–279.

(176) Ettinger, A.; Wittmann, T. Fluorescence Live Cell Imaging. *Methods Cell Biol.* **2014**, *123*, 77–94.

(177) ThermoFisher. Epifluorescence Microscope Basics. https://www.thermofisher.com/es/es/home/life-science/cell-analysis/cell-analysis-learning-center/molecular-probes-school-of-fluorescence/fundamentals-of-fluorescence-microscopy/epifluorescence-microscope-basics.html (accessed March 17, 2020).

(178) Nikon. Introductory Confocal Concepts. https://www.microscopyu.com/techniques/confocal/introductory-confocal-concepts (accessed March 20, 2020).

(179) Laser2000. Confocal Microscopy. https://www.laser2000.co.uk/applications/confocal-

microscopy (accessed March 20, 2020).

(180) Olympus. Concepts in Confocal Microscopy. https://www.olympus-lifescience.com/en/microscope-resource/primer/techniques/confocal/confocalintro/ (accesed March 20, 2020).

(181) Carvalho, P. M.; Felício, M. R.; Santos, N. C.; Gonçalves, S.; Domingues, M. M. Application of Light Scattering Techniques to Nanoparticle Characterization and Development. *Front. Chem.* **2018**, *6*, 237.

(182) Lim, J.; Yeap, S. P.; Che, H. X.; Low, S. C. Characterization of Magnetic Nanoparticle by Dynamic Light Scattering. *Nanoscale Res. Lett.* **2013**, *8* (1), 381.

(183) TechnicalCommitteeISO/TC24. ISO 22412:2017 Particle size analysis - Dynamic light scattering (DLS). https://www.iso.org/obp/ui/#iso:std:iso:22412:ed-2:v1:en (accessed March 25, 2020).

(184) Kaszuba, M.; Corbett, J.; Watson, F. M. N.; Jones, A. High-Concentration Zeta Potential Measurements Using Light-Scattering Techniques. *Philos. Trans. A Math. Phys. Eng. Sci.* **2010**, *368* (1927), 4439–4451.

(185) Bhattacharjee, S. DLS and Zeta Potential - What They Are and What They Are Not? *J. Control. Release* **2016**, *235*, 337–351.

(186) Smith, P. K.; Krohn, R. I.; Hermanson, G. T.; Mallia, A. K.; Gartner, F. H.; Provenzano, M. D.; Fujimoto, E. K.; Goeke, N. M.; Olson, B. J.; Klenk, D. C. Measurement of Protein Using Bicinchoninic Acid. *Anal. Biochem.* **1985**, *150* (1), 76–85.

(187) Wiechelman, K. J.; Braun, R. D.; Fitzpatrick, J. D. Investigation of the Bicinchoninic Acid Protein Assay: Identification of the Groups Responsible for Color Formation. *Anal. Biochem.* **1988**, *175* (1), 231–237.

(188) Mosmann, T. Rapid Colorimetric Assay for Cellular Growth and Survival: Application to Proliferation and Cytotoxicity Assays. *J. Immunol. Methods* **1983**, *65* (1–2), 55–63.

(189) Berridge, M. V.; Tan, A. S. Characterization of the Cellular Reduction of 3-(4,5-Dimethylthiazol-2-Yl)-2,5-Diphenyltetrazolium Bromide (MTT): Subcellular Localization, Substrate Dependence, and Involvement of Mitochondrial Electron Transport in MTT Reduction. *Arch. Biochem. Biophys.* **1993**, *303* (2), 474–482.

(190) Berridge, M.; Tan, A.; McCoy, K.; Wang, R. The Biochemical and Cellular Basis of Cell Proliferation Assays That Use Tetrazolium Salts. *Biochemica* **1996**, *4*, 15–20.

(191) Marshall, N. J.; Goodwin, C. J.; Holt, S. J. A Critical Assessment of the Use of Microculture Tetrazolium Assays to Measure Cell Growth and Function. *Growth Regul.* **1995**, *5* (2), 69–84.

(192) Murphy, E. A.; Majeti, B. K.; Barnes, L. A.; Makale, M.; Weis, S. M.; Lutu-Fuga, K.; Wrasidlo, W.; Cheresh, D. A. Nanoparticle-Mediated Drug Delivery to Tumor Vasculature Suppresses Metastasis. *Proc. Natl. Acad. Sci. U. S. A.* **2008**, *105*, 9343–9348.

(193) Danhier, F.; Pourcelle, V.; Marchand-Brynaert, J.; Jérôme, C.; Feron, O.; Préat, V. Targeting of Tumor Endothelium by RGD-Grafted PLGA-Nanoparticles. *Methods Enzymol.* **2012**, *508*, 157–175.

(194) Boix-Garriga, E.; Acedo, P.; Casadó, A.; Villanueva, A.; Stockert, J. C.; Cañete, M.; Mora, M.; Sagristá, M. L.; Nonell, S. Poly(D,L-Lactide-Co-Glycolide) Nanoparticles as Delivery Agents for Photodynamic Therapy: Enhancing Singlet Oxygen Release and Phototototoxicity by Surface PEG Coating. *Nanotechnology* **2015**, *26* (36), 365104.

(195) de las Heras, E.; Boix-Garriga, E.; Bryden, F.; Agut, M.; Mora, M.; Sagristá, M. L.; Boyle, R. W.; Lange, N.; Nonell, S. C(RGDfK)- and ZnTriMPyP-Bound Polymeric Nanocarriers for Tumor-Targeted Photodynamic Therapy. *Photochem. Photobiol.* **2020**, *96* (3), 570–580.

(196) Cheng, J.; Teply, B. A.; Sherifi, I.; Sung, J.; Luther, G.; Gu, F. X.; Levy-Nissenbaum, E.; Radovic-Moreno, A. F.; Langer, R.; Farokhzad, O. C. Formulation of Functionalized PLGA-PEG Nanoparticles for in Vivo Targeted Drug Delivery. *Biomaterials* **2007**, *28* (5), 869–876.

(197) Langer, R.; Verbavatz, J. M.; Quellec, P.; Gref, R.; Domb, A.; Müller, R. H.; Blunk, T. The Controlled Intravenous Delivery of Drugs Using PEG-Coated Sterically Stabilized Nanospheres. *Adv. Drug Deliv. Rev.* **1995**, *16* (2–3), 215–233.

(198) Otsuka, H.; Nagasaki, Y.; Kataoka, K. PEGylated Nanoparticles for Biological and Pharmaceutical Applications. *Adv. Drug Deliv. Rev.* **2003**, *55* (3), 403–419.

(199) Yang, Q.; Lai, S. K. Anti-PEG Immunity: Emergence, Characteristics, and Unaddressed Questions. *Wiley Interdiscip. Rev. Nanomed. Nanobiotechnol.* **2015**, *7* (5), 655–677.

(200) Boix-Garriga, E. Biodegradable Poly-(D,L-Lactide) and Poly-(D,L-Lactide-Co-Glycolide) Nanoparticles for Photodynamic Therapy (PhD Thesis), 2016.

(201) Danhier, F.; Lecouturier, N.; Vroman, B.; Jérôme, C.; Marchand-Brynaert, J.; Feron, O.; Préat, V. Paclitaxel-Loaded PEGylated PLGA-Based Nanoparticles: In Vitro and in Vivo Evaluation. *J. Control. Release* **2009**, *133* (1), 11–17.

(202) Fang, J.; Nakamura, H.; Maeda, H. The EPR Effect: Unique Features of Tumor Blood Vessels for Drug Delivery, Factors Involved, and Limitations and Augmentation of the Effect. *Adv. Drug Deliv. Rev.* **2011**, *63* (3), 136–151.

(203) Graf, N.; Bielenberg, D. R.; Kolishetti, N.; Muus, C.; Banyard, J.; Farokhzad, O. C.; Lippard, S. J. Alphavbeta3 Integrin-Targeted PLGA-PEG Nanoparticles for Enhanced Anti-Tumor Efficacy of a Pt(IV) Prodrug. *ACS Nano* **2012**, *6* (5), 4530–4539.

(204) Foged, C.; Brodin, B.; Frokjaer, S.; Sundblad, A. Particle Size and Surface Charge Affect Particle Uptake by Human Dendritic Cells in an in Vitro Model. *Int. J. Pharm.* **2005**, *298* (2), 315–322.

(205) Vasir, J. K.; Labhasetwar, V. Quantification of the Force of Nanoparticle-Cell Membrane Interactions and Its Influence on Intracellular Trafficking of Nanoparticles. *Biomaterials* **2008**, *29* (31), 4244–4252.

(206) Gajbhiye, K. R.; Gajbhiye, V.; Siddiqui, I. A.; Gajbhiye, J. M. CRGD Functionalised Nanocarriers for Targeted Delivery of Bioactives. *J. Drug Target.* **2019**, *27* (2), 111–124.

(207) Cai, W.; Chen, X. Preparation of Peptide-Conjugated Quantum Dots for Tumor

Vasculature-Targeted Imaging. *Nat. Protoc.* **2008**, *3* (1), 89–96.

(208) Liu, Y.; Li, L.; Guo, Q.; Wang, L.; Liu, D.; Wei, Z.; Zhou, J. Novel Cs-Based Upconversion Nanoparticles as Dual-Modal CT and UCL Imaging Agents for Chemo-Photothermal Synergistic Therapy. *Theranostics* **2016**, *6* (10), 1491–1505.

(209) Xu, Q.; Liu, Y.; Su, S.; Li, W.; Chen, C.; Wu, Y. Anti-Tumor Activity of Paclitaxel through Dual-Targeting Carrier of Cyclic RGD and Transferrin Conjugated Hyperbranched Copolymer Nanoparticles. *Biomaterials* **2012**, *33* (5), 1627–1639.

(210) Borgne-Sanchez, A.; Dupont, S.; Langonné, A.; Baux, L.; Lecoeur, H.; Chauvier, D.; Lassalle, M.; Déas, O.; Brière, J. J.; Brabant, M.; et al. Targeted Vpr-Derived Peptides Reach Mitochondria to Induce Apoptosis of Alphavbeta3-Expressing Endothelial Cells. *Cell Death Differ.* **2007**, *14* (3), 422–435.

(211) He, S.; Cen, B.; Liao, L.; Wang, Z.; Qin, Y.; Wu, Z.; Liao, W.; Zhang, Z.; Ji, A. A Tumor-Targeting CRGD-EGFR SiRNA Conjugate and Its Anti-Tumor Effect on Glioblastoma in Vitro and in Vivo. *Drug Deliv.* **2017**, *24* (1), 471–481.

(212) Tang, X. long; Wu, J.; Lin, B. lan; Cui, S.; Liu, H. mei; Yu, R. tong; Shen, X. dong; Wang, T. wei; Xia, W. Near-Infrared Light-Activated Red-Emitting Upconverting Nanoplatform for T1-Weighted Magnetic Resonance Imaging and Photodynamic Therapy. *Acta Biomater.* **2018**, *74*, 360–373.

(213) Yan, F.; Wu, H.; Liu, H.; Deng, Z.; Liu, H.; Duan, W.; Liu, X.; Zheng, H. Molecular Imaging-Guided Photothermal/Photodynamic Therapy against Tumor by IRGD-Modified Indocyanine Green Nanoparticles. *J. Control. Release* **2016**, *224*, 217–228.

(214) Wu, J.; Lin, Y.; Li, H.; Jin, Q.; Ji, J. Zwitterionic Stealth Peptide-Capped 5-Aminolevulinic Acid Prodrug Nanoparticles for Targeted Photodynamic Therapy. *J. Colloid Interface Sci.* **2017**, *485*, 251–259.

(215) Zhang, Y.; Huang, F.; Ren, C.; Yang, L.; Liu, J.; Cheng, Z.; Chu, L.; Liu, J. Targeted Chemo-Photodynamic Combination Platform Based on the DOX Prodrug Nanoparticles for Enhanced Cancer Therapy. *ACS Appl. Mater. Interfaces* **2017**, *9* (15), 13016–13028.

(216) Lim, C.; Moon, J.; Sim, T.; Hoang, N. H.; Won, W. R.; Lee, E. S.; Youn, Y. S.; Choi, H. G.; Oh, K.; Oh, K. T. Cyclic RGD-Conjugated Pluronic® Blending System for Active, Targeted Drug Delivery. *Int. J. Nanomedicine* **2018**, *13*, 4627–4639.

(217) Yin, P.; Wang, Y.; Qiu, Y. Y.; Hou, L. L.; Liu, X.; Qin, J.; Duan, Y.; Liu, P.; Qiu, M.; Li, Q. Bufalin-Loaded MPEG-PLGA-PLL-CRGD Nanoparticles: Preparation, Cellular Uptake, Tissue Distribution, and Anticancer Activity. *Int. J. Nanomedicine* **2012**, *7*, 3961–3969.

(218) Galstyan, A.; Riehemann, K.; Schäfers, M.; Faust, A. A Combined Experimental and Computational Study of the Substituent Effect on the Photodynamic Efficacy of Amphiphilic Zn(II)Phthalocyanines. *J. Mater. Chem. B* **2016**, *4* (34), 5683–5691.

(219) von Felbert, V.; Bauerschlag, D.; Maass, N.; Bräutigam, K.; Meinhold-Heerlein, I.; Woitok, M.; Barth, S.; Hussain, A. F. A Specific Photoimmunotheranostics Agent to Detect and Eliminate Skin Cancer Cells Expressing EGFR. *J. Cancer Res. Clin. Oncol.* **2016**, *142* (5), 1003–1011.

(220) Sadraeian, M.; Bahou, C.; da Cruz, E. F.; Janini, L. M. R.; Diaz, R. S.; Boyle, R. W.;

Chudasama, V.; Guimarães, F. E. G. Photoimmunotherapy Using Cationic and Anionic Photosensitizer-Antibody Conjugates against Hiv Env-Expressing Cells. *Int. J. Mol. Sci.* **2020**, *21* (23), 9151.

(221) Boss, M.; Bos, D.; Frielink, C.; Sandker, G.; Bronkhorst, P.; Van Lith, S. A. M.; Brom, M.; Buitinga, M.; Gotthardt, M. Receptor-Targeted Photodynamic Therapy of Glucagon-like Peptide 1 Receptor-Positive Lesions. *J. Nucl. Med.* **2020**, *61* (11), 1588–1593.

(222) Ngen, E. J.; Chen, Y.; Azad, B. B.; Boinapally, S.; Jacob, D.; Lisok, A.; Shen, C.; Hossain, M. S.; Jin, J.; Bhujwalla, Z. M.; et al. Prostate-Specific Membrane Antigen (PSMA)-Targeted Photodynamic Therapy Enhances the Delivery of PSMA-Targeted Magnetic Nanoparticles to PSMA-Expressing Prostate Tumors. *Nanotheranostics* **2021**, *5* (2), 182–196.

(223) Baker, J. W.; Gaunt, J. The Mechanism of the Reaction of Aryl Isocyanates with Alcohols and Amines. Part II. The Base-Catalysed Reaction of Phenyl Isocyanate with Alcohols. *J. Chem. Soc.* **1949**, 9–18.

(224) Hermanson, G. T. *Bioconjugate Techniques*; Academic Press, 2013.

(225) Grabarek, Z.; Gergely, J. Zero-Length Crosslinking Procedure with the Use of Active Esters. *Anal. Biochem.* **1990**, *185* (1), 131–135.

(226) Nakajima, N.; Ikada, Y. Mechanism of Amide Formation by Carbodiimide for Bioconjugation in Aqueous Media. *Bioconjug. Chem.* **1995**, *6* (1), 123–130.

(227) *Phthalocyanines: Properties and Applications*; Leznoff, C. C., Lever, A. B. P., Eds.; VCH PUBLISHERS INC: New York, NY, 1989.

(228) Scalise, I.; Durantini, E. N. Synthesis, Properties, and Photodynamic Inactivation of Escherichia Coli Using a Cationic and a Noncharged Zn(II) Pyridyloxyphthalocyanine Derivatives. *Bioorg. Med. Chem.* **2005**, *13* (8), 3037–3045.

(229) Spiller, W.; Kliesch, H.; Wöhrle, D.; Hackbarth, S.; Röder, B.; Schnurpfeil, G. Singlet Oxygen Quantum Yields of Different Photo-Sensitizers in Polar Solvents and Micellar Solutions. *J. Porphyr. Phthalocyanines* **1998**, *2* (2), 145–158.

(230) Nonell, S.; González, M.; Trull, F. R. 1H-Phenalen-1-One-2-Sulfonic Acid: An Extremely Efficient Singlet Molecular Oxygen Sensitizer for Aqueous Media. *Afinidad* **1993**, *44*, 445–450.

(231) Martí, C.; Jürgens, O.; Cuenca, O.; Casals, M.; Nonell, S. Aromatic Ketones as Standards for Singlet Molecular Oxygen Photosensitization. Time-Resolved Photoacoustic and near-IR Emission Studies. *J. Photochem. Photobiol. A* **1996**, *97*, 11–18.

(232) Wilkinson, F.; Helman, W. P.; Ross, A. B. Rate Constants for the Decay and Reactions of the Lowest Electronically Excited Singlet State of Molecular Oxygen in Solution. An Expanded and Revised Compilation. *J. Phys. Chem. Ref. Data* **1995**, *24* (2), 663–677.

(233) Patra, C. R.; Bhattacharya, R.; Wang, E.; Katarya, A.; Lau, J. S.; Dutta, S.; Muders, M.; Wang, S.; Buhrow, S. A.; Safgren, S. L.; et al. Targeted Delivery of Gemcitabine to Pancreatic Adenocarcinoma Using Cetuximab as a Targeting Agent. *Cancer Res.* **2008**, *68* (6), 1970–1978.

(234) Er, Ö.; Colak, S. G.; Ocakoglu, K.; Ince, M.; Bresolí-Obach, R.; Mora, M.; Sagristá, M. L.; Yurt, F.; Nonell, S. Selective Photokilling of Human Pancreatic Cancer Cells Using Cetuximab-Targeted Mesoporous Silica Nanoparticles for Delivery of Zinc Phthalocyanine. *Molecules* **2018**, *23* (11), 2749.

(235) Fan, Z.; Shang, B. Y.; Lu, Y.; Chou, J. L.; Mendelsohn, J. Reciprocal Changes in P27(Kip1) and P21(Cip1) in Growth Inhibition Mediated by Blockade or Overstimulation of Epidermal Growth Factor Receptors. *Clin. Cancer Res.* **1997**, *3* (11), 1943–1948.

(236) Wu, X.; Fan, Z.; Masui, H.; Rosen, N.; Mendelsohn, J. Apoptosis Induced by an Anti-Epidermal Growth Factor Receptor Monoclonal Antibody in a Human Colorectal Carcinoma Cell Line and Its Delay by Insulin. *J. Clin. Invest.* **1995**, *95* (4), 1897–1905.

(237) Huang, S. M.; Harari, P. M. Modulation of Radiation Response after Epidermal Growth Factor Receptor Blockade in Squamous Cell Carcinomas: Inhibition of Damage Repair, Cell Cycle Kinetics, and Tumor Angiogenesis. *Clin. Cancer Res.* **2000**, *6* (6), 2166–2174.

(238) Bruns, C. J.; Harbison, M. T.; Davis, D. W.; Portera, C. A.; Tsan, R.; McConkey, D. J.; Evans, D. B.; Abbruzzese, J. L.; Hicklin, D. J.; Radinsky, R. Epidermal Growth Factor Receptor Blockade with C225 plus Gemcitabine Results in Regression of Human Pancreatic Carcinoma Growing Orthotopically in Nude Mice by Antiangiogenic Mechanisms. *Clin. Cancer Res.* **2000**, *6* (5), 1936–1948.

(239) LICOR. IRDye® 700DX NHS Ester Infrared Dye. https://www.licor.com/documents/4oxjnh3t7n8i4wo9mgby0cyxqojcbauq (accessed August 25, 2020).

(240) Li, F.; Zhao, Y.; Mao, C.; Kong, Y.; Ming, X. RGD-Modified Albumin Nanoconjugates for Targeted Delivery of a Porphyrin Photosensitizer. *Mol. Pharm.* **2017**, *14* (8), 2793–2804.

(241) Deken, M. M.; Kijanka, M. M.; Beltrán Hernández, I.; Slooter, M. D.; de Bruijn, H. S.; van Diest, P. J.; van Bergen en Henegouwen, P. M. P.; Lowik, C. W. G. M.; Robinson, D. J.; Vahrmeijer, A. L.; et al. Nanobody-Targeted Photodynamic Therapy Induces Significant Tumor Regression of Trastuzumab-Resistant HER2-Positive Breast Cancer, after a Single Treatment Session. *J. Control. Release* **2020**, *323*, 269–281.

(242) Remzi Becer, C.; Hoogenboom, R.; Schubert, U. S. Click Chemistry beyond Metal-Catalyzed Cycloaddition. *Angew. Chem. Int. Ed. Engl.* **2009**, *48* (27), 4900–4908.

APPENDIX A: ADDITIONAL INFORMATION FOR CHAPTER 4

A.1 Synthesis of PLGA-ZnTriMPyP

The synthetic procedure of the conjugate PLGA-ZnTriMPyP is shown in Figure A1. The conjugate was previously synthesized as described in Boix-Garriga *et al.*[200]. Briefly, the synthetic strategy followed to covalently bind the PS to PLGA was a two-step procedure comprising: (i) the derivatization of the terminal carboxylic acid group of the PLGA into a terminal alkyne group; (ii) its subsequent linkage to the azido-derivatized ZnTriMPyP by CuAAC. This strategy enabled the attachment of the porphyrin to the polymeric chain of PLGA in good yield, 71% conjugation as quantified by absorption spectroscopy. ^{1}H-NMR of the final PLGA-ZnTriMPyP conjugate confirmed the presence of the porphyrin.

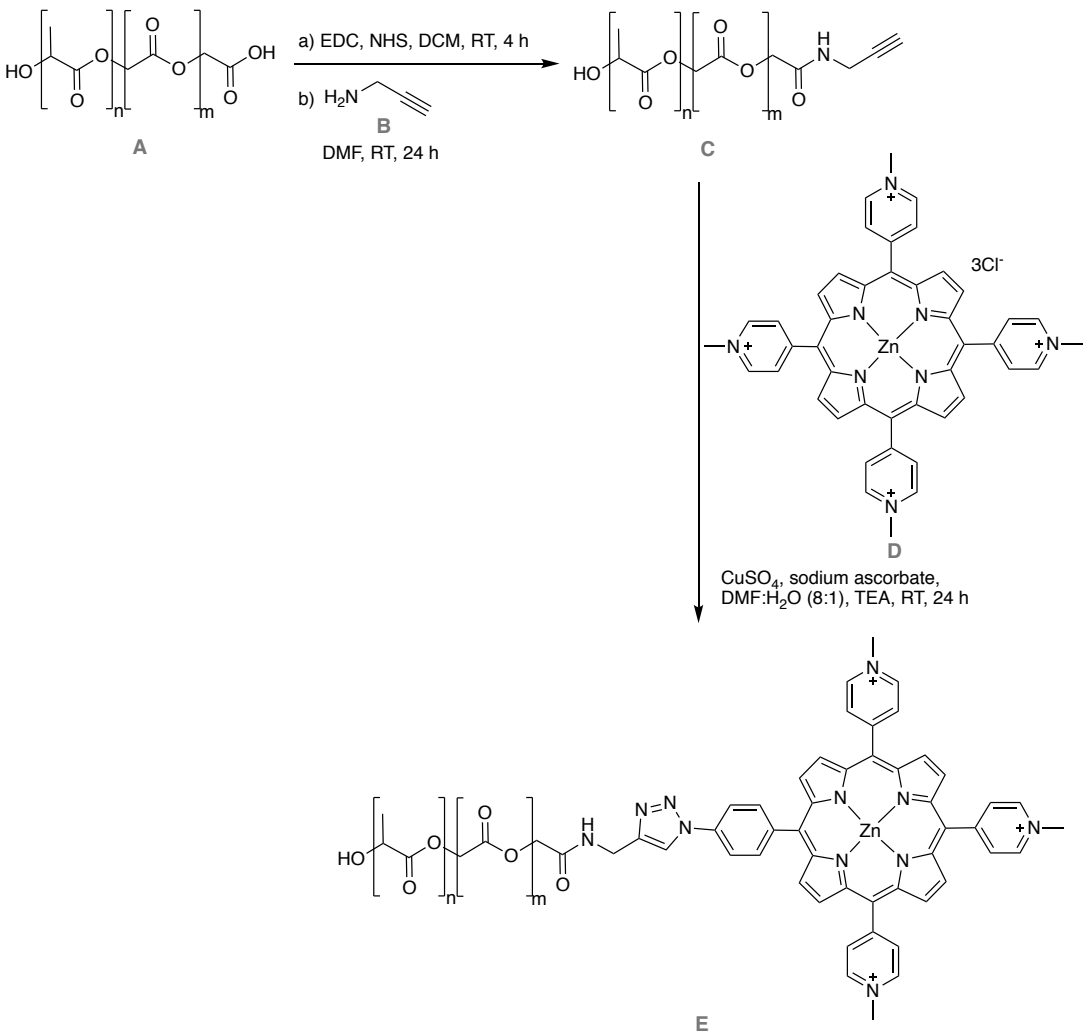

Figure A1. Synthetic steps for the preparation of PLGA-ZnTriMPyP conjugate.

A.2 Synthesis of PLA-PEG-c(RGDfK)

The synthesis of the conjugate PLA-PEG-c(RGDfK) is shown in Figure A2 and Figure A3. The conjugate was previously synthesized as described in de las Heras *et al*.[195]. PLA was conjugated to polyethylene glycol (PEG) and c(RGDfK) peptide by 5 main steps. On the one hand, the terminal group of PLA (**F**) was chemically modified with 2*H*-1-(3'-amino-propionyl)-dibenzo[b,f]azacyclooctyne (DBCO-NH_2) (**G**) *via N*-acylation in order to introduce an alkyne group to further perform an azide-alkyne cycloaddition (Figure A2).

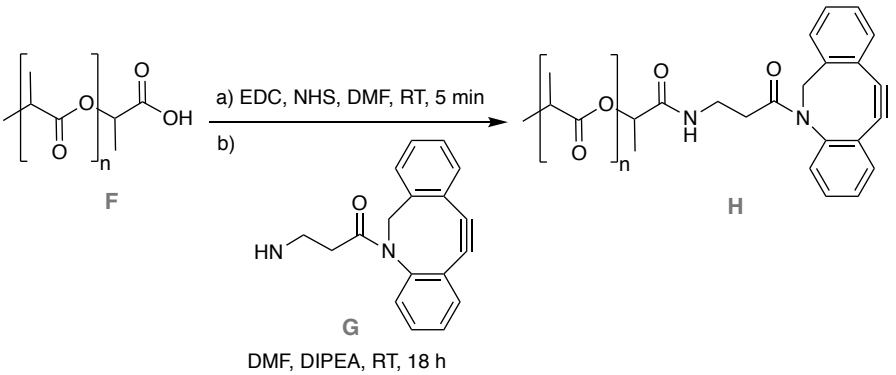

Figure A2. Conjugation of PLA with DBCO-NH_2 *via N*-acylation.

On the other hand, c(RGDfK) peptide (**J**) was first coupled to a bifunctional PEG (NHS-PEG-Boc, **I**) *via N*-acylation. Next, the terminal Boc protecting group of the synthesized Boc-PEG-c(RGDfK) (**K**) was deprotected to yield NH_2-PEG-c(RGDfK) (**L**). Subsequently, this amino group was chemically modified by *N*-acylation with azidoacetic acid NHS ester in order to introduce a terminal azido group on PEG-c(RGDfK) (**N**). Finally, the previously synthesized PLA-DBCO (**H**) was coupled by metal free azide-alkyne [3+2] cycloaddition[242], yielding PLA-PEG-c(RGDfK) (**O**) (Figure A3).

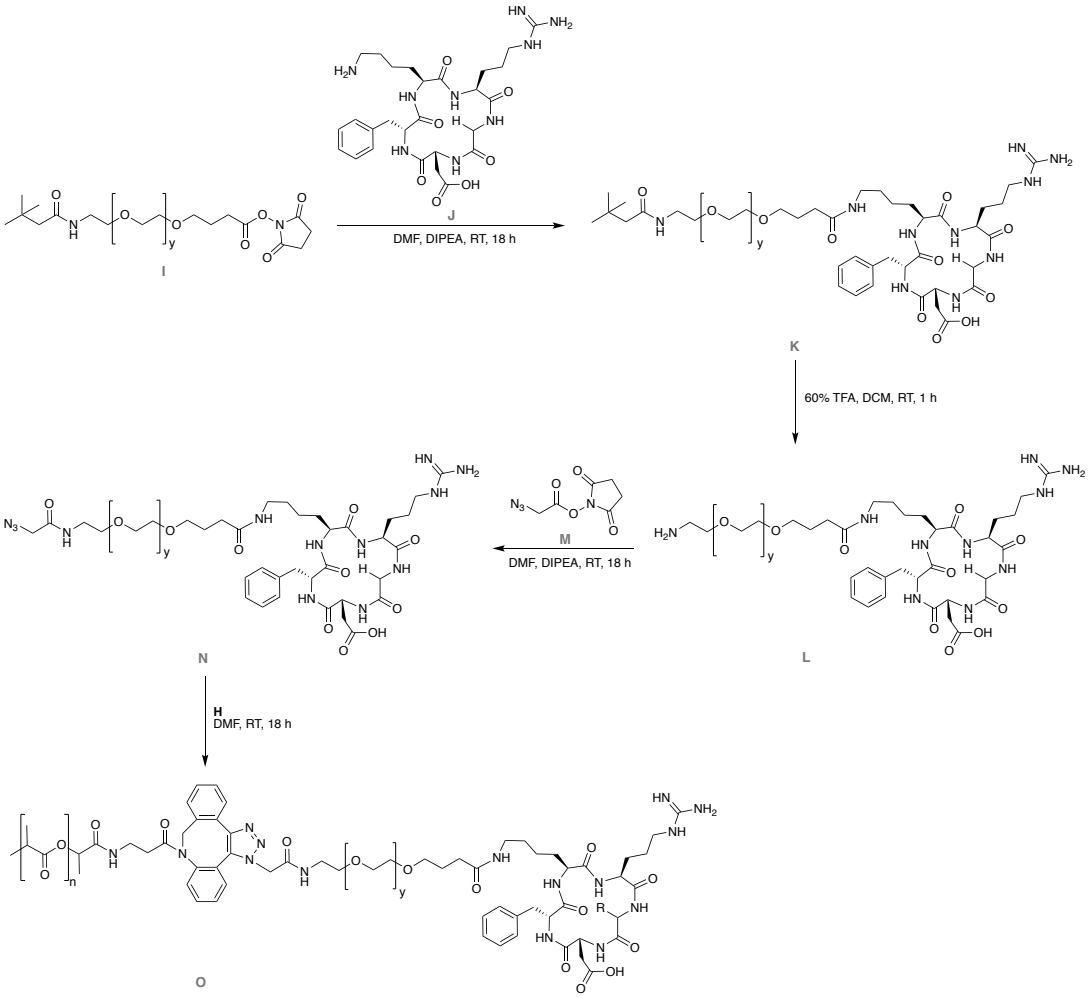

Figure A3. Firstly, conjugation of bifunctional PEG to c(RGDfK) peptide and subsequent PEG terminal amine deprotection. Secondly, functionalization of PEG with an azido group and following conjugation to PLA-alkynyl derivative.

A.3 Study of c(RGDfK)-bound and Ppa occluded polymeric NPs

A study of c(RGDfK)-bound and Ppa occluded polymeric nanoparticles was previously carried out in our group with the collaboration of the Laboratory of Pharmaceutical Technology from the University of Geneva (Switzerland), led by Prof. Norbert Lange. The results of this investigation are not published. Since the nanoparticle system studied in this prior investigation is really interesting for a better comprehension and comparison of the results obtained in Chapter 4, the relevant data of this work are shown on following. The results in this section have been extracted from the PhD thesis of Ester Boix Garriga.

A.3.1 Preparation and Characterization of c(RGDfK)-bound and Ppa Occluded NPs

Nanoparticles were prepared following the same procedure as described in Chapter 4. An acetone solution containing 9 mg/mL of polymer and 1.2% w/w pyropheophorbide *a* (Ppa) was injected dropwise to an aqueous solution of 0.4% PVA (organic phase : aqueous phase 1:2). All formulations contained 90% PLA R202 (ester end-capped). The remaining 10% of polymer was the peptide conjugate PLA-PEG-c(RGDfK). The results of the physicochemical characterization of the nanoparticle are shown in Table A1.

Table A1. Physicochemical characteristics of peptide-conjugated PEG-PLA NP suspensions.

NP formulation	Size / nm	PdI	Zeta-potential / mV	[PS] / μM	% D.L.
Ppa / cRGD-PEG-PLA	167 ± 22	0.205 ± 0.057	-18 ± 2	37	37

A.3.2 Cellular Internalization of Ppa Delivered by Targeted and Non-targeted PLA-PEG NPs

In order to ascertain the targeting ability of the cRGD-grafted PLA-PEG NPs, U-87 MG were incubated with Ppa-loaded, targeted and non-targeted PLA-PEG NPs, at 1 μM of Ppa and for various time periods up to 8 h. After incubation, NPs still present in the culture medium were removed by washing and internalization of Ppa was assessed by recording its fluorescence in the attached cells, which was normalized by the amount of protein present in each sample (Figure A4).

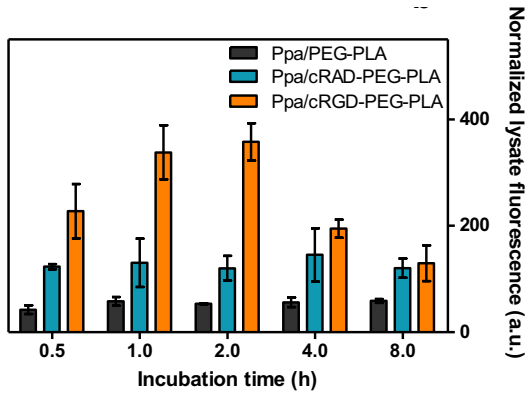

Figure A4. Normalized fluorescence of Ppa in U-87 MG cells after various incubation times Ppa / PEG-PLA, Ppa / cRAD-PEG-PLA or Ppa /cRGD-PEG-PLA NPs. Values are the mean ± SD of three replicates.

A.3.3 Photosensitization of U-87 MG cells with Ppa delivered by targeted and non-targeted PLA-PEG NPs

U-87 MG cells were incubated with Ppa / cRGD-PEG-PLA targeted NPs and the corresponding non-targeted NP suspensions at Ppa concentration of 0.1, 1 and 5 μM and subsequently irradiated at various light fluences. Cell proliferation was assessed 24 h after irradiation by the MTT assay (Figure A5). The incubation time of cells with the NPs was chosen as 1.5 h to achieve a maximum selectivity for internalization of Ppa in the cells.

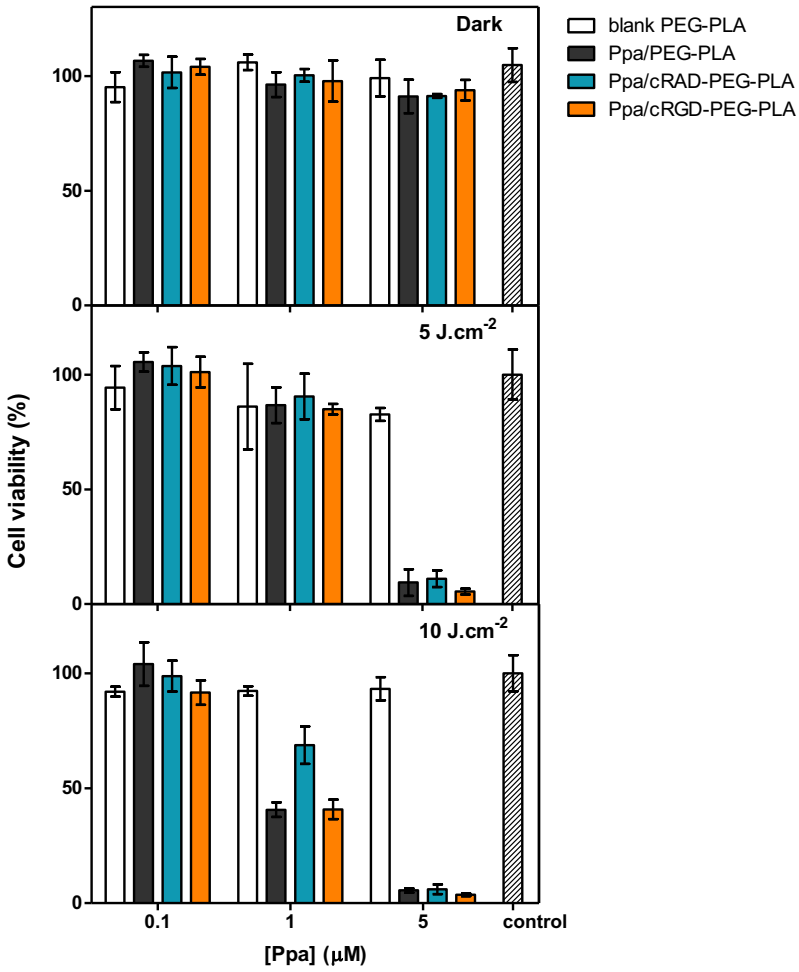

Figure A5. U-87 MG cells viability (expressed as percentage) after incubation for 1.5 h with Ppa / PEG-PLA, Ppa / cRAD-PEG-PLA and Ppa / cRGD-PEG-PLA NPs at Ppa concentrations of 0.1, 1 and 5 μM and subsequent irradiation at 0, 5 or 10 J·cm^{-2}. Control stands for cells incubated only in complete culture medium and irradiated at the corresponding light fluence. Values are the mean ± SD of three replicates.

APPENDIX B: ADDITIONAL INFORMATION FOR CHAPTER 5

SUBCHAPTER 5A: ZnPcSMP as Photosensitizer

B.1 Synthesis

B.1.1 Spectral Data of the Cleavable Linker (4)

^{1}H NMR, ^{13}C NMR, gHSQC and COSY spectra of (*Z*)-3, 3'-(Ethene-1,2-diylbis(sulfanediyl)dipropanoic acid (**4**) are shown in Figure B1.

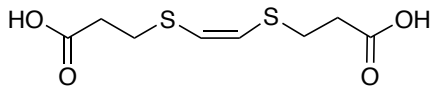

4

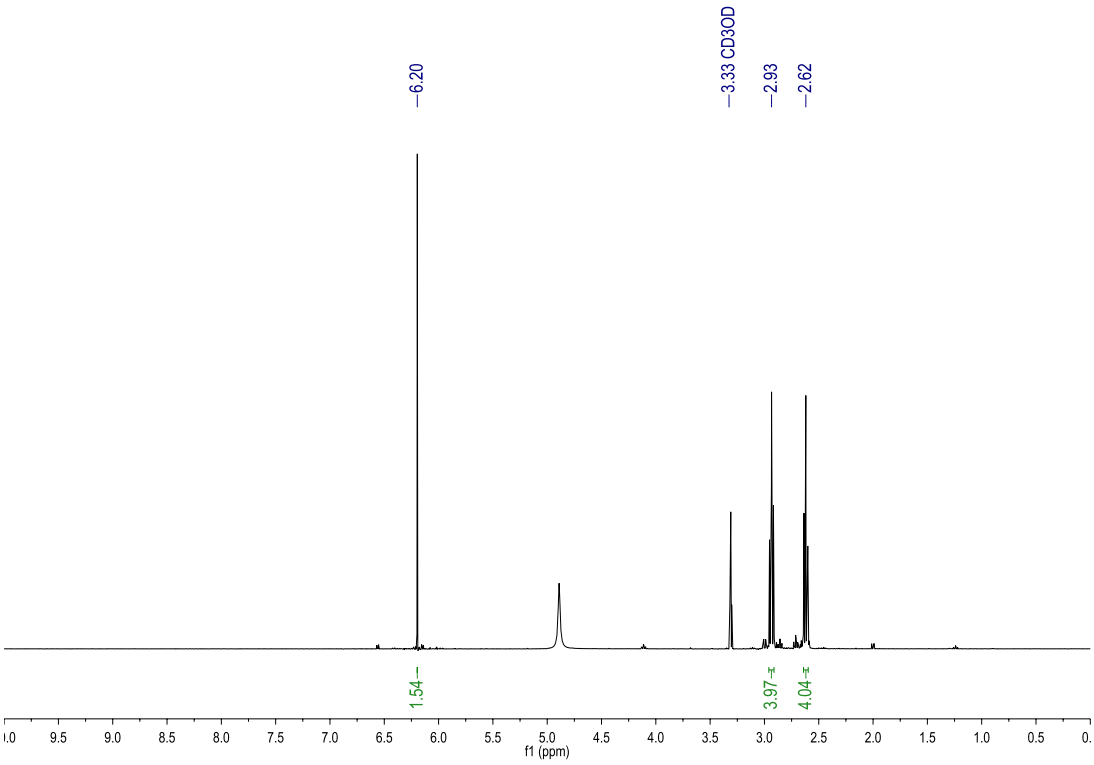

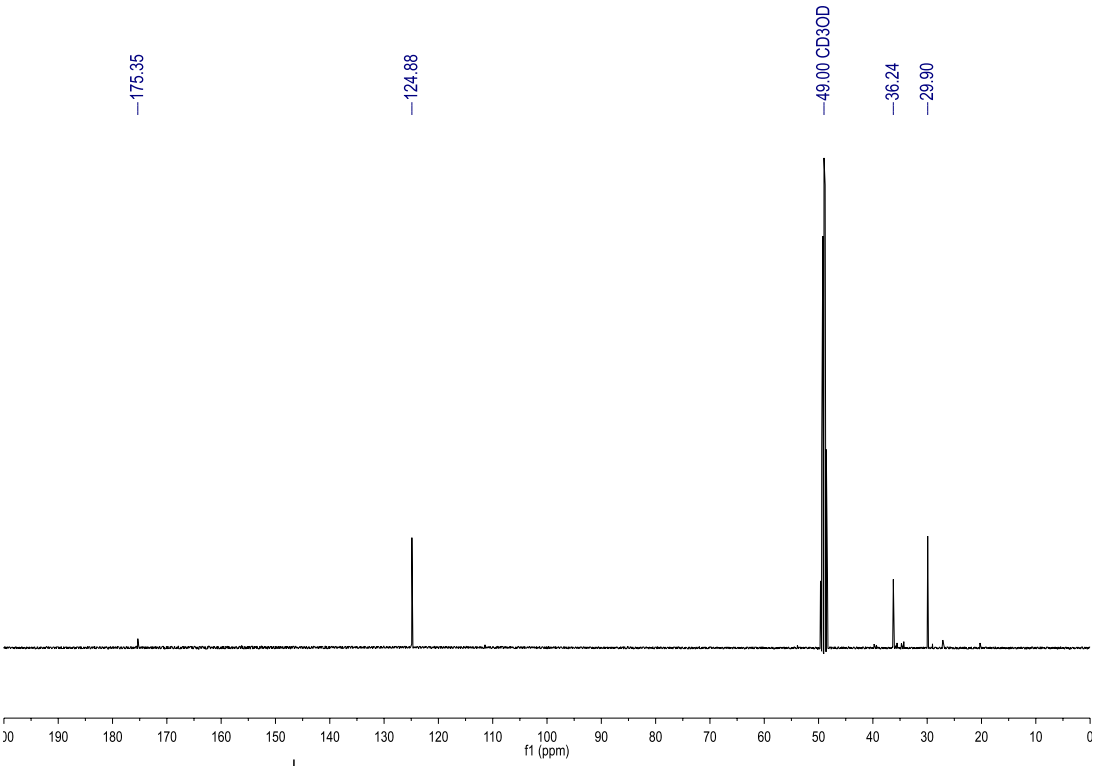
175.35
124.88
49.00 CD3OD
36.24
29.90
f1 (ppm)

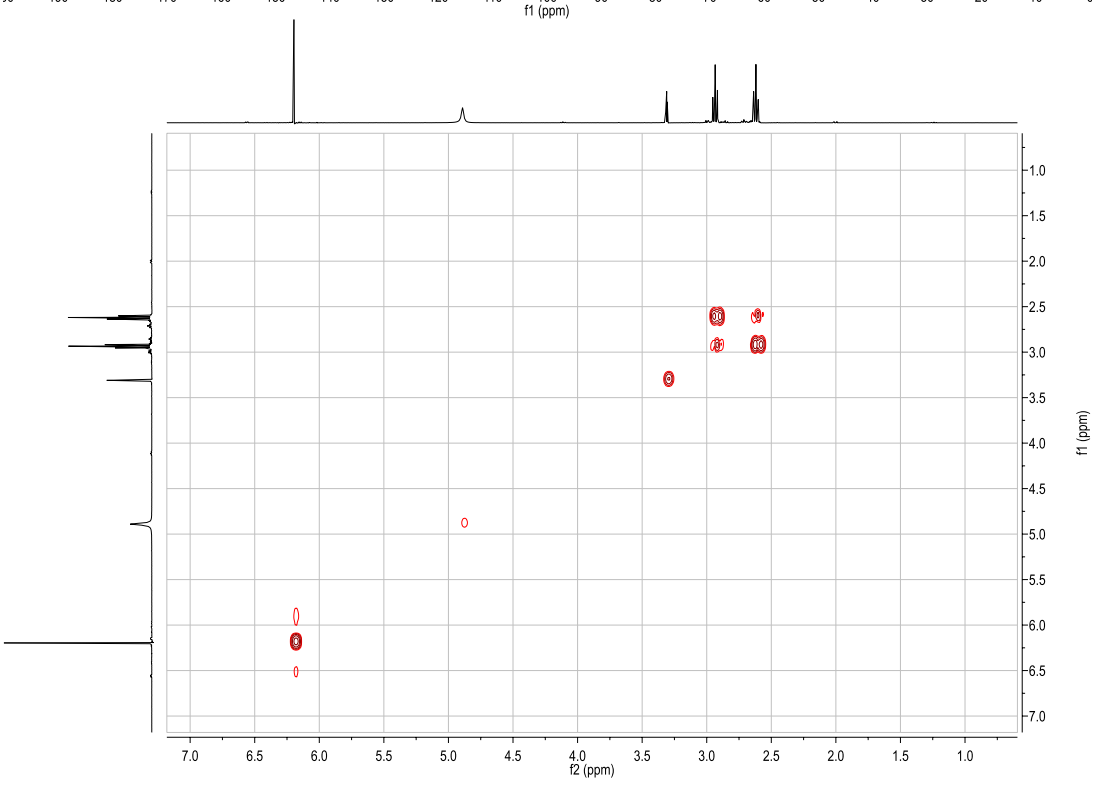
f2 (ppm)
f1 (ppm)

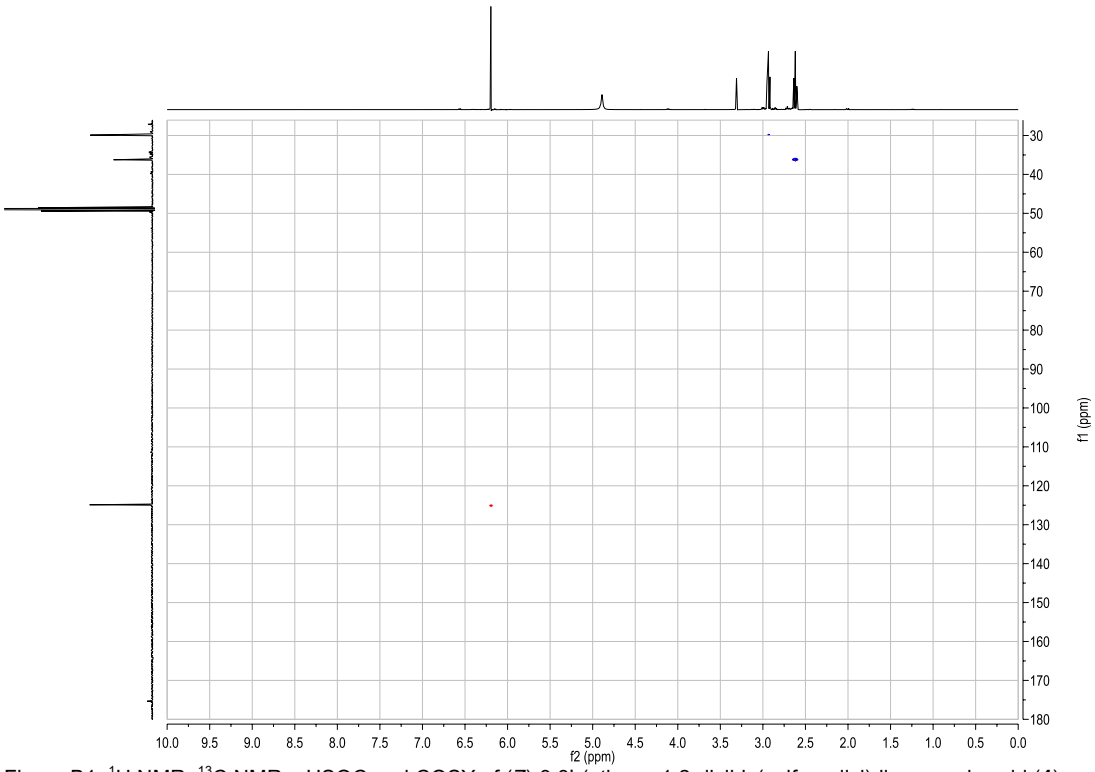

Figure B1. ^{1}H NMR, ^{13}C NMR, gHSQC and COSY of (*Z*)-3,3'-(ethene-1,2-diylbis(sulfanediyl)dipropanoic acid (**4**)

B.1.2 Synthesis of Non-Targeted Nanoparticles: MSNPA, MSNPB and MSNPC

The preparation of MSNP**A**, mesoporous silica nanoparticles with the photosensitizer ZnPcSMP covalently attached and without the antibody Cetuximab, was carried out in three steps (Figure B2):

i. Preparation of mesoporous silica nanoparticles with ZnPcSMP covalently attached (MSNP2).

ii. Modification of the surface of MSNPs with amino groups (MSNP3).

iii. Attachment of the PEG chain *via N*-acylation between the NHS from PEG and an amino group on surface of MSNP (MSNP**A**).

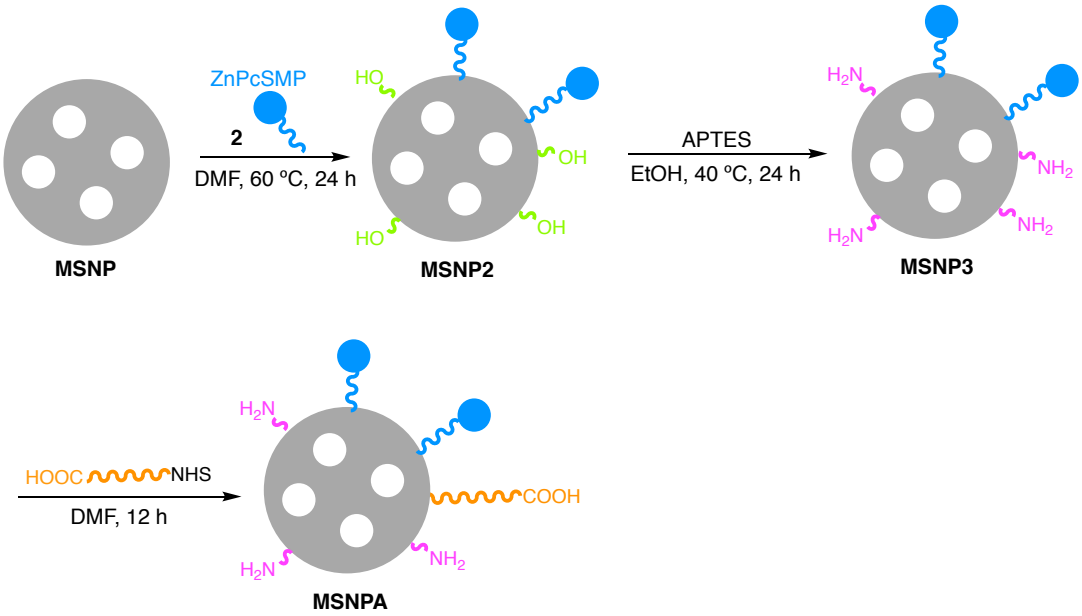

Figure B2. Preparation of the nanoparticle MSNP**A**.

The preparation of MSNP**B**, mesoporous silica nanoparticles with ZnPcSMP and DOX covalently attached (the last one by means of a $^1O_2$-clevable linker) and without the antibody Cetuximab, was carried out in four steps (Figure B3):

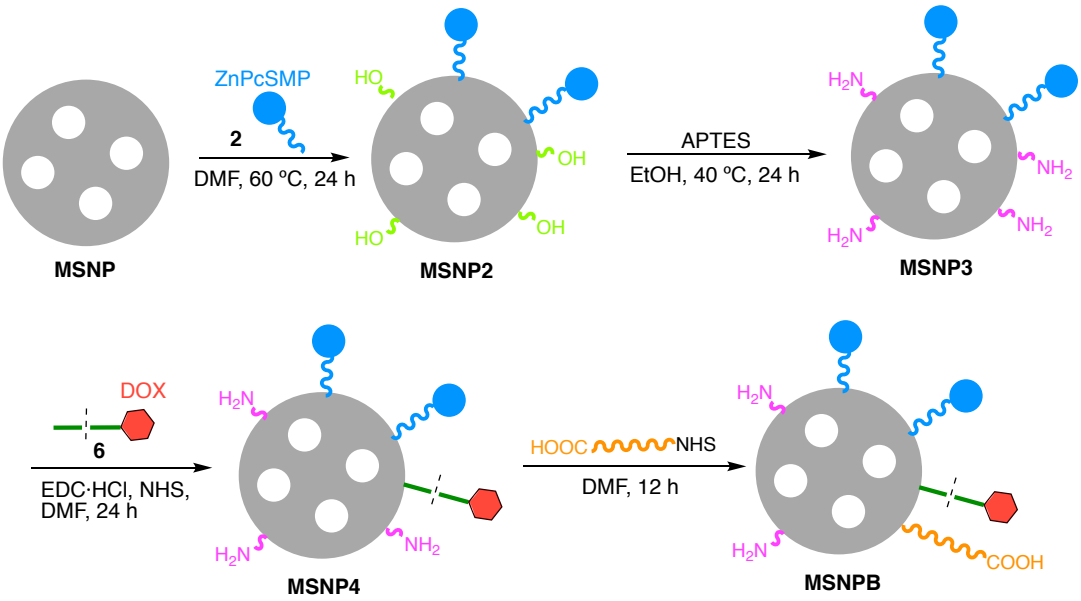

Figure B3. Preparation of the nanoparticle MSNP**B**.

i. Preparation of mesoporous silica nanoparticles with ZnPcSMP covalently attached (MSNP2).

ii. Modification of the surface of MSNPs with amino groups (MSNP3).

iii. Attachment of compound **6**. The activated acid of compound **6** reacted with an amino group on surface of MSNP (MSNP4).

iv. Attachment of the PEG chain (MSNP**B**).

The preparation of mesoporous silica nanoparticles with ZnPcSMP and DOX covalently attached and without the antibody Cetuximab, was carried out in four steps (Figure B4):

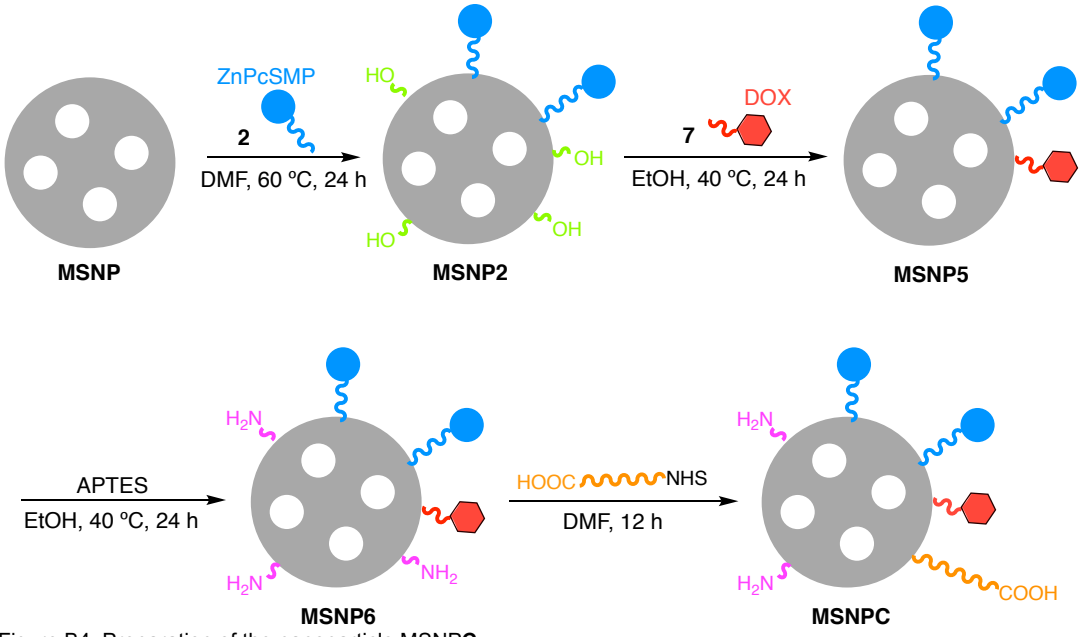

Figure B4. Preparation of the nanoparticle MSNP**C**.

i. Preparation of mesoporous silica nanoparticles with ZnPcSMP covalently attached (MSNP2).

ii. Modification of the surface of MSNPs with the compound **7** (MSNP5).

iii. Modification of the surface of MSNPs with amino groups (MSNP6).

iv. Attachment of the PEG chain (MSNP**C**).

B.1.3 Synthesis of MSNPA Nanoparticle Labelled with FITC

The preparation of mesoporous silica nanoparticles with the photosensitizer ZnPcSMP and the antibody Cetuximab covalently attached and labeled with FITC (MSNP**A**-FITC-Cet) was carried out in four steps (Figure B5):

i. Preparation of mesoporous silica nanoparticles with ZnPcSMP covalently attached (MSNP2).

ii. Modification of the surface of MSNPs with amino groups (MSNP3).

iii. Attachment of FITC to MSNP by reaction with an amino group on surface of MSNP3 (MSNP3-FITC).

iv. Attachment of compound **10** (PEG-Cet) (MSNP**A**-FITC-Cet).

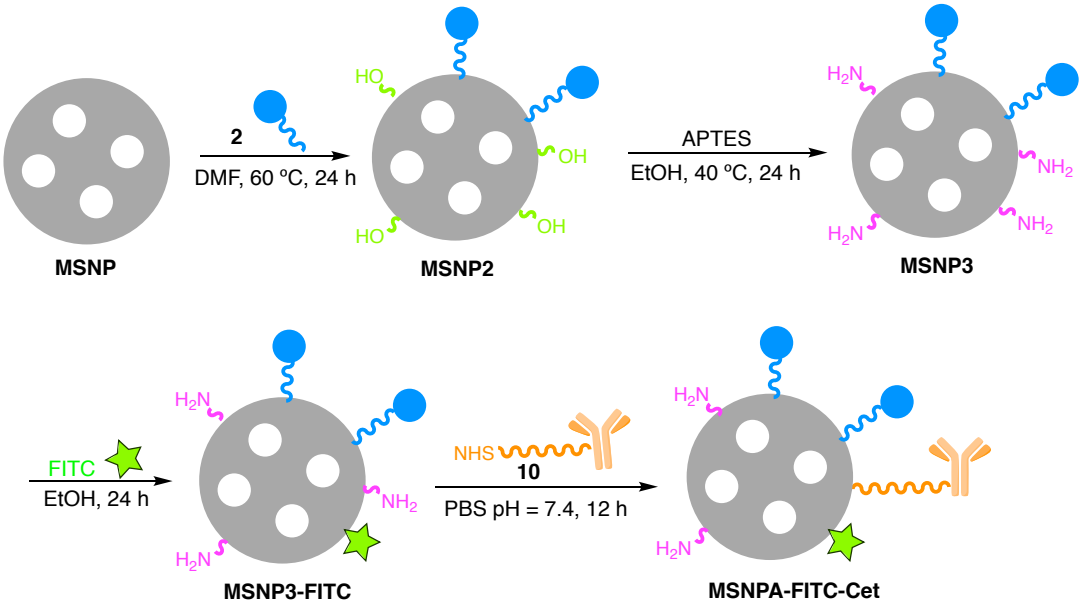

Figure B5. Preparation of the nanoparticle MSNP**A**-Cet labeled with FITC.

The overall preparation scheme of the non-targeted analog is shown in Figure B6. The synthetic route is the same as for MSNP**A**-FITC-Cet except the last step, in which NHS-PEG-COOH is attached to the nanoparticles without its prior conjugation with Cetuximab.

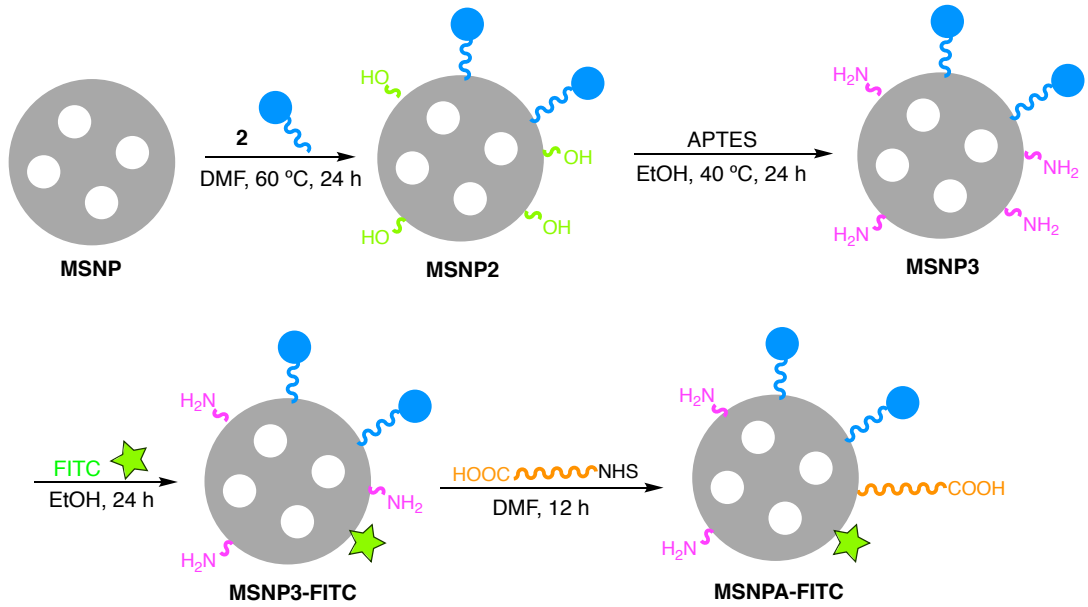

Figure B6. Preparation of the nanoparticle MSNP**A** labeled with FITC.

B.2 Physicochemical Characterization

Table B1 summarizes the values obtained from the physicochemical characterization of FITC-labeled nanoparticles.

Table B1. Characterization of nanoparticles. PdI: polydispersity index. EE.: entrapment efficiency.

NPs formulation	Size / nm	PdI	Zeta-potential / mV	[ZnPcsMP] / µM	[FITC] /µM	EE
MSNP**A**-FITC	276 ± 5	0.24 ± 0.04	20.1 ± 0.5	11.9	21.0	100%
MSNP**A**-FITC-Cet	440 ± 32	0.94 ± 0.05	-	"	"	-

B.3 Photophysical Characterization

B.3.1 Calculation of Molar Extinction Coefficients of ZnPcSMP in DMF and in Water

For the verification of the Lambert-Beer law, an analysis of linear regression between the intensity of the Q-band and the concentration was performed, with values of 0.999 for ZnPcSMP in both DMF and H_2O (Figure B7).

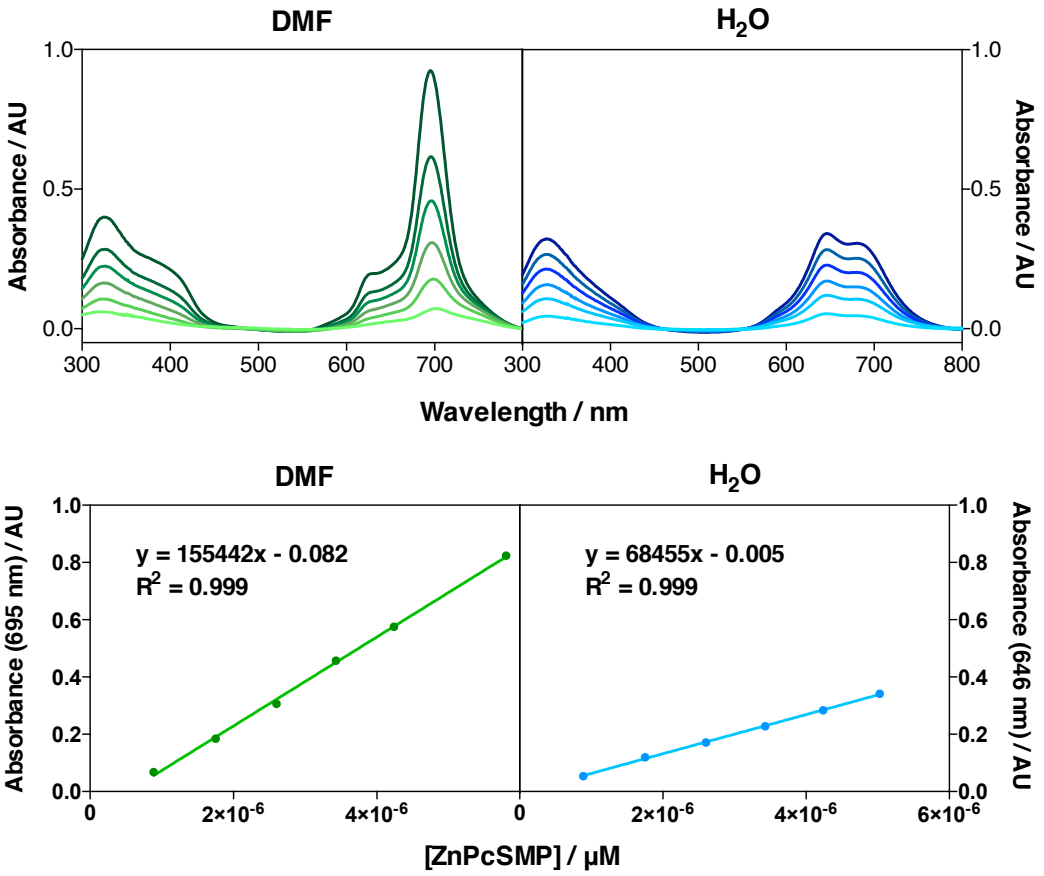

Figure B7. UV-vis spectra of ZnPcSMP in DMF and H_2O at different concentrations. Below, linear regression between the intensity of the Q-band and the concentration of ZnPcSMP in DMF and H_2O.

B.3.2 Calculation of Fluorescence Quantum Yield of ZnPcSMP in DMF and in Water

The calculation of fluorescence quantum yield from acquired data was performed as described in Section 3.2.2.1 in Chapter 3. The gradients of the graphs obtained in Figure B8 are proportional to the quantum yield of the different samples. Absolute values are calculated using the standard sample ZnPc in DMF which have a fixed and known fluorescence quantum yield value (Φ_F = 0.28). For ZnPcSMP in aqueous suspension, a correction for the solvent was performed using the following refractive index values: 1.43 for DMF and 1.33 for H_2O.

The linear regression values obtained from the different samples are the following:

i. For ZnPc in DMF: y = 1835696770x + 982793 with R^2 = 0.999.

ii. For ZnPcSMP in DMF: y = 203618858x – 238828 with R^2 = 0.999.

iii. For ZnPcSMP in H_2O: y = 3268213x + 750518 with R^2 = 0.975.

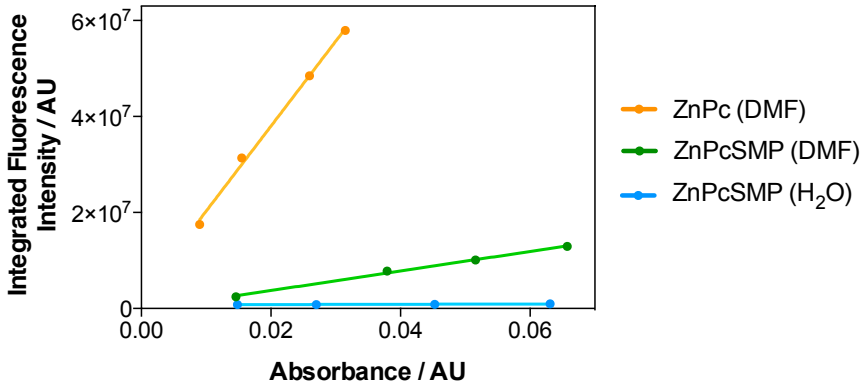

Figure B8. Linear plots for ZnPcSMP in DMF and H_2O and for the reference ZnPc in DMF.

B.3.3 Calculation of Singlet Oxygen Quantum Yield of ZnPcSMP in DMF and in Water

The calculation of singlet oxygen quantum yield from acquired data was performed as described in Section 3.2.2.2 in Chapter 3. The gradients of the graphs obtained in Figure B10 are proportional to the quantum yield of the different samples. Absolute values are calculated using the standard sample which have a fixed and known fluorescence quantum yield value: ZnPc in DMF (Φ_Δ = 0.56) and PNS in D_2O (Φ_Δ = 0.98).

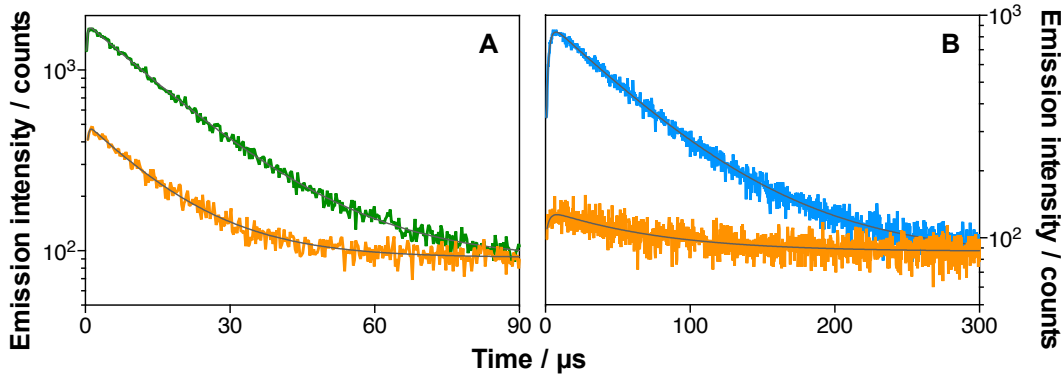

Figure B9. Time-resolved phosphorescence decays at 1275 nm of free ZnPcSMP (in green) in DMF (A) in D_2O (B). ZnPc (in green) was employed as reference in DMF. PNS (in blue) was used as a reference in D_2O. λ_{exc} = 1275 nm. λ_{em} = 355 nm.

The linear regression values obtained from the different samples are the following:

i. For ZnPc in DMF: y = 4999x – 47 with R^2 = 0.999.

ii. For ZnPcSMP in DMF: y = 1518x – 127 with R^2 = 0.996.

iii. For PNS in D_2O: y = 2274x + 35 with R^2 = 0.999.

iv. For ZnPcSMP in D_2O: y = 137x – 1 with R^2 = 0.993.

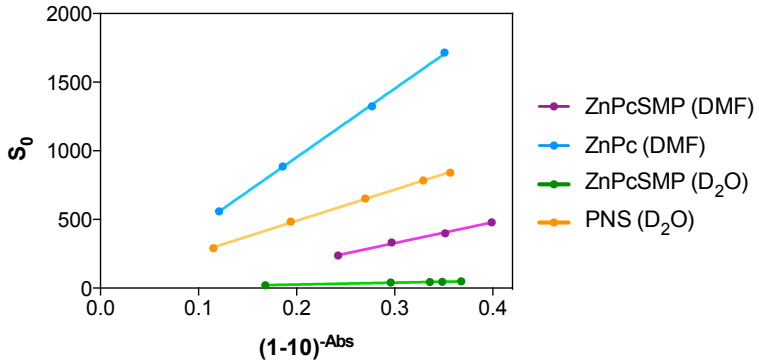

Figure B10. Linear plots for ZnPcSMP (in DMF and D_2O) and for the references ZnPc in DMF and PNS in D_2O.

B.4 Biological Studies

Figure B11 summarizes the results obtained from *in vitro* phototoxicity studies performed in AsPC-1 cells with the free photosensitizer ZnPcSMP, MSNP**A**-Cet, MSNP**B**-Cet, MSNP**C**-Cet and their non-targeted analogous. Same concentration of the photosensitizer (2 μM) was incubated for 24 h for each sample. Afterwards, cells were irradiated with 30 J·cm^{-2} of red light. This study is the same reported in Section 5.2.4.2 in Chapter 5 but using 30 J·cm^{-2} light dose instead of 60 J·cm^{-2}.

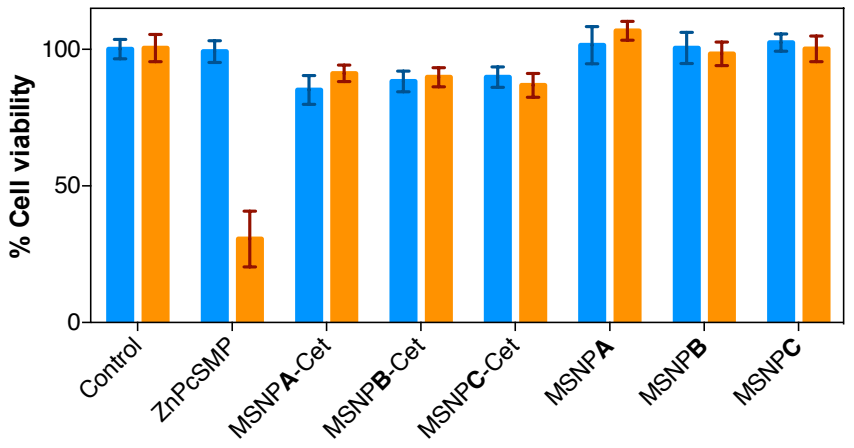

Figure B11. Phototoxicity studies in AsPC-1 of MSNP**A**-Cet MSNP**B**-Cet and MSNP**C-Cet** nanoparticles and their non-targeted analogs. Cells were irradiated with 30 J·cm^{-2} (in orange). Dark controls were also performed for each sample (in blue). Non-treated cells were used as control. Values reported are the mean ± SD of at least three independent experiments.

SUBCHAPTER 5B: IRDye700DX as Photosensitizer

B.5 Synthesis

B.5.1 Synthesis of Non-Targeted Nanoparticles: MSNPD and MSNPE

The preparation of MSNP**D**, mesoporous silica nanoparticles with the photosensitizer IRDye700DX and without the targeting moiety Cetuximab, was carried out in three steps (Figure B12):

i. Modification of the surface of MSNPs with amino groups (MSNP7).

ii. Attachment of IRDye700DX *via N*-acylation between an amino group on surface of MSNP and the activated carboxylic acid (NHS) of the IRDye700DX (MSNP8).

iii. Anchoring of PEG. *N*-acylation between the NHS group from the PEG and an amino group on surface of MSNP (MSNP**D**).

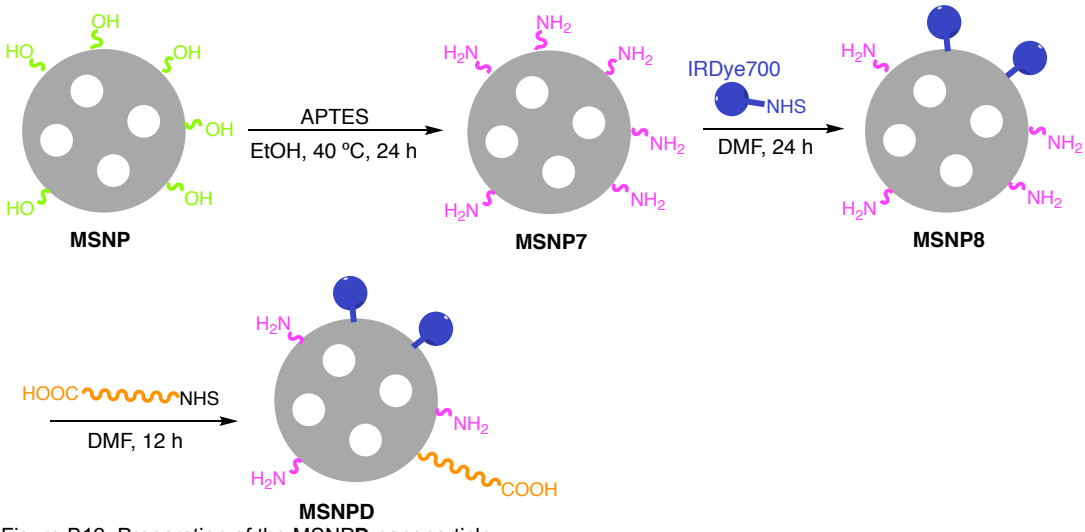

Figure B12. Preparation of the MSNP**D** nanoparticle.

The preparation of MSNP**E**, mesoporous silica nanoparticles with the photosensitizer IRDye700DX and the chemotherapeutic agent Doxorubicin covalently attached (the last one attached by means of a $^1O_2$-cleavable linker) was performed in four steps (Figure B13):

i. Modification of the surface of MSNPs with amino groups (MSNP7).

ii. Attachment of IRDye700DX (MSNP8).

iii. Conjugation *via* *N*-acylation of the compound **6** (after its activation with EDC/NHS) to an amino group on surface of MSNP (MSNP9).

iv. Anchoring of PEG (MSNP**E**).

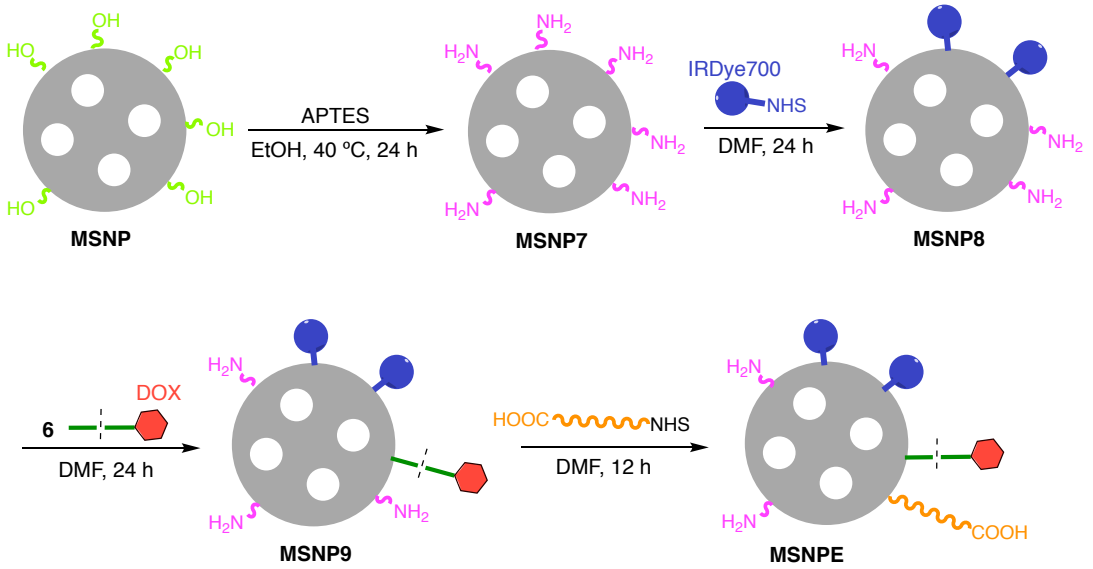

Figure B13. Preparation of the MSNP**E** nanoparticle.

B.5.2 Synthesis of Faraway DOX Nanoparticles

In order to distance the DOX from the nanocarrier and thus, from the IRDye700DX; DOX was conjugated to a NHS-PEG$_{5kDa}$-COOH molecule *via* *N*-acylation (Figure B14).

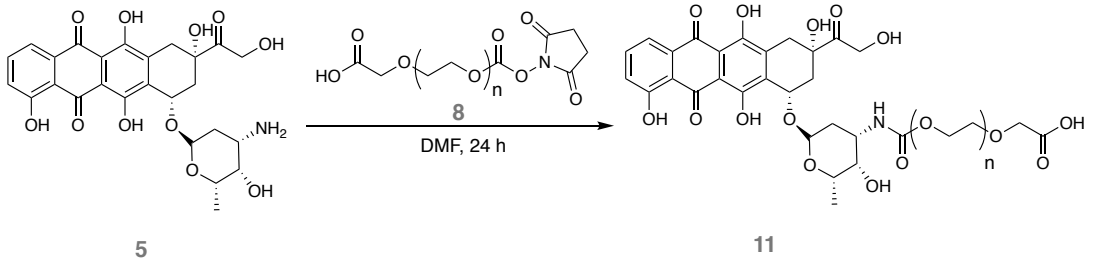

Figure B14. Preparation of the DOX-PEG conjugate (compound **11**).

The preparation of MSNP10, mesoporous silica nanoparticle with IRDye700DX and DOX covalently attached (the last one attached by means of a large PEG) was performed in three steps (Figure B15):

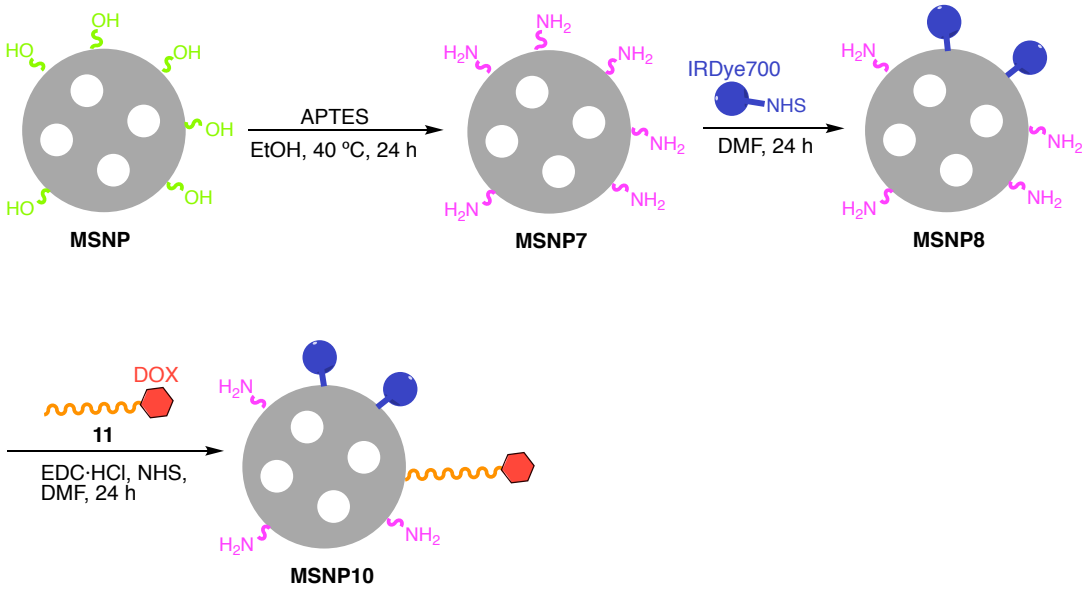

Figure B15. Preparation of the MSNP10 nanoparticles, in which DOX is attached to the MSNP by means of a long PEG chain.

i. Modification of the surface of MSNPs with amino groups (MSNP7).

ii. Attachment of IRDye700DX (MSNP8).

iii. Anchoring *via N*-acylation with EDC/NHS chemistry of the compound **11** to an amino group on surface of MSNP (MSNP10). MSNP10 was obtained with a DOX concentration of 110.3 μM.

B.6 Biological Studies

A cell viability study was performed to study the cytotoxicity of free Cetuximab at the same concentrations as were incubated for MSNP**D**-Cet (Section 5.6.4.3.2 of Chapter 5) in AsPC-1 and MIA PaCa-2 cells. Cetuximab was incubated for 24 h. MTT assay was performed 48 h after the incubation time finished. The results are summarized in Figure B16.

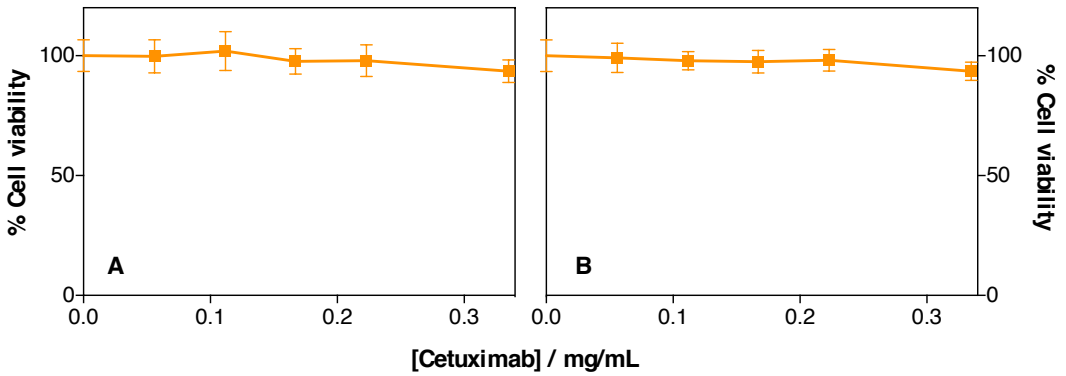

Figure B16. Phototoxicity studies of free Cetuximab in AsPC-1 (A) and MIA PaCa-2 cells (B). A range of Cetuximab concentrations (0.06, 0.11, 0.17, 0.22 and 0.33 mg/mL) were incubated in the cells for 24 h. Values reported are the mean ± SD of at least three independent experiments.